Università degli Studi di Ferrara

DOCTORAL COURSE IN PHYSICS

CYCLE XXXIII

COORDINATOR Prof. Eleonora Luppi

Digging for treasure: delving deep into maps of polarized CMB radiation in light of next-generation experiments

Scientific/Disciplinary (SDS) FIS/02

Candidate
Margherita Lembo

Supervisor
Dr. Massimiliano Lattanzi

Co-advisor
Prof. Paolo Natoli

Years 2017-2020

Università degli Studi di Ferrara

DOCTORAL COURSE IN PHYSICS

CYCLE XXXIII

COORDINATOR Prof. Eleonora Luppi

Digging for treasure: delving deep into maps of polarized CMB radiation in light of next-generation experiments

Scientific/Disciplinary (SDS) FIS/02

Candidate
Margherita Lembo

Supervisor
Dr. Massimiliano Lattanzi

Co-advisor
Prof. Paolo Natoli

Years 2017-2020

Dopo tanta
nebbia
a una
a una
si svelano
le stelle
[...]

G. Ungaretti

Abstract

Observations of the Cosmic Microwave Background (CMB) have substantially changed how humanity perceived the Universe. Planck satellite measured the temperature anisotropy with unprecedented precision, but we have only begun to tap the information encoded in CMB polarization and CMB lensing. Hence, lines of investigation seeking to extract information from the CMB beyond that contained in its temperature anisotropies are particularly timing. Both these lines of research are explored in this thesis.

In the first part, we will indeed explore the possibility of extracting new information from CMB polarization. The idea is to infer, from the parity-violating power spectra (*e.g.*, EB and TB) and the CMB circular polarization power spectrum, the optical properties of our Universe. We will discuss our formalism which describes the in-vacuo conversion between polarization states of propagating radiation, also known as generalized Faraday effect (GFE), in a cosmological context. Then, thinking of GFE as a potential tracer of new, isotropy- and/or parity-violating physics, we will recast the GFE parameters as the components of an effective "cosmic susceptibility tensor". For the case of a wavenumber-independent susceptibility tensor, we will also derive constraints using the current linear and circular polarization data.

In the second part of this thesis, we will analyze the impact of masking bright extragalactic sources on both the reconstructed CMB lensing potential and the lensed CMB power spectra. This is particularly relevant for future data, where large populations of extragalactic sources will be resolved. We will assess this bias using realistic numerical simulations which include non-Gaussian correlated maps of the CMB lensing convergence, tSZ and CIB emission at various frequencies as well as a halo catalogue.

In the last part of this thesis, we will discuss the prospects of both these two projects in view of the future CMB experiments.

Contents

Introduction

The Cosmic Microwave Background (CMB) is the oldest light of the Universe, dating back to about 400 000 years after the Big Bang, when the Universe *moved from opaque to transparent.*
Our knowledge about the Universe, its history and its composition, is mainly due to the crucial observation of this radiation, that allowed us to test the predictions of the Hot Big Bang model and to compare different cosmological models with each other. We might say that CMB observation enable us to set a milestone for the confirmation of the standard cosmological model (ΛCDM).

The CMB was detected for the first time in 1964 by Arno Penzias and Robert Wilson, that observed by chance an isotropic and homogeneous noise in the microwave band, with an equivalent black-body temperature of about 3 K [1]. Then, thanks to the pioneering satellite experiment named COBE (Cosmic Background Explorer), launched in 1989, we have been able to also detect the temperature anisotropies ($\Delta T/T < 10^{-5}$) of this radiation.

After COBE, several ground-based and satellite experiments have followed, having as main goal the measurement of the CMB temperature anisotropies with increasing angular resolution and accuracy. The dramatic technological improvement culminated in the Planck satellite by ESA, launched in 2009 [2]. These measurements have allowed us to get tight constraints on cosmological parameters, addressing questions about the structure, evolution, content, age and ultimate fate of our Universe.

Additionally, more recently, it has been discovered that the CMB radiation is also partially linearly polarized, with polarization anisotropies having an amplitude of about 10% of temperature anisotropies [3]. There are two CMB linear polarization modes, the E-modes and the B-modes, which have different behavior under a parity transformation. This explains the nomenclature, chosen in analogy with electric and magnetic fields.

Alongside these modes, we have also to mention the so-called V-modes, describing the degree of circularly polarized CMB radiation. The CMB anisotropies are expected to be linearly polarized by Compton scattering at the epoch of recombination. The circular polarization of CMB is therefore usually taken to be zero. Nevertheless, a primordial degree of circular polarization is not observationally excluded [4, 5], and, indeed, there are several standard and non-standard mechanisms which could generate it. Part of the original work discussed in this thesis is related to the studies of CMB circular polarization. The V-mode polarization can be a powerful tool for constraining new physics beyond the standard model.

In the Planck legacy release of 2018, the collaboration delivered the ultimate measurement of CMB temperature anisotropies in terms of accuracy with the first small scale (E-mode) polarization measurement on large sky fractions [6]. Definitely, Planck has almost exhausted all the information contained in the temperature field of the CMB, but we have only begun to tap the information encoded in CMB polarization. Constraining Cosmology through CMB polarization is indeed the focus of the next-decade experiments.

In this context, the so-called B-modes of CMB polarization are the key observable of the coming decade. These modes represent the imprinting, in the CMB polarization maps, of the gravitational waves emitted during a brief phase of accelerated expansion occurring in the primordial stages of our Universe, called inflation.
The measurement of B-modes on large angular scales will be the focus of LiteBIRD satellite, recently approved by the JAXA (Japan Aerospace Exploration Agency), whose launch is expected in the next decade [7]. Alongside future space missions, ground-based experiments must be also mentioned, including Simons Observatory (SO) [8] and CMB-Stage4 (CMB-S4) [9], which are complementary to LiteBIRD satellite and will target the measurement of CMB polarization at small angular scales and high angular resolution. SO is expected to start observations in the early 2020s, while the construction phase of CMB-S4 is planned to start in 2021.

Despite its incredible successes, ΛCDM still cannot explain fundamental concepts in the understanding of our Universe, that, at the moment, is based on unknown entities like dark energy, dark matter and inflation. The ΛCDM model might be seen as an approximation to a more realistic scenario that still needs to be fully understood. In the next decade, the main challenge would be to answer this question, and the CMB polarization will help us to fulfill this task.

To this picture, we have to further add another important piece.
The CMB anisotropies can be indeed distinguished in two types depending on the epoch in which these were originated. The primary anisotropies are imprinted

at the CMB last scattering surface[1] and, hence, due to effects that occur at the time of recombination and before. They provide us an unparalleled probe of the primordial density fluctuations that seeded large-scale structure formation, opening a window on the primordial Universe.
The secondary anisotropies are instead generated by processes happening after recombination. Among them, it is worth mentioning the gravitational lensing, *i.e.* the slight distortion suffered by the temperature and the polarization fields, generated when the CMB photons pass close to large distributions of matter. As predicted by General Relativity, indeed, light is deflected by the gravitational field generated by matter.
The gravitational lensing generates a spurious B-mode component that acts as a contaminant for all the measurements of primordial B-modes. Thus to constrain the primordial gravitational wave background and the physics of inflation, it has to be accounted for in the analysis and potentially removed from CMB maps.

Moreover, the CMB lensing is, without any doubt, one of the crucial observables of 2020's Cosmology, as it provides an invaluable tool to reconstruct the integrated distribution of matter in the Universe, including dark matter, and to place even more stringent constraints on neutrino masses. Hence, a not completely exhaustive comprehension of this effect could preclude us the possibility of constraining Cosmology, or even the chance to faithfully reconstruct the spectrum of primordial B modes.
The lensing power spectrum, reconstructed from CMB maps, is, however, strongly influenced by the way the initial CMB maps are masked; in other words by how the regions most contaminated by signals other than the CMB (generally known as foregrounds) are removed from the analysis [10]. The increase in angular resolution of future experiments will allow us to observe the sky in more detail, revealing a growing number of particularly bright point sources (*e.g.* clusters of galaxies) that will have to be masked. To avoid biased estimate of both the CMB lensing potential and the CMB unlensed field, studying the effect of these masks is crucial, since it may impact substantially forthcoming high-resolution experiments, such as SO and CMB-S4.

The purpose of this thesis can be framed into the questions: Which information can be still extracted from the CMB? How to extract this information in a reliable way?

[1] CMB radiation appears to come from a spherical surface around the observer such that the radius of the shell is the distance each photon has travelled since it was last scattered at the epoch of recombination. This surface is what is called the last scattering surface.

The thesis is organized as follows:

1. In Chpt. 1, we introduce the theoretical background of CMB radiation, laying the essential tools for the comprehension of the next chapters. We start with a brief description of the processes giving rise to this radiation. Then, we present the full set of Boltzmann equations for the evolution of cosmological perturbations, providing a formal integration of this set of equations. Finally, we derive the expressions for the angular power spectra sourced by both scalar and tensor primordial perturbations. We show how their peculiar shapes encode information on cosmological parameters.

2. In Chpt. 2, we go beyond the picture outlined in Chpt. 1. We review the cosmic birefringence, presenting also the state-of-the-art measurements. Moreover, we introduce the CMB circular polarization, discussing the possibility that it can be generated by standard model extensions. We also review the most recent experiments that have measured it. In this chapter, we present then our unified model, a phenomenological framework describing the mixing of different polarization states during CMB photon propagation. This mixing is known as generalized Faraday effect (GFE). In the last part of this chapter, we interpret GFE as the result of light propagating into a medium with an anisotropic and/or parity-violating susceptibility tensor. Finally, we present bounds on GFE from current cosmological data in the case of a wavenumber-independent susceptibility tensor.
   The results presented in this chapter are based on the following paper:

   - [11, M. Lembo, M. Lattanzi, L. Pagano, A. Gruppuso, P. Natoli, F. Forastieri, *Through a dark crystal: CMB polarization as a tool to constrain the optical properties of the Universe*]

3. Chpt. 3 can be divided into two parts. In the first, we introduce the CMB lensing theory, extracting the modifications induced on the CMB power spectra. Then, we discuss how to reconstruct the lensing potential from the observed CMB maps, focusing on the lensing reconstruction pipeline that we use in the second part of this chapter. In the second part, we assess the impact of masking bright extragalactic sources on CMB maps and, indeed on the lensing reconstruction itself. We explore this fundamental topic in view of the next-decade CMB experiments.
   The results presented in this chapter are based on the following papers:

- [12, G. Fabbian, J. Carron, A. Lewis, M. Lembo, *Lensed CMB power spectrum biases from masking extragalactic sources*]
- [13, M. Lembo, G. Fabbian, J. Carron, A. Lewis *CMB lensing reconstruction biases from masking extragalactic sources*]

4. In Chpt. 4, we provide an overview of the state-of-the-art CMB measurements, highlighting the achievements and the open questions that have to be addressed. Then, we discuss the near-future experiments, placing our works in this context. In particular, we discuss the implications of the results reported in Chpt. 2 and Chpt. 3 for next-generation experiments.

1

The Cosmic Microwave Background

Much of what we know about the origin and early history of the Universe comes from a relic radiation discovered by chance more than 50 years ago: the Cosmic Microwave Background (CMB).
In 1948, this radiation was hypothesized as a probe of the Hot Big Bang model, by Alpher and Herman, following the arguments by Gamow [14, 15].
The CMB was actually observed for the first time in 1964, when two researchers of the Bell Industries, Arno Penzias and Robert Wilson, working with a Dicke radiometer, accidentally bumped into a temperature excess of about 4.2 K. They were looking at an isotropic radiation in the radio-microwave region of the electromagnetic spectrum, a panoramic snapshot of the Universe around 400.000 years after the Big Bang, when photons started to travel freely through space rather than constantly being scattered by electrons and protons in plasma. Fourteen years later, Penzias and Wilson received the Nobel Prize in physics for this discovery.

After this first observation, many (ground-based, airborne and space) experiments came one after another targeting this microwave radiation from the early Universe. The first accurate measurements of the CMB frequency spectrum and the first detection of small temperature anisotropies ($\delta T/T \sim 10^{-5}$) were performed by the COBE (COsmic Background Explorer) satellite launched by NASA in 1992 [16]. The scientific goals reached were: a full sky map of the CMB radiation, showing the small temperature fluctuations at large angular scales, and a remarkably precise measurement of the black body spectrum with $T = 2.72548 \pm 0.00057\,\mathrm{K}$. This was a turning point for modern Cosmology since these anisotropies can be traced back to small quantum fluctuations in the early Universe, and paved the way for the new generation space missions.
WMAP (Wilkinson Microwave Anisotropy Probe) of NASA [3] and Planck of

ESA [2], launched in 2001 and 2009 respectively, were devoted to fully analyze the anisotropies with an improved sensitivity and angular resolution.
In 2018, Planck collaboration, made up of hundreds of scientists around the world, delivered the ultimate measurement of CMB temperature anisotropies in terms of accuracy together with the first polarization measurement on large sky fractions [6].
CMB radiation, in fact, is also linearly polarized at the $\simeq 10\%$ level ($\delta P \sim 0.1\,\delta T$). The first detection was actually achieved by DASI (Degree Angular Scale Interferometer) instruments in 2002 [17]. This degree of polarization is mainly due to Thomson scattering during the epoch of recombination (please see Sec. *1.1* and Sec. *1.2.1.1* for details).

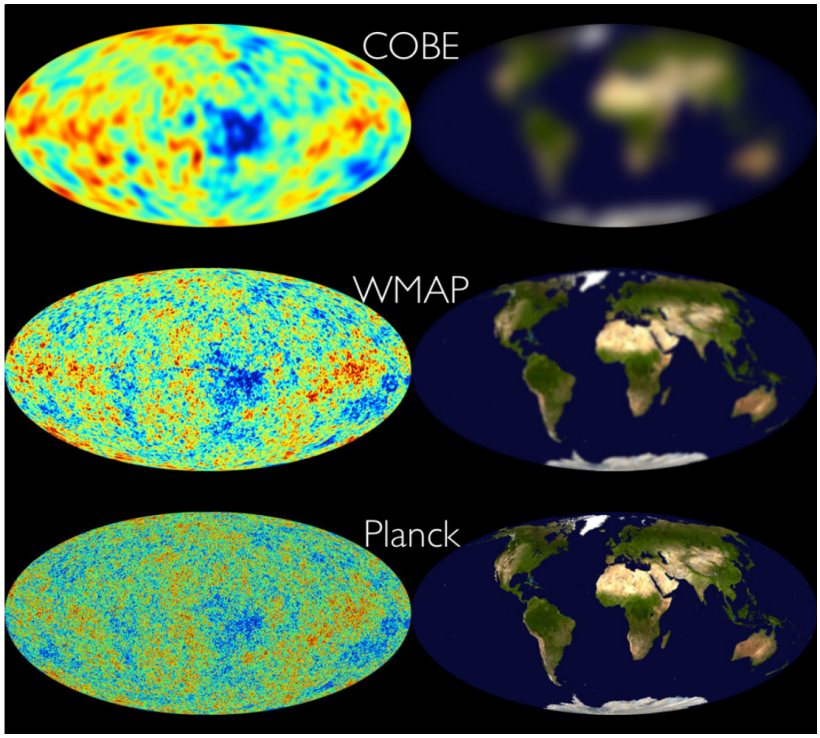

Figure 1.1: *CMB radiation as seen by COBE, WMAP and Planck, from left to right. For comparison, on the right, a picture of Earth showing the increase in resolution and sensitivity.*

Thanks to these measurements with unprecedented precision, Planck provided the most accurate estimates of several key cosmological parameters. Nevertheless, we have only begun to tap the information encoded in the CMB radiation.
Constraining Cosmology through CMB polarization is, indeed, the focus of the next-decades experiments, such as LiteBIRD satellite [7], recently approved by the JAXA (Japan Aerospace Exploration Agency) or the ground-based experiments,

like Simons Observatory [8] and CMB-Stage4 [9]. See Chpt. 4 for more details about next-generation CMB experiments.
CMB polarization together with the CMB lensing (discussed in more detail in Chpt. 2 and Chpt. 3, respectively) are truly 21st century-phenomena, that will allow us to to test, confirm or rule out cosmological models and our understanding of the fundamental physical laws of the Universe we live in.

This chapter is organized as an overview of the CMB theory, laying the essential tools for the comprehension of the next chapters. After a brief description of the thermal history of the early Universe, in Sec. *1.1*, the main steps to write the Boltzmann equations for photons are outlined in Sec. *1.2*. All the information about the formation and the evolution of CMB anisotropies are encoded in these two coupled differential equations, one for temperature and one for polarization anisotropies. At the end of this section, a formal integration of this set of equations, following the *line of sight approach* introduced by U. Seljak and M. Zaldarriaga in 1996 [18], is also provided. In Sec. *1.3*, we finally construct the auto- and cross-correlation power spectra describing their peculiar shapes and outlining their dependencies on cosmological parameters, Sec. *1.4*.

1.1 A brief thermal *history of* early *time*

We are living in an expanding and adiabatically cooling Universe (a prediction of the Hot Big Bang model). Hence, going back in time means meeting epochs with increasing temperatures and energies. If we push this concept to the extreme, we inevitably reach a singularity, a point of infinite density, temperature and gravity, where (or when) the Einstein theory of General Relativity is not able to describe anymore what is going on. This initial singularity, called Big Bang, is located at a finite time in the past, around 13.78 billion years ago. The measurement of the *age* of the Universe is another achievement that was possible thanks to CMB observations [19].

After the Big Bang, the Universe has experienced an epoch of exponential expansion called inflation. This epoch was theorized about 50 years ago by several theoretical physicists, notably Alexei Starobinsky, Alan Guth and Andrei Linde. Beside solving some problems of the standard cosmological model (*e.g.* flatness and horizon problems), inflation provides an elegant explanation to the homogeneity and isotropy of the Universe, seeding the primordial perturbations (of both kinds, scalar and tensor). These perturbations are therefore the imprint

generated by the inflaton field (*i.e.* the hypothetical scalar field which has driven cosmic inflation) during the accelerated expansion. This means that measuring the amplitudes of these perturbations can provide us information on the energy scale of inflation. We will shortly come back to this point in the last section of this chapter, Sec. *1.4*.
Nevertheless, the inflationary paradigm is not the subject of this thesis and we limit ourselves to start our brief description of the Universe thermal history from times (and energies) where the Universe was composed by all the species described in the standard model of particles. Interested readers might see *e.g.* Refs. [20–24].

Hence, considering our starting point the end of inflation, the CMB radiation is the final result of a chain of processes which can be described through strong and electroweak interactions of the standard model of particles.
The first relevant event is baryogenesis, the production of a slight matter-antimatter asymmetry that will evolve in the imbalance of particles and antiparticles seen in the today observed Universe. The origin of this process is still a matter of discussion.
Baryogenesis could be the result (*i.e.* the observable) of the first symmetry breaking phase transition predicted by the standard model of particles, the so-called electroweak phase transition. It occurred $\sim 10^{-12}$ seconds after the Big Bang, when the temperature was $\sim 10^{15}\,\mathrm{K}$. This transition, through the Higgs mechanism, leads particles to have mass. See *e.g.* Refs. [25, 26] for details.
At the end of this phase, the Universe was a plasma mainly filled by leptons and quarks. The latter behaved like free particles since the coupling constant for strong interactions was still small enough. Usually this state is called quark-gluon plasma. As the Universe cooled further, at the temperature of $\sim 10^{12}\,\mathrm{K}$, quarks passed from being free in the quark-gluon plasma to be confined into hadrons due to strong interaction. The standard model of particles predicts here the second and last phase transition, the so-called quantum chromodynamics phase transition. At this point the only relativistic particles left in the primordial soup were photons, neutrinos and electrons.

Going further, when the Universe was ~ 1 second old, neutrinos, which have been in equilibrium due to weak interactions, such as

$$\bar{\nu} + \nu \rightleftharpoons e^+ + e^- \qquad \text{and} \qquad e^- + \bar{\nu} \rightleftharpoons e^- + \bar{\nu}\,, \tag{1.1}$$

started decoupling and propagating freely, with their distribution temperature

scaling as a^{-1} [1]. This process happened when the temperature of the Universe was the same of a supernovae, $\sim 10^{10}$ K.

When the temperature dropped below 10^9 K ($t \sim 10$ s), the Universe went through a period where the temperature and density of the baryon component (protons and neutrons) allowed nuclear reactions to be efficient in building nuclei. This phase is called the Big Bang Nucleosynthesis (BBN) [27]. Initially, nuclear reactions between neutrons and protons form deuterium

$$n + p \rightleftharpoons \mathrm{D} + \gamma\,. \tag{1.2}$$

However, the temperature was still high enough, so many photons have an energy greater than the binding energy of deuterium [2]. At this stage, any deuterium that was formed was immediately destroyed. This impasse at the beginning of BBN is called *deuterium bottleneck*. Once this deadlock is overcome, heavier nuclei starts to form, in particular tritium, ^{3}H, and helium ^{3}He, ^{4}He. As the light elements production ends, other elements have been produced in relatively low abundance such as lithium ^{7}Li, and beryllium ^{7}Be, but the synthesis of heavier elements is hampered by the absence of stable mass-8 nuclei.
After 10^3 seconds from the Big Bang, T $\sim 10^7$ K, the BBN can be considered as ended and the baryon content is now divided into $\sim 75\%$ of H nuclei (*i.e.* free protons), $\sim 25\%$ of ^{4}He nuclei and traces of other elements, mainly D, ^{3}H, ^{7}Li, ^{7}Be. The primordial soup is now made of e^-, survived to electron-positron annihilation due to matter-antimatter asymmetry, γ, p and light nuclei produced during BBN. In the following, we neglect the number of helium atoms forming during recombination. Moreover, the neutrinos do not influence directly the dynamics of this epoch, since they have already started to free-stream.
The thermal equilibrium is still valid through reactions such as $e^- + p \rightleftharpoons H + \gamma$, where neutral hydrogen atoms are continuously formed and then ionized due to interaction with photons. On the other hand, photons and electrons are tightly coupled via Compton scattering, while electrons and protons strongly interact via Coulomb scattering. In this situation of thermal equilibrium, $T_{eq} = T$, the number densities n_i follow the Maxwell-Boltzmann distribution for non-relativistic

[1] Also known as Robertson Walker scale factor, $a \equiv a(t)$ is the dimensionless scale factor of the expansion. Moreover, the Hubble parameter (*i.e.* the expansion rate of the Universe) is define as $H \equiv \dot{a}(t)/a(t)$. We will come back later on this factor, Eq. 1.26.

[2] The binding energy of deuterium is ~ 2225 keV.

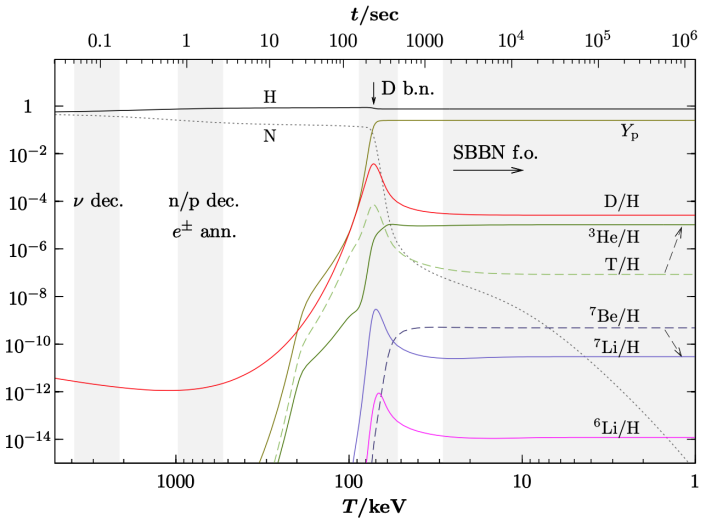

Figure 1.2: *BBN timeline [28].*

particles ($T < m_i$) [29]

$$n_i = g_i \left(\frac{m_i T}{2\pi}\right)^{3/2} e^{-\frac{m_i}{T}}, \qquad i = e(=e^-),\, p \text{ and } H\,; \tag{1.3}$$

where g_i is the statistical weight and m_i the mass of the particle i. Using Eq. 1.3 in the equilibrium abundance ratio among hydrogen atoms, protons and electrons

$$\frac{n_e n_p}{n_H} = \frac{g_e g_p}{g_H} \left(\frac{m_e m_p}{m_H}\right)^{3/2} \left(\frac{T}{2\pi}\right)^{3/2} e^{-\frac{(m_e+m_p-m_H)}{T}} \simeq \left(\frac{m_e T}{2\pi}\right)^{3/2} e^{-\frac{B_H}{T}}, \tag{1.4}$$

where $B_H \equiv (m_e + m_p - m_H)$ is the binding energy of the hydrogen atom, $g_e = g_p = 2$ and $g_H = 4$. In the prefactor, we have used $m_H \simeq m_p$.
Because of the neutrality of the Universe, we can assume $n_p = n_e$. Moreover, since we are neglecting the relatively small number of helium atoms, $n_p + n_H$ is equal to the the baryon density, $n_b \sim 10^{-9} T^3$. Therefore, defining the free electron fraction as

$$X_e \equiv \frac{n_e}{n_p n_H}, \tag{1.5}$$

Eq. 1.4 reads

$$\frac{X_e^2}{1 - X_e} = \frac{10^9}{T^3} \left(\frac{m_e T}{2\pi}\right)^{3/2} e^{-\frac{B_H}{T}}. \tag{1.6}$$

This equation is known as Saha equation. As long as $T \gtrsim B_H$, X_e is ≈ 1, *i.e.* all hydrogen is ionized. While, when T becomes well below B_H, the right side of

Eq. 1.6 decreases very rapidly and X_e goes fast to zero, *i.e.* hydrogen atoms are forming.

The recombination temperature, T_{rec} is usually defined as the temperature when almost 90% of electrons are already bounded into hydrogen atoms, $X_e\left(T_{rec}\right) \sim 0.1$. Hence, using Saha equation, $T_{rec} \simeq 0.3$ eV $\simeq 3600$ K, implying a recombination redshift $z_{rec} \simeq 1320$[3].
Recombination happens when the Universe is already dominated by matter[4] and, using the fact that the scale factor goes as

$$a\left(t\right) = \left(\frac{t}{t_0}\right)^{2/3}, \tag{1.7}$$

the time of recombination is $t_{rec} \approx 290000$ yrs.

Before recombination, free electrons interacted frequently with photons through Thomson scattering

$$e + \gamma \rightleftharpoons e + \gamma\,, \tag{1.8}$$

but, when hydrogen recombines, the free electron density drops down quickly and photons inside the plasma no longer interact. They start to free stream in a neutral Universe. This process takes the name of photon decoupling.

We can evaluate the temperature of decoupling by considering that Compton scattering is efficient until $\Gamma \gtrsim H$, where Γ is the scattering rate and H is Hubble rate of expansion. Therefore, $\Gamma\left(T_{dec}\right) \sim H\left(T_{dec}\right)$ implies $T_{dec} \simeq 0.27$eV $\simeq$ K. Following the above calculation, $z_{dec} \simeq 1100$ and $t_{dec} \simeq 380000$ yrs. This is the last moment when photons interact with the primordial plasma, the so-called *Last Scattering Surface* (LSS). It is worth highlighting that, even if the two events (recombination and decoupling) are quite close in time, they originate a last scattering layer. Nevertheless, comparing its size (thickness) with the Universe time scale, it can be considered a surface.
From now on, photons are free to travel in the Universe that is, now, transparent to electromagnetic radiation. These photons, carrying on information of the pre-last-scattering Universe, combine together and form the relic radiation known as Cosmic Microwave Background (CMB) radiation: one of the most important discoveries of mankind.

[3] $T_{rec} = T_0\left(1 + z_{rec}\right)$, with T_0 the photon temperature today.

[4] The Universe is supposed to be dominate by different components during its timeline. At very early time, most of the energy in the Universe was in the form of radiation. Nevertheless, since the energy of a relativistic particle falls as $1/a$ while that of non relativistic matter remains constant at m, matter overtook radation. At relatively recent times, the Universe seems to be dominated by another component whose density remains constant with time, dark energy.

Before moving on, it is worth underlining that the physics behind the decoupling cannot be explained only using the Saha equation, see Fig. 1.3. We need a complete discussion through the Boltzmann equation, as we will see in the next section.

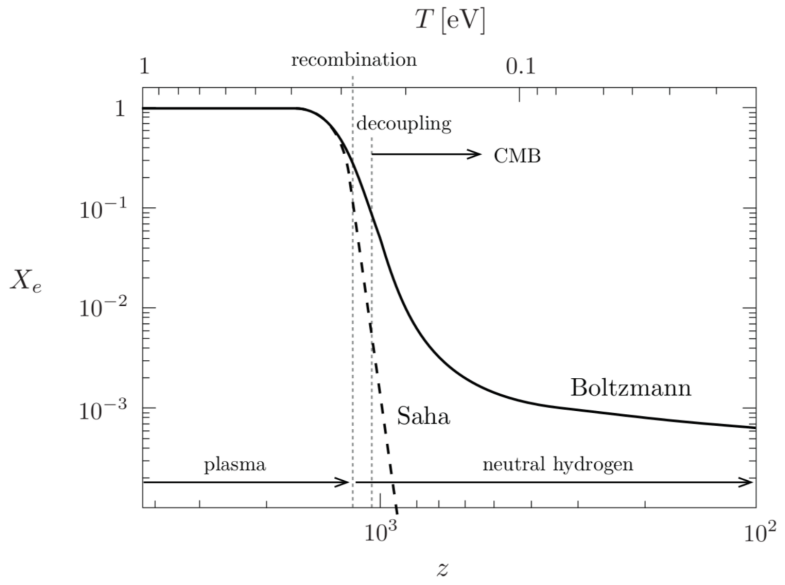

Figure 1.3: *Free electron fraction as function of redshift [29].*

1.2 Boltzmann equation for photons

To derive the fluctuations of the CMB radiation, we will have to follow the complicated set of interactions between all the components until recombination. The photons are affected by gravity and by Compton scattering with free electrons. The latter are tightly coupled to protons by Coulomb interaction. Both are affected by gravity. The metric (scalar and tensor) perturbations couple gravitationally to all these components in the primordial plasma, including neutrinos and dark matter. Thus, to solve for the photon distributions, we need to solve the other components, see Fig 1.4.

The main tool for doing this is the Boltzmann equation, that schematically can be written as

$$\frac{\mathrm{d}f}{\mathrm{d}t} = C\left[f\right] , \tag{1.9}$$

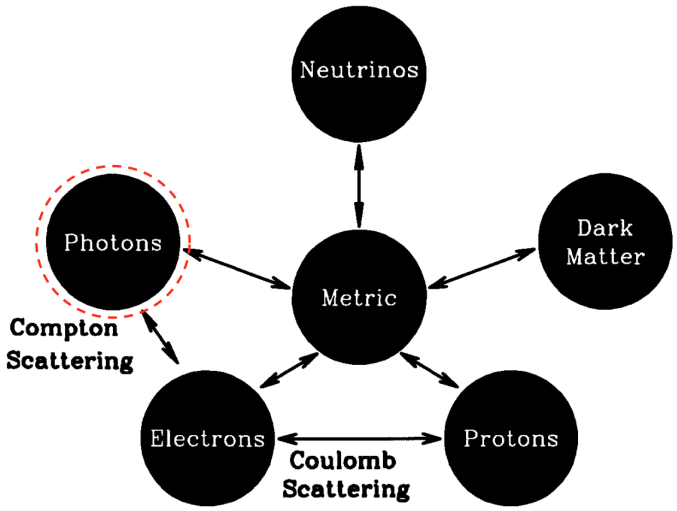

Figure 1.4: *The intricate ways in which the different components of the Universe interact with each other. Based on [29].*

where f is the phase-space distribution function of a single species and C is the collision term, that, in principle, can depend on the distribution functions of several species, *i.e.* we will have coupled equations. In absence of collisions, the distribution function clearly obeys to the collisionless Boltzmann equations $\mathrm{d}f/\mathrm{d}t = 0$, also known as Liouville equation.
We are interested in the evolution of the photon distribution function, $f_\gamma \equiv f$. Photons mostly interact with the electrons, so Eq. 1.9 reads

$$\frac{\mathrm{d}f}{\mathrm{d}t} = C\left[f,\, f_e\right] . \tag{1.10}$$

Nevertheless, due to Coulomb scattering, electrons are strongly coupled to the rest of the plasma. For this reason, electrons and baryons can be treated as a single tightly-coupled fluid and it makes no difference to think at the right-hand side of Eq. 1.10 as the photon-electron or photon-baryon coupling term.

The common procedure to write down the full Boltzmann equation for photons consists in spitting the problem in half, calculating the collision term alone and the Liouville equation separately. Moreover, the former is usually computed assuming the Thomson amplitude as constant and independent on propagation direction and polarization of the radiation. In this way, we are only accounting for temperature anisotropies. For more detail about this calculation, see [29].

For the purpose of this thesis, we include polarization from the beginning. As we will see in the next section, Sec. *1.2.1*, Thomson scattering couples the total

intensity of radiation with its polarization. Therefore, it is convenient to adopt the density matrix formalism [30].
The density matrix, ρ, for a system of photons, in terms of the Stokes parameters (please see App. C for a review), can be written as

$$\rho = \begin{pmatrix} I+Q & U-iV \\ U-iV & I-Q \end{pmatrix} = \\ = \frac{1}{2}\left(I\mathbb{1} + Q\sigma_3 + U\sigma_1 + V\sigma_2\right) , \tag{1.11}$$

where $\mathbb{1}$ is the identity matrix and σ_i are the Pauli spin matrices. Following [30], the Boltzmann equation for the density matrix, a generalization of Eq. 1.10, can be written as

$$\frac{\mathrm{d}\rho_{ij}(\mathbf{p})}{\mathrm{d}t} = -\frac{1}{2\Xi\, p^0}\int_{-\infty}^{+\infty}\langle\left[H_I(t),\,\left[H_I(0),\,\mathcal{D}^0_{ij}(\mathbf{p})\right]\right]\rangle \equiv \mathcal{C} \ . \tag{1.12}$$

The right-hand side, $\mathcal{C}$, is simply the collision term, with H_I the interaction Hamiltonian describing Compton scattering of photons off electrons [5]. $\mathcal{D}_{ab}(\mathbf{p})$ is the photon number operator, $\mathcal{D}_{ij}(\mathbf{p}) \equiv a_i^\dagger(\mathbf{p}')a_j(\mathbf{p})$, with the superscript $^{(0)}$ referring to the free-field operators. $\{a_r^\dagger,\, a_r\}$ are the photon creation and annihilation operators. The expectation value of $\mathcal{D}$ is related to the density matrix through the constant Ξ, $\langle\mathcal{D}_{ab}(\mathbf{p})\rangle = \Xi\, p^0\, \rho_{ab}(\mathbf{p})$.

In the next sections, we hint the calculations, computing Compton scattering term in Sec. *1.2.1* and the collisionless equation in Sec. *1.2.2*. We will assemble all the ingredients in Sec. *1.2.3*, achieving the final evolution equations for both temperature and polarization anisotropies, starting from both scalar and tensor perturbations.
The interested reader can find more details about these calculations in [29–33].

1.2.1 Collision term

1.2.1.1 Thomson scattering

As already mentioned in the previous section, the dominant scattering process close to recombination is the Thomson scattering of the photons off the free

[5] In principle, a second coupled equation for the electron density matrix must be solved simultaneously. However, in the early Universe, the electrons are, with good approximation, in a thermal distribution. Therefore, the evolution of their density matrix becomes trivial.

electrons in the plasma,

$$e(\mathbf{q}) + \gamma(\mathbf{p}) \rightleftharpoons e(\mathbf{q}') + \gamma(\mathbf{p}')\,. \tag{1.13}$$

Thomson scattering is the low-energy limit of Compton scattering and is a valid description in the regime where the photon energy is much less than the rest-mass energy of the electron. An important feature of Thomson scattering is that an initially unpolarized radiation can be polarized if the incident intensity varies with direction.

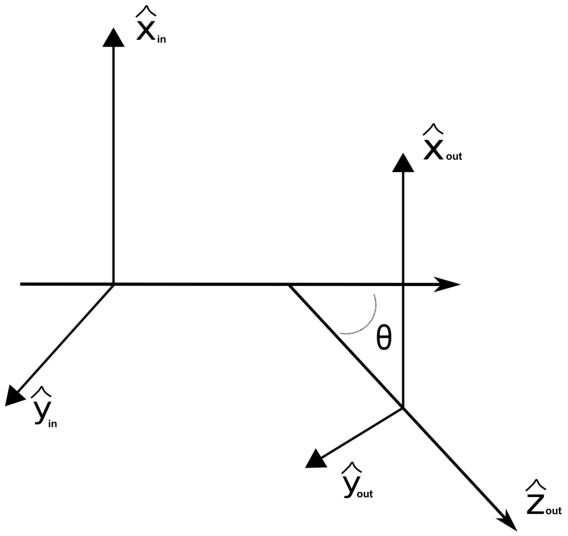

Figure 1.5: *Scheme of the reference frames defined for incoming and outgoing radiation involved in Thomson scattering.*

Let us describe the outgoing radiation in terms of the Stokes I , U , Q and V parameters with the subscript *out* and the incoming radiation with the subscript *in*.

We choose the $\hat{z}$-axis to lie in the direction of the outgoing radiation, and we define the outgoing radiation reference frame, $\hat{x}_{out}$, $\hat{y}_{out}$, and, respectively, the incoming radiation reference frame, $\hat{x}_{in}$, $\hat{y}_{in}$, such that $\hat{x}_{out}$ and $\hat{x}_{in}$ are orthogonal to the scattering plane and, $\hat{y}_{out}$ and $\hat{y}_{in}$ are in the polarization plane. See Fig. 1.5. Therefore, the Thomson scattering differential cross-section for an incident wave with linear polarization $\hat{\mathcal{E}}_{in}$ into a scattered wave with linear polarization $\hat{\mathcal{E}}_{out}$ is given by

$$\frac{\mathrm{d}\sigma}{\mathrm{d}\Omega} = \frac{3\sigma_T}{8\pi}|\hat{\mathcal{E}}_{in}\cdot\hat{\mathcal{E}}_{out}|^2\,, \tag{1.14}$$

where σ_T is the total Thomson cross-section,

$$\sigma_T = \frac{8\pi}{3}\left(\frac{q_e^2}{4\pi\epsilon_0 m_e c^2}\right)^2 = 6.6 \cdot 10^{-25}\,\mathrm{cm}^2\,. \tag{1.15}$$

To derive the Stokes parameters of scattered radiation in terms of those of incoming radiation, it is useful to introduce the incoming (outgoing) radiation intensities along the $\hat{x}_{in}$ and $\hat{y}_{in}$ ($\hat{x}_{out}$ and $\hat{y}_{out}$) directions as

$$I_x = \frac{I+Q}{2}\,; \tag{1.16a}$$

$$I_y = \frac{I-Q}{2}\,. \tag{1.16b}$$

The scattered intensities are [30]:

$$\begin{aligned} I_{x,\,out} &= \frac{3\sigma_T}{8\pi}\left[I_{x,\,in}\left(\hat{\epsilon}_{x,\,in}\cdot\hat{\epsilon}_{x,\,out}\right)^2 + I_{y,\,in}\left(\hat{\epsilon}_{y,\,in}\cdot\hat{\epsilon}_{x,\,out}\right)^2\right] = \\ &= \frac{3\sigma_T}{16\pi}\,I_{in}\,; \end{aligned} \tag{1.17a}$$

$$\begin{aligned} I_{y,\,out} &= \frac{3\sigma_T}{8\pi}\left[I_{x,\,in}\left(\hat{\epsilon}_{x,\,in}\cdot\hat{\epsilon}_{y,\,out}\right)^2 + I_{y,\,in}\left(\hat{\epsilon}_{y,\,in}\cdot\hat{\epsilon}_{y,\,out}\right)^2\right] = \\ &= \frac{3\sigma_T}{16\pi}\,I_{in}\,\cos^2\theta\,, \end{aligned} \tag{1.17b}$$

where $\hat{\epsilon}_{j,\,in(out)}$ are the unit vectors along the $j = x,\,y$ directions and $\cos\theta \equiv \hat{\epsilon}_{y,\,in}\cdot\hat{\epsilon}_{y,\,out}$.
Thus, using Eq. 1.16, the Stokes parameters of the scattered radiation in terms of the incoming radiation intensity reads

$$I_{out} = \frac{3\sigma_T}{16\pi}\,I_{in}\,\left(1+\cos^2\theta\right)\,; \tag{1.18a}$$

$$Q_{out} = \frac{3\sigma_T}{16\pi}\,I_{in}\,\sin^2\theta\,. \tag{1.18b}$$

This calculation gives no information about the Stokes U or V parameters. As will be shown later, the V parameter remains zero after Thomson scattering. In other words, circular polarization is not expected to be present at the time of last scattering. As we will see later, it can be generated by known physics as CMB photons propagate across the Universe [34–38], but only in tiny amounts; however, physics beyond the standard model might be responsible for the generation of a larger amount of circular polarization [39–47].

The Stokes U is, instead, zero only in this reference frame. Therefore, rotating the $\{x_{in}\,, y_{in}\}$ reference frame by an angle ϕ, and using the transformation properties of the Stokes Q and U parameters (see App. C), we get

$$I_{out} = \frac{3\sigma_T}{16\pi}\int \mathrm{d}\Omega\, \left(1+\cos^2\theta\right) I_{in}(\theta,\phi)\,; \tag{1.19a}$$

$$Q_{out} = \frac{3\sigma_T}{16\pi}\int \mathrm{d}\Omega\, \sin^2\theta\cos 2\phi I_{in}(\theta,\phi)\,; \tag{1.19b}$$

$$U_{out} = -\frac{3\sigma_T}{16\pi}\int \mathrm{d}\Omega\, \sin^2\theta\sin 2\phi I_{in}(\theta,\phi)\,. \tag{1.19c}$$

We have also integrated over all the incoming directions. Eq. 1.18 is, indeed, valid for a single incoming propagation direction at a time. It is interesting to note that the outgoing polarization state depends only on the intensity distribution of the unpolarized incident radiation.
Then, simply expanding the intensity of the incident radiation in spherical harmonics,

$$I_{in}\,(\theta,\phi) \;=\; \sum_{\ell m} a_{\ell m} Y_{\ell,m}\,(\theta,\;\phi)\;, \tag{1.20}$$

leads to the following

$$I_{out} = \frac{3\sigma_T}{16\pi}\left[\frac{8}{3}\sqrt{\pi}\,a_{00} + \frac{4}{3}\sqrt{\frac{\pi}{5}}\,a_{20}\right]; \tag{1.21a}$$

$$Q_{out} = \frac{3\sigma_T}{4\pi}\sqrt{\frac{2\pi}{15}}\,\mathrm{Re}\,a_{22}\,; \tag{1.21b}$$

$$U_{out} = -\frac{3\sigma_T}{4\pi}\sqrt{\frac{2\pi}{15}}\,\mathrm{Im}\,a_{22}\,. \tag{1.21c}$$

These expressions are telling us the already anticipated important property of the Thomson scattering: the outgoing radiation originating from the scattering of an originally unpolarized radiation gets linearly polarized if the incoming radiation has a non-zero quadrupole.

1.2.1.2 (A hint of) Computation of the scattering term

In the following, the calculation for the right-hand side of Eq. 1.12 is outlined. The full calculation are performed in [30]. This term is quite lengthy to evaluate since it is quadratic in the interaction Hamiltonian

$$H_I \equiv H_{QED}(t) \;=\; \int \mathrm{d}^3\mathbf{x}\, \mathcal{H}_{QED}\,, \tag{1.22a}$$

with

$$\mathcal{H}_{QED}(x) \;=\; -e \;:\; \overline{\psi}(x) A(x) \psi(x) \;:\,, \tag{1.22b}$$

where ψ is the electron field operator, $A \equiv A^\mu \gamma_\mu$ is the photon field operator contracted with the covariant gamma matrices, and : ... : means normal ordering of the operator product [48]. After some math, the resulting interaction Hamiltonian can be re-arranged as

$$H_I^0(t) \;=\; \int \frac{\mathrm{d}^3\mathbf{q}\, m_e}{(2\pi)^3\, q^0} \frac{\mathrm{d}^3\mathbf{q}'\, m_e}{(2\pi)^3\, q'^0} \frac{\mathrm{d}^3\mathbf{p}}{(2\pi)^3\, 2p^0} \frac{\mathrm{d}^3\mathbf{p}'}{(2\pi)^3\, 2p'^0} (2\pi)^3 \delta^3\left(\mathbf{q}' + \mathbf{p}' - \mathbf{q} - \mathbf{p}\right) \times$$
$$\times \exp\left[i\left(q'^0 + p'^0 - q^0 - p^0\right) t\right] \left[b^\dagger_{r'}(q') a^\dagger_{s'}(p') \left(\mathcal{M}_1 + \mathcal{M}_2\right) a_s(p) b_r(q)\right], \tag{1.23a}$$

where the scattering matrices are

$$\mathcal{M}_1 \;\equiv\; e^2 \frac{\overline{u}_{r'}(q') \epsilon_{s'}(p') \left[p + q + m_e\right] \epsilon_s(p) u_r(q)}{2\,(p \cdot q)}\,; \tag{1.23b}$$

$$\mathcal{M}_2 \;\equiv\; -e^2 \frac{\overline{u}_{r'}(q') \epsilon_{s'}(p') \left[q - p + m_e\right] \epsilon_s(p) u_r(q)}{2\,(p' \cdot q)}\,. \tag{1.23c}$$

In the previous expression the summation convention over repeated spin and polarization indices is always implied and

- q and q' are the electrons momenta;
- p and p' are the photons momenta;
- u_r is the spinor solution to the Dirac equation with spin index $r = 1,\, 2$;
- ϵ^μ_s is the photon four-vector, chosen to be real, with index $s = 1,\, 2$ labelling the physical transverse polarizations of the photon;
- $\{b^\dagger_r,\, b_r\}$ and $\{a^\dagger_r,\, a_r\}$ are the creation and annihilation operators for photons and electrons, respectively.

After substituting Eq. 1.23 in Eq. 1.12, the collision term can be written as

$$
\begin{aligned}
&\mathcal{C}[\mathbf{x},\mathbf{p}] \;= \\
&-\frac{e^4}{16\,p}\int \frac{\mathrm{d}^3\mathbf{q}}{(2\pi)^3\,q^0}\,\frac{\mathrm{d}^3\mathbf{p}'}{(2\pi)^3\,2p^0}\,\frac{1}{E(\mathbf{q}+\mathbf{p}-\mathbf{p}')}\,\delta\Big(E(\mathbf{q}+\mathbf{p}-\mathbf{p}')+p'-E(\mathbf{q})-p\Big)\times \\
&\times\left[n_e(\mathbf{x},\mathbf{q})\,\delta_{s_2 s_1'}\Big(\delta_{is_1}\,\rho_{s_2' j}(\mathbf{x},\mathbf{p})+\delta_{js_2'}\,\rho_{is_1}(\mathbf{x},\mathbf{p})\Big)\;-\;2n_e(\mathbf{p},\mathbf{q}')\,\delta_{is_1}\,\delta_{js_2'}\,\rho_{s_1' s_2}(\mathbf{x},\mathbf{p}')\right]\times \\
&\times\Bigg\{\mathcal{S}\Bigg[\Big(\epsilon_{s_1'}(\mathbf{p}')\cdot\epsilon_{s_1}(\mathbf{p})\Big)\Big(\epsilon_{s_2'}(\mathbf{p})\cdot\epsilon_{s_2}(\mathbf{p}')\Big)\;-\;\Big(\epsilon_{s_1}(\mathbf{p})\cdot\epsilon_{s_2}(\mathbf{p}')\Big)\Big(\epsilon_{s_1'}(\mathbf{p}')\cdot\epsilon_{s_2'}(\mathbf{p})\Big)+ \\
&\qquad\qquad+\;\delta_{s_1' s2}\,\delta_{s_1 s_2'}\Bigg]+ \\
&+\;2\Bigg[\Big(\epsilon_{s_1'}(\mathbf{p}')\cdot\epsilon_{s_1}(\mathbf{p})\Big)\Big(\epsilon_{s_2'}(\mathbf{p})\cdot\epsilon_{s_2}(\mathbf{p}')\Big)\;+\;\Big(\epsilon_{s_1}(\mathbf{p})\cdot\epsilon_{s_2}(\mathbf{p}')\Big)\Big(\epsilon_{s_1'}(\mathbf{p}')\cdot\epsilon_{s_2'}(\mathbf{p})\Big)\;+ \\
&\qquad\qquad-\;\delta_{s_1' s2}\,\delta_{s_1 s_2'}\Bigg]\Bigg\}\,,
\end{aligned}
\tag{1.24}
$$

where $\mathcal{S}\equiv\left(\frac{q\cdot p'}{q\cdot p}+\frac{q\cdot p}{q\cdot p'}\right)$, $E(\mathbf{q})=\left(\mathbf{q}^2+m_e^2\right)^{1/2}$ is the energy of an electron with momentum $\mathbf{q}$ and $n_e\,(\mathbf{x},\mathbf{q})$ is the unpolarized thermal Maxwell-Boltzmann distribution.

It is safe to assume that the photons and electrons kinetic energies are small compared to the electron mass, so that $p \ll m_e$ and $q \ll m_e$. Moreover, in the tight coupling regime, the temperatures of photons and electrons are the same, implying that the kinetic energy of the photons are much smaller than those of

electrons, $p \ll q$. Under these assumption Eq. 1.24 becomes

$$
\begin{aligned}
&\frac{\mathrm{d}\rho_{ij}(\mathbf{x},\mathbf{p})}{\mathrm{d}t} = \mathcal{C}[\mathbf{x},\mathbf{p}] = \\
&= \frac{e^4 n_e(x)}{16\pi m_e^2\, p}\int_0^\infty \mathrm{d}p'\, p' \int \frac{\mathrm{d}\Omega}{4\pi}\left[\delta\big(p-p'\big) + \big(\mathbf{p}-\mathbf{p}'\big)\cdot\mathbf{v}(\mathbf{x})\,\frac{\partial\delta\big(p-p'\big)}{\partial p'}\right]\times \\
&\times \left\{ -2\left(\frac{p'}{p}+\frac{p}{p'}\right)\rho_{ij}(\mathbf{x},\mathbf{p}) + 4\Big(\hat{\mathbf{p}}'\cdot\hat{\epsilon}_i(\mathbf{p})\Big)\Big(\hat{\mathbf{p}}'\cdot\hat{\epsilon}_1(\mathbf{p})\Big)\,\rho_{1j}(\mathbf{x},\mathbf{p}) + \right. \\
&+\ 4\Big(\hat{\mathbf{p}}'\cdot\hat{\epsilon}_i(\mathbf{p})\Big)\Big(\hat{\mathbf{p}}'\cdot\hat{\epsilon}_2(\mathbf{p})\Big)\,\rho_{2j}(\mathbf{x},\mathbf{p}) + \left(\frac{p'}{p}+\frac{p}{p'}-2\right)\delta_{ij}\Big(\rho_{11}(\mathbf{x},\mathbf{p}')+\rho_{22}(\mathbf{x},\mathbf{p}')\Big) + \\
&+\ \left(\frac{p'}{p}+\frac{p}{p'}\right)\times\Big[\Big(\epsilon_i(\mathbf{p})\cdot\epsilon_1(\mathbf{p}')\Big)\Big(\epsilon_j(\mathbf{p})\cdot\epsilon_2(\mathbf{p}')\Big) - \\
&\qquad + \Big(\epsilon_i(\mathbf{p})\cdot\epsilon_2(\mathbf{p}')\Big)\Big(\epsilon_j(\mathbf{p})\cdot\epsilon_1(\mathbf{p}')\Big)\Big]\Big(\rho_{12}(\mathbf{x},\mathbf{p}')-\rho_{21}(\mathbf{x},\mathbf{p}')\Big) + \\
&+\ 2\Big[\Big(\epsilon_i(\mathbf{p})\cdot\epsilon_1(\mathbf{p}')\Big)\Big(\epsilon_j(\mathbf{p})\cdot\epsilon_2(\mathbf{p}')\Big) + \\
&\qquad + \Big(\epsilon_i(\mathbf{p})\cdot\epsilon_2(\mathbf{p}')\Big)\Big(\epsilon_j(\mathbf{p})\cdot\epsilon_1(\mathbf{p}')\Big)\Big]\Big(\rho_{12}(\mathbf{x},\mathbf{p}')+\rho_{21}(\mathbf{x},\mathbf{p}')\Big) + \\
&+\ 4\Big(\epsilon_i(\mathbf{p})\cdot\epsilon_1(\mathbf{p}')\Big)\Big(\epsilon_j(\mathbf{p})\cdot\epsilon_1(\mathbf{p}')\Big)\,\rho_{11}(\mathbf{x},\mathbf{p}') + \\
&+\ \left. 4\Big(\epsilon_i(\mathbf{p})\cdot\epsilon_2(\mathbf{p}')\Big)\Big(\epsilon_j(\mathbf{p})\cdot\epsilon_2(\mathbf{p}')\Big)\,\rho_{22}(\mathbf{x},\mathbf{p}')\right\}
\end{aligned}
\tag{1.25}
$$

This equation describe the evolution of the photon density matrix to the first order in the kinematic variables. Before performing the final angular integrals, we must consider the left-hand side of Eq. 1.12 that depends on the space-time geometry we are interested on. This is done in the next section.

1.2.2 Collisionless Boltzmann equation

The left-side of Eq. 1.12 describes the propagation of photons in the space-time. To deal with it we must specify the form of the metric. For the purpose of this manuscript, we account for scalar and tensor perturbations around the

smooth Universe described by

$$g_{\mu\nu} = \begin{pmatrix} 1 & 0 & 0 & 0 \\ 0 & -a^2(t) & 0 & 0 \\ 0 & 0 & -a^2(t) & 0 \\ 0 & 0 & 0 & -a^2(t) \end{pmatrix} , \tag{1.26}$$

where the function $a(t)$ is the usual cosmological scale factor. This metric, called the Friedmann-Lemaître-Robertson-Walker (FLRW) metric[6], is describing an expanding flat Universe. Whereas the smooth Universe is characterized by a single function, $a(t)$, which depends only on time and not on space, the perturbed Universe requires more functions depending on both space and time.
In the following we take into account scalar and tensor perturbations, neglecting vector perturbations since, in absence of topological defects, they kinematically decay as $\propto a^{-1}$ [49]. The scalar perturbations are also called density perturbations since they arise as a result of the varying distribution of mass density across the Universe. Whereas tensor perturbations, also known as gravity waves, are caused by freely traveling gravitational radiation (*i.e.* waves).

In this case, the metric becomes

$$\begin{aligned} g_{00}(\mathbf{x},t) &= 1 + 2\Phi(\mathbf{x},t)\,; \\ g_{0i}(\mathbf{x},t) &= 0\,; \\ g_{ij}(\mathbf{x},t) &= -a^2(t)\left[(1-2\Psi(\mathbf{x},t))\,\delta_{ij} + h_{ij}(\mathbf{x},t)\right] , \end{aligned} \tag{1.27}$$

where the Roman subscripts refer to spatial indices running from 1 to 3. The scalar perturbations, defined in the longitudinal gauge (or conformal newtonian gauge), are given by the two scalar function, Φ and Ψ, also known as the Bardeen potentials, while the tensor perturbations, h_{ij}, are defined in the transverse-traceless gauge and are subject to the constraints

$$h^i_i = 0 \qquad \text{and} \qquad \partial_i h_{ij} = 0\,. \tag{1.28}$$

Note that, physically, h_{ij} precisely corresponds to gravitational wave fluctuations. With the definition in Eq. 1.28, no residual gauge freedom remains, in contrast to the synchronous gauge condition[7]. Moreover, an advantage of this gauge choice

[6] The metric signature is (+ - - -), as in [30]. In Ref. [29], (- + + +) is used.
[7] A treatment of the cosmological perturbation theory both in the synchronous and conformal

is that the metric perturbation Φ, in the Newtonian limit, simply corresponds to the Newtonian potential [50].

Considering now Eq. 1.12 with no collision term on the right side

$$\frac{\mathrm{d}\rho}{\mathrm{d}t} = \frac{\partial\rho}{\partial x^\mu}\frac{\mathrm{d}x^\mu}{\mathrm{d}t} + \frac{\partial\rho}{\partial p^\mu}\frac{\mathrm{d}p^\mu}{\mathrm{d}t} = 0\,, \tag{1.29}$$

with x^μ and p^μ the photon space-time coordinate and the four-momentum, respectively. This equation describes the evolution of a collisionless system of photons.

We expand, to the first order in perturbations, the density matrix as

$$\rho(\mathbf{x},\, t,\, \mathbf{p}) = \rho^{(0)}(p,t) + \rho^{(1)}(\mathbf{x},\, t,\, \mathbf{p})\,. \tag{1.30}$$

Notice that, since the zero order is only unpolarized radiation, we have $\rho^{(0)}_{11} = \rho^{(0)}_{12} = \rho^{(0)}_{21} = \rho^{(0)}_{22} = 0$. The first-order Liouville equation with the metric considered in Eq. 1.27 is

$$\begin{aligned}&\frac{\partial}{\partial t}\tilde{\rho}^{(1)}(\mathbf{k},\, t,\, p,\, \hat{\mathbf{p}}) + \frac{i}{a}\Big(\mathbf{k}\cdot\hat{\mathbf{p}}\Big)\,\tilde{\rho}^{(1)}(\mathbf{k},\, t,\, p,\, \hat{\mathbf{p}}) - \frac{\dot{a}}{a}\,p\frac{\partial}{\partial p}\tilde{\rho}^{(1)}(\mathbf{k},\, t,\, p,\, \hat{\mathbf{p}}) + \\ &- p\frac{\partial}{\partial p}\tilde{\rho}^{(0)}(p)\left[\frac{\partial}{\partial t}\tilde{\Phi}(\mathbf{k},\, t) - \frac{\partial}{\partial t}\tilde{\Psi}(\mathbf{k},\, t) + \frac{i}{a}\Big(\mathbf{k}\cdot\hat{\mathbf{p}}\Big)\tilde{\Phi}(\mathbf{k},\, t) + \frac{1}{2}\hat{\mathbf{p}}^i\hat{\mathbf{p}}^j\,\frac{\partial}{\partial t}\tilde{h}_{ij}(\mathbf{k},\, t)\right] = 0\,,\end{aligned} \tag{1.31}$$

where we have performed a Fourier transform over the spatial dependence.

Before moving to the next section, where we are going to assemble these results with the results of Sec. *1.2.1*, it is worth underlining that, for scalar perturbations, $\tilde{\rho}^{(1)}$ depends only on the angle between $\mathbf{p}$ and $\mathbf{k}$, $\tilde{\rho}^{(1)}(\mathbf{k},\, t,\, p,\, \hat{\mathbf{p}}) = \tilde{\rho}^{(1)}(\mathbf{k},\, t,\, p,\, \mu)$ with $\mu = \mathbf{k}\cdot\mathbf{p}$, while tensor perturbations exhibit an azimuthal dependency, $\tilde{\rho}^{(1)}(\mathbf{k},\, t,\, p,\, \hat{\mathbf{p}}) = \tilde{\rho}^{(1)}(\mathbf{k},\, t,\, p,\, \mu)\mathcal{G}(2\phi)$.

1.2.3 Complete Boltzmann equation

Before writing the final set of evolution equations, both for scalar and tensor perturbations. it is useful to convert the density matrix elements $\tilde{\rho}^{(1)}_{ij}$ to Stokes

newtonian gauge is given in [50].

parameter brightness perturbations [30, 50]

$$\begin{aligned}
\tilde{\Delta}_I^{(i)}(\mathbf{k},\, t,\, p,\, \mu) &\equiv \frac{4}{p}\left[\frac{\partial\tilde{\rho}_{11}^{(0)}(p,\, t)}{\partial p}\right]^{-1}\left(\tilde{\rho}_{11}^{(1)}(\mathbf{k},\, t,\, p,\, \mu) + \tilde{\rho}_{22}^{(1)}(\mathbf{k},\, t,\, p,\, \mu)\right);\\
\tilde{\Delta}_Q^{(i)}(\mathbf{k},\, t,\, p,\, \mu) &\equiv \frac{4}{p}\left[\frac{\partial\tilde{\rho}_{11}^{(0)}(p,\, t)}{\partial p}\right]^{-1}\left(\tilde{\rho}_{11}^{(1)}(\mathbf{k},\, t,\, p,\, \mu) - \tilde{\rho}_{22}^{(1)}(\mathbf{k},\, t,\, p,\, \mu)\right);\\
\Delta_U^{(i)}(\mathbf{k},\, t,\, p,\, \mu) &\equiv \frac{4}{p}\left[\frac{\partial\tilde{\rho}_{11}^{(0)}(p,\, t)}{\partial p}\right]^{-1}\left(\tilde{\rho}_{12}^{(1)}(\mathbf{k},\, t,\, p,\, \mu) + \tilde{\rho}_{21}^{(1)}(\mathbf{k},\, t,\, p,\, \mu)\right);\\
\tilde{\Delta}_V^{(i)}(\mathbf{k},\, t,\, p,\, \mu) &\equiv -i\,\frac{4}{p}\left[\frac{\partial\tilde{\rho}_{11}^{(0)}(p,\, t)}{\partial p}\right]^{-1}\left(\tilde{\rho}_{12}^{(1)}(\mathbf{k},\, t,\, p,\, \mu) - \tilde{\rho}_{21}^{(1)}(\mathbf{k},\, t,\, p,\, \mu)\right),
\end{aligned} \tag{1.32}$$

where i stands for scalar (S) and tensor (T) perturbations. In this case $\Delta_T = \Delta_I/4$ is the temperature fluctuation $\delta T/T_0$.

Then gathering all the results of the previous sections, we are able to write the evolution equations in terms of Eqs. 1.32.

1.2.3.1 Scalar perturbation

$$\begin{aligned}
&\dot{\tilde{\Delta}}_T^{(S)} + ik\mu\tilde{\Delta}_T^{(S)} + \left[\dot{\tilde{\Psi}} - ik\mu\tilde{\Phi}\right] = -\dot{\kappa}\left[\tilde{\Delta}_T^{(S)} - \tilde{\Delta}_{T0}^{(S)} + v_b\mu - \frac{1}{2}\mathcal{P}_2(\mu)\Pi\right];\\
&\dot{\tilde{\Delta}}_Q^{(S)} + ik\mu\tilde{\Delta}_Q^{(S)} = -\dot{\kappa}\left[\tilde{\Delta}_Q^{(S)} + \frac{1}{2}\left(1 - \mathcal{P}_2(\mu)\right)\Pi\right];\\
&\dot{\tilde{\Delta}}_U^{(S)} + ik\mu\tilde{\Delta}_U^{(S)} = -\dot{\kappa}\,\tilde{\Delta}_U^{(S)};\\
&\dot{\tilde{\Delta}}_V^{(S)} + ik\mu\,\tilde{\Delta}_V^{(S)} = -\dot{\kappa}\left[\tilde{\Delta}_V^{(S)} - \frac{3}{2}\mu\tilde{\Delta}_{V1}^{(S)}\right],
\end{aligned} \tag{1.33}$$

where $\Pi = \tilde{\Delta}_{T2}^{(S)} + \tilde{\Delta}_{Q2}^{(S)} - \tilde{\Delta}_{Q0}^{(S)}$ and

$$\tilde{\Delta}_T^{(S)}(p,\mu) = \sum_{\ell=0}^{\infty}(2\ell+1)(-1)^\ell\tilde{\Delta}_{I\ell}^{(S)}(p)\,\mathcal{P}_\ell(\mu)\,, \tag{1.34}$$

with $\mathcal{P}_\ell$ the Legendre polynomial of order ℓ and p the comoving wave number. The dot over variables indicates derivatives taken with respect to conformal time,

η. We have defined the total optical depth as the integral

$$\kappa(\eta) \;=\; \int_{\eta}^{\eta_0} \mathrm{d}\eta\, \dot{\kappa}(\eta)\,, \qquad \text{with} \qquad \dot{\kappa} \;=\; a(\eta)\bar{n}_e\sigma_T\,, \tag{1.35}$$

where $\bar{n}_e$ is the mean electron density.
Looking at Eq. 1.33, it is clear that, if we take into account only scalar perturbations, the evolution of the brightnesses depends only on the magnitude of $\mathbf{p}$ and not on its direction. Moreover, the equations for the Stokes U and the Stokes V have no source term, meaning that, the evolution leaves $U = V = 0$. Regarding $V = 0$, we have already clarified that, by symmetry, Thomson scattering can not generate circular polarization. Rather, the amazing fact is that these scalar perturbations only create polarization patterns of a particular type, known as E modes, while B modes can be only sourced by tensor perturbations. This will be clarified in the next section, Sec. *1.3*.

1.2.3.2 Tensor perturbation

$$\begin{aligned}
&\dot{\bar{\Delta}}^{(T)}_T + ik\mu\bar{\Delta}^{(T)}_T = -\dot{h} - \dot{\kappa}\left[\bar{\Delta}^{(T)}_T + \Lambda\right];\\
&\dot{\bar{\Delta}}^{(T)}_P + ik\mu\bar{\Delta}^{(T)}_P = -\dot{\kappa}\left[\bar{\Delta}^{(T)}_P - \Lambda\right];\\
&\dot{\bar{\Delta}}^{(T)}_V + ik\mu\,\bar{\Delta}^{(T)}_V = -\dot{\kappa}\,\bar{\Delta}^{(T)}_V\,,
\end{aligned} \tag{1.36}$$

where

$$\Lambda = -\frac{1}{10}\bar{\Delta}^{(T)}_{T0} + \frac{1}{7}\bar{\Delta}^{(T)}_{T2} - \frac{3}{70}\bar{\Delta}^{(T)}_{T4} + \frac{3}{5}\bar{\Delta}^{(T)}_{P0} + \frac{6}{7}\bar{\Delta}^{(T)}_{P2} + \frac{3}{70}\bar{\Delta}^{(T)}_{Q4}\,. \tag{1.37}$$

The bar over the brightnesses indicates the variables introduced by Polnarev in [51], $\bar{\Delta}^{(T)}_i$, to describe the temperature and polarization perturbations generate by gravity waves. These variables are related to the usual variables, $\tilde{\Delta}^{(T)}_i$, defined

as in Eq. 1.34, by the following

$$\begin{aligned}
&\tilde{\Delta}_T^{(T)}(\mathbf{k},\eta,\hat{\mathbf{p}}) = \left[\left(1-\mu^2\right)e^{2i\phi}\xi^1(\mathbf{k}) + \left(1-\mu^2\right)e^{-2i\phi}\xi^2(\mathbf{k})\right]\bar{\Delta}_T^{(T)}(k,\eta,\mu);\\
&\left(\tilde{\Delta}_Q^{(T)} + i\tilde{\Delta}_U^{(T)}\right)(\mathbf{k},\eta,\hat{\mathbf{p}}) = \left[(1-\mu)^2 e^{2i\phi}\xi^1(\mathbf{k}) + (1+\mu)^2 e^{-2i\phi}\xi^2(\mathbf{k})\right]\bar{\Delta}_P^{(T)}(k,\eta,\mu)\,;\\
&\left(\tilde{\Delta}_Q^{(T)} - i\tilde{\Delta}_U^{(T)}\right)(\mathbf{k},\eta,\hat{\mathbf{p}}) = \left[(1+\mu)^2 e^{2i\phi}\xi^1(\mathbf{k}) + (1-\mu)^2 e^{-2i\phi}\xi^2(\mathbf{k})\right]\bar{\Delta}_P^{(T)}(k,\eta,\mu)\,,
\end{aligned} \tag{1.38}$$

where

$$\xi^1 = \frac{(\xi^+ - i\xi^\times)}{\sqrt{2}} \qquad \text{and} \qquad \xi^2 = \frac{(\xi^+ + i\xi^\times)}{\sqrt{2}} \tag{1.39}$$

are the independent random variables used to characterize the statistics of the gravity waves. These variables satisfy the following

$$\langle \xi^{1*}(\mathbf{k}_1)\xi^1(\mathbf{k}_2)\rangle = \langle \xi^{2*}(\mathbf{k}_1)\xi^2(\mathbf{k}_2)\rangle = \frac{P_h(k)}{2}\delta(\mathbf{k}_1-\mathbf{k}_2)\,; \tag{1.40a}$$

$$\langle \xi^{1*}(\mathbf{k}_1)\xi^1(\mathbf{k}_2)\rangle = 0\,, \tag{1.40b}$$

where $P_h(k)$ is the primordial power spectrum of gravity waves. We will see later the analogous for scalar perturbations.

1.2.4 Integrating the Boltzmann equations

The results of the previous sections are two sets of equations, one for each kind of metric perturbations considered, describing the evolution of temperature anisotropies and polarization of CMB. The next step is to write down the CMB temperature and polarization anisotropies observed today. This is useful for the purposes of comparing the predictions coming from this model with the observations that we are able to perform.
Therefore, in this section we integrate, at least formally, the Boltzmann equations up to our time, η_0.

Each equation in the sets of Eqs. 1.33 and Eqs. 1.36 can be generically written as

$$\dot{\tilde{\Delta}}_X^{(i)}(\eta) + \Big(ik\mu + \dot{\kappa}(\eta)\Big)\tilde{\Delta}_X^{(i)}(\eta) = \overline{\mathcal{B}}_{i,X}(\eta)\,, \tag{1.41}$$

where only the time dependence is shown. The left-hand side of this equation

can be arranged as

$$e^{-ik\mu\,\eta+\kappa(\eta)}\,\frac{\mathrm{d}}{\mathrm{d}\eta}\Big(\tilde{\Delta}_X^{(i)}(\eta)e^{ik\mu\,\eta-\kappa(\eta)}\Big)=\overline{\mathcal{B}}_{i,X}(\eta)\,. \tag{1.42}$$

Then, performing a formal integration of Eq. 1.42 along the photon past light cone we get

$$\Big(\tilde{\Delta}_X^{(i)}(\eta)e^{ik\mu\,\eta-\kappa(\eta)}\Big)\Big|_0^{\eta_0}=\int_0^{\eta_0}\mathrm{d}\eta\;e^{ik\mu\,\eta-\kappa(\eta)}\,\overline{\mathcal{B}}_{i,X}(\eta)\,. \tag{1.43}$$

Then, since $\kappa(\eta_0)=0$ by definition and, at early enough times, the optical depth is large enough that $e^{-\kappa(\eta\to 0)}$ vanishes, it follows

$$\tilde{\Delta}_X^{(i)}(\eta_0)=\int_0^{\eta_0}\mathrm{d}\eta\;e^{ik\mu\,(\eta-\eta_0)-\kappa(\eta)}\,\overline{\mathcal{B}}_{i,X}(\eta)\,. \tag{1.44}$$

Moreover, expanding $\tilde{\Delta}_X^{(i)}$ into Legendre polynomials through Eq. 1.34 and noticing that

$$e^{ik\mu(\eta-\eta_0)}=\sum_{\ell=0}^{\infty}(2\ell+1)i^\ell j_\ell\big[k(\eta_0-\eta)\big]\mathcal{P}_\ell(\mu)\,, \tag{1.45}$$

we get an equation for each multipole moment $\tilde{\Delta}_{X\ell}^{(i)}$:

$$\tilde{\Delta}_{X\ell}^{(i)}(\eta_0,k)=\int_0^{\eta_0}\mathrm{d}\eta\;j_\ell\big[k(\eta_0-\eta)\big]\;S_X^{(i)}(\eta,k)\,, \tag{1.46}$$

where $S_X^{(i)}\equiv\!=e^{-\kappa}\,\overline{\mathcal{B}}_{i,X}$, usually called source term and $j_\ell(x)$ are the Bessel functions and we have used the orthogonality of Legendre polynomials.

This procedure can be repeated for all the brightness $\tilde{\Delta}_A^{(i)}$ with $i=S,\,T$ and $A=T,\,Q,\,U,\,V$. In the following, only the results are reported. More details about the calculations can be found in [33].

$$\begin{aligned}S_T^{(S)}(\eta,k)=g\Big(\tilde{\Delta}_{T0}^{(S)}+\tilde{\Psi}-\frac{\dot{v}_b}{k}-\frac{\Pi}{4}-\frac{3\ddot{\Pi}}{4k^2}\Big)+\\+e^{-\kappa}\big(\dot{\tilde{\Phi}}\dot{\tilde{\Psi}}\big)-\dot{g}\Big(\frac{v_b}{k}+\frac{3\dot{\Pi}}{4k^2}\Big)-\frac{3\ddot{g}\Pi}{4k^2}\,;\end{aligned} \tag{1.47a}$$

$$S_E^{(S)}(\eta,k)=-\frac{3}{4k^2}\Big[g\big(k^2\Pi+\ddot{\Pi}\big)+2\dot{g}\dot{\Pi}+\ddot{\Pi}\Big]\,; \tag{1.47b}$$

$$S_T^{(T)}(\eta,k) = \Big(-\dot{h}e^{-\kappa} + g\Lambda \Big)\,; \tag{1.47c}$$

$$S_E^{(T)}(\eta,k) = g\Big(\Lambda - \frac{\ddot{\Lambda}}{k^2} + \frac{2\Lambda}{k^2(\eta_0-\eta)^2} - \frac{\dot{\Lambda}}{k^(\eta_0-\eta)}\Big) + \\ - \dot{g}\Big(\frac{2\dot{\Lambda}}{k^2} + \frac{4\Lambda}{k^2(\eta_0-\eta)}\Big) - 2\ddot{g}\frac{\Lambda}{k^2}\,; \tag{1.47d}$$

$$S_B^{(T)}(\eta,k) = g\Big(\frac{4\Lambda}{k(\eta_0-\eta} + \frac{2\dot{\Lambda}}{k}\Big) + 2\dot{g}\frac{\Lambda}{k}\ . \tag{1.47e}$$

Let us clarify some aspects of the above equations[8]. First of all, we have introduced the the visibility function $g(\eta) = \dot{\kappa}e^{-\kappa}$, that is, basically, the probability that a photon is last scattered at a given η. It is peaked at recombination time and rapidly declines after that. See Fig. 1.6 for its profile in terms of the scale factor. Another thing to be noticed is the appearance of (E,B). Switching from (Q,U) to these new parameters is a little tricky but useful from both the observationally and theoretically point of view. Please see App. D for more details.

Before moving to the next section, where we finally get in touch with the theoretical power spectra of the CMB radiation, it worth mentioning that the source terms in Eqs. 1.47 are the key ingredients of many codes numerically computing CMB anisotropies, such as `camb` [52]. In this thesis, this code has been largely used to compute the power spectra.

1.3 Statistical treatment of anisotropies

The main results of the previous section is that the primordial inhomogeneities, generated in the inflationary epoch, are in some way related to the CMB anisotropies seen today. The purpose of this section is to express these anisotropies in such a way to allow an easy comparison with observations.

The better way to study the anisotropies is expanding them in harmonic space, so operating an angular decomposition

$$\Delta_X^{(i)}(\mathbf{x},\eta,\hat{\mathbf{p}}) = \sum_{\ell=0}^{\infty}\sum_{m=-\ell}^{\ell} a_{\ell m}^X(\mathbf{x},\eta)\,Y_{\ell m}(\hat{\mathbf{p}})\,. \tag{1.48}$$

[8] In the case of $S_T^{(T)}(\eta,k)$ we have to multiply the integral in Eq. 1.46 by $\sqrt{\frac{(\ell+2)!}{(\ell-2)!}}$

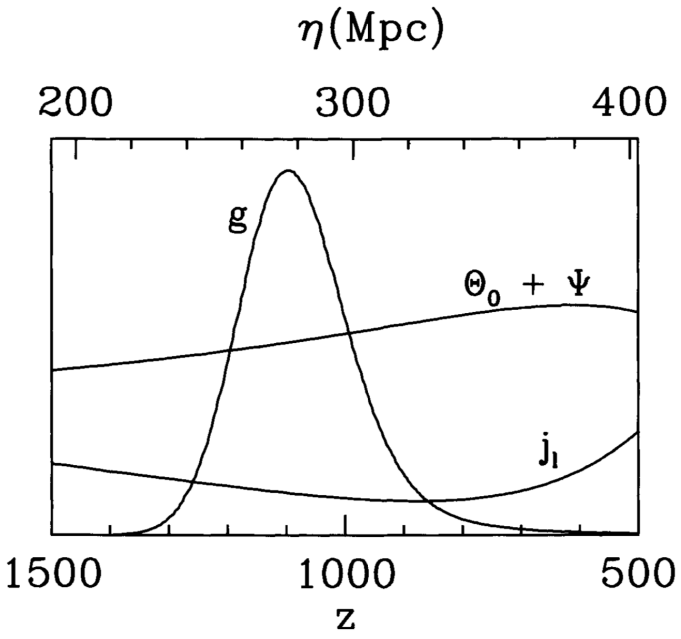

Figure 1.6: *Visibility function g, monopole term $\Theta_0 + \Psi$ ($\Theta_0 \propto \tilde{\Delta}_{I0}^{(S)}$) and Bessel function j_ℓ contributions in function of the scale factor [29].*

This equation can be inverted by multiplying both sides by $Y^*_{\ell m}(\hat{\mathbf{p}})$, reading

$$a^X_{\ell m}(\mathbf{x},\eta) = \int \frac{\mathrm{d}^3k}{(2\pi)^3}\, e^{i\mathbf{k}\cdot\mathbf{x}} \int \mathrm{d}\Omega\; Y^*_{\ell m}(\hat{\mathbf{p}})\, \tilde{\Delta}^{(i)}_X(\mathbf{k},\eta,\hat{\mathbf{p}})\,, \tag{1.49}$$

where we have already performed the Fourier transform. All the information contained in the field $\Delta^{(i)}_X$ is also encoded in the space-time dependent amplitudes $a^X_{\ell m}$.

The potential fluctuations as well as the matter inhomogeneities, the temperature anisotropies and all the structure on large scales are originated from primordial quantum fluctuations. However, the theory is only able to give predictions about the stochastic properties of the primordial perturbations. Thus, it has no meaning to study every fluctuation one by one, the most important information is, by far, the statistical distribution of the anisotropies. Moreover, inflation predicts that the initial perturbations are, to a high degree, Gaussian distributed, and, if the evolution is linear, the Gaussianity is conserved in time [53].

Under this assumption, the $a_{\ell m}$s follow the Normal distribution with zero mean value and non-zero variance:

$$\langle a_{\ell m}\rangle \;=\; 0\,, \qquad \langle a_{\ell m}\, a^*_{\ell' m'}\rangle \;=\; \delta_{\ell\ell'}\delta_{mm'}\, C_\ell\,. \tag{1.50}$$

Note that the variance C_ℓ is independent on both m and $\mathbf{x}$, while $\langle ... \rangle$ denotes the average over the ensemble of all the possible realizations of the stochastic fluctuations that generated the anisotropies.
Let us start, computing the two-point correlation function

$$C^{XY}(\theta) = \langle \Delta_X(\mathbf{x},\eta,\hat{\mathbf{p}}) \Delta_Y^*(\mathbf{x},\eta,\hat{\mathbf{p}}') \rangle = \sum_{\ell m} \sum_{\ell' m'} Y_{\ell m}(\hat{\mathbf{p}}) Y^*_{\ell' m'}(\hat{\mathbf{p}}') \langle a^X_{\ell m}\, a^{*Y}_{\ell' m'} \rangle =$$
$$= \sum_{\ell m} \sum_{\ell' m'} Y_{\ell m}(\hat{\mathbf{p}}) Y^*_{\ell' m'}(\hat{\mathbf{p}}')\, \delta_{\ell\ell'} \delta_{m m'}\, C_\ell^{XY} = \sum_\ell \frac{2\ell+1}{4\pi} \mathcal{P}_\ell(\hat{\mathbf{p}}\cdot\hat{\mathbf{p}}')\, C_\ell^{XY}\,, \qquad (1.51)$$

where we have used Eq. 1.50 and the addition theorem for spherical harmonic (the standard proof of this theorem can be found in Ref. [54])

$$\sum_m Y_{\ell m}(\hat{\mathbf{p}}) Y^*_{\ell' m'}(\hat{\mathbf{p}}') = \frac{2\ell+1}{4\pi} \mathcal{P}_\ell(\hat{\mathbf{p}}\cdot\hat{\mathbf{p}}')\,, \qquad (1.52)$$

where $\mathcal{P}_\ell$ is the Legendre polynomial of degree ℓ. From Eq. 1.51 we can deduce the relation for the angular power spectrum

$$C_\ell^{XY} = \frac{1}{2\ell+1} \sum_{m=-\ell}^{\ell} \langle a^X_{\ell m}\, a^{*Y}_{\ell m} \rangle\,, \qquad (1.53)$$

which is the statistical object to which we are interested in.
The expectation value $\langle a^X_{\ell m}\, a^{*Y}_{\ell m} \rangle$ is related, through Eq. 1.49, to the quantity $\langle \tilde{\Delta}_X^{(i)}\, \tilde{\Delta}_Y^{*(i)} \rangle$, which, in turn, depends, on one hand, on the initial amplitude and phase of the perturbation chosen from a Gaussian distribution during inflation, and, on the other hand, on the evolution of this initial perturbation into anisotropies, discussed in the previous sections. For this reason, the quantity $\tilde{\Delta}(\mathbf{k},\eta,\hat{\mathbf{p}})$ can be decomposed [33,50] as the product of a random unitary gaussian variable $\xi(\mathbf{k})$, related to the primordial fluctuation by

$$\langle \xi(\mathbf{k}_1)\, \xi(\mathbf{k}_2) \rangle = P(k) \delta^3(\mathbf{k}_1 - \mathbf{k}_2)\,, \qquad (1.54)$$

and a function $\tilde{\Delta}(\hat{\mathbf{k}},\eta,\hat{\mathbf{p}})$, depending on the direction of $\mathbf{k}$. This is true for scalar perturbations, with $P(k) = P_\phi(k)$ the initial power spectrum for scalar perturbations. We have already seen this decomposition for tensor perturbations in Sec.*1.2.3.2*, see Eq. 1.38.

Going back to Eq. 1.53, using the decomposition mentioned above, another

way to write the C_ℓ is in terms of the primordial power spectra, as

$$C_\ell^{(i),XY} = (4\pi)^2 \int k^2 \mathrm{d}k \, P_i(k) \, \tilde{\Delta}^{(i)}_{X\ell}(k,\eta_0) \tilde{\Delta}^{(i)}_{Y\ell}(k,\eta_0) \,, \tag{1.55}$$

where $i = \phi, h$, for scalar and tensor perturbations, respectively. To get Eq. 1.55, we have also used Eq. 1.34.
Moreover, in linear perturbation theory, the scalar and tensor perturbations evolve independently and, therefore, the total angular power spectrum is simply given by the sum of the two contributions,

$$C_\ell^{XY} \; = \; C_\ell^{(S),XY} + C_\ell^{(T),XY} \,. \tag{1.56}$$

Hence, Eq. 1.55, combined with Eq. 1.46 and Eqs. 1.47, are the expressions we are looking for: the angular power spectrum describing the temperature and the polarization anisotropies as they are seen today. For completeness, the angular power spectrum is usually plotted using the combination

$$D_\ell = \frac{\ell\big(\ell+1\big)}{2\pi} C_\ell \,. \tag{1.57}$$

Before looking in detail at the unique shapes of the CMB angular power spectra, let us highlight the existence of an intrinsic limit, particularly at small ℓ, in the evaluation of the angular power spectrum. Looking at Eq. 1.50, we can note that for a given ℓ, each $a_{\ell m}$ has the same variance. Basically, since we can observe only one CMB sky, for every multipole the quantity of information that we can get is limited and encoded in the amount of $m \in [-\ell, \ell]$, *i.e.* $(2\ell+1)$ moments. For examples, for $\ell = 500$, all 1001 a_{500m}'s are drawn from the same distribution. When we measure these 1001 coefficients, we are sampling the distribution. This will give us a good handle on the underlying variance of the distribution. Whereas, the information that we get when we measure the 5 a_{2m}'s is definitely less.
This unavoidable uncertainty, called cosmic variance, scales as

$$\left(\frac{\Delta C_\ell}{C_\ell}\right) \; = \; \sqrt{\frac{2}{2\ell+1}} \,. \tag{1.58}$$

Hence, as anticipated, this quantity decreases with larger ℓ, implying that the larger uncertainties in determining the angular power spectrum are related to low multipoles.

1.3.1 Temperature power spectra

Collecting the results of the previous sections, we can write the temperature (TT) angular power spectrum

$$C_\ell^{TT} = (4\pi)^2 \left\{ \int k^2 \mathrm{d}k \; P_\phi(k) \left[\tilde{\Delta}_{T,\ell}^{(S)}(k) \right]^2 + \int k^2 \mathrm{d}k \; P_h(k) \left[\tilde{\Delta}_{T,\ell}^{(T)}(k) \right]^2 \right\}, \quad (1.59)$$

with $\tilde{\Delta}_{T,\ell}^{(S/T)}$ given in Eq. 1.46 and Eqs. 1.47.

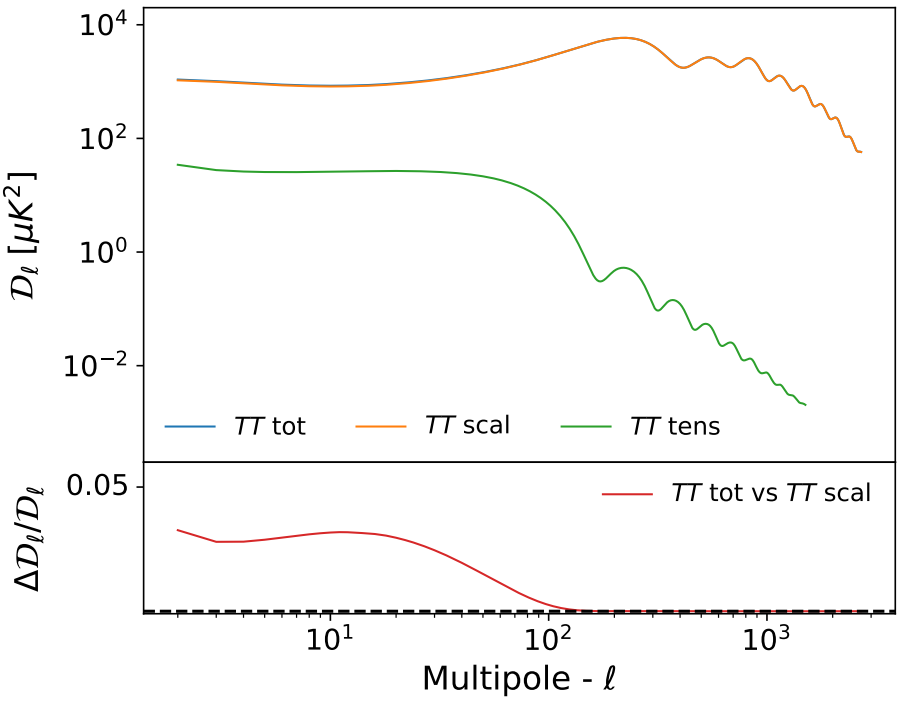

Figure 1.7: Top: *Temperature anisotropies power spectrum from scalar, tensor and scalar plus tensor perturbations.* Bottom: *Relative difference between the temperature anisotropies power spectrum generated by scalar plus tensor perturbations and the one from scalar only. This plot has been produced using* `camb` *code with the Planck 2018 best-fit values for the ΛCDM parameters [55]. The tensor-to-scalar ratio is $r = 0.07$.*

The peculiar shape of the function in Eq. 1.59, shown in Fig. 1.7, gives us all the information discussed in the following (see also Sec. *1.4* for a more detailed discussion on how the cosmological parameters can affect this shape). First of all, we can distinguish between the two components, coming from scalar and tensor perturbations, respectively. Looking at the relative difference between the total

and the scalar power spectra, the imprinting of tensor perturbations on the total power spectrum is mostly located at small ℓ. The tensor-to-scalar ratio used is $r = 0.07$[9].

Besides, looking at Fig. 1.7 in a more general way, this is the result of essentially two components, also known as primary and secondary anisotropies. The former are related to "intrinsic temperature variations" which happen directly at the decoupling, the latter are, instead, related to photons energy variation on their journey from the last scattering source to us.

Looking more closely Fig. 1.7 we can recognize three different regimes, a flat plateau, at very small ℓ, a series of bumps and wiggles and finally, at large ℓ, a quasi-exponentially dump. The origin of these features can be found going back in time to just before recombination, when the Universe was made up by photons tightly coupled with baryons and dark matter. The perturbations in the dark matter grow continuously in time, whereas the perturbations in the baryon-photon fluid are in a *dance* conducted by gravity and pressure force of the photons. Eventually, photon pressure stops the collapse. On the other side, the expansion is slowed and halted owing to the weight of the fluid and the gravitational potential, causing the mode to recollapse once more. In other word, this is producing an acoustic wave, with gravity the driving force and pressure the restoring force. This statement allow us to understand the aforementioned features.

Starting from the plateau at $\ell < 100$, also known as Sachs-Wolfe plateau [56], this is due to perturbations having a period longer than the age of the Universe at the last scattering surface. In other words, these perturbations are larger than the horizon, and, so, are essentially frozen in their initial configuration, providing us information about the pre-recombination physics. When CMB photons emerge from the potential wells associated with these long-wavelength density perturbations, they lose energy. The differences in the gravitational potentials at the time of the last scattering reflects, indeed, the temperature differences seen on the CMB sky today. Tensor perturbations of spacetime do not create the same baryon-photon oscillations that we see in the other zones, but can contribute to the Sachs-Wolfe plateau.

In the central region of the spectrum, $100 < \ell < 1000$, we have to deal with perturbations that enter the horizon, or are already sub-horizon, before recombination. We are in a condition of ionized plasma where all the electrons are unbound. The photon mean free path is much smaller that the horizon size and Compton scattering keep photons and baryons tightly coupled. In this regime,

[9] This parameter is the ratio between P_ϕ and P_h computed at a given pivot scale $k_* = 0.05$

the baryon-photon fluctuations have sufficient time to undergo the oscillations, leading to peaks and valleys in the angular power spectrum.
Finally, we arrive to the third zone, $\ell > 1000$, where we observe a reduction of the inequalities, *i.e.* anisotropies, of the early Universe.
During recombination, the photons can random walk a distance given by the mean free path times the square root of the number of scatterings. This means, that photons can diffuse out of any overdensity having a smaller scale than this distance, that is increasing since the mean free path is increasing during recombination. This leads to an exponential damping of the spectrum on small scales. This process is also known as Silk damping [57]. Hence, this damping is due to the finite *thickness* of the last scattering surface, that, indeed, is a layer not a surface.

Upon a closer inspection of Fig. 1.7, we should mention some of the secondary effects. First of all, the integrated Sachs-Wolfe (ISW) effect [56, 58]. As photons travel through the Universe from the last scattering surface to us, they interact gravitationally with the matter. If the gravitational potentials are still evolving, additional temperature perturbations are generated. Let us consider a photon falling into a gravitational potential. If the potential is varying in time, the energy that the photon gained falling in will be different from the amount of energy used to climbing back out of the well. This leads to a net anisotropy.
We can distinguish between the Early ISW, just after recombination, when radiative component is not completely negligible yet, and the Late ISW, in the Dark Energy dominated Universe.
Moreover, even in the matter dominated Universe, when non-linear structures form the potential can change with time, leading to new anisotropies. This effect, nearly negligible, is known as Rees-Sciama effect [59].

Another effect to be considered is reionization [60–62], when photons can again scatter off free electrons, in a second scattering surface. However, the electron density in this epoch is quite low, and the baryons and photons do not become tightly coupled. Because of this the two fluids can have a large relative velocity, which enhances the power of the Doppler effect. Reionization damps power on angular scales smaller than the horizon subtended by the epoch of reionization while generating extra power owing to Doppler effect [63]. It is unlikely that the reionization of the Universe will occur uniformly throughout space, so other anisotropies will be generated owing to the "patchiness" of reionization.

At this point, once structure formation is well underway, the photons can interact with hot gas in the intergalactic medium. In hot clusters of galaxies, electrons of ionized gas ($T \sim 10^7$ K) interact through Inverse Compton with

CMB photons. The energy of the latter increases and this produces a distortion in the frequency spectrum. This effect, known as thermal Sunyaev-Zeldovich (tSZ) effect [64], is probably the largest source of anisotropy on small scales, $\ell > 2000$. This will be discussed in Chpt. 3.
Beside this, we also have to mention the kinetic Sunyaev-Zeldovich (kSZ) effect [65], which is related to clusters motion along the line of sight.

On top of these effects, of course, there are foregrounds, such as dust, free-free emission, synchrotron, point sources and many others, which mask the *real* CMB signal [66, 67].

We have not mentioned yet the slight experienced distortion by the photon path when they pass close to large distributions of matter. Light is deflected by the gravitational field generated by matter. This distortion, called gravitational lensing, does not constitute a primordial effect and it is, indeed, one of the most important mechanisms that can generate secondary anisotropies in the CMB. Not only the temperature but also, and specially, polarization power spectra are affected by gravitational lensing. We will come back on this topic in Chpt. 3.

1.3.2 Polarization power spectra

Collecting again the results of the previous sections, we can now write the polarization power spectra for E and B modes:

$$C_\ell^{EE} = (4\pi)^2 \left\{ \int k^2 \mathrm{d}k \; P_\phi(k) \left[\tilde{\Delta}^{(S)}_{E,\ell}(k)\right]^2 + \int k^2 \mathrm{d}k \; P_h(k) \left[\tilde{\Delta}^{(T)}_{E,\ell}(k)\right]^2 \right\}; \tag{1.60a}$$

$$C_\ell^{BB} = (4\pi)^2 \int k^2 \mathrm{d}k \; P_h(k) \left[\tilde{\Delta}^{(T)}_{E,\ell}(k)\right]^2, \tag{1.60b}$$

with $\tilde{\Delta}^{(S/T)}_{E,\ell}$ and $\tilde{\Delta}^{(T)}_{B,\ell}$ given in Eq. 1.46 and Eqs. 1.47.

Looking at Fig. 1.8, two things "strike the eye": as anticipated, scalar perturbations generate only E-modes polarization while tensor perturbations create both, and the power contained in CMB polarization fluctuations is about a factor of 100 less than the power contained in the temperature fluctuations.

Since E-modes polarization are due to velocity gradients in the photon-baryon fluid, we see again acoustic oscillations. In particular, the acoustic peaks in the EE power spectra are out of phase with those in the temperature one. Given the different origin of B-modes, we do not see acoustic peaks in BB power spectra.

As for the temperature power spectrum, we can recognize the imprint of

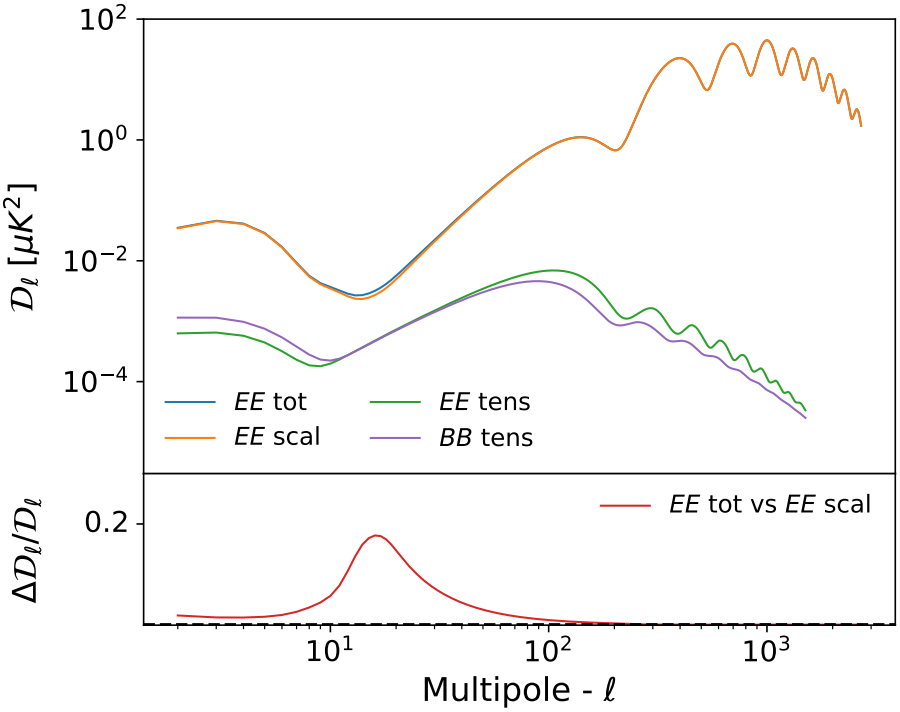

Figure 1.8: Top: *Polarization anisotropies power spectrum from scalar, tensor and scalar plus tensor perturbations. E-modes and B-modes are both shown.* Bottom: *Relative difference between the E-mode power spectrum generated by scalar plus tensor perturbations and the one from scalar only. This plot had been produced using* `camb` *with the Planck 2018 best-fit value for the ΛCDM parameters [55]. The tensor to scalar ratio $r = 0.07$.*

different phases of the evolution of the Universe. The bump at $\ell \lesssim 10$ is certainly noteworthy. In fact, at large scales, polarization power spectra should have a power-law decay trend, since those scales are larger than the photon mean free path at recombination.
However, after recombination, when reionization is supposed to happen, as already said, photons can again scatter off free electrons. This interaction with re-ionized matter produces a bump, also known as reionization bump, in the power spectra at low multipoles.

High-precision measurements of CMB polarization are indeed able to constrain the still quite unknown reionization process better than CMB temperature. Moreover, B modes are considered to be a smoking gun for detecting primordial gravitational waves created during inflation.
Definitely, the polarization of the CMB still contains a lot of valuable information about our Universe and, not surprisingly, it is the target of the next-decade CMB

experiments.

Also in this case, we have variations in power spectra due to gravitational effects. We are going to discuss them in detail in Chpt. 3.

Before proceeding further, it is worth noticing that the B-modes so far discussed are the so-called *primordial* B-modes (see Fig. 1.12). In Chpt. 3, we will discuss the *spurious* B-modes generated by gravitational lensing effect (see also Fig. 3.2).

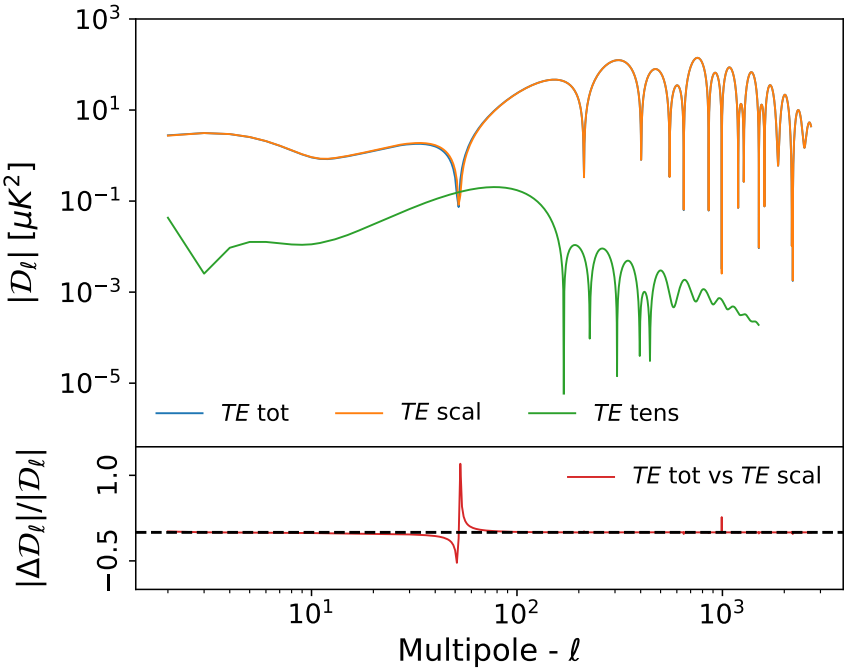

Figure 1.9: Top: *Temperature and Polarization anisotropies cross spectrum from scalar, tensor and scalar plus tensor perturbations.* Bottom: *Relative difference between the cross spectrum generated by scalar plus tensor perturbations and the one from scalar only. This plot had been produced using* `camb` *with the Planck 2018 best-fit value for the ΛCDM parameters [55]. The tensor to scalar ratio $r = 0.07$.*

1.3.3 Temperature-polarization cross spectra

Since, in standard Cosmology, the physics governing photon propagation is parity invariant, the only non-vanishing combination is TE. Please check the App. D for more information.
As we will see in the Chpt. 2, TB and EB correlations can arise in presence of parity violation theories.

Collecting again the results of previous sections, the cross spectrum between temperature and E-mode polarization reads

$$C_\ell^{TE} = (4\pi)^2 \left\{ \int k^2 \mathrm{d}k \; P_\phi(k) \left[\tilde{\Delta}_{T,\ell}^{(S)}(k) \, \Delta_{E,\ell}^{(S)}(k) \right] + \int k^2 \mathrm{d}k \; P_h(k) \left[\tilde{\Delta}_{T,\ell}^{(T)}(k) \, \tilde{\Delta}_{E,\ell}^{(T)}(k) \right]^2 \right\}, \tag{1.61}$$

with $\Delta_{T/E,\ell}^{(S/T)}$ and $\Delta_{T/E,\ell}^{(S/T)}$ given in Eq. 1.46 and Eqs. 1.47.

The relevant thing to be noticed is that, as in temperature and E-mode polarization power spectra, the cross spectrum also shows pronounced acoustic peaks.

1.4 Cosmology from CMB power spectra

From what we have seen in previous sections, it is clear that that the physics beyond the formation of temperature and polarization anisotropies is fully related to the evolution of the Universe, from early times until the present. In this respect, the shape of the CMB power spectrum depends on cosmological parameters, and so it can be used to constrain the standard cosmological model (ΛCDM) and some extensions.

The ΛCDM model is based on only six independent parameters. The specific set of six parameters used to define the cosmological model is somewhat open to choice. Nevertheless, within the context of fitting a ΛCDM model to CMB data, there are preferred combinations, chosen to avoid degeneracies [68]. In Planck 2018 [55], the baseline parameters are the baryon and cold dark matter density, $\Omega_b h^2$ and $\Omega_c h^2$, respectively (where $h = H_0/(100 \mathrm{km\,s^{-1}\,Mpc^{-1}})$ is the reduced Hubble constant), the amplitude of primordial curvature perturbations, A_s, and its spectral index n_s, the optical depth τ and the angular size of the sound horizon, $\theta_* \equiv r_*/D_M$, where r_* is the comoving sound horizon at recombination and D_M is the comoving angular diameter distance.

The two parameters, A_s and n_s, define the shape of the power spectrum of the primordial scalar perturbations, as

$$P_\phi(k) \; = \; A_s(k_*) \Big(\frac{k}{k_*} \Big)^{n_s - 1}, \tag{1.62}$$

where k_* is a reference scale (pivot). This is generally fixed to $k_* = 0.05\,\mathrm{Mpc}^{-1}$. We have already introduced this power spectrum in the previous section, see Eq. 1.54 and the power spectra in Eqs. 1.59, 1.60 and 1.61.

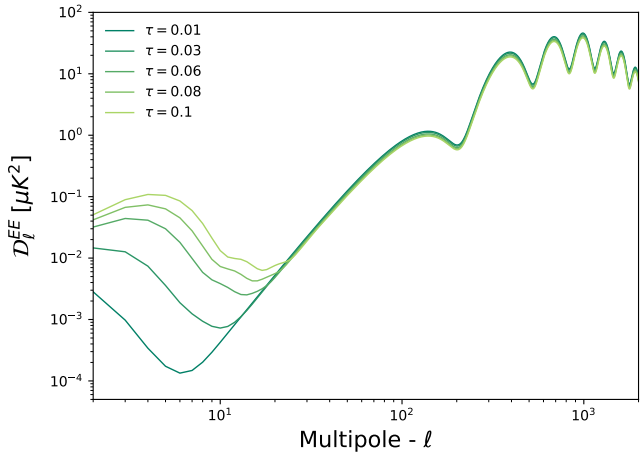

Figure 1.10: *Impact on the EE power spectrum of varying the optical depth, τ. This plot has been produced using* `camb` *code with the Planck 2018 best-fit values for the ΛCDM parameters [55]. The tensor-to-scalar ratio is $r = 0$. Then, we have varied τ, keeping the others fixed.*

Starting from the amplitude A_s, changing A_s obviously just shifts the CMB spectrum up and down. The n_s parameter is, instead, the tilt of scalar perturbations spectrum, and, as the name promises, it tilts the CMB spectrum. For $n_s = 1$ the spectrum $\ell(\ell+1)C_\ell$ has equal power on all scales, while for $n_s > 1$ ($n_s < 1$) it has more power on small (large) scales.
As it will be discussed later in this section, these parameters are related to the inflation mechanisms and their predictions. The simplest models of cosmic inflation predict an almost scale invariant primordial spectrum with $n_s \approx 1$ (see *e.g.* Refs. [21, 22]).

Baryon and cold dark matter abundances, $\Omega_b h^2$ and $\Omega_c h^2$ respectively, affect the acoustic peaks in temperature power spectrum. We can distinguish different effects. First of all there is the so called baryon drag, that has the effect of shifting the equilibrium position in the photo-baryon fluid oscillation. It causes mainly a modulation in odd and even peaks, in particular odd peaks have higher amplitude than even ones. The increase in baryon abundance leads therefore in higher amplitude of odd peaks. Moreover, decreasing $\Omega_b h^2$ causes the baryon damping, a general smoothing in acoustic peaks amplitude.
In general, the total matter content has strong effects on angular power spectrum, in particular it determines the matter-radiation equality and therefore which scales enter the horizon before or after this equality and how they evolve. Lowering the matter density shifts matter-radiation equality to later times, *i.e.* closer to recombination. This affects the forcing term for the photon-baryon oscillations.

In particular, the forcing term is stronger near equality, so the heights of the peaks are higher when the matter density is lower.
As we have described in the previous section, as dark energy becomes the dominant component, the gravitational potential stops being time-independent. This leads to the late ISW effect which boosts the power of the low-ℓ modes.

Regarding the optical depth, τ, this is strictly related to reionization. The Universe is supposed to became reionized at late times, around $z \sim 6$. This increases the optical depth to last-scattering. On scales smaller than the horizon after reionization, the CMB anisotropies get suppressed by a factor of $e^{-\tau}$ due to the rescattering of photons. This effect is somewhat degenerate with an $n_s > 1$ tilt of the primordial spectrum. Nevertheless, the effect on the polarization spectrum is distinct and from the EE power spectra we can constrain directly the optical depth of reionization.
In Fig. 1.10, the "bump" in the EE power spectrum is shown for different values of τ.

To conclude, the acoustic angular scale, θ_*, has the effect of horizontally shifting the acoustic peaks. Because of its simple geometrical interpretation, this parameter is almost independent of the cosmological model and its measurement is very robust.

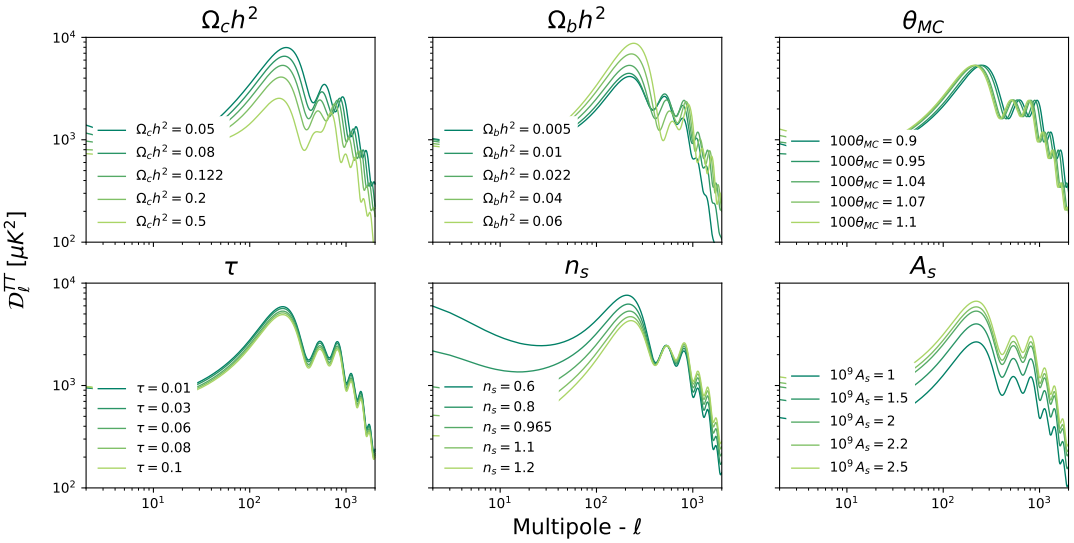

Figure 1.11: *Impact on the TT power spectrum of varying the six-baseline cosmological parameters. These plots have been produced using* `camb` *code with the Planck 2018 best-fit values for the ΛCDM parameters [55]. The tensor-to-scalar ratio is $r = 0$. Then, in each panel, we have varied a single parameter, keeping the others fixed.*

In Fig. 1.11, we can appreciate the impact on the TT power spectrum of varying these six parameters
It is worth mentioning that Fig. 1.11 is obtained assuming a flat Universe. If we allow the curvature parameter, Ω_K, to vary, it affects the position of the first peak of the temperature power spectrum. This is a very sensitive feature that allows the Planck collaboration to constrain the curvature of the Universe with an astonishing precision level, $\Omega_K = -0.0106 \pm 0.0065$ (68%, using TT,TE,EE+lowE+lensing) [55].

Beyond the baseline-ΛCDM model, there are many interesting extensions to be considered. Here we are considering only, the tensor-to-scalar ratio, r, and the effective number of relativistic species, N_{eff}.

Introducing tensor perturbations, as we have seen, generates a *new kind* of polarization mode, the so-called primordial B-modes. As for scalar perturbations, we can introduce the amplitude, A_t, and the spectral index, n_t, of tensor perturbations. The power spectrum of the primordial tensor perturbations is,

$$P_h(k) \;=\; A_t(k_*)\Big(\frac{k}{k_*}\Big)^{n_t}\,, \tag{1.63}$$

where k_* is again the pivot scale. The tensor-to-scalar ratio, used to parametrized tensor perturbations inside the standard cosmological model, is therefore defined as

$$r \equiv \left.\frac{P_h}{P_\phi}\right|_{k_*}\,, \tag{1.64}$$

where the two power spectra are measured at the same pivot scale, k_*.
Moreover, since r provides a measure of the expansion rate during inflation, which can be related to the energy scale of inflation [10],

$$V^{1/4} \;\sim\; \Big(\frac{r}{0.01}\Big)^{1/4} 10^{16}\,\mathrm{GeV}\,, \tag{1.65}$$

a measurement of the tensor-to-scalar ratio with $r \sim 0.01$ would therefore associate inflation with physics at the Grand Unified Theory (GUT) scale, estimated to be around 10^{16} GeV. These energy scales are far beyond the reach of the LHC or any conceivable collider experiment. Moreover, the measurement of the energy scale of inflation would have implications for many other aspects of fundamental physics, including, for example, string theory.
It is clear now why the detection of primordial B-mode polarization is the target

[10] We have considered P_ϕ roughly constant and $P_h \propto H^2 \sim V$.

of the next-decade CMB experiments. A detection would confirm definitively the validity of inflationary scenario, constraining also (with the tensor-to-scalar ratio r and the tensor tilt n_t) the specific model for inflation.
However, the gravitational waves decay inside the horizon, so the tensor contribution is only significant on large scales (small ℓ). This feature makes the detection of B-modes harder. Moreover, the already mentioned *spurious* B-modes complicate the picture. See Fig. 1.12 or Chpt. 3 for more details. In Fig. 1.12, we show the effect of increasing r on primordial B-modes. The black line, represents the *spurious* B-modes due only to gravitational lensing ($r = 0$).

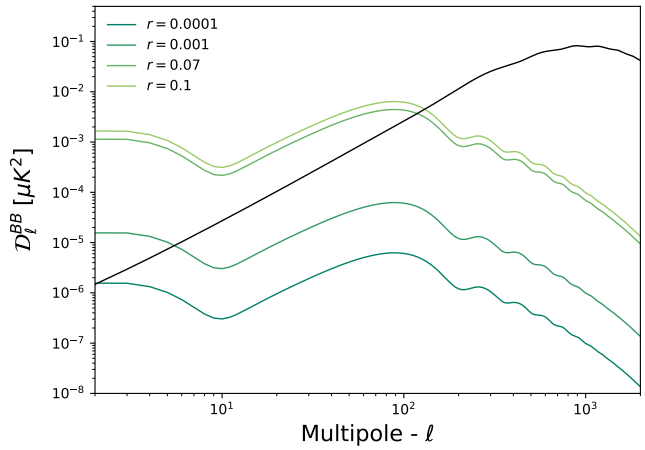

Figure 1.12: *Impact on the BB power spectrum of varying the tensor-to-scalar ratio, r. This plot has been produced using* `camb` *code with the Planck 2018 best-fit values for the ΛCDM parameters [55]. Then, we have varied r, keeping the other parameters fixed. The black line shows the lensed BB power spectrum with $r = 0$.*

Concerning the parameter N_{eff}, the standard model predicts $N_{eff} = 3.046$. This parameter is well constrained by Planck satellite, since deviations from the standard model value can affect the damping tail and shift the phase of the acoustic peaks.

In conclusion, it is clear, from the picture we have drawn, the importance of measuring both the temperature and polarization anisotropies, since the information encoded are nearly complementary. Polarization depends on some cosmological parameters differently than the temperature anisotropy, allowing us to remove degeneracies in the fitted parameters and to largely improve the constrains.

2

The polarization of the CMB

Lines of investigation, seeking to extract information from the CMB beyond that contained in its temperature anisotropies, are particularly timing.
The primary scientific target of the next ground- and space-based CMB experiments, such as LiteBIRD, SO, and CMB-S4, is, indeed, the detection of primordial tensor perturbations (see Chpt. 4).
Next-generation projects have the potential of measuring the CMB E-mode polarization down to the cosmic variance limit over a wide range of angular scales, and, moreover, to push the search for primordial B-modes down to a tensor to scalar ratio $r \sim 0.001$. Primordial B-modes, as already discussed in Chpt. 1 are extremely sought for both Cosmology and fundamental physics because they provide a measure of the energy scale driving inflation.

Nevertheless, there is *more* beyond this *standard* picture. The physics that governs the CMB is purely electromagnetic. This means that observing properties of the CMB pattern can be used to constrain deviations from the standard model of particle physics, and so, to search for violations in the photon sector.
Since the Maxwell lagrangian in the standard model is expected to conserve parity (hereafter P symmetry), in Chpt. 1, we have seen that we can potentially extract information from four[1] CMB angular power spectra: TT, EE, BB and TE. The cross-correlation between temperature and B-mode polarization and E-mode and B-mode polarization are forbidden in a P invariant Universe[2].
Models beyond the standard model predict, instead, P violations that may also

[1] In principle, we also have the lensing potential and its cross-correlations, but we will discuss this topic in Chpt. 3.

[2] It is worth underlining that the sources (*e.g.* scalar and tensor perturbations in standard inflationary setting) are also parity invariant, hence vanishing TB and EB spectra come from both parity invariant source of anisotropies and the properties of electromagnetism.

result in a global violation of the CPT symmetry. Moreover, CPT violation implies Lorentz-symmetry breakdown, as it has recently been proved in Greenberg's "anti-CPT theorem" [69].
In this kind of theory, the cross-correlation TB and EB angular power spectra might arise, becoming the *litmus test* for constraining physics beyond the standard model.

In this generalized picture, we are still missing something. As we have seen in Chpt. 1, CMB photons are expected to be linearly polarized by Compton scattering at the epochs of recombination and reionization. In contrast, circular polarization is not expected to be present at the time of last scattering. It can be generated, on one hand, by known physics as CMB photons propagate across the Universe, but only in tiny amounts; on the other hand, the aforementioned models, or some generalization of them, might be responsible for the generation of a larger amount of circular polarization. Hence, observing circular polarization in the CMB, and its cross-correlations with temperature and E and B mode polarization, could provide evidence for new physics or constrain certain classes of extensions of the standard model of particle physics.

It is worth also mentioning that these effects, a non zero TB/EB power spectra and/or a degree of circular polarization in the CMB radiation, might also arise from observational systematics as for example miscalibration of polarimeters (see *e.g* Ref. [70]), as well as interaction of CMB photons with magnetic fields (see *e.g* Refs. [37, 71, 72]).

This chapter has definitely a phenomenological imprint. In Sec. *2.1*, the cosmic birefringence is introduced. This phenomena, that consists in the rotation of linear polarization direction during the in vacuo propagation of radiation, can be the *visible tip* of Lorentz- and CPT- violating theories. The CMB circular polarization is, instead, discussed in Sec. *2.2*. In Sec. *2.3*, we present our unified model, a phenomenological framework allowing to describe the mixing of different polarization states during CMB photon propagation. This section is based on [11]. Finally, in the last section, Sec. *2.4*, we interpret this mixing as the result of light propagating into a medium with an anisotropic and/or parity-violating susceptibility tensor. This allows us to take a step back and to relate our phenomenological framework to physical models.

2.1 Cosmic birefringence

In the cosmological literature, the term "cosmic birefringence" usually describes the specific case of different propagation velocity of circular polarization states, leading to in-vacuo rotation of the linear polarization plane. In crystal optics, the same effect is dubbed "optical activity". If the radiation is propagating in a magnetic medium, leading again to a rotation of linear polarization plane, it is common to use the term "Faraday rotation". In the rest of this chapter, we will use the term "Faraday rotation" without implying the presence of a magnetic field.

In a completely general way, we can say that "cosmic birefringence" naturally arises in different theoretical contexts, which can be roughly broken down into two main classes: parity-violating extensions of the standard model, *e.g.* [73–76] and primordial magnetic fields, *e.g* [77–79]. Depending on the specific details of the physical process sourcing this rotation, we can expect a uniform rotation angle $\Delta\chi$, an anisotropic rotation $\Delta\chi(\hat{\mathbf{n}})$ across the sky, or both.

Focusing on the parity-violating scenario, that is the one of our interest, birefringence usually arises when we add to the Maxwell Lagrange density, $\mathcal{L}_{EM}$, a Chen-Simons term, such as [73]

$$\mathcal{L}_{CS} \;=\; -\frac{1}{2} p_\mu \, A_\nu \widetilde{F}^{\mu\nu} \,, \tag{2.1}$$

where $\widetilde{F}^{\mu\nu}$ is the dual electromagnetic tensor and p_μ is a generic four-vector coupling with the photon field, A_ν. As a result, the Maxwell equations, which follow from $\mathcal{L} = \mathcal{L}_{EM} + \mathcal{L}_{CS}$, are modified as

$$\partial_\mu F^{\mu\nu} \;=\; p_\mu \widetilde{F}^{\mu\nu} \,, \tag{2.2a}$$

or in terms of the electric, $\mathbf{E}$, and magnetic, $\mathbf{B}$, fields

$$\nabla \mathbf{E} = 4\pi\rho - \mathbf{p}\cdot\mathbf{B} \,, \tag{2.2b}$$

$$-\partial_t + \nabla \times \mathbf{B} = -p_0 \mathbf{B} + \mathbf{p}\cdot\mathbf{E} \,. \tag{2.2c}$$

Note that the homogeneous Maxwell equations $\widetilde{F}^{\alpha\beta} = 0$ are not modified.
From Eqs. 2.2, we can compute the wave equation and the corresponding dispersion relation, that is [73]

$$\omega^2 - k^2 = \pm\big(p_0 k - \omega p \cos\theta\big)\Big(1 - \frac{p^2 \sin\theta}{\omega^2 - k^2}\Big)^{-\frac{1}{2}} \,, \tag{2.3}$$

where ω is the frequency, k is the module of the wave vector, p is the module of the spatial component of the four-vector coupled with the photon field and θ is the angle between $\mathbf{p}$ and $\mathbf{k}$. The $+$ and $-$ stand for the right- and left-handed circularly polarized waves, respectively. Hence, the Chern-Simons term, in Eq. 2.1, affects the propagation of right- and left-handed photons asymmetrically, giving rise to the rotation of the plane of linear polarization.

For the moment, let us suppose that birefringence arises because of a "sudden rotation" by an angle $\Delta\chi > 0$[3] of the polarization after photon propagation from the last scattering surface to now. Then the Stokes parameters Q and U get mixed in the following way,

$$Q^{obs} = \tilde{Q}\cos 2\Delta\chi + \tilde{U}\sin 2\Delta\chi\,; \tag{2.4}$$

$$U^{obs} = \tilde{U}\cos 2\Delta\chi - \tilde{Q}\sin 2\Delta\chi\,, \tag{2.5}$$

or, in a more compact way, as

$$\big(Q \pm iU\big)^{obs} = \exp\big(\mp 2i\,\Delta\chi\big)\big(\tilde{Q} \pm i\tilde{U}\big)\,. \tag{2.6}$$

The tilde's indicates the Stokes parameters in absence of polarization rotation (*i.e.*, in absence of cosmic birefringence). From now on, for simplicity, we drop the superscript ^{obs}, that stands for "observed".

Let us assume that the rotation angle is homogeneous and isotropic, $\Delta\chi = \Delta\bar{\chi}$. In this case, the so-called *isotropic birefringence*, the CMB power spectra would be rotated as [75, 80]

$$C_\ell^{TT} = \tilde{C}_\ell^{TT}\,; \tag{2.7a}$$

$$C_\ell^{TE} = \tilde{C}_\ell^{TE}\cos(2\Delta\bar{\chi}) - \tilde{C}_\ell^{TB}\sin(2\Delta\bar{\chi})\,; \tag{2.7b}$$

$$C_\ell^{TB} = \tilde{C}_\ell^{TE}\sin(2\Delta\bar{\chi}) + \tilde{C}_\ell^{TB}\cos(2\Delta\bar{\chi})\,; \tag{2.7c}$$

$$C_\ell^{EE} = \tilde{C}_\ell^{EE}\cos^2(2\Delta\bar{\chi}) + \tilde{C}_\ell^{BB}\sin^2(2\Delta\bar{\chi}) - \tilde{C}_\ell^{EB}\sin(4\Delta\bar{\chi})\,; \tag{2.7d}$$

$$C_\ell^{BB} = \tilde{C}_\ell^{BB}\cos^2(2\Delta\bar{\chi}) + \tilde{C}_\ell^{EE}\sin^2(2\Delta\bar{\chi}) + \tilde{C}_\ell^{EB}\sin(4\Delta\bar{\chi})\,; \tag{2.7e}$$

$$C_\ell^{EB} = \frac{1}{2}\Big(\tilde{C}_\ell^{EE} - \tilde{C}_\ell^{BB}\Big)\sin(4\Delta\bar{\chi}) + \tilde{C}_\ell^{EB}\Big(\cos^2(2\Delta\bar{\chi}) - \sin^2(2\Delta\bar{\chi})\Big)\,, \tag{2.7f}$$

[3]The rotation is chosen to be counterclockwise looking at the photons coming toward us, corresponding to a rotation of the reference frame from the $\hat{\mathbf{x}}$ axis to the $\hat{\mathbf{y}}$ axis. This is different from the convention considered in [75].

where $\tilde{C}_\ell^{EB} = \tilde{C}_\ell^{TB} = 0$, if the physics before the rotation is not parity-violating. As we aspected, the rotation of the linear polarization plane has no effects on the temperature and, moreover, it is not able to generate circular polarization.

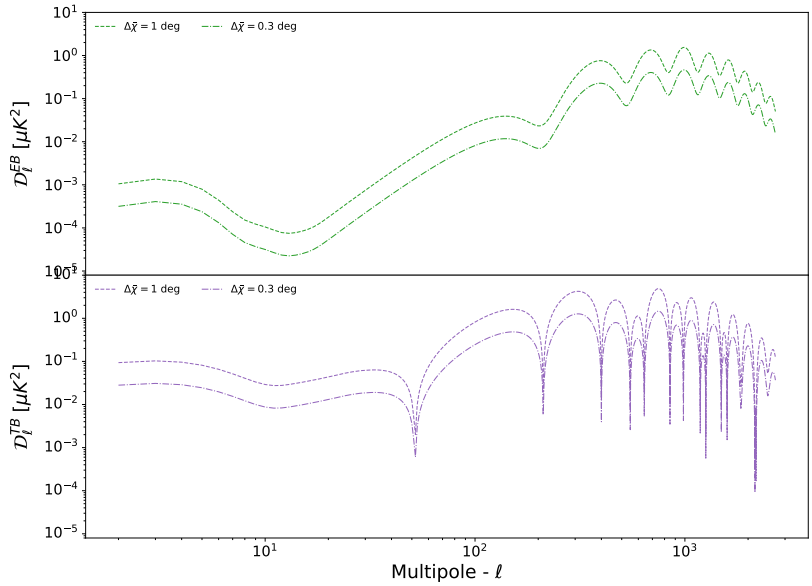

Figure 2.1: *Parity-violating CMB power spectra in presence of isotropic birefringence, according to Eqs. 2.7. The rotation angles are* $1.0°$ *(dashed lines) and* $0.35°$ *(dash-dotted lines). This plot has been produced using* `camb` *code with the Planck 2018 best-fit values for the* ΛCDM *parameters [55]. The tensor-to-scalar ratio is* $r = 0.07$.

In Fig. 2.1, we can see the parity-violating power spectra, while in Fig. 2.2, we can appreciate the effect of this rotation on the standard power spectra, which are computed, using the Boltzmann code `camb`, assuming the best-fit Planck 2018 Cosmology [55]. Two values have been considered for the rotation angle, $1.0°$, a value already excluded by observations, simply to make more visible the effect, and $0.35°$.

Using Planck 2015 data, there is still no evidence for a nonzero $\Delta\bar{\chi}$. The collaboration has found, indeed, a uniform rotation angle of $\sim 0.3°$, with statistical errors of $0.05°$ and systematic uncertainties dominating the error budget, $\sigma_{syst} = 0.28°$ [81, 82].

The issue of this measurement using CMB data is that $\Delta\bar{\chi}$ is degenerate with β, that is, the angle at which the polarimeter is maximally sensitive to a linear polarization, in the telescope reference frame. A miscalibration of this angle leads to the same effect of the isotropic rotation angle, $\Delta\bar{\chi}$. In the result quoted above, the most relevant uncertainty is, indeed, due to this effect.

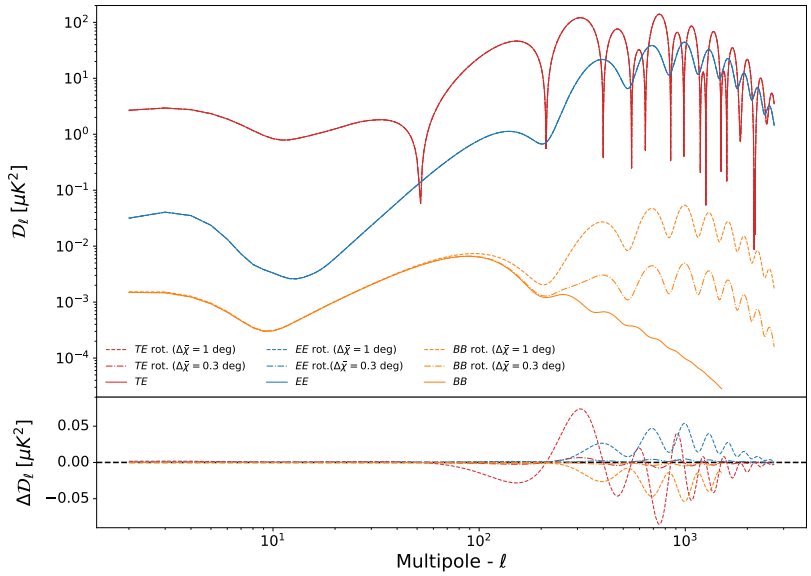

Figure 2.2: *Rotated CMB power spectra in presence of isotropic birefringence, according to Eqs. 2.7. The rotation angles are* $1.0°$ *(dashed lines) and* $0.35°$ *(dash-dotted lines). Solid lines are the CMB power spectra that we would observe in absence of this effect. In the bottom part, the absolute differences between the observed CMB power spectra in presence of cosmic birefringence and the ones that we would observe in absence of this effect. This plot has been produced using* `camb` *code with the Planck 2018 best-fit values for the* ΛCDM *parameters [55]. The tensor-to-scalar ratio is* $r = 0.07$.

In Ref. [83], the authors have solved this problems estimating $\Delta\bar{\chi}$ and β simultaneously. This has been done using the fact that while both CMB and Galactic foreground emission are rotated by β, CMB might be, instead, the only rotated by $\Delta\bar{\chi}$ [84, 85]. Hence, they estimated $\Delta\bar{\chi} = 0.35° \pm 0.14°$, where, in the error budget, $\sigma_{syst} = \sigma(\beta)$ is no longer included. This result is still consistent with the Planck 2015 result, but excludes $\Delta\bar{\chi} = 0$ with a statistical significance of 2.4σ.

In principle, the rotation angle in Eqs. 2.7 might depend on time as well as position. We can therefore consider a more general case, where the rotation angle can be written as

$$\Delta\chi = \Delta\bar{\chi} + \Delta\delta\chi\,. \tag{2.8}$$

We have separated the angle in two components: the background part, $\Delta\bar{\chi}$, which is homogeneous and isotropic, and the perturbation, which is randomly distributed on the sky, $\Delta\delta\chi$. In this case, the term *anisotropic cosmic birefringence* is generally used .

We can expand $\Delta\delta\chi$ on the sky [86] as

$$\Delta\delta\chi = \sum_{\ell m} b_{\ell m} Y_{\ell m}(\hat{\mathbf{n}}) \,, \tag{2.9}$$

and define its angular power spectrum as

$$< b^*_{\ell' m'} \, b_{\ell m} > = \, C^{\chi}_{\ell} \, \delta_{\ell' \ell} \, \delta_{m' m} \,, \tag{2.10}$$

where we have also assumed the statistical isotropy of $b_{\ell m}$. Moreover, summing over the multipoles ℓ, we find

$$\sum_{\ell} \big(2\ell + 1\big) C^{\chi}_{\ell} \; = \; 4\pi < \Delta\delta\chi^2 > \; . \tag{2.11}$$

Using Eq. 2.6, we can calculate the expansion coefficients, ${}_{\pm 2}a_{\ell m}$, after the rotation of the angle in Eq. 2.8

$$\begin{aligned}
{}_{\pm 2}a_{\ell m} \; &= \; \int \mathrm{d}\Omega \;\; {}_{\pm}Y^*_{\ell m}(\hat{\mathbf{n}}) \, \big(Q \pm iU\big)(\hat{\mathbf{n}}) \; = \\
&= \; \int \mathrm{d}\Omega \;\; {}_{\pm}Y^*_{\ell m}(\hat{\mathbf{n}}) \; \exp(\mp i 2\Delta\chi) \big(\tilde{Q} \pm i\tilde{U}\big)(\hat{\mathbf{n}}) \; = \\
&= \; \int \mathrm{d}\Omega \;\; {}_{\pm 2}Y^*_{\ell m}(\hat{\mathbf{n}}) \exp(\mp i 2\Delta\chi) \sum_{\ell' m'} \; {}_{\pm 2}\tilde{a}_{\ell' m'} \; {}_{\pm 2}Y_{\ell' m'}(\hat{\mathbf{n}}) \; = \\
&= \; \exp(\mp i 2\Delta\bar{\chi}) \sum_{\ell' m'} \; {}_{\pm 2}\tilde{a}_{\ell' m'} \, \mathcal{F}^{\pm}_{\ell m \ell' m'}
\end{aligned} \tag{2.12}$$

where

$$\mathcal{F}^{\pm}_{\ell m \ell' m'} \; = \; \int \mathrm{d}\Omega \;\; {}_{\pm 2}Y^*_{\ell m}(\hat{\mathbf{n}}) \exp(\mp i 2\Delta\delta\chi) \; {}_{\pm 2}Y_{\ell' m'}(\hat{\mathbf{n}}) \, . \tag{2.13}$$

If we consider $\Delta\delta\chi = 0$ in the above equations, after some math, we are able to recover the angular power spectra of the isotropic cosmic birefringence , shown in Eqs. 2.7.
In the case of anisotropic birefringence, instead, the computation is slightly more complicate, because of $\Delta\delta\chi = \Delta\delta\chi(\eta, \mathbf{x})$.
Hence, supposing that the rotation angle is small everywhere, up to the quadratic

order in $\Delta\delta\chi$, the angular power spectra are [75]

$$C_\ell^{TT} = \tilde{C}_\ell^{TT}\,; \tag{2.14a}$$

$$C_\ell^{TE} = \tilde{C}_\ell^{TE}\cos(2\Delta\bar{\chi})\big(1-2<\Delta\delta\chi^2>\big)\,; \tag{2.14b}$$

$$C_\ell^{TB} = \tilde{C}_\ell^{TE}\sin(2\Delta\bar{\chi})\big(1-2<\Delta\delta\chi^2>\big)\,; \tag{2.14c}$$

$$\begin{aligned} C_\ell^{EE} &= \Big[\tilde{C}_\ell^{EE}\cos^2(2\Delta\bar{\chi})+\tilde{C}_\ell^{BB}\sin^2(2\Delta\bar{\chi})\Big]\big(1-4<\Delta\delta\chi^2>\big)+ \\ &+\sum_{\ell_1\ell_2}\begin{pmatrix}\ell & \ell_1 & \ell_2\\ 2 & -2 & 0\end{pmatrix}^2\frac{(2\ell_1+1)(2\ell_2+1)}{2\pi}\mathcal{C}_{\ell_2}^{\chi}\cdot \\ &\cdot\left\{\Big[1+(-1)^{L+1}\cos(4\Delta\bar{\chi})\Big]\tilde{\mathcal{C}}_{\ell_1}^{EE}+\Big[1+(-1)^{L}\cos(4\Delta\bar{\chi})\Big]\tilde{\mathcal{C}}_{\ell_1}^{BB}\right\}; \end{aligned} \tag{2.14d}$$

$$\begin{aligned} C_\ell^{BB} &= \Big[\tilde{C}_\ell^{BB}\cos^2(2\Delta\bar{\chi})+\tilde{C}_\ell^{EE}\sin^2(2\Delta\bar{\chi})\Big]\big(1-4<\Delta\delta\chi^2>\big)+ \\ &+\sum_{\ell_1\ell_2}\begin{pmatrix}\ell & \ell_1 & \ell_2\\ 2 & -2 & 0\end{pmatrix}^2\frac{(2\ell_1+1)(2\ell_2+1)}{2\pi}\mathcal{C}_{\ell_2}^{\chi}\cdot \\ &\cdot\left\{\Big[1+(-1)^{L+1}\cos(4\Delta\bar{\chi})\Big]\tilde{\mathcal{C}}_{\ell_1}^{BB}+\Big[1+(-1)^{L}\cos(4\Delta\bar{\chi})\Big]\tilde{\mathcal{C}}_{\ell_1}^{EE}\right\}; \end{aligned} \tag{2.14e}$$

$$\begin{aligned} C_\ell^{EB} &= \frac{1}{2}\sin(4\Delta\bar{\chi})\Big(\tilde{C}_\ell^{EE}-\tilde{C}_\ell^{BB}\Big)\big(1-4<\Delta\delta\chi^2>\big)\;+\;\sin(4\Delta\bar{\chi})\cdot \\ &\cdot\sum_{\ell_1\ell_2}\begin{pmatrix}\ell & \ell_1 & \ell_2\\ 2 & -2 & 0\end{pmatrix}^2\frac{(2\ell_1+1)(2\ell_2+1)}{2\pi}\mathcal{C}_{\ell_2}^{\chi}\,(-1)^{L+1}\Big(\tilde{\mathcal{C}}_{\ell_1}^{EE}-\tilde{\mathcal{C}}_{\ell_1}^{BB}\Big), \end{aligned} \tag{2.14f}$$

where $L=\ell+\ell_1+\ell_2$, and, we have already set $\tilde{C}_\ell^{TB}=\tilde{C}_\ell^{TE}=0$.
We also have introduced the Wigner-3j symbol

$$\begin{pmatrix}\ell_1 & \ell_2 & \ell_3\\ m_1 & m_2 & m_3\end{pmatrix}, \tag{2.15}$$

that are defined in App. A.

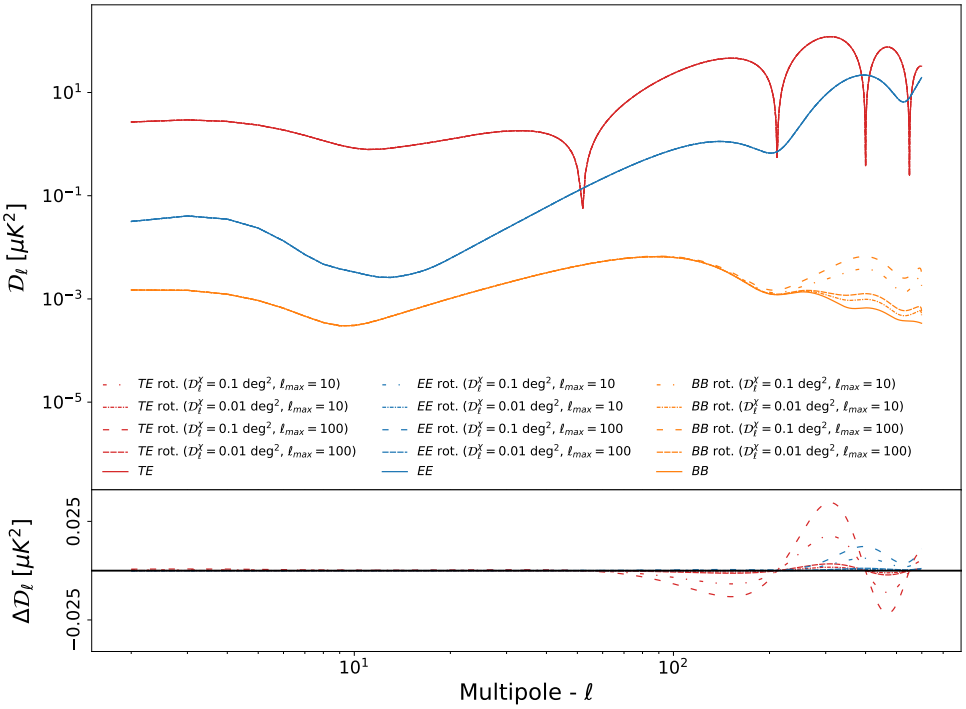

Figure 2.3: *Rotated CMB power spectra in presence of anisotropic birefringence, according to Eqs. 2.14. The rotation-angle power spectra, $\mathcal{D}_\ell^\chi$, has been consider scale-invariant up to a certain ℓ_{max}. We choose $\Delta\bar{\chi} = 0$. Solid lines are the CMB power spectra that we would observe in absence of this effect. In the bottom part, the absolute differences between the observed CMB power spectra in presence of cosmic birefringence and the ones that we would observe in absence of this effect, only for TE and EE. This plot has been produced using* `camb` *code with the Planck 2018 best-fit values for the ΛCDM parameters [55]. The tensor-to-scalar ratio is $r = 0.07$.*

In the above angular power spectra, if we chose $\Delta\delta\chi = 0$, we recover again Eqs. 2.7.
Moreover, it is interesting to note that C_ℓ^{TB} and C_ℓ^{EB} are proportional to $\sin(\Delta\bar{\chi})$, which vanish when $\Delta\bar{\chi} = 0$. This means that P is violated only by the background field, at least up to the second order in $\Delta\delta\chi$. This can be also seen in Fig. 2.3, where, since we have chosen $\Delta\bar{\chi} = 0$, C_ℓ^{TB} and C_ℓ^{EB} are vanishing. Again, the standard power spectra are computed using the Boltzmann code `camb` and assuming the best-fit Planck 2018 Cosmology [55].
Following a standard procedure (see *e.g.* [87]), we have assumed a scale-invariant spectrum for $\Delta\delta\chi$: $\mathcal{D}_\ell^\chi = A^\chi$ up to a certain ℓ_{max}, then $\mathcal{D}_\ell^\chi = 0$ from $\ell > \ell_{max}$. In Fig. 2.3, four cases are considered :

(i) $A^\chi = 0.1$ deg^2 with $\ell_{max} = 10$ (long-dashed lines);

(ii) $A^\chi = 0.1$ deg^2 with $\ell_{max} = 100$ (dashed lines);

(iii) $A^\chi = 0.01$ deg^2 with $\ell_{max} = 10$ (long-dash-dotted lines);

(iv) $A^\chi = 0.01$ deg^2 with $\ell_{max} = 100$.

Clearly, as we increase A^χ and ℓ_{max}, the modifications on the standard power spectra grow. The most relevant modifications are on the BB spectra. It is dramatically modified due to the power leaks from the much larger E-modes.

The most updated constraints on A^χ, using Planck 2018 data, can be found in [87]. They claim that no evidence of birefringence within the error budget, obtaining $A^\chi < 0.104$ deg^2.

2.2 CMB circular polarization

As we have already seen in the previous chapter, the circular polarization of the cosmic microwave background, also called V-mode polarization, is usually taken to be zero since it is not generated by Thomson scattering.
Nevertheless, there are several physical mechanisms that, at the second order in the primordial-perturbation amplitude, can induce circular polarization from the primordial linear polarization. In addition to this, circular polarization might be induced at a more significant level, by other late-time astrophysical effects, and/or by new physics beyond the standard model.

In [88], for example, it is shown that CMB photons can acquire circular polarization when propagating through a magnetized plasma, through the conversion of linear polarization. This mechanism is the so-called "Faraday conversion". In the rest of this thesis, we somehow inappropriately use this term to generally refer to the in-vacuo generation of circular polarization from linear polarization.
Many standard and non standard physical mechanism can source a degree of circular polarization in the CMB photons through this conversion of the linear polarization generated at the surface of last scattering. Among the former, it is worth mentioning the photon-photon interactions via Heisenberg-Euler interaction at recombination, that produces the strongest circular polarization. See *e.g.* Refs. [89, 90] for more details.

Moreover, although we do not expect such a process from conventional physics, CMB photons could become circularly polarized because the anisotropies of the cosmic neutrino background acts as a birefringent medium [91].
Looking at extensions of QED, V-modes arise when Lorentz-violating operators are considered [40, 92, 93]. In Ref. [94], instead, it is shown that a cosmological pseudo-scalar field may generate circular polarization in the CMB. Also axion inflation, as it is discussed in Ref. [95], leads to V-mode generation. There is also a class of effects called magneto-optic effects which generate CMB circular polarization, see [71, 96, 97]

For an exhaustive compilation of mechanisms that can source V-mode polarization in the CMB radiation, see Ref. [37, 98].

In any case, as we can deduce from the above list, there are several mechanisms, with a completely different physical background, that can induce a degree of circular polarization in the CMB radiation. Therefore, despite the fact that, so far, not too much attention has been devoted to CMB circular polarization, its detection might reveal interesting phenomena occurring in the evolution of the Universe.

Moreover, from the observational point of view, a relative large degree of CMB circular polarization is not excluded.

The SPIDER collaboration has recently provided new constraints on the Stokes parameter V at 95 and 150 GHz, by observing angular scales corresponding to $33 < \ell < 307$ [4]. These upper limits have been obtained by exploiting the non-idealities of the half-wave plate (HWP) polarization modulators used by SPIDER to measure linear polarization during a 2015 Antarctic flight. Let us briefly go into more details.
A birefringent material forms a HWP when the difference in the optical path length between waves polarized along the fast and slow crystal axes is exactly

half of the photon wavelength [99]. This means that the polarization plane of the light passing through an ideal HWP is rotated by $2\theta_{HWP}$, where θ_{HWP} is the angle between the incoming polarization plane and the slow crystal axis, with no coupling between linear and circular polarization.
A HWP can be described by four parameters: the total transmission T, the difference in transmission between the fast and slow axes ρ, the linear polarization response c, and the coupling to circular polarization s. For an ideal HWP, $T = 1$, $c = -1$, and $\rho = s = 0$. However, in real HWPs, these parameters can deviate significantly from these values. They can be calculated as described in [100], from the thicknesses and refractive indices of the HWP materials, the spectrum of the observed source, and the shape of the observing band.
The sky signal in the detector d, in terms of the Stokes parameters I , Q , U , and V and the instrument Mueller matrix elements M_{XY}, is

$$d = I\, M_{II} + Q\, M_{IQ} + U\, M_{IU} + V\, M_{IV}\,, \tag{2.16}$$

where the part concerning our discussion is M_{IV}, that reads

$$M_{IV} = s\gamma \sin\left(2\theta_{HWP} - 2\xi_{dec}\right) \tag{2.17}$$

where ξ_{det} and γ are the detector orientation angle and the polarization efficiency, respectively. It is interesting to note that in Eq. 2.16, s does not appear in the M_{II}, M_{IQ}, or M_{IU} matrix elements. This means that the coupling with linear polarization is not problematic for detecting a B-mode signal.

Even more recently, another experiment placed constraints on the VV power spectra. Precisely, CLASS, the Cosmology Large Angular Scale Surveyor based in the Atacama desert, presented a new upper limit, at 95% C.L., of 0.4 μK^2 to 13.5 μK^2 on $\ell(\ell+1)\, C_\ell^{VV}/2\pi$ between $1 \leq \ell \leq 120$. This is the result of the first two years of observation with the 40 GHz polarimeter and it represents a two-orders-of-magnitude improvement over the previous limits, as you can see in Fig. 2.4.
The CLASS experiments, differently from SPIDER, is designed to measure circular polarization, in that it employs the Variable-delay Polarization Modulator (VPM) technology.

The VPM is a simple instrument, only made by a flat mirror and, in parallel, a polarizing grid, placed in front of the mirror. The light approaching the grid is therefore reflected or transmitted depending on along which axis is polarized. Due to the mirror (that is placed after the grid), the transmitted light is reflected, and, then, it recombines with light reflected by the grid with an optical path

difference that depends on the grid-mirror separation. Choosing coordinates such that Stokes Q gives the difference between the polarization states parallel and perpendicular to the grid, the polarization transfer function can be expressed as

$$U' = U\cos\delta + V\sin\delta\,, \tag{2.18}$$

where the Stokes U and V are the input parameters and the Stokes U' is the output parameter. The phase δ encodes the delay between the polarized transmitted and reflected component at the output port of the device. This parameter is proportional to the grid-mirror separation and to the cosine of the light incident angle. This means that during one cycle of operation, the VPM switches the Stokes parameter U for the incoming light into Stokes V , and then into Stokes $-U$, see Fig. 1 of [101].

CLASS has been observing 75% of the sky with the 40 GHz instrument since 2016 (even though CLASS collaboration reports the results over 56% of the sky), and the remaining frequencies of 90, 150, and 220 GHz have been deployed and are currently collecting data.

Alongside these experiments, it is also worth mentioning the LiteBIRD satellite (see Chpt. 4 for more details), planned to be launched in 2027, is equipped with an HWP, so potentially new measurements of circular polarization are going to come in the next decades.

This wealth of data, along with the plenty of mechanisms sourcing a degree of circular polarization in the CMB radiation, brings into focus the importance of having a formalism able to account for all of them, or at least most of, and going one step further, that will allow us to easily set constrains on the parameters of these models.
Such a goal is one of the main purpose of this thesis. In the next section, we are going to see a unified framework describing the mixing of different polarization states during CMB photon propagation, that could also lead to the generation of CMB circular polarization from a pure linearly polarized initial state.

2.2.1 V-mode polarization power spectra

For completeness, let us define the angular power spectra of circular polarization, as done for temperature and linear polarization in Sec. 1.3.
We can consider $V(\hat{\mathbf{n}})$ as the amount of circular polarization at a given direction $\hat{\mathbf{n}}$ on the sky. The Stokes V is a scalar quantity (see App. C). Hence, $V(\hat{\mathbf{n}})$ can

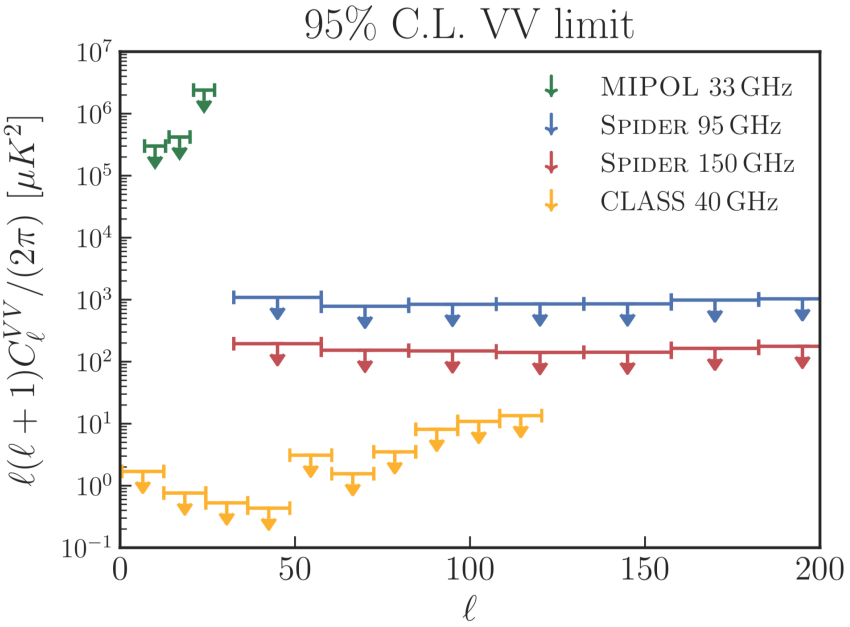

Figure 2.4: *MIPOL [5], SPIDER and CLASS 95% C.L. upper limits to extraterrestrial circular polarization.*

be expanded as

$$V(\hat{\mathbf{n}}) = \sum_{\ell m} a_{V,\ell m}\, Y_{\ell m}(\hat{\mathbf{n}}) \quad \text{and} \quad a_{V,\ell m} = \int \mathrm{d}\hat{\mathbf{n}}\, V(\hat{\mathbf{n}}) Y^*_{\ell m}(\hat{\mathbf{n}})\,, \tag{2.19}$$

where $Y_{\ell m}(\hat{\mathbf{n}})$ is a scalar spherical harmonics. It is worth mentioning that V is a pseudo-scalar under parity transformation, *i.e.* transforms as $V(\hat{\mathbf{n}}') = -V(\hat{\mathbf{n}})$ (see App. C for more details).
As in Sec. 1.3, we can assume that these $a_{V,\ell m}$s follow the normal distribution with zero mean value and non-zero variance, C_ℓ^{VV}[4].
So that, the angular power spectrum of V-mode polarization can be therefore defined as

$$C_\ell^{VV} = \frac{1}{2\ell+1}\langle a^*_{V,\ell m}\, a_{V,\ell m}\rangle\,, \tag{2.20}$$

where the $a_{V,\ell m}$s are given in Eq. 2.19.

[4]This assumption is motivated by the fact that inflation predict initial Gaussian perturbations.

2.3 A unified framework [5]

The common line between 2.1 and 2.2 lies in the fact that both cosmic birefringence and generation of a degree of circular polarization in the CMB can be seen as the result of a mixing among the CMB polarization components.
For this reason, we have studied the in-vacuo conversion between different polarization states of propagating radiation in a cosmological setting and, in the following, we are going to present the *unified framework* describing such a conversion. Precisely, the framework allows describing the "generalized Faraday effect" (GFE), the mixing among all polarization components, occurring when the natural modes of the radiation are elliptically polarized.

The starting point is the radiative transfer equation in terms of the Stokes parameters, as it is written and broadly discussed in many books of electromagnetism. After some assumptions, we will able to write this equation in a perturbed FLRW Universe and to solve it. Then, we will use the powerful tool of spherical harmonics expansion, to calculate the CMB angular power spectra. These formulas, Eqs. 2.49, express, in a completely general way, the modifications to the angular power spectra of CMB polarization induced by GFE in terms of the angular power spectrum of the GFE itself and of the CMB power spectra that would be observed if the GFE were absent. In the appropriate limits, these spectra describe cosmic birefringence and Faraday conversion, respectively.

2.3.1 Radiative transfer equation in perturbed FLRW Universe

The transfer equation for polarized radiation in a weakly[6] anisotropic medium reads [102–104]

$$\frac{d}{ds}\begin{pmatrix} I \\ Q \\ U \\ V \end{pmatrix} = \begin{pmatrix} \epsilon_I \\ \epsilon_Q \\ \epsilon_U \\ \epsilon_V \end{pmatrix} - \begin{pmatrix} \eta_I & \eta_Q & \eta_U & \eta_V \\ \eta_Q & \eta_I & \rho_V & -\rho_U \\ \eta_U & -\rho_V & \eta_I & \rho_Q \\ \eta_V & \rho_U & -\rho_Q & \eta_I \end{pmatrix} \begin{pmatrix} I \\ Q \\ U \\ V \end{pmatrix}, \tag{2.21}$$

where s is some affine parameter measuring length along the photon path, the ϵ's are the spontaneous emissivities, the η_{abs}'s describe absorption, and the

[5] Based on M. Lembo et al. [11].
[6] We want to treat the anisotropies as a perturbation.

ρ's describe what we have called the generalized Faraday effect: the mixing between different polarization components. In particular, ρ_V mixes Q and U polarization and is thus responsible for Faraday rotation, while ρ_Q and ρ_U mix linear polarization with V and are responsible for Faraday conversion.
It is worth underlining that the Stokes parameters, as well as the elements of the mixing matrix and the emissivities, depend, in principle, on conformal time η, position $\mathbf{x}$ and radiation wavenumber $\mathbf{p}$.

To reach the case of our interest, we have to make some assumptions. First of all, we only consider the case of a non-absorbing medium[7], and thus all the $\eta_{\rm abs}$'s are equal to 0. In this case, the total intensity decouples from polarization, and we are allowed to write an equation for the polarization-only Stokes vector $\mathbf{S} \equiv (Q, U, V)$.
Moreover, as described in Chpt. 1, CMB linear polarization is sourced by Thomson scattering at the epochs of recombination and reionization. This enables us to assume that the V emissivity is always zero, while the Q and U emissivities are strongly peaked at the time of hydrogen recombination, $\tau_{\rm rec}$, but vanishing elsewhere, and study Eq. 2.21 with $\epsilon = 0$ for $\tau > \tau_{\rm rec}$ and suitable initial conditions at recombination. Note that this basically amounts to neglecting the linear polarization generated at the time of cosmic reionization, see Chpt. 1. We also neglect the effect of gravitational lensing due to matter distribution along the line of sight. We will come back to these approximations later.

In light of these assumptions, Eq. 2.21 can be recast as

$$\frac{d\mathbf{S}}{ds} = \boldsymbol{\rho} \wedge \mathbf{S}\,, \tag{2.22}$$

where we have introduced the vector in polarization space $\boldsymbol{\rho} \equiv (\rho_Q, \rho_U, \rho_V)$, while $\wedge$ represents the usual cross product.
Looking at Eq. 2.22, it is clear that the direction of $\boldsymbol{\rho}$ defines the polarization of the natural modes of the medium: when $\boldsymbol{\rho}$ is aligned along the V direction ($\rho_Q = \rho_U = 0$, $\rho_V \neq 0$), the normal modes are circularly-polarized waves and Faraday rotation arises; when ρ is orthogonal to the V direction (ρ_Q, $\rho_U \neq 0$, $\rho_V = 0$) the normal modes are linearly-polarized and Faraday conversion takes place. In the general case, the normal modes are elliptically-polarized states.
Moreover, in this form, the equation lends itself to a simple interpretation: total

[7] We have made this assumption since the two effects (absorption and mixing of polarization states) are not necessarily related, and we were interested in studying the effects due to the mixing of the polarization states only. As a concrete example of a model in which one has GFE but not absorption, please see *e.g.* Ref. [40] and in particular their Eqs. (46-49) and (58-61).

polarization intensity $P = |S| = (Q^2 + U^2 + V^2)^{1/2}$ is conserved and the vector $\mathbf{S}$ precedes with angular velocity $|\boldsymbol{\rho}|$ around the direction of $\boldsymbol{\rho}$, $\hat{\boldsymbol{\rho}}$. In other words, after some time t, the vector $\mathbf{S}$ will have been rotated by an angle $2\alpha(t) = \int |\boldsymbol{\rho}|\, dt'$ around $\hat{\boldsymbol{\rho}}$. we have defined the precession angle with a factor 2 so that, in the Faraday rotation limit, α is the angle of rotation of the linear polarization plane. Indeed, if we think of $\mathbf{S}$ and $\boldsymbol{\rho}$ as vectors in polarization space, we have that a rotation of an angle α in the plane of the polarimeter corresponds to a rotation of an angle 2α in polarization space around the V axis for both vectors:

$$\underbrace{\hat{\boldsymbol{R}}^{(2)} = \begin{pmatrix} \cos\alpha & \sin\alpha \\ -\sin\alpha & \cos\alpha \end{pmatrix}}_{\text{plane orthogonal to the propagation direction}} \longrightarrow \underbrace{\hat{\boldsymbol{R}}_{\rm pol} = \begin{pmatrix} \cos 2\alpha & \sin 2\alpha & 0 \\ -\sin 2\alpha & \cos 2\alpha & 0 \\ 0 & 0 & 1 \end{pmatrix}}_{\text{polarization space}} \tag{2.23}$$

It is straightforward to show that, under the above rotations, Eq. 2.22 behaves well because the cross-product on the RHS is still a "good" vector and conserves the total polarization intensity $P = |S| = (Q^2 + U^2 + V^2)^{1/2}$.

For the purpose of calculating CMB anisotropies, it is more convenient to work with quantities with definite spin. Let us introduce the auxiliary polarization vector

$$\boldsymbol{\Delta}_P(\eta, \mathbf{x}, \mathbf{q}) = \left(\Delta_{P+}, \Delta_{P-}, V\right), \tag{2.24}$$

where $\Delta_{P\pm} = (Q \pm iU)/\sqrt{2}$ are the usual spin ± 2 combinations of Q and U. See App. C for more details. The effect of a rotation of the polarimeter by an angle α, *i.e.* a rotation in the plane orthogonal to the direction of light propagation, is thus equivalent to multiplying $\boldsymbol{\Delta}_P$ by

$$\hat{\boldsymbol{R}}(\alpha) \equiv \begin{pmatrix} e^{+2i\alpha} & 0 & 0 \\ 0 & e^{-2i\alpha} & 0 \\ 0 & 0 & 1 \end{pmatrix}. \tag{2.25}$$

Similarly, let us define $\rho_\pm \equiv (\rho_Q \pm i\rho_U)/\sqrt{2}$ and, from the above considerations, it follows that these should also be spin ± 2 quantities, respectively, while ρ_V is a pseudo-scalar. Note that we have introduced the comoving wavenumber $\mathbf{q} = a\mathbf{p}$, with $a(\eta)$ being the cosmological scale factor, to describe the wavenumber dependence.

Since we are interested in a cosmological setting, we have to write Eq. 2.22 in a perturbed FRLW Universe, see Eqs. 1.26 in Sec. *1.2.2*. Expanding the spatial dependence of $\boldsymbol{\Delta}_P$ in Fourier modes and keeping terms up to first order in cosmological perturbations yields

$$\frac{\partial \boldsymbol{\Delta}_P}{\partial \eta} + ik\mu\boldsymbol{\Delta}_P = i\boldsymbol{K}\boldsymbol{\Delta}_P\,, \tag{2.26}$$

where we have taken into account the fact that the background radiation field is unpolarized. This equation is valid both for scalar and tensor modes. Here, $\mathbf{k}$ is the wavevector of the perturbation, $\mu \equiv \hat{\mathbf{k}}\cdot\hat{\mathbf{q}}$, and $\boldsymbol{K}$ is the mixing matrix, defined as

$$\boldsymbol{K} \equiv \begin{pmatrix} \rho_V & 0 & -\rho_+ \\ 0 & -\rho_V & \rho_- \\ -\rho_- & \rho_+ & 0 \end{pmatrix}\,. \tag{2.27}$$

In deriving Eq. 2.26, we have assumed that the ρ's do not depend on $\mathbf{x}$. This is equivalent to require that the physics behind the generalized Faraday effect preserves homogeneity. In other words, we are considering a medium that is anisotropic/parity not conserving, but homogeneous.
Note that $\boldsymbol{K}$ is hermitian, because $\rho_+ = \rho_-^*$, and that a rotation around the direction of propagation sends $\hat{\mathbf{K}} \to \hat{\boldsymbol{R}}(\alpha)\boldsymbol{K}\hat{\boldsymbol{R}}(\alpha)^{-1}$.

We also require that the ρ's have the same time-dependency, *e.g.* from the scale factor. This case is still quite general, since it is not unreasonable to assume that the mixing parameters depend on time in the same way, if they share a common physical origin.
This is equivalent to consider

$$\boldsymbol{K} \;=\; f(\eta)\boldsymbol{K}_0\,, \tag{2.28}$$

where $f(\eta)$ is a generic function of time encoding the time-dependency of the ρ's and $\boldsymbol{K}_0$ is the time-independent part of Eq. 2.27.

A formal solution to this equation with given initial conditions at last scattering $\boldsymbol{\Delta}_P(\eta_{\rm LS}) = \boldsymbol{\Delta}_{\rm LS}$ can be written as:

$$\boldsymbol{\Delta}_P(\eta) = \exp\left(i\int_{\eta_{\rm LS}}^{\eta} \boldsymbol{K}\,d\eta'\right)\widetilde{\boldsymbol{\Delta}}_P(\eta)\,, \tag{2.29}$$

where $\widetilde{\boldsymbol{\Delta}}_P$ is a solution of the initial value problem

$$\frac{\partial \widetilde{\boldsymbol{\Delta}}_P}{\partial \eta} + ik\mu \widetilde{\boldsymbol{\Delta}}_P = 0\,; \qquad \widetilde{\boldsymbol{\Delta}}_P(\eta_{\rm LS}) = \boldsymbol{\Delta}_{\rm LS}\,. \tag{2.30}$$

In other words, Eq. 2.30 ensures that the components of $\widetilde{\Delta}$ are $\tilde{\Delta}$'s that would be observed in the absence of GFE, already calculated in Chpt. 1. Thus, it suffices to rotate these solutions through Eq. 2.29 to get the polarization perturbations modified by the GFE, at the present time.

It is worth mentioning that the solution as is written in Eq. 2.29 is valid only if the commutator $\big[\boldsymbol{K}(t_1),\, \boldsymbol{K}(t_2)\big]$ is equal to 0 for any pair of t_1 and t_2 (*i.e.*, $\boldsymbol{K}(t_1)\boldsymbol{K}(t_2) - \boldsymbol{K}(t_2)\boldsymbol{K}(t_1) = 0$). Clearly, this condition is trivially satisfied if $\boldsymbol{K}$ is independent of time or if we assume Eq. 2.28.
If we want to consider the case in which $\boldsymbol{K}$ depends on time in a more general way, we have to replace the integral in Eq. 2.29 with the Magnus series. Hence, Eq. 2.29 becomes

$$\boldsymbol{\Delta}_P(\eta) = \exp\Big[\Omega(\eta, \eta_{\rm LS})\Big]\, \widetilde{\boldsymbol{\Delta}}_P(\eta)\,, \tag{2.31}$$

where

$$\Omega(\eta, \eta_{\rm LS}) \;=\; \sum_{k=1}^{\infty} \Omega_k(\eta, \eta_{\rm LS}) \tag{2.32}$$

is the Magnus series. The terms of this series are defined as

$$\begin{aligned}
\Omega_1(\eta, \eta_{\rm LS}) \;&=\; \int_{\eta_{\rm LS}}^{\eta} \mathrm{d}\eta_1\; i\boldsymbol{K}(\eta_1)\,; \\
\Omega_2(\eta, \eta_{\rm LS}) \;&=\; \frac{1}{2}\int_{\eta_{\rm LS}}^{\eta} \mathrm{d}\eta_1 \int_{\eta_{\rm LS}}^{\eta_1} \mathrm{d}\eta_2\; \big[i\boldsymbol{K}(\eta_1),\, i\boldsymbol{K}(\eta_2)\big],\,; \\
\Omega_3(\eta, \eta_{\rm LS}) \;&=\; \frac{1}{6}\int_{\eta_{\rm LS}}^{\eta} \mathrm{d}\eta_1 \int_{\eta_{\rm LS}}^{\eta_1} \mathrm{d}\eta_2 \int_{\eta_{\rm LS}}^{\eta_2} \mathrm{d}\eta_3\; \Big(\Big[i\boldsymbol{K}(\eta_1), \big[i\boldsymbol{K}(\eta_2),\, i\boldsymbol{K}(\eta_3)\big]\Big] + \\
&\qquad + \Big[i\boldsymbol{K}(\eta_3), \big[i\boldsymbol{K}(\eta_2),\, i\boldsymbol{K}(\eta_1)\big]\Big]\Big)\,; \\
&\;\;\vdots
\end{aligned} \tag{2.33}$$

In applications, one can rarely sum exactly the Magnus series, and, it is usual to get approximate solutions, truncating the series. However, we have chosen to directly solve Eq. 2.29, assuming Eq. 2.28.

Let us rearrange Eq. 2.29 in a more convenient way. We can define the *average*

angular velocity $\bar{\boldsymbol{K}}$ as

$$\bar{\boldsymbol{K}} \equiv \frac{1}{\eta - \eta_{\rm LS}} \int_{\eta_{\rm LS}}^{\eta} \boldsymbol{K}(\eta') \mathrm{d}\eta' \;=\; \frac{1}{\eta} \boldsymbol{K}_0 \int_{\eta_{\rm LS}}^{\eta} f(\eta') \mathrm{d}\eta' \,, \tag{2.34}$$

and, the elements of $\bar{\boldsymbol{K}}$ are, therefore, quantities averaged along the line of sight,

$$\bar{\rho}_X \equiv \frac{1}{\eta - \eta_{\rm LS}} \int_{\eta_{\rm LS}}^{\eta} \rho_X(\eta') d\eta' \;=\; \frac{1}{\eta - \eta_{\rm LS}} \rho_{0,X} \int_{\eta_{\rm LS}}^{\eta} f(\eta') d\eta' \,. \tag{2.35}$$

With the above definitions, Eq. 2.29 becomes

$$\boldsymbol{\Delta}_P(\eta) = \exp\left(i \bar{\boldsymbol{K}} \Delta\eta\right) \widetilde{\boldsymbol{\Delta}}_P(\eta) \,. \tag{2.36}$$

Defining $\bar{\rho} \equiv \bar{\rho}_Q^2 + \bar{\rho}_U^2 + \bar{\rho}_V^2 = 2\bar{\rho}_+\bar{\rho}_- + \bar{\rho}_V^2$ and $2\alpha(\eta) \equiv \bar{\rho}(\eta - \eta_{LS})$, and, using the Rodrigues' rotation formula, the exponential in the RHS of Eq. 2.36 reads

$$\begin{aligned}
&\exp\left(i \bar{\boldsymbol{K}} \Delta\eta\right) \;=\; \exp\left(i \bar{\rho} \Delta\eta \bar{\boldsymbol{K}}'\right) \;= \\
&= \mathbf{1} + i\bar{\rho}\Delta\eta \; \bar{\boldsymbol{K}}' - \frac{(\bar{\rho}\Delta\eta)^2}{2} \bar{\boldsymbol{K}}'^2 - i\frac{(\bar{\rho}\Delta\eta)^3}{3!} \bar{\boldsymbol{K}}' + \frac{(\bar{\rho}\Delta\eta)^4}{4!} \bar{\boldsymbol{K}}'^2 + \cdots = \\
&= \mathbf{1} + [i \sin 2\alpha(\eta)] \bar{\boldsymbol{K}}' + [\cos 2\alpha(\eta) - 1] \bar{\boldsymbol{K}}'^2 \,,
\end{aligned} \tag{2.37}$$

where $\Delta\eta = \eta - \eta_{\rm LS}$ and $\bar{\boldsymbol{K}}' = \bar{\boldsymbol{K}}/\bar{\rho}$,

$$\bar{\boldsymbol{K}}^2 \equiv \begin{pmatrix} \bar{\rho}_-\bar{\rho}_+ + \bar{\rho}_V^2 & -\bar{\rho}_+^2 & -\bar{\rho}_+\bar{\rho}_V \\ -\bar{\rho}_-^2 & \bar{\rho}_-\bar{\rho}_+ + \bar{\rho}_V^2 & -\bar{\rho}_-\bar{\rho}_V \\ -\bar{\rho}_-\bar{\rho}_V & -\bar{\rho}_+\bar{\rho}_V & 2\bar{\rho}_-\bar{\rho}_+ \end{pmatrix} , \qquad \text{and} \qquad \bar{\boldsymbol{K}}^3 = \bar{\rho}^2 \bar{\boldsymbol{K}} . \tag{2.38}$$

Collecting all the above results, we get the following relations between the components of $\boldsymbol{\Delta}$ and $\widetilde{\boldsymbol{\Delta}}$ at a given time:

$$\begin{aligned}
\Delta_{P+}(\eta) \;=\; &\widetilde{\Delta}_{P+} \;+\; i \, \sin 2\alpha(\eta) \, \frac{\bar{\rho}_V \widetilde{\Delta}_{P+} - \bar{\rho}_+ \widetilde{V}}{\bar{\rho}} \;+ \\
&+ \left(1 - \cos 2\alpha(\eta)\right) \frac{1}{\bar{\rho}^2} \left[\left(\bar{\rho}_+\bar{\rho}_- - \bar{\rho}^2\right) \widetilde{\Delta}_{P+} + \bar{\rho}_+^2 \widetilde{\Delta}_{P-} + \bar{\rho}_+\bar{\rho}_V \widetilde{V} \right] ;
\end{aligned} \tag{2.39a}$$

$$\Delta_{P-}(\eta) = \widetilde{\Delta}_{P-} - i \sin 2\alpha(\eta) \frac{\bar{\rho}_V \widetilde{\Delta}_{P-} - \bar{\rho}_- \widetilde{V}}{\bar{\rho}} + \\ + (1 - \cos 2\alpha(\eta)) \frac{1}{\bar{\rho}^2} \left[\bar{\rho}_-^2 \widetilde{\Delta}_{P+} + \left(\bar{\rho}_+ \bar{\rho}_- - \bar{\rho}^2\right) \widetilde{\Delta}_{P-} + \bar{\rho}_- \bar{\rho}_V \widetilde{V} \right]; \tag{2.39b}$$

$$V(\eta) = \widetilde{V} - i \sin 2\alpha(\eta) \frac{\bar{\rho}_- \widetilde{\Delta}_{P+} - \bar{\rho}_+ \widetilde{\Delta}_{P-}}{\bar{\rho}} + \\ + (1 - \cos 2\alpha(\eta)) \frac{1}{\bar{\rho}^2} \left[\bar{\rho}_- \bar{\rho}_V \widetilde{\Delta}_{P+} + \bar{\rho}_+ \bar{\rho}_V \widetilde{\Delta}_{P-} + \left(\bar{\rho}_V^2 - \bar{\rho}^2\right) \widetilde{V} \right]. \tag{2.39c}$$

These equations are the exact solution of Eq. 2.29 and express the polarization perturbations after the mixing, the "un-tilded" quantities appearing in the LHS, in terms of those that would be realized in the sky if such a mixing were absent, the "tilded" quantities appearing on the RHS. They can be seen as a generalization of the equations for anisotropic cosmic birefringence, that is sourced by $Q - U$ mixing, to the case of a $Q - U - V$ mixing.

2.3.2 CMB power spectra in presence of GFE

In order to characterize the statistics of the CMB perturbations, we need to calculate angular power spectra. We thus expand in spherical harmonics both sides of Eqs. 2.39b.
While V, $\widetilde{V}$ and $\bar{\rho}_V$ are scalar quantities and can be naturally expanded in spin-0 spherical harmonics, $\Delta_{P\pm}$, $\widetilde{\Delta}_{P\pm}$ and $\bar{\rho}_\pm$ should be expanded in spin-weighted $s = \pm 2$ harmonics. See App. B for more details about the spin-wighted harmonics. Therefore:

$$V(\hat{\mathbf{n}}) = \sum_{\ell m} a_{V,\ell m} Y_{\ell m}(\hat{\mathbf{n}}), \qquad \widetilde{V}(\hat{\mathbf{n}}) = \sum_{\ell m} \widetilde{a}_{V,\ell m} Y_{\ell m}(\hat{\mathbf{n}}); \tag{2.40a}$$

$$\Delta_{P+}(\hat{\mathbf{n}}) = \sum_{\ell m} a_{2,\ell m\, 2} Y_{\ell m}(\hat{\mathbf{n}}), \qquad \widetilde{\Delta}_{P+}(\hat{\mathbf{n}}) = \sum_{\ell m} \widetilde{a}_{2,\ell m\, 2} Y_{\ell m}(\hat{\mathbf{n}}); \tag{2.40b}$$

$$\Delta_{P-}(\hat{\mathbf{n}}) = \sum_{\ell m} a_{-2,\ell m\, -2} Y_{\ell m}(\hat{\mathbf{n}}), \qquad \widetilde{\Delta}_{P-}(\hat{\mathbf{n}}) = \sum_{\ell m} \widetilde{a}_{-2,\ell m\, -2} Y_{\ell m}(\hat{\mathbf{n}}), \tag{2.40c}$$

and

$$\Delta\eta\, \bar{\rho}_V(\hat{\mathbf{n}}) = \sum_{\ell m} b_{V,\ell m} Y_{\ell m}(\hat{\mathbf{n}}); \tag{2.40d}$$

$$\Delta\eta\,\bar{\rho}_+(\hat{\mathbf{n}}) = \sum_{\ell m} b_{2,\ell m}\,{}_2Y_{\ell m}(\hat{\mathbf{n}})\,; \tag{2.40e}$$

$$\Delta\eta\,\bar{\rho}_-(\hat{\mathbf{n}}) = \sum_{\ell m} b_{-2,\ell m}\,{}_{-2}Y_{\ell m}(\hat{\mathbf{n}})\,, \tag{2.40f}$$

where $\Delta\eta = \eta - \eta_{\rm LS}$.
Given an explicit form of the ρ's, the $b_{\ell m}$'s can be computed explicitly, as it will be done in the next section.

Since we expect violations of isotropy/parity conservation to be small, we keep only terms up to second order in α. This allows us to drop all the terms of order higher than the second in Eqs. 2.39b, obtaining

$$\begin{aligned}
\Delta_{P+} &= \left(1 + i\Delta\eta\,\bar{\rho}_V - \frac{\Delta\eta^2\,\bar{\rho}_V\bar{\rho}_V}{2} - \frac{\Delta\eta^2\,\bar{\rho}_+\bar{\rho}_-}{2}\right)\widetilde{\Delta}_{P+} + \frac{\Delta\eta^2\,\bar{\rho}_+\bar{\rho}_+}{2}\widetilde{\Delta}_{P-}\,;\\
\Delta_{P-} &= \left(1 - i\Delta\eta\,\bar{\rho}_V - \frac{\Delta\eta^2\,\bar{\rho}_V\bar{\rho}_V}{2} - \frac{\Delta\eta^2\,\bar{\rho}_+\bar{\rho}_-}{2}\right)\widetilde{\Delta}_{P-} + \frac{\Delta\eta^2\,\bar{\rho}_-\bar{\rho}_-}{2}\widetilde{\Delta}_{P+}\,;\\
V &= \left(-i\Delta\eta\,\bar{\rho}_- + \frac{\Delta\eta^2\,\bar{\rho}_-\bar{\rho}_V}{2}\right)\widetilde{\Delta}_{P+} + \left(i\bar{\rho}_+ + \frac{\Delta\eta^2\,\bar{\rho}_+\bar{\rho}_V}{2}\right)\widetilde{\Delta}_{P-}\,,
\end{aligned} \tag{2.41}$$

where we took $\widetilde{V} = 0$, coherently with the standard model expectation of vanishing primordial V-mode.

Before proceeding further, let us simplify the calculation introducing the expansion coefficients $\mathcal{B}_{xy,\ell m}$ for the product $\Delta\eta^2\,\bar{\rho}_x\bar{\rho}_y$. For example:

$$\Delta\eta^2\,\bar{\rho}_V\bar{\rho}_V = \sum_{L_1}\sum_{L_2} b_{V,L_1}Y_{L_1}\,b_{V,L_2}Y_{L_2} = \tag{2.42a}$$

$$= \sum_{L,L_1,L_2} (-1)^m F_{\ell\ell_1\ell_2} \begin{pmatrix} \ell_1 & \ell_2 & \ell \\ m_1 & m_2 & m \end{pmatrix} \begin{pmatrix} \ell_1 & \ell_2 & \ell \\ 0 & 0 & 0 \end{pmatrix} b_{V,L_1}b_{V,L_2}\,Y_L =$$

$$= \sum_L \mathcal{B}_{VV,L}\,Y_L\,,$$

with

$$\mathcal{B}_{VV,L} = (-1)^m \sum_{L_1L_2} F_{\ell\ell_1\ell_2} \begin{pmatrix} \ell_1 & \ell_2 & \ell \\ m_1 & m_2 & m \end{pmatrix} \begin{pmatrix} \ell_1 & \ell_2 & \ell \\ 0 & 0 & 0 \end{pmatrix} b_{V,L_1}b_{V,L_2}\,, \tag{2.42b}$$

where $F_{\ell\ell_1\ell_2} = \left[(2\ell+1)\big(2\ell_1+1\big)\big(2\ell_2+1\big)/\big(4\pi\big)\right]^{(1/2)}$ and $L = (\ell, m)$. The latter notation will be often used in this Chapter. In the above calculation, we have used the contraction rule of two spherical harmonics, that can be extended to the case of spin-weighted spherical harmonics (see App. B). Similarly, we get:

$$\Delta\eta^2\, \bar{\rho}_+(\hat{\mathbf{n}})\bar{\rho}_-(\hat{\mathbf{n}}) \;=\; \sum_L \mathcal{B}_{+-,L}\; Y_L(\hat{\mathbf{n}})\,; \tag{2.43a}$$

$$\Delta\eta^2\, \bar{\rho}_+(\hat{\mathbf{n}})\bar{\rho}_+(\hat{\mathbf{n}}) \;=\; \sum_L \mathcal{B}_{++,L}\; {}_4Y_L(\hat{\mathbf{n}})\,; \tag{2.43b}$$

$$\Delta\eta^2\, \bar{\rho}_-(\hat{\mathbf{n}})\bar{\rho}_-(\hat{\mathbf{n}}) \;=\; \sum_L \mathcal{B}_{--,L}\; {}_{-4}Y_L(\hat{\mathbf{n}})\,; \tag{2.43c}$$

$$\Delta\eta^2\, \bar{\rho}_+(\hat{\mathbf{n}})\bar{\rho}_V(\hat{\mathbf{n}}) \;=\; \sum_L \mathcal{B}_{-V,L}\; {}_2Y_L(\hat{\mathbf{n}})\,; \tag{2.43d}$$

$$\Delta\eta^2\, \bar{\rho}_-(\hat{\mathbf{n}})\bar{\rho}_V(\hat{\mathbf{n}}) \;=\; \sum_L \mathcal{B}_{-V,L}\; {}_{-2}Y_L(\hat{\mathbf{n}})\,, \tag{2.43e}$$

where

$$\mathcal{B}_{+-,L} \;=\; (-1)^m \sum_{L_1 L_2} F_{\ell\ell_1\ell_2} \begin{pmatrix} \ell_1 & \ell_2 & \ell \\ m_1 & m_2 & m \end{pmatrix} \begin{pmatrix} \ell_1 & \ell_2 & \ell \\ -2 & 2 & 0 \end{pmatrix} b_{+,L_1} b_{-,L_2}\,; \tag{2.44a}$$

$$\mathcal{B}_{++,L} \;=\; (-1)^m \sum_{L_1 L_2} F_{\ell\ell_1\ell_2} \begin{pmatrix} \ell_1 & \ell_2 & \ell \\ m_1 & m_2 & m \end{pmatrix} \begin{pmatrix} \ell_1 & \ell_2 & \ell \\ -2 & -2 & 4 \end{pmatrix} b_{+,L_1} b_{+,L_2}\,; \tag{2.44b}$$

$$\mathcal{B}_{--,L} \;=\; (-1)^m \sum_{L_1 L_2} F_{\ell\ell_1\ell_2} \begin{pmatrix} \ell_1 & \ell_2 & \ell \\ m_1 & m_2 & m \end{pmatrix} \begin{pmatrix} \ell_1 & \ell_2 & \ell \\ 2 & 2 & -4 \end{pmatrix} b_{-,L_1} b_{-,L_2}\,; \tag{2.44c}$$

$$\mathcal{B}_{+V,L} \;=\; (-1)^m \sum_{L_1 L_2} F_{\ell\ell_1\ell_2} \begin{pmatrix} \ell_1 & \ell_2 & \ell \\ m_1 & m_2 & m \end{pmatrix} \begin{pmatrix} \ell_1 & \ell_2 & \ell \\ -2 & 0 & 2 \end{pmatrix} b_{+,L_1} b_{V,L_2}\,; \tag{2.44d}$$

$$\mathcal{B}_{-V,L} \;=\; (-1)^m \sum_{L_1 L_2} F_{\ell\ell_1\ell_2} \begin{pmatrix} \ell_1 & \ell_2 & \ell \\ m_1 & m_2 & m \end{pmatrix} \begin{pmatrix} \ell_1 & \ell_2 & \ell \\ 2 & 0 & -2 \end{pmatrix} b_{-,L_1} b_{V,L_2}\,. \tag{2.44e}$$

Projecting both sides of Eqs. 2.41 over the appropriate spherical harmonics

and keeping only terms up to second order in α, we get:

$$
\begin{aligned}
a_{E,L} &= \widetilde{a}_{E,L} + \left(\mathcal{G}^{(1)}_{L_1L} - \mathcal{H}^{(1)}_{L_1L} + \mathcal{H}^{(3)}_{L_1L}\right)\widetilde{a}_{E,L_1} - \left(\mathcal{G}^{(2)}_{L_1L} + \mathcal{H}^{(2)}_{L_1L} - \mathcal{H}^{(4)}_{L_1L}\right)\widetilde{a}_{B,L_1}\,; \\
a_{B,L} &= \widetilde{a}_{B,L} + \left(\mathcal{G}^{(1)}_{L_1L} - \mathcal{H}^{(1)}_{L_1L} - \mathcal{H}^{(3)}_{L_1L}\right)\widetilde{a}_{B,L_1} + \left(\mathcal{G}^{(2)}_{L_1L} + \mathcal{H}^{(2)}_{L_1L} + \mathcal{H}^{(4)}_{L_1L}\right)\widetilde{a}_{E,L_1}\,; \\
a_{V,L} &= \left(\mathcal{G}^{(3)}_{L_1L} - \mathcal{H}^{(5)}_{L_1L}\right)\widetilde{a}_{E,L_1} - \left(\mathcal{G}^{(4)}_{L_1L} + \mathcal{H}^{(6)}_{L_1L}\right)\widetilde{a}_{B,L_1}\,,
\end{aligned}
\tag{2.45}
$$

where we have made the usual definition $a_{E,L} = -(a_{2,L} + a_{-2,L})/2$ and $a_{B,L} = i(a_{2,L} - a_{-2,L})/2$, and, from now on, if not specified, summation over repeated indices is understood.
The $\mathcal{G}$ and $\mathcal{H}$ kernels contain only geometrical factors (products of Wigner-3j symbols), and, the b and $\mathcal{B}$ expansion coefficients respectively, and as such do not depend on the other cosmological parameters. Their explicit form is given in App. E.

We can now use Eqs. 2.45 to build correlators $C^{XY}_{LL'} \equiv \langle a_{X,L} a^*_{Y,L'}\rangle$. Note that the ordering of the fields is important: $C^{XY} \neq C^{YX}$. However, $C^{YX}_{LL'} = (-1)^{m+m'} C^{XY}_{-L-L'} = \left(C^{XY}_{L'L}\right)^*$.
Then, using $\langle \widetilde{a}_{X,L} \widetilde{a}^*_{Y,L'}\rangle = \widetilde{C}^{XY}_\ell \delta_{\ell\ell'}\delta_{mm'}$ for the "unrotated" fields, and the fact that primordial TB and EB correlations should be vanishing, we get (no implicit summation in the following):

$$
C^{TE}_{LL'} = \left[\delta_{\ell\ell'}\delta_{mm'} - \mathcal{G}^{(1)}_{L'L} - \mathcal{H}^{(1)}_{L'L} + \mathcal{H}^{(3)*}_{LL'} + \right]\widetilde{C}^{TE}_\ell\,; \tag{2.46a}
$$

$$
C^{TB}_{LL'} = \left[\mathcal{G}^{(2)}_{L'L} - \mathcal{H}^{(2)}_{L'L} + \mathcal{H}^{(4)*}_{LL'}\right]\widetilde{C}^{TE}_\ell\,; \tag{2.46b}
$$

$$
C^{TV}_{LL'} = \left[\mathcal{G}^{(3)*}_{LL'} - \mathcal{H}^{(5)*}_{LL'}\right]\widetilde{C}^{TE}_\ell; \tag{2.46c}
$$

$$
\begin{aligned}
C^{EE}_{LL'} = \widetilde{C}^{EE}_\ell \delta_{\ell\ell'}\delta_{mm'} - \left[\mathcal{G}^{(1)}_{L'L} + \mathcal{H}^{(1)}_{L'L} - \mathcal{H}^{(3)*}_{LL'}\right]\widetilde{C}^{EE}_\ell + \left[\mathcal{G}^{(1)}_{L'L} - \mathcal{H}^{(1)}_{L'L} + \mathcal{H}^{(3)}_{L'L}\right]\widetilde{C}^{EE}_{\ell'} + \\
- \sum_{L_1}\left[\mathcal{G}^{(1)}_{L'L_1}\mathcal{G}^{(1)}_{L_1L}\widetilde{C}^{EE}_{\ell_1} - \mathcal{G}^{(2)}_{L'L_1}\mathcal{G}^{(2)}_{L_1L}\widetilde{C}^{BB}_{\ell_1}\right];
\end{aligned}
\tag{2.46d}
$$

$$
\begin{aligned}
C^{BB}_{LL'} = \widetilde{C}^{BB}_\ell \delta_{\ell\ell'}\delta_{mm'} - \left[\mathcal{G}^{(1)}_{L'L} + \mathcal{H}^{(1)}_{L'L} + \mathcal{H}^{(3)*}_{LL'}\right]\widetilde{C}^{BB}_\ell + \left[\mathcal{G}^{(1)}_{L'L} - \mathcal{H}^{(1)}_{L'L} - \mathcal{H}^{(3)}_{L'L}\right]\widetilde{C}^{BB}_{\ell'} + \\
- \sum_{L_1}\left[\mathcal{G}^{(1)}_{L'L_1}\mathcal{G}^{(1)}_{L_1L}\widetilde{C}^{BB}_{\ell_1} - \mathcal{G}^{(2)}_{L'L_1}\mathcal{G}^{(2)}_{L_1L}\widetilde{C}^{EE}_{\ell_1}\right];
\end{aligned}
\tag{2.46e}
$$

$$C_{LL'}^{EB} = \left[\mathcal{G}_{L'L}^{(2)} - \mathcal{H}_{L'L}^{(2)} + \mathcal{H}_{LL'}^{(4)*}\right]\widetilde{C}_{\ell}^{EE} - \left[\mathcal{G}_{L'L}^{(2)} + \mathcal{H}_{L'L}^{(2)} - \mathcal{H}_{L'L}^{(4)}\right]\widetilde{C}_{\ell'}^{BB} + \\ + \sum_{L_1}\left[\mathcal{G}_{L'L_1}^{(2)}\mathcal{G}_{L_1L}^{(1)}\widetilde{C}_{\ell_1}^{EE} + \mathcal{G}_{L'L_1}^{(1)}\mathcal{G}_{L_1L}^{(2)}\widetilde{C}_{\ell_1}^{BB}\right]; \tag{2.46f}$$

$$C_{LL'}^{EV} = \left[\mathcal{G}_{LL'}^{(3)*} - \mathcal{H}_{LL'}^{(5)*}\right]\widetilde{C}_{\ell}^{EE} + \sum_{L_1}\left[\mathcal{G}_{L_1L'}^{(3)*}\mathcal{G}_{L_1L}^{(1)}\widetilde{C}_{\ell_1}^{EE} + \mathcal{G}_{L_1L'}^{(4)*}\mathcal{G}_{L_1L}^{(2)}\widetilde{C}_{\ell_1}^{BB}\right]; \tag{2.46g}$$

$$C_{LL'}^{BV} = -\left[\mathcal{G}_{LL'}^{(4)*} + \mathcal{H}_{LL'}^{(6)*}\right]\widetilde{C}_{\ell}^{BB} - \sum_{L_1}\left[\mathcal{G}_{L_1L'}^{(4)*}\mathcal{G}_{L_1L}^{(1)}\widetilde{C}_{\ell_1}^{BB} - \mathcal{G}_{L_1L'}^{(3)*}\mathcal{G}_{L_1L}^{(2)}\widetilde{C}_{\ell_1}^{EE}\right]; \tag{2.46h}$$

$$C_{LL'}^{VV} = \sum_{L_1}\left[\mathcal{G}_{L_1L'}^{(3)*}\mathcal{G}_{L_1L}^{(3)}\widetilde{C}_{\ell_1}^{EE} + \mathcal{G}_{L_1L'}^{(4)*}\mathcal{G}_{L_1L}^{(4)}\widetilde{C}_{\ell_1}^{BB}\right]. \tag{2.46i}$$

In view of comparison with observations, let us focus on the diagonal components ($L = L'$), but, in principle, there is potentially valuable information also in the off-diagonal terms.
Averaging over m and introducing

$$C_{\ell}^{XY} \equiv \frac{1}{2\ell+1}\sum_{m=-\ell}^{+\ell} C_{LL}^{XY}\,, \tag{2.47}$$

we end up with the following expressions:

$$C_{\ell}^{TE} = \left[1 - \frac{1}{2\ell+1}\sum_{m=-\ell}^{+\ell}\left(\mathcal{G}_{LL}^{(1)} + \mathcal{H}_{LL}^{(1)} - \mathcal{H}_{LL}^{(3)*}\right)\right]\widetilde{C}_{\ell}^{TE}\,; \tag{2.48a}$$

$$C_{\ell}^{TB} = \left[\frac{1}{2\ell+1}\sum_{m=-\ell}^{+\ell}\left(\mathcal{G}_{LL}^{(2)} - \mathcal{H}_{LL}^{(2)} + \mathcal{H}_{LL}^{(4)*}\right)\right]\widetilde{C}_{\ell}^{TE}\,; \tag{2.48b}$$

$$C_{\ell}^{TV} = \left[\frac{1}{2\ell+1}\sum_{m=-\ell}^{+\ell}\left(\mathcal{G}_{LL}^{(3)*} - \mathcal{H}_{LL}^{(5)*}\right)\right]\widetilde{C}_{\ell}^{TE}\,; \tag{2.48c}$$

$$C_{\ell}^{EE} = \left[1 - \frac{1}{2\ell+1}\sum_{m=-\ell}^{+\ell}\left(2\mathcal{H}_{LL}^{(1)} - \mathcal{H}_{LL}^{(3)} - \mathcal{H}_{LL}^{(3)*}\right)\right]\widetilde{C}_{\ell}^{EE} + \\ - \frac{1}{2\ell+1}\sum_{L_1}\left[\left(\sum_{m=-\ell}^{+\ell}\mathcal{G}_{LL_1}^{(1)}\mathcal{G}_{L_1L}^{(1)}\right)\widetilde{C}_{\ell_1}^{EE} - \left(\sum_{m=-\ell}^{+\ell}\mathcal{G}_{LL_1}^{(2)}\mathcal{G}_{L_1L}^{(2)}\right)\widetilde{C}_{\ell_1}^{BB}\right]\,; \tag{2.48d}$$

$$C_\ell^{BB} = \left[1 - \frac{1}{2\ell+1}\sum_{m=-\ell}^{+\ell}\left(2\mathcal{H}_{LL}^{(1)} + \mathcal{H}_{LL}^{(3)} + \mathcal{H}_{LL}^{(3)*}\right)\right]\widetilde{C}_\ell^{BB} + \\ - \frac{1}{2\ell+1}\sum_{L_1}\left[\left(\sum_{m=-\ell}^{+\ell}\mathcal{G}_{LL_1}^{(1)}\mathcal{G}_{L_1L}^{(1)}\right)\widetilde{C}_{\ell_1}^{BB} - \left(\sum_{m=-\ell}^{+\ell}\mathcal{G}_{LL_1}^{(2)}\mathcal{G}_{L_1L}^{(2)}\right)\widetilde{C}_{\ell_1}^{EE}\right]\,; \quad (2.48e)$$

$$C_\ell^{EB} = \frac{1}{2\ell+1}\sum_{m=-\ell}^{+\ell}\left[\left(\mathcal{G}_{LL}^{(2)} - \mathcal{H}_{LL}^{(2)} + \mathcal{H}_{LL}^{(4)*}\right)\widetilde{C}_\ell^{EE} - \left(\mathcal{G}_{LL}^{(2)} + \mathcal{H}_{LL}^{(2)} - \mathcal{H}_{LL}^{(4)}\right)\widetilde{C}_\ell^{BB}\right] + \\ + \frac{1}{2\ell+1}\sum_{L_1}\left[\left(\sum_{m=-\ell}^{+\ell}\mathcal{G}_{LL_1}^{(2)}\mathcal{G}_{L_1L}^{(1)}\right)\widetilde{C}_{\ell_1}^{EE} + \left(\sum_{m=-\ell}^{+\ell}\mathcal{G}_{LL_1}^{(1)}\mathcal{G}_{L_1L}^{(2)}\right)\widetilde{C}_{\ell_1}^{BB}\right]\,; \quad (2.48f)$$

$$C_\ell^{EV} = \left[\frac{1}{2\ell+1}\sum_{m=-\ell}^{+\ell}\left(\mathcal{G}_{LL}^{(3)*} - \mathcal{H}_{LL}^{(5)*}\right)\right]\widetilde{C}_\ell^{EE} + \\ + \frac{1}{2\ell+1}\sum_{L_1}\left[\left(\sum_{m=-\ell}^{+\ell}\mathcal{G}_{L_1L}^{(3)*}\mathcal{G}_{L_1L}^{(1)}\right)\widetilde{C}_{\ell_1}^{EE} + \left(\sum_{m=-\ell}^{+\ell}\mathcal{G}_{L_1L}^{(4)*}\mathcal{G}_{L_1L}^{(2)}\right)\widetilde{C}_{\ell_1}^{BB}\right]\,; \quad (2.48g)$$

$$C_\ell^{BV} = -\left[\frac{1}{2\ell+1}\sum_{m=-\ell}^{+\ell}\left(\mathcal{G}_{LL}^{(4)*} + \mathcal{H}_{LL}^{(6)*}\right)\right]\widetilde{C}_\ell^{BB} + \\ + \frac{1}{2\ell+1}\sum_{L_1}\left[\left(\sum_{m=-\ell}^{+\ell}\mathcal{G}_{L_1L}^{(4)*}\mathcal{G}_{L_1L}^{(1)}\right)\widetilde{C}_{\ell_1}^{BB} - \left(\sum_{m=-\ell}^{+\ell}\mathcal{G}_{L_1L}^{(3)*}\mathcal{G}_{L_1L}^{(2)}\right)\widetilde{C}_{\ell_1}^{EE}\right]\,; \quad (2.48h)$$

$$C_\ell^{VV} = \frac{1}{2\ell+1}\sum_{L_1}\left[\left(\sum_{m=-\ell}^{+\ell}\mathcal{G}_{L_1L}^{(3)}\mathcal{G}_{L_1L}^{(3)*}\right)\widetilde{C}_{\ell_1}^{EE} + \left(\sum_{m=-\ell}^{+\ell}\mathcal{G}_{L_1L}^{(4)}\mathcal{G}_{L_1L}^{(4)*}\right)\widetilde{C}_{\ell_1}^{BB}\right]\,. \quad (2.48i)$$

Note that now, since we have chosen $L = L'$, the order of the fields is unimportant: $C_\ell^{XY} = C_\ell^{YX}$. Also, the C_ℓ's are real.

Some of the sums can be further simplified by using the properties of the Wigner symbols (see App. E).

Definitely , the spectra that are not trivially equal to their "unrotated" counterparts are (note that we have restored the implicit summation convention here):

$$C_\ell^{TE} = \left(1 - \frac{\mathcal{Z}}{2}\right) \widetilde{C}_\ell^{TE} \,; \tag{2.49a}$$

$$C_\ell^{TB} = \frac{b_{V,00}}{\sqrt{4\pi}} \widetilde{C}_\ell^{TE} \,; \tag{2.49b}$$

$$C_\ell^{EE} = \left(1 - \mathcal{Z}\right) \widetilde{C}_\ell^{EE} + \mathcal{K}^{11}_{\ell_1\ell} \widetilde{C}_{\ell_1}^{EE} + \mathcal{K}^{22}_{\ell_1\ell} \widetilde{C}_{\ell_1}^{BB} \,; \tag{2.49c}$$

$$C_\ell^{BB} = \left(1 - \mathcal{Z}\right) \widetilde{C}_\ell^{BB} + \mathcal{K}^{11}_{\ell_1\ell} \widetilde{C}_{\ell_1}^{BB} + \mathcal{K}^{22}_{\ell_1\ell} \widetilde{C}_{\ell_1}^{EE} \,; \tag{2.49d}$$

$$C_\ell^{EB} = \frac{b_{V,00}}{\sqrt{4\pi}} \left(\widetilde{C}_\ell^{EE} - \widetilde{C}_\ell^{BB}\right) \,; \tag{2.49e}$$

$$C_\ell^{EV} = \mathcal{K}^{13}_{\ell_1\ell} \widetilde{C}_{\ell_1}^{EE} + \mathcal{K}^{24}_{\ell_1\ell} \widetilde{C}_{\ell_1}^{BB} \,; \tag{2.49f}$$

$$C_\ell^{BV} = \mathcal{K}^{23}_{\ell_1\ell} \widetilde{C}_{\ell_1}^{EE} - \mathcal{K}^{14}_{\ell_1\ell} \widetilde{C}_{\ell_1}^{BB} \,; \tag{2.49g}$$

$$C_\ell^{VV} = \mathcal{K}^{33}_{\ell_1\ell} \widetilde{C}_{\ell_1}^{EE} + \mathcal{K}^{44}_{\ell_1\ell} \widetilde{C}_{\ell_1}^{BB} \,, \tag{2.49h}$$

where we have defined the $\mathcal{K}$ kernels as

$$\mathcal{K}^{a\,b}_{\ell_1\ell} = (2\ell+1)^{-1} \sum_{m_1,m} \mathcal{G}^{(a)}_{L_1 L} \mathcal{G}^{(b)*}_{L_1 L} \,, \tag{2.50}$$

and

$$4\pi\mathcal{Z} = \sum_{\ell m} \left(|b_{V,\ell m}|^2 + |b_{2,\ell m}|^2\right) \,. \tag{2.51}$$

It is interesting to note that, if the ρ's have to be interpreted as stochastic quantities, $\mathcal{Z}$ gives their variance.

In the following table, we gather each kernels appearing in Eqs. (2.49), $\mathcal{K}$ and $\mathcal{Z}$, with their dependences in terms of the ρ's coefficients. The full expression of these kernels is shown in App. E. Moreover, in the last column, we added the power spectra in which these kernels appear.

Equations 2.49 encode, in a very general way, the modifications due to GFE, linking the modified power spectra to the power spectra that we would have in absence of this effect: they follow quite strightly from Eq. 2.21, after assuming a non-absorbing medium, $\eta_{\rm abs} = 0$, a zero emissivity for V, $\epsilon_V = 0$, and neglecting the linear polarization generated at the time of cosmic reionization, $\epsilon_Q = \epsilon_U = 0$. It is useful to recall that we have also made the assumption in Eq. 2.28 to ensure $\left[\boldsymbol{K}(\eta_1), \boldsymbol{K}(\eta_2)\right] = 0$. Moreover, Eqs. 2.49 are valid only up to second order in α

$\mathcal{K}^{ab}$ - $\mathcal{Z}$	ρ_x	C_ℓ^{AB}
$\mathcal{K}^{11}$	ρ_V (odd multipoles only)	C_ℓ^{EE}, C_ℓ^{BB}
$\mathcal{K}^{13}$	ρ_V, ρ_Q, ρ_U (odd multipoles only)	C_ℓ^{EV}
$\mathcal{K}^{14}$	ρ_V, ρ_Q, ρ_U (odd multipoles only)	C_ℓ^{BV}
$\mathcal{K}^{22}$	ρ_V (even multipoles only)	C_ℓ^{EE}, C_ℓ^{BB}
$\mathcal{K}^{23}$	ρ_V, ρ_Q, ρ_U (even multipoles only)	C_ℓ^{BV}
$\mathcal{K}^{24}$	ρ_V, ρ_Q, ρ_U (even multipoles only)	C_ℓ^{EV}
$\mathcal{K}^{33}$	ρ_Q, ρ_U	C_ℓ^{VV}
$\mathcal{K}^{44}$	ρ_Q, ρ_U	C_ℓ^{VV}
$\mathcal{Z}$	ρ_V, ρ_Q, ρ_U	C_ℓ^{TE}, C_ℓ^{EE}, C_ℓ^{BB}

and assuming no primordial EB/TB spectra.

Let us recall the behavior of the Stokes parameters under parity transformations: T and E are scalars while B and V are pseudo-scalars. As aspected, the mixing among the polarization components leads to parity-violating power spectra, such as EB, TB and EV.

To deeply understand the strength of this formalism, we can consider some limiting cases of Eqs. 2.49.

2.3.2.1 *Cosmic birefringence,* $\rho_V \neq 0$ *and* $\rho_Q = \rho_U = 0$*:*

The Stokes vector rotates around the $V-$direction and only Q and U mix. This is the "cosmic birefringence", widely discussed in Sec. 2.1. It is immediate to convince oneself that in this case α is the birefringence angle, i.e. the angle of rotation of the plane of linear polarization. From Eqs. 2.49, we get

$$C_\ell^{TE} = \left[1 - \frac{1}{2}\left(\frac{b_{V,00}^2}{4\pi} + \sum_{\substack{\ell m \\ \ell \geq 1}} \frac{|b_{V,\ell m}|^2}{4\pi}\right)\right] \widetilde{C}_\ell^{TE}\,; \tag{2.52a}$$

$$C_\ell^{TB} = \frac{b_{V,00}}{\sqrt{4\pi}}\,\widetilde{C}_\ell^{TE}\,; \tag{2.52b}$$

$$C_\ell^{EE} = \left[1 - \left(\frac{b_{V,00}^2}{4\pi} + \sum_{\substack{\ell m \\ \ell \geq 1}} \frac{|b_{V,\ell m}|^2}{4\pi}\right)\right] \widetilde{C}_\ell^{EE} + \mathcal{K}^{11}_{\ell_1 \ell}\widetilde{C}_{\ell_1}^{EE} + \mathcal{K}^{22}_{\ell_1 \ell}\widetilde{C}_{\ell_1}^{BB}\,; \tag{2.52c}$$

$$C_\ell^{BB} = \left[1 - \left(\frac{b_{V,00}^2}{4\pi} + \sum_{\substack{\ell m \\ \ell \geq 1}} \frac{|b_{V,\ell m}|^2}{4\pi}\right)\right] \widetilde{C}_\ell^{BB} + \mathcal{K}^{11}_{\ell_1 \ell} \widetilde{C}^{BB}_{\ell_1} + \mathcal{K}^{22}_{\ell_1 \ell} \widetilde{C}^{EE}_{\ell_1} ; \quad (2.52d)$$

$$C_\ell^{EB} = \frac{b_{V,00}}{\sqrt{4\pi}} \left(\widetilde{C}_\ell^{EE} - \widetilde{C}_\ell^{BB}\right) , \quad (2.52e)$$

and we recover the second-order equations for both isotropic, Eqs. 2.7, and anisotropic birefringence, Eqs. 2.14, with the identifications

$$2\Delta\bar{\chi} \equiv \frac{b_{V,00}}{\sqrt{4\pi}} \qquad \text{and} \qquad 4\langle \Delta\delta\chi^2 \rangle \equiv \sum_{\substack{\ell m \\ \ell \geq 1}} \frac{|b_{V,00}|^2}{4\pi} . \quad (2.53a)$$

2.3.2.2 *Faraday Conversion,* $\rho_V = 0$*,* $\rho_Q \neq 0$ *and/or* $\rho_U \neq 0$*:*

Circular polarization is generated by *conversion* of the primordial linear polarization as CMB photon propagate through a birefringent medium along the line of sight. See Sec. *2.2* for more details. In particular, from Eqs. (2.49), it can be seen that a non-zero VV power spectrum is sourced, while the cross-spectra between circular and linear polarization remain vanishing, at least up to second order, if $\rho_V = 0$. From Eqs. 2.49,

$$C_\ell^{TE} = \left(1 - \frac{1}{2} \sum_{\ell m} \frac{|b_{2,\ell m}|^2}{4\pi}\right) \widetilde{C}_\ell^{TE} ; \quad (2.54a)$$

$$C_\ell^{EE} = \left(1 - \sum_{\ell m} \frac{|b_{2,\ell m}|^2}{4\pi}\right) \widetilde{C}_\ell^{EE} ; \quad (2.54b)$$

$$C_\ell^{BB} = \left(1 - \sum_{\ell m} \frac{|b_{2,\ell m}|^2}{4\pi}\right) \widetilde{C}_\ell^{BB} ; \quad (2.54c)$$

$$C_\ell^{VV} = \mathcal{K}^{33}_{\ell_1 \ell} \widetilde{C}^{EE}_{\ell_1} + \mathcal{K}^{44}_{\ell_1 \ell} \widetilde{C}^{BB}_{\ell_1} . \quad (2.54d)$$

2.4 A tool to constrain the optical properties of the Universe[8]

The unified framework introduced in the previous section, and so even better Eqs. 2.49, allow for in-vacuo conversion of polarization states in a cosmological setting is understood.
Mixing of the polarization components can arise through several mechanisms, involving either known physics or more exotic models. Given such a mechanism, the ρ's in Eqs. 2.49 can be computed and specific predictions for the observed power spectra can be obtained. Moreover, even though the mixing of CMB polarization states has been studied in the literature, most of the previous studies concentrated on specific models giving rise to mixing between linear polarization, or to the conversion of linear to circular polarization. There was no attempt to provide a general, model-independent framework to study these effects. In this sense, this framework filled that gap, also providing a neat physical description of the GFE as the precession of the Stokes vector.

Here, we make a further step. Drawing inspiration from the propagation of light in anisotropic or chiral media (e.g., crystals), we can describe GFE as the result of light propagating into a medium with an anisotropic and/or parity-violating susceptibility tensor. In other words, we are relating the GFE parameters to the optical properties of the medium traversed by CMB photons.

Let us start from fundamental concepts. The polarization $\mathbf{P}$ produced in a medium by a given electric field $\mathbf{E}$ is related to the field itself by

$$\mathbf{P} = \epsilon_0 \chi \mathbf{E}\,, \tag{2.55}$$

where ϵ_0 is the dielectric constant. If the medium is anisotropic (e.g. a crystal), $\mathbf{P}$ and $\mathbf{E}$ are not aligned and χ is a tensor, called the susceptibility tensor. This tensor encodes all the optical properties of the medium.

If we consider a non-dispersive medium, the more general form of the susceptibility tensor is

$$\boldsymbol{\chi} = \begin{pmatrix} \chi_{xx} & i\,\chi_{xy} & -i\,\chi_{xz} \\ -i\,\chi_{xy} & \chi_{yy} & i\,\chi_{yz} \\ i\,\chi_{xz} & -i\,\chi_{yz} & \chi_{zz} \end{pmatrix}\,, \tag{2.56}$$

where the χ_{ij}'s are all real. The reference frame in which the susceptibility

[8] Based on M. Lembo et al. [11].

tensor takes this form is the one aligned with the principal axes of the crystal, i.e., the eigenvectors of $\mathrm{Re}(\boldsymbol{\chi})$. The elements of $\boldsymbol{\chi}$ in this basis have a simple physical interpretation. The diagonal elements are responsible for different linear polarization states propagating with different velocities, and as such they violate isotropy. These elements are so related to birefringence. The off-diagonal elements are, instead, related to optical activity. In other words, waves with different chirality are propagating with different speeds, violating parity.

We assume that the medium is homogeneous (homogeneous does not mean isotropic), therefore $\boldsymbol{\chi}$ in Eq. 2.56 does not depend on position; it might however depend on the radiation wavenumber.

To the purpose of making a connection between the three-dimensional susceptibility tensor and the ρ's, we compare Eq. 2.21 with the radiative transfer equation written in terms of the susceptibility tensor [102, 103, 105]:

$$\left(\frac{\partial}{\partial t}+\hat{\mathbf{p}}\cdot\nabla\right)\mathcal{I}_{ab}=\mathcal{E}_{ab}+i(2\pi\nu)\left(\chi^{(2)}_{ac}\mathcal{I}_{cb}-\mathcal{I}_{ac}(\chi^{(2)\dagger})_{cb}\right)\,, \tag{2.57}$$

where $\mathcal{I}_{ab}$ is the polarization tensor,

$$\mathcal{I}_{ab}=\langle E_a E_b^*\rangle=\frac{1}{2}\begin{pmatrix} I+Q & U+iV \\ U-iV & I-Q\end{pmatrix}, \tag{2.58}$$

$\mathcal{E}_{ab}$ is the tensor of spontaneous emission intensity per unit volume, ν is the radiation frequency, and $\chi^{(2)}_{ab}$ is the susceptibility tensor in the plane perpendicular to the direction of light propagation,

$$\begin{aligned}\boldsymbol{\chi}^{(2)}=&\begin{pmatrix}\left(\chi_{xx}c_\phi^2+\chi_{yy}s_\phi^2\right)c_\theta^2+\chi_{zz}s_\theta^2 & (\chi_{yy}-\chi_{xx})c_\theta s_\phi c_\phi \\ (\chi_{yy}-\chi_{xx})c_\theta s_\phi c_\phi & \left(\chi_{xx}s_\phi^2+\chi_{yy}c_\phi^2\right)\end{pmatrix}+\\ &+i\begin{pmatrix}0 & \chi_{xy}c_\theta+(\chi_{yz}c_\phi+\chi_{xz}s_\phi)\,s_\theta \\ -\chi_{xy}c_\theta-(\chi_{yz}c_\phi+\chi_{xz}s_\phi)\,s_\theta & 0\end{pmatrix},\end{aligned} \tag{2.59}$$

where we have introduced the short-hand notation $s_X\equiv\sin X$ and $c_X\equiv\cos X$. For the moment, we do not make any assumption about $\boldsymbol{\chi}$ and $\boldsymbol{\chi}^{(2)}$, so the latter should be regarded as the most general 2×2 tensor, having 8 degrees of freedom.

Eq. 2.57 can be rearranged in terms of the Stokes vector $S = (I, Q, U, V)$ as

$$\frac{d}{ds}\begin{pmatrix} I \\ Q \\ U \\ V \end{pmatrix} = \begin{pmatrix} \epsilon_I \\ \epsilon_Q \\ \epsilon_U \\ \epsilon_V \end{pmatrix} + 2\pi\nu \underbrace{\begin{pmatrix} T_{II} & T_{IQ} & T_{IU} & T_{IV} \\ T_{QI} & T_{QQ} & T_{QU} & T_{QV} \\ T_{UI} & T_{UQ} & T_{UU} & T_{UV} \\ T_{VI} & T_{VQ} & T_{VU} & T_{VV} \end{pmatrix}}_{\boldsymbol{\mathcal{T}}} \begin{pmatrix} I \\ Q \\ U \\ V \end{pmatrix}, \tag{2.60}$$

where

$$\epsilon_I = \mathcal{E}_{11} + \mathcal{E}_{22}; \quad \epsilon_Q = \mathcal{E}_{11} - \mathcal{E}_{22}; \quad \epsilon_U = \mathcal{E}_{12} + \mathcal{E}_{21}; \quad \epsilon_V = -i\left(\mathcal{E}_{12} - \mathcal{E}_{21}\right), \tag{2.61}$$

and

$$T_{II} = T_{QQ} = T_{UU} = T_{VV} = -\operatorname{Im}\left\{\left(\chi^{(2)}_{11} + \chi^{(2)}_{22}\right)\right\}; \tag{2.62}$$

$$T_{IQ} = T_{QI} = -\operatorname{Im}\left\{\left(\chi^{(2)}_{11} - \chi^{(2)}_{22}\right)\right\}; \tag{2.63}$$

$$T_{IU} = T_{UI} = -\operatorname{Im}\left\{\left(\chi^{(2)}_{12} + \chi^{(2)}_{21}\right)\right\}; \tag{2.64}$$

$$T_{IV} = T_{VI} = \operatorname{Re}\left\{\left(\chi^{(2)}_{12} - \chi^{(2)}_{21}\right)\right\}; \tag{2.65}$$

$$T_{QU} = -T_{UQ} = -\operatorname{Im}\left\{\left(\chi^{(2)}_{12} - \chi^{(2)}_{21}\right)\right\} \tag{2.66}$$

$$T_{QV} = -T_{VQ} = \operatorname{Re}\left\{\left(\chi^{(2)}_{12} + \chi^{(2)}_{21}\right)\right\}; \tag{2.67}$$

$$T_{UV} = -T_{VU} = -\operatorname{Re}\left\{\left(\chi^{(2)}_{11} - \chi^{(2)}_{22}\right)\right\}. \tag{2.68}$$

Note that $\boldsymbol{\mathcal{T}}$ has 7 independent components, even though we started with 8 d.o.f.'s from $\boldsymbol{\chi}^{(2)}$. The reason lies in the fact that the real part of the trace of $\boldsymbol{\chi}^{(2)}$ does not enter the RHS of Eq. 2.57, since

$$A\delta_{ac}\mathcal{I}_{cb} - \mathcal{I}_{ac}(A\delta_{cb})^{\dagger} = (A - A^{*})\mathcal{I}_{ab} = 0\,, \tag{2.69}$$

if A is a real quantity. In other words, the substitution $\chi^{(2)}_{ab} \to \chi^{(2)}_{ab} + A\delta_{ab}$, where A is a real scalar, does not change the RHS of Eq. 2.57.

Let us go back to the case of our interest: no absorption, $T_{II} = T_{IQ} = T_{IU} = T_{IV} \propto \eta_I = 0$, so we end up with an hermitian susceptibility tensor, and no emission, $\epsilon_{II} = \epsilon_{IQ} = \epsilon_{IU} = \epsilon_{IV} = 0$, at least studying the equation for $\tau > \tau_{rec}$.

In that case, the number of dof's of $\boldsymbol{\chi}^{(2)}$ goes down to 3 (4 minus 1 for the

trace) and the only surviving components of $\boldsymbol{\mathcal{T}}$ are:

$$\rho_Q \equiv -(2\pi\nu_0)\, T_{UV} = (2\pi\nu_0)\, \left(\chi^{(2)}_{11} - \chi^{(2)}_{22}\right) ; \tag{2.70a}$$

$$\rho_U \equiv (2\pi\nu_0)\, T_{QV} = (4\pi\nu_0)\, \mathrm{Re}\left\{\chi^{(2)}_{12}\right\} ; \tag{2.70b}$$

$$\rho_V \equiv -(2\pi\nu_0)\, T_{QU} = (4\pi\nu_0)\, \mathrm{Im}\left\{\chi^{(2)}_{12}\right\} , \tag{2.70c}$$

where we have introduced the ρ's to make connection with the notation that we have been using since the beginning of this chapter. Moreover, since we are interested in the radiative transfer problem in an expanding Universe, we have introduced $\nu_0 = a\nu$.

The final step is to make connection with the three-dimensional susceptibility tensor. Combing Eqs. 2.70 with Eq. 2.59, we get:

$$\rho_Q = 2\pi\nu_0 \left[\left(\chi_{xx}c^2_\theta - \chi_{yy}\right)c^2_\phi + \left(\chi_{yy}c^2_\theta - \chi_{xx}\right)s^2_\phi + \chi_{zz}s^2_\theta\right] ; \tag{2.71a}$$

$$\rho_U = 4\pi\nu_0 \left(\chi_{yy} - \chi_{xx}\right)c_\theta s_\phi c_\phi ; \tag{2.71b}$$

$$\rho_V = 4\pi\nu_0 \left(\chi_{xy}c_\theta + \chi_{yz}s_\theta c_\phi + \chi_{xz}s_\theta s_\phi\right) , \tag{2.71c}$$

or introducing the time-averaged variables $\bar{\chi}_{ij} \equiv (\eta - \eta_{\rm LS})^{-1} \int_{\eta_{\rm LS}}^{\eta} \chi_{ij}\, d\eta$,

$$\bar{\rho}_Q = 2\pi\nu_0 \left[\left(\bar{\chi}_{xx}c^2_\theta - \bar{\chi}_{yy}\right)c^2_\phi + \left(\bar{\chi}_{yy}c^2_\theta - \bar{\chi}_{xx}\right)s^2_\phi + \bar{\chi}_{zz}s^2_\theta\right] ; \tag{2.72a}$$

$$\bar{\rho}_U = 4\pi\nu_0 \left(\bar{\chi}_{yy} - \bar{\chi}_{xx}\right)c_\theta s_\phi c_\phi ; \tag{2.72b}$$

$$\bar{\rho}_V = 4\pi\nu_0 \left(\bar{\chi}_{xy}c_\theta + \bar{\chi}_{yz}s_\theta c_\phi + \bar{\chi}_{xz}s_\theta s_\phi\right) . \tag{2.72c}$$

This set of equations allows us to connect the observed spectra in presence of GFE to the components of an effective "cosmic susceptibility tensor", that has the makings of describing, in a completely model-independent way, the optical properties of the Universe between us and the CMB last scattering surface. In other words, we are recasting a mechanism that alters the propagation of photons across cosmological distances, the GFE, in terms of an effective susceptibility tensor, for example by looking at how the wave equation is modified.
Moreover, given a model predicting GFE, it will suffice to express its effects on light propagation in terms of a susceptibility tensor, which can be easily done by examining how, for example, Maxwell's equations are modified in the model under consideration, and apply Eqs. 2.49 combined with Eqs. 2.72, to get the observed CMB spectra.

In the following, we choose to carry on a phenomenological approach, and, without making any assumptions on the physical mechanism beyond GFE, we are going to focus on the simplest case: a susceptibility tensor that does not depend on the radiation wavenumber.

2.4.1 Toy model: a wavenumber-independent susceptibility tensor

In this section, to see the formalism at work, we will consider a $\boldsymbol{\chi}$ that does not depend on the radiation wavenumber.

First of all, we have to explicitly compute the expression for the expansion coefficients $b_{x,\ell m}$ in terms of the χ_{ij}'s.
Let us start from

$$\bar{\rho}_V(\theta,\phi) \;=\; 4\pi\nu_0 \left(\bar{\chi}_{xy}c_\theta + \bar{\chi}_{yz}s_\theta c_\phi + \bar{\chi}_{xz}s_\theta s_\phi\right) \;=\; \sum_{\ell m} b_{V,\ell m} Y_{\ell m}(\theta,\phi)\,. \tag{2.73}$$

Inverting this expression, we obtain

$$\begin{aligned} b_{V,\ell m} \;&=\; \int_0^\pi \mathrm{d}\theta\, \sin\theta \int_0^{2\pi} \mathrm{d}\phi\, \bar{\rho}_V\, Y^*_{\ell m}(\theta,\phi) \;= \\ &= (-1)^m \int_0^\pi \mathrm{d}\theta\, \sin\theta \int_0^{2\pi} \mathrm{d}\phi\, \bar{\rho}_V\, Y_{\ell -m}(\theta,\phi) \;= \\ &= (-1)^m \sqrt{\frac{2\ell+1}{4\pi}\frac{(\ell+m)!}{(\ell-m)!}} \int_0^\pi \mathrm{d}\theta\, \sin\theta\, \mathcal{P}_\ell^{-m}(\cos\theta) \int_0^{2\pi} \mathrm{d}\phi\, e^{-im\phi}\, \bar{\rho}_V(\theta,\phi)\,. \end{aligned} \tag{2.74}$$

It is easy to verify that the integral over ϕ is non-zero only if $m = -1, 0, 1$. Then, solving Eq. 2.74 for these values of m, we found, as expected, that only the $b_{\ell m}$'s with $\ell = 1$ survive. Therefore, we get:

$$b_{V,10} \;=\; (2\pi\nu_0)\sqrt{\frac{16\pi}{3}}\bar{\chi}_{xy}\,; \tag{2.75a}$$

$$b_{V,11} \;=\; (2\pi\nu_0)\sqrt{\frac{8\pi}{3}}\,(i\bar{\chi}_{xz} - \bar{\chi}_{yz})\;; \tag{2.75b}$$

$$b_{V,1\,-1} \;=\; -b^*_{V,11} = (2\pi\nu_0)\sqrt{\frac{8\pi}{3}}\,(i\bar{\chi}_{xz} + \bar{\chi}_{yz})\;. \tag{2.75c}$$

Turning to $\bar{\rho}_\pm \equiv (\bar{\rho}_Q \pm i\bar{\rho}_U)/\sqrt{2}$, since $\bar{\rho}_- = \bar{\rho}^*_+$, it follows that $b_{-2,\ell m} = (-1)^m b_{2,\ell m}$. This means that we only need to compute the coefficients for one

between $\bar{\rho}_+$ and $\bar{\rho}_+$. Let us choose $\bar{\rho}_+$.
To simplify the calculation, we use the spin lowering operator, described in App. B. Thus, since $\bar{\rho}_+$ is a spin-2 function,

$$\bar{\eth}^{\,2}\bar{\rho}_+ = \bar{\eth}^{\,2}\sum_{\ell m} b_{2,\ell m}\,{}_2Y_{\ell m}(\hat{\mathbf{n}}) = \sum_{\ell m}\left[\frac{(\ell+2)!}{(\ell-2)!}\right]^{1/2} b_{2,\ell m}Y_{\ell m}(\hat{\mathbf{n}})\,. \tag{2.76}$$

Performing explicitly the derivative, after some manipulation, yields

$$\begin{aligned}\bar{\eth}^{\,2}\bar{\rho}_+ &= \bar{\eth}^{\,2}\left[\frac{\rho_Q + i\rho_U}{\sqrt{2}}\right] = \\ &= (2\pi\nu)\sqrt{2}\Big[\left(\bar{\chi}_{xx}+\bar{\chi}_{yy}-2\bar{\chi}_{zz}\right)\left(1-3\cos^2\theta\right)+3\left(\bar{\chi}_{xx}-\bar{\chi}_{yy}\right)\cos 2\phi\sin^2\theta\Big]\,.\end{aligned} \tag{2.77}$$

We expect this quantity to have only components with $\ell = 2$ and $|m| = 0,\,2$. Indeed, it can be rearranged as

$$\bar{\eth}^{\,2}\rho_+ = (2\pi\nu)\left\{\sqrt{\frac{32\pi}{5}}\left(-\bar{\chi}_{xx}-\bar{\chi}_{yy}+2\bar{\chi}_{zz}\right)Y_{20}+\sqrt{\frac{48\pi}{5}}\left(\bar{\chi}_{xx}-\bar{\chi}_{yy}\right)\left(Y_{22}+Y_{2-2}\right)\right\}. \tag{2.78}$$

Combining this result with Eq. 2.76, and, performing calculations similar to those in Eq. 2.74, we arrive to

$$b_{2,20} = b_{-2,20} = (2\pi\nu_0)\sqrt{\frac{4\pi}{15}}\left(-\bar{\chi}_{xx}-\chi_{yy}+2\bar{\chi}_{zz}\right)\,; \tag{2.79a}$$

$$b_{2,22} = b_{2,2-2} = b_{-2,22} = b_{-2,2-2} = (2\pi\nu_0)\sqrt{\frac{2\pi}{5}}\left(\bar{\chi}_{xx}-\bar{\chi}_{yy}\right)\,. \tag{2.79b}$$

Defining $b_{E,\ell m} \equiv -(b_{2,\ell m}+b_{-2,\ell m})/2$ and $b_{B,\ell m} \equiv i(b_{2,\ell m}-b_{-2,\ell m})/2$, we have

$$b_{E,20} = (2\pi\nu_0)\sqrt{\frac{4\pi}{15}}\left(\bar{\chi}_{xx}+\bar{\chi}_{yy}-2\bar{\chi}_{zz}\right)\,; \tag{2.80a}$$

$$b_{E,22} = b_{E,2-2} = (2\pi\nu_0)\sqrt{\frac{2\pi}{5}}\left(-\bar{\chi}_{xx}+\bar{\chi}_{yy}\right)\,, \tag{2.80b}$$

while the b_B's are all vanishing.
Combing Eqs. 2.44 with Eqs. 2.75 and 2.79, we can easily recover the expansion coefficients $\mathcal{B}_{xy,\ell m}$.

Now, thanks to the above calculations and using some properties of the Wigner-3j symbols (see App. A and App. E), we can simplify Eqs. 2.49. After

some math, we get:

$$C_\ell^{TB} = C_\ell^{EB} = C_\ell^{EV} = C_\ell^{BV} = 0\,; \tag{2.81a}$$

$$C_\ell^{TE} = \widetilde{C}_\ell^{TE} - \frac{1}{2}\left(\frac{\sum_m |b_{V,1m}|^2 + \sum_m |b_{E,2m}|^2}{4\pi}\right)\widetilde{C}_\ell^{TE}\,; \tag{2.81b}$$

$$\begin{aligned} C_\ell^{EE} = \widetilde{C}_\ell^{EE} &- \left(\frac{\sum_m |b_{V,1m}|^2 + \sum_m |b_{E,2m}|^2}{4\pi}\right)\widetilde{C}_\ell^{EE} + \\ &+ \left\{\frac{2\ell+1}{4\pi}\begin{pmatrix}\ell & 1 & \ell\\ -2 & 0 & 2\end{pmatrix}^2 \widetilde{C}_\ell^{EE} + \frac{2\ell+3}{4\pi}\begin{pmatrix}\ell+1 & 1 & \ell\\ -2 & 0 & 2\end{pmatrix}^2 \widetilde{C}_{\ell+1}^{BB} + \right. \\ &\left. + \frac{2\ell-1}{4\pi}\begin{pmatrix}\ell-1 & 1 & \ell\\ -2 & 0 & 2\end{pmatrix}^2 \widetilde{C}_{\ell-1}^{BB}\right\}\sum_{m'} |b_{V,1m'}|^2\,; \end{aligned} \tag{2.81c}$$

$$\begin{aligned} C_\ell^{BB} = \widetilde{C}_\ell^{BB} &- \left(\frac{\sum_m |b_{V,1m}|^2 + \sum_m |b_{E,2m}|^2}{4\pi}\right)\widetilde{C}_\ell^{BB} + \\ &+ \left\{\frac{2\ell+1}{4\pi}\begin{pmatrix}\ell & 1 & \ell\\ -2 & 0 & 2\end{pmatrix}^2 \widetilde{C}_\ell^{BB} + \frac{2\ell+3}{4\pi}\begin{pmatrix}\ell+1 & 1 & \ell\\ -2 & 0 & 2\end{pmatrix}^2 \widetilde{C}_{\ell+1}^{EE} + \right. \\ &\left. + \frac{2\ell-1}{4\pi}\begin{pmatrix}\ell-1 & 1 & \ell\\ -2 & 0 & 2\end{pmatrix}^2 \widetilde{C}_{\ell-1}^{EE}\right\}\sum_{m'} |b_{V,1m'}|^2\,; \end{aligned} \tag{2.81d}$$

$$\begin{aligned} C_\ell^{VV} = &\left\{\frac{2\ell+5}{\pi}\begin{pmatrix}\ell+2 & 2 & \ell\\ -2 & 2 & 0\end{pmatrix}^2 \widetilde{C}_{\ell+2}^{BB} + \frac{2\ell+3}{\pi}\begin{pmatrix}\ell+1 & 2 & \ell\\ -2 & 2 & 0\end{pmatrix}^2 \widetilde{C}_{\ell+1}^{EE} + \right. \\ &+ \frac{2\ell+1}{\pi}\begin{pmatrix}\ell & 2 & \ell\\ -2 & 2 & 0\end{pmatrix}^2 \widetilde{C}_\ell^{BB} + \frac{2\ell-1}{\pi}\begin{pmatrix}\ell-1 & 2 & \ell\\ -2 & 2 & 0\end{pmatrix}^2 \widetilde{C}_{\ell-1}^{EE} + \\ &\left. + \frac{2\ell-3}{\pi}\begin{pmatrix}\ell-2 & 2 & \ell\\ -2 & 2 & 0\end{pmatrix}^2 \widetilde{C}_{\ell-2}^{BB}\right\}\sum_{m'} |b_{E,2m'}|^2\,. \end{aligned} \tag{2.81e}$$

It is useful to introduced the variables

$$\beta_V^2 \equiv \sum_m |b_{V,1m}|^2 = \frac{16\pi}{3}\left(\xi_{xy}^2 + \xi_{yz}^2 + \xi_{xz}^2\right) ; \tag{2.82a}$$

$$\beta_E^2 \equiv \sum_m \left|\frac{1}{2}(b_{2,\ell m} + b_{-2,\ell m})\right|^2 \equiv \sum_m |b_{E,\ell m}|^2 =$$

$$= \frac{8\pi}{15}\left[(\xi_{xx} - \xi_{yy})^2 + (\xi_{yy} - \xi_{zz})^2 + (\xi_{zz} - \xi_{xx})^2\right] , \tag{2.82b}$$

where

$$\xi_{ij} = \int_{\eta_{\rm LS}}^{\eta^0} 2\pi\nu_0\, \chi_{ij}\, {\rm d}\eta. \tag{2.83}$$

Looking at Eqs. 2.81, we can immediately see that the amplitude of the non-standard contributions to the power spectra is controlled by these two parameters, β_V^2 and β_E^2. Moreover, note that they are probing independent combinations of the χ_{ij}'s, since they only depend on the *off*- and *on* diagonal components, respectively.

Using the above definition, Eqs. 2.81 can be recasted as

$$C_\ell^{TB} = C_\ell^{EB} = C_\ell^{EV} = C_\ell^{BV} = 0 \tag{2.84a}$$

$$C_\ell^{TE} = \widetilde{C}_\ell^{TE} - \frac{1}{2}\left(\frac{\beta_V^2 + \beta_E^2}{4\pi}\right)\widetilde{C}_\ell^{TE} ; \tag{2.84b}$$

$$C_\ell^{EE} = \widetilde{C}_\ell^{EE} - \left(\frac{\beta_V^2 + \beta_E^2}{4\pi}\right)\widetilde{C}_\ell^{EE} + \frac{\beta_V^2}{4\pi}\left[\mathcal{W}_\ell^{(1)}\,\widetilde{C}_\ell^{EE} + \mathcal{W}_{\ell+1}^{(1)}\,\widetilde{C}_{\ell+1}^{BB} + \mathcal{W}_{\ell-1}^{(1)}\,\widetilde{C}_{\ell-1}^{BB}\right] ; \tag{2.84c}$$

$$C_\ell^{BB} = \widetilde{C}_\ell^{BB} - \left(\frac{\beta_V^2 + \beta_E^2}{4\pi}\right)\widetilde{C}_\ell^{BB} + \frac{\beta_V^2}{4\pi}\left[\mathcal{W}_\ell^{(1)}\,\widetilde{C}_\ell^{BB} + \mathcal{W}_{\ell+1}^{(1)}\,\widetilde{C}_{\ell+1}^{EE} + \mathcal{W}_{\ell-1}^{(1)}\,\widetilde{C}_{\ell-1}^{EE}\right] ; \tag{2.84d}$$

$$C_\ell^{VV} = \frac{\beta_E^2}{\pi}\left[\mathcal{W}_{\ell+2}^{(2)}\,\widetilde{C}_{\ell+2}^{BB} + \mathcal{W}_{\ell+1}^{(2)}\,\widetilde{C}_{\ell+1}^{EE} + \mathcal{W}_\ell^{(2)}\,\widetilde{C}_\ell^{BB} + \mathcal{W}_{\ell-1}^{(2)}\,\widetilde{C}_{\ell-1}^{EE} + \mathcal{W}_{\ell-2}^{(2)}\,\widetilde{C}_{\ell-2}^{BB}\right] , \tag{2.84e}$$

where the $\mathcal{W}$ kernels are combinations of Wigner $3j$-symbols,

$$\mathcal{W}_{\ell'}^{(1)} \equiv (2\ell'+1)\begin{pmatrix} \ell' & 1 & \ell \\ -2 & 0 & 2 \end{pmatrix}^2 , \qquad \mathcal{W}_{\ell'}^{(2)} \equiv (2\ell'+1)\begin{pmatrix} \ell' & 2 & \ell \\ -2 & 2 & 0 \end{pmatrix}^2 . \tag{2.85}$$

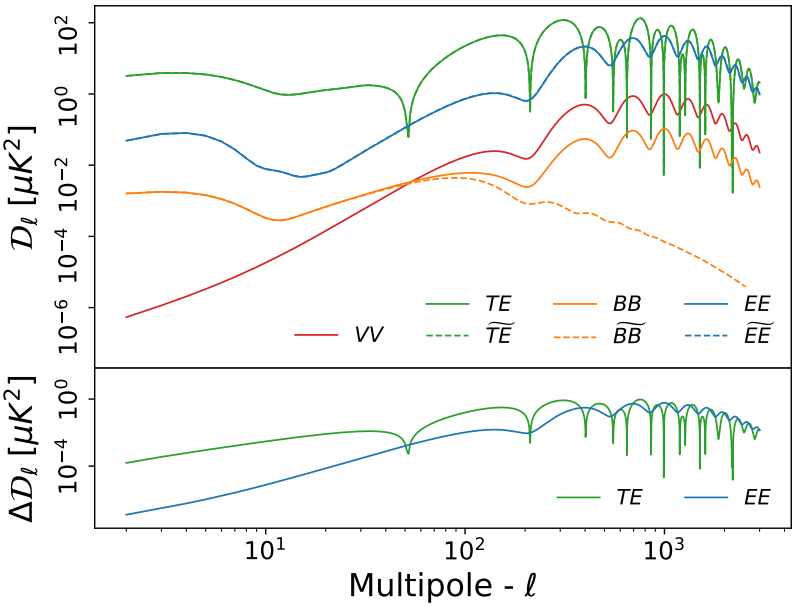

Figure 2.5: Top: *"Rotated" (solid line) and "unrotated" angular power spectra (dashed line). For the rotated ones we have used* $\beta_V^2 = 0.03$ *and* $\beta_E^2 = 0.14$. *In both case, the other cosmological parameters are the best-fit values of Planck 2018 and* $r_{0.05} = 0.07$. Bottom: *Absolute differences between "rotated" and "unrotated" for EE and TE.*

The effect of these modifications are made clear in Fig. 2.5, and, both in Fig. 2.6 and Fig. 2.7. Note that in generating the curves, only the polarization produced at last scattering has been rotated.
The standard power spectra are, also in this case, computed using the Boltzmann code `camb`, assuming the best-fit Planck 2018 Cosmology [55]. These spectra are then rotated through Eqs. 2.84, in order to obtain the GFE-induced power spectra. A `Python` code has been developed for the latter computation. You can find it on github: `https://github.com/mlembo00/circular-polarization.git`.

In Fig. 2.5, we see the GFE-induced power spectra for $\beta_V^2 = 0.03$ and $\beta_E^2 = 0.14$. A non-vanishing V-modes power spectrum is generated, whose shape mostly follows that of the E-modes spectrum, as expected from Eqs. 2.84. The B-modes power spectrum is dramatically affected even for relatively small values β_V^2, because power leaks from the much larger E-modes.

In Fig. 2.6, instead, we can appreciate the different effect that the two parameters β_V^2 and β_E^2 have on the observed power spectra. Clearly, when $\beta_E^2 = 0$, we will not have an induced VV power spectrum. This case is equivalent to anisotropic birefringence with a very specific rotation-angle power spectrum: $C_\ell^\chi \neq 0$ only if $\ell = 1$.

On the other side, when $\beta_V^2 = 0$, the standard power spectra are just rescaled by a factor $1 - \beta_E^2/8\pi$ for TE and $1 - \beta_E^2/4\pi$ for EE and BB. This rescaling is even more evident looking at Fig. 2.7. In this case, circular polarization is produced.

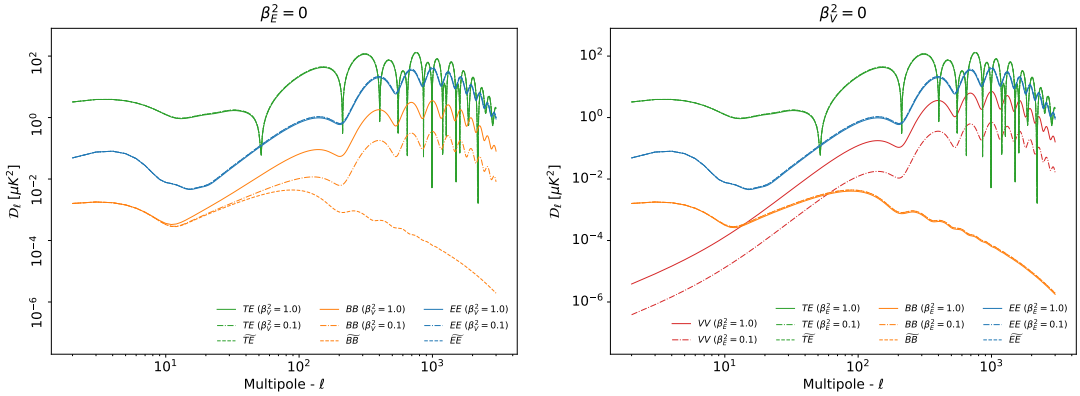

Figure 2.6: *"Rotated" (solid line and dash-dotthed) and "unrotated" angular power spectra (dashed line). On the left, $\beta_E^2 = 0$ and $\beta_V^2 = 1.0, 0.1$; on the right, $\beta_V^2 = 0$ and $\beta_E^2 = 1.0, 0.1$. In both case the other cosmological parameters are the best-fit values of Planck 2018 and $r_{0.05} = 0.07$.*

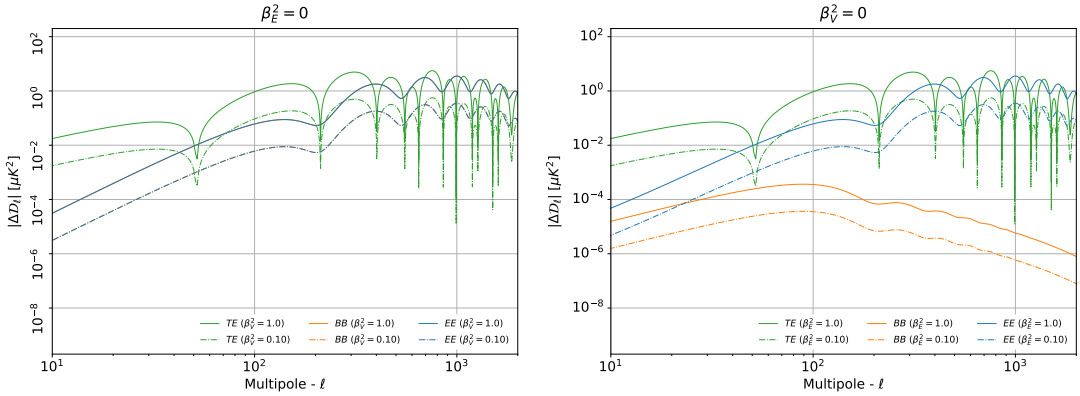

Figure 2.7: *Absolute differences between "Rotated" and "unrotated" angular power spectra of Fig. [2.6]. On the left, $\beta_E^2 = 0$ and $\beta_V^2 = 1.0, 0.1$; on the right, $\beta_V^2 = 0$ and $\beta_E^2 = 1.0, 0.1$.*

2.4.2 Observational constraints

Observations of CMB polarization can be used to constrain the values of β_V^2 and β_E^2, in the framework of simple extensions of the ΛCDM model.
We have used observations of temperature and linear polarization anisotropies from the Planck legacy release (`Planck18`) [106] and BICEP2/Keck 2015 (`BK15`) [107] to derive bounds on both β_V^2 and β_E^2 in the presence of primordial tensor modes., parameterized by the tensor-to-scalar ratio r. Precisely, `Planck18` stands for the sum of the *lowE* (EE power spectrum over $2 \leq \ell < 30$) and *Planck TTTEEE* (TT power spectrum over $2 \leq \ell \lesssim 2500$, and EE and TE power spectra over $30 \leq \ell \lesssim 2000$) datasets, see Ref. [106] for more details; while `BK15` consists in a BB power spectrum over $20 < \ell < 330$ divided into 9 band-powers, see Ref. [108] for details.

Our baseline model is $\Lambda CDM + r$, *i.e.* without GFE. To this baseline case, we have added the GFE parameters. We have examined the following four cases:

`BK15`:

1(a). $\Lambda CDM + r + \beta_E^2$;

1(b). $\Lambda CDM + r + \beta_V^2 + \beta_E^2$;

`BK15`+`Planck18`:

2(a). $\Lambda CDM + r + \beta_E^2$;

2(b). $\Lambda CDM + r + \beta_V^2 + \beta_E^2$;

Additionally, we have also examined the $\Lambda CDM + r + \beta_V^2$ case, using both datasets. This model is equivalent to consider anisotropic birefringence with a non-zero rotation-angle power spectra only for $\ell - 1, \ell, \ell + 1$. The result are consistent with those discussed in Sec. 2.1.

To sample the posterior distributions for the model parameters, we have used the Monte Carlo engine `CosmoMC` [109]. We have slightly modified the code adding the GFE-parameters, β_V^2 and β_E^2.
Using the Gelman-Rubin convergence statistics [110], we have assumed that our MCMC chains have been converged when R $-1 \sim 0.001$.

The one dimensional posterior probabilities for r, β_V^2 and β_E^2 are shown in Fig. 2.8.
Looking at Fig. 2.8b, it is worth underlining that, if we use only B-modes data (`BK15`), we are not able to set any constraints on β_E^2, varying neither β_E^2 alone nor both, β_V^2 and β_E^2. The reason is evident considering the BB power spectrum in Eqs. 2.84. The E-mode polarization power spectra is much bigger than the B-mode polarization one, $\widetilde{C}_\ell^{EE} \gg \widetilde{C}_\ell^{BB}$. The modifications on C_ℓ^{BB} are therefore driven by the terms $\propto \beta_V^2\, \widetilde{C}_{\ell\pm1}^{EE}$, as you can see in Eq. 2.84d.
Hence, if we vary both β_V^2 and β_E^2, we are able to constrain only β_V^2 since the term $\propto \beta_E^2$ is negligible.

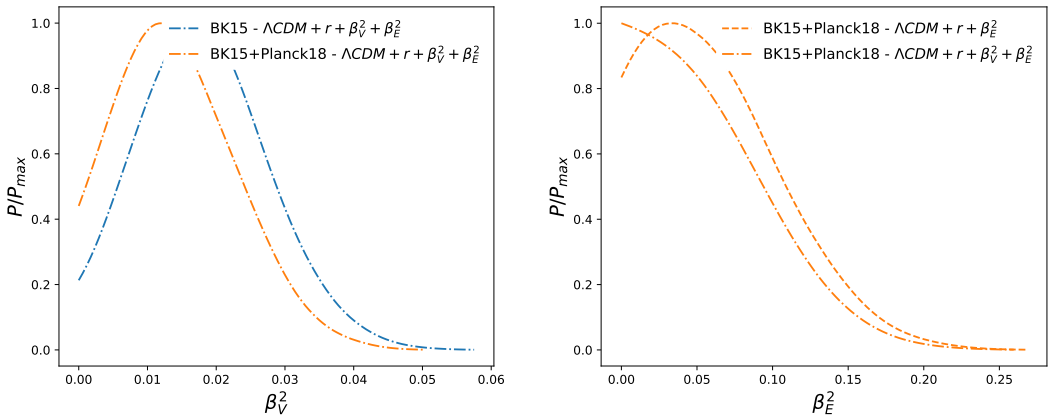

(a) *One dimensional posterior probability for* β_V^2. **(b)** *One dimensional posterior probability for* β_E^2.

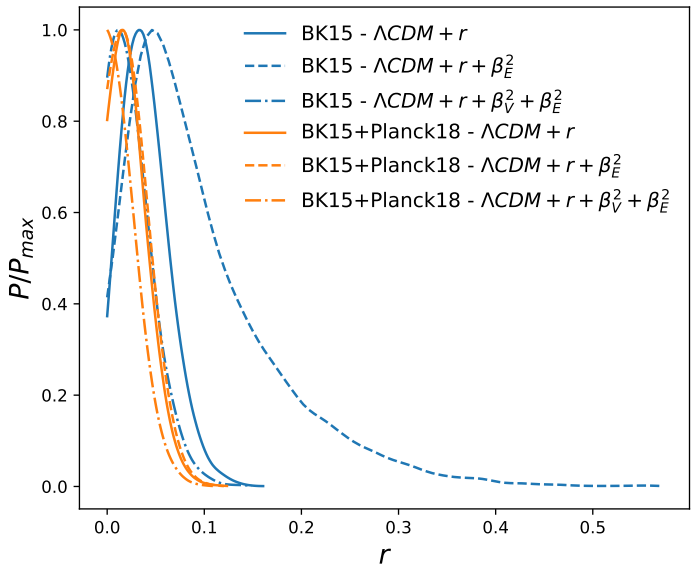

(c) *One dimensional posterior probability for* r.

Figure 2.8: *One dimensional posterior probability for* β_V^2, β_E^2 *and* r. *In blue, we reported the constraints obtained using* `BK15`, *in orange, the constraints obtained using* `Planck18 BK15`. *We show the results for* $\Lambda CDM + r$ *(solid lines),* $\Lambda CDM + r + \beta_E^2$ *(dashed lines) and* $\Lambda CDM + r + \beta_E^2 + \beta_V^2$ *(dash-dotted lines).*

On the other hand, if we allow to vary β_E^2 only ($\beta_V^2 = 0$), Eq. 2.84d becomes $C_\ell^{BB} = \left(1 - \frac{\beta_E^2}{4\pi}\right) \widetilde{C}_\ell^{BB}$. The β_E^2 parameter is rescaling the B-modes power spectra. The error bars of `BK15` are still quite wide to appreciate a small effect as this is.

Regarding the tensor-to-scalar ratio, r, the bound on r is slightly stronger that the corresponding value for $\beta_V^2 = 0$ due to degeneracy between the two parameters. See Fig. 2.8c.

The combined `BK15`+`Planck18` dataset has clearly more constraining power. Hence, considering the more general case, the *2(b)*, we found $\beta_V^2 < 0.030$, $\beta_E^2 < 0.14$ and $r_{0.05} < 0.055$ at 95% C.L.. It is worth mentioning that the data have slight preference for a non-zero value of both β_V^2 and β_E^2, as much as it is not statistically significant ($\sim 1\sigma$).
Though, this can be related to the fact that $\beta_V^2 = 0$ and $\beta_E^2 = 0$ are the borders of the priors in which the parameters are allowed to vary: the MCMC might have trouble in sampling these points and they would appear less likely than others.

Moreover, since circular polarization data are also sensitive to β_E^2, see Eq. (2.84), we have used the V-modes CMB polarization data from the CLASS telescope [101, 111], discussed in Sec. 2.2 and shown in Fig. 2.4, to constrain β_E^2 (see Eq. 2.84e).
Assuming the Planck 2018 best-fit EE and BB spectra, we found $\beta_E^2 < 38$ (95% CL). This constrain clearly violates our assumption that $\rho_{Q,U} \ll 1$, nevertheless it indicates that current V-mode data allow a large mixing of linear and circular polarization. We have shown that such a large mixing is however excluded by current observations of E and B polarization.
In Fig. 2.9, we show the current data on the CMB VV power spectrum, together with theoretical power spectra for $\beta_E^2 = 38$, corresponding to the 95% upper limit allowed by current circular polarization data, and $\beta_E^2 = 0.14$, corresponding to the 95% upper limit allowed by current temperature and linear polarization data.

To conclude, it is interesting to notice that these constraints on the β's can be recasted in terms of the χ_{ij}. Taking $\nu_0 \simeq 150$ GHz as the frequency of the CMB photons today, $\xi_{ij} \simeq 1.5 \cdot 10^{30}\, \chi_{ij}$ if the χ's do not depend on time. The constraint on β_V^2 implies a bound $\chi_{ij} \leq 2.7 \cdot 10^{-32}$ for the largest off-diagonal element, while the one on β_E^2 implies $\chi_{ii} - \chi_{jj} \leq 1.3 \cdot 10^{-31}$ for the largest difference between diagonal elements.
In the case of a time-dependent susceptibility tensor, the same constraints apply to the time-averages $\overline{\chi}_{ij}$.

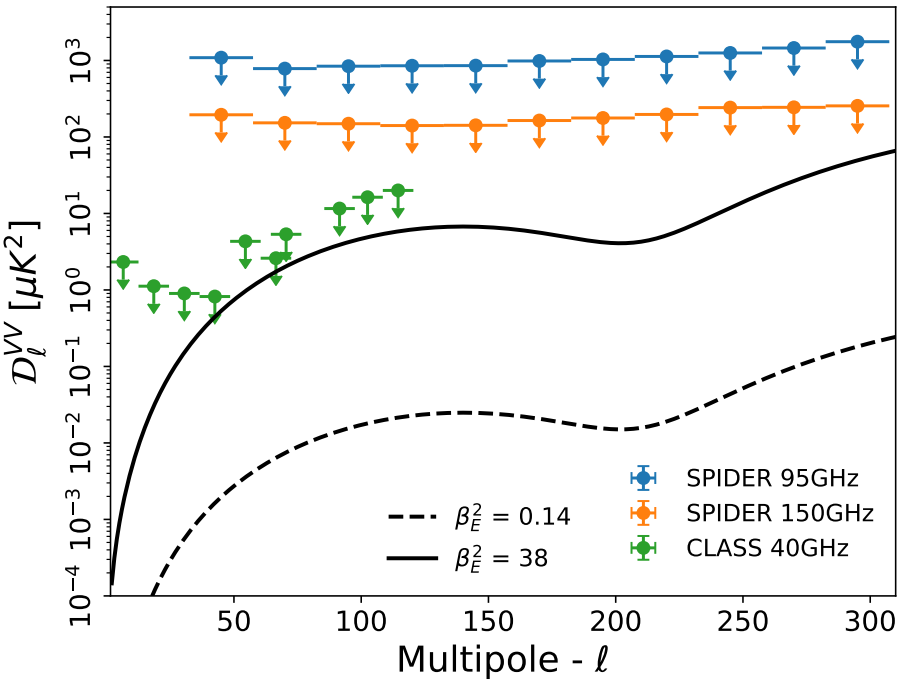

Figure 2.9: *V-modes power spectra as predicted by CLASS (solid line) and Planck/BICEP2/Keck (dashed line), compared with SPIDER [4] and CLASS [101] data.*

3

Gravitational lensing of the CMB

In Chpt. 1, we have introduced the *nuts and bolts* of CMB theory. In Chpt. 2, instead, we have focused our attention on some less investigated aspects of CMB polarization, proposing a phenomenological framework that might gather under one flag several, and at first glance various, mechanisms affecting the polarization states of the CMB radiation.

In this picture, we have only marginally touched a fundamental topic: the CMB pattern we observe today is not the original distribution as it emerges from the last scattering surface. The original CMB field is, indeed, in some way distorted and modified as CMB photons interact with the forming structures while traveling from recombination to the observer. These distortions are usually called *secondaries anisotropies*.

Among them, weak gravitational lensing is one of the most important. According to General Relativity, the gravitational potential of a mass bends light rays. This means that the CMB photons are deflected from their original path due to the presence of mass between the last scattering surface and us. As we will see, regarding the temperature spectrum, lensing does not generate additional power, but rather redistributes it from larger scales to smaller ones (for close multipoles). More or less, the effect on the E-mode polarization is similar to the temperature case: the convolution with the lensing potential smooths out the acoustic peaks and troughs of the power spectrum.

The most intriguing effect is, instead, the generation, by distortion of the primordial E-modes, of spurious B-modes, which unfortunately act as a contaminant for all the measurements of primordial B-modes. Hence, B-mode polarization signal can serve as a "smoking gun" for primordial gravitational waves, as long as we are able to distinguish it from the lensing signal. Delensing, the act of measuring and removing the effect of lensing from CMB maps, is therefore essential for

next-decade experiments in order to better constrain the tensor-to-scalar ratio r.

Beside this aspect, CMB lensing provides an invaluable tool to map the matter distribution of the Universe between us and the last scattering surface. This allows, in particular, to study the clustering of both dark and luminous matter, and infer from it the key elements of structure formation (dark energy equation of state, mass of neutrinos).

CMB lensing is thus, without any doubt, one of the crucial observables of next-decade experiments, and a not completely exhaustive comprehension of this effect could preclude us the possibility of constraining cosmology, or even the chance to faithfully reconstruct the spectrum of primordial B-modes.

On top of this, CMB observations are also inevitably contaminated at some level by foregrounds, from galactic dust and synchrotron emission to a range of extragalactic signals including the cosmic infrared background (CIB) caused by stellar dust, the already mentioned Sunyaev-Zeldovich effect from hot gas in galaxy clusters, and radio point sources.
Much of these foreground signals can either be modeled or removed using their distinct frequency dependence. However, bright sources can be problematic and are often masked out. It is usually tacitly assumed that the CMB power spectra estimated over the unmasked areas are then unbiased estimates that can be used to study cosmology. As long as sources with a strong correlation to lensing are not masked, for current data, this is likely to be a safe approximation. For future data, where large populations of extragalactic sources will be resolved, corrections may become important.

Assessing the impact of masking bright extragalactic sources on CMB maps and, indeed on the lensing reconstruction itself, is a fundamental topic in view of the next-decade CMB experiments, and is discussed in Sec. *3.4* and in Sec. *3.5*. These sections are based on two original works [12, 13], one of which is still in preparation.
Before reaching Sec. *3.4*, we introduce the bases of the lensing theory, in Sec. *3.1*, showing the modifications induced on the CMB power spectra in Sec. *3.2*. In Sec. *3.3*, instead, how to reconstruct the lensing potential from the observed CMB maps is discussed.

3.1 The lensing deflection angle and the lensing potential

The idea that gravity can bend light is a well-established result and dates back over more than hundreds of years. The question we want to answer in this section is about how much the gravitational potentials in the Universe will deflect CMB photons.
Given the gravitational potential $\Psi(\hat{\mathbf{x}}, \eta)$, the total deflection angle is a sum over all of the individual deflections due to gravitational potentials between the surface of last scattering and today

$$\boldsymbol{\alpha}(\hat{\mathbf{n}}) \;=\; -2\int_0^{\chi^*} \mathrm{d}\chi\; \frac{f_K(\chi * -\chi)}{f_K(\chi*)\, f_K(\chi)} \nabla_{\hat{\mathbf{n}}}\Psi(\chi\hat{\mathbf{n}}, \eta_0 - \chi)\,, \tag{3.1}$$

where $\nabla_\perp \Psi = (\nabla_{\hat{\mathbf{n}}}\Psi)/f_K(\chi)$. We have introduced the comoving distance between the observer and the gravitational potential Ψ, χ, and the comoving distance between the observer and the source, $\chi*$. $f_K(\chi)$ is instead the angular diameter distance, defined as

$$f_K(\chi) \;=\; \begin{cases} K^{-1/2}\sin\!\big(K^{1/2}\chi\big) & K > 0 \text{ (close)} \\ \chi & K = 0 \text{ (flat)} \\ |K|^{-1/2}\sinh\!\big(|K|^{1/2}\chi\big) & K < 0 \text{ (open)} \end{cases} . \tag{3.2}$$

Notice that Eq. 3.1 has been derived assuming small angles (weak lensing) and to the lowest order in the potential. For a more rigorous derivation, using General Relativity, and also a discussion on higher-order corrections, you may check [112].

We can now define the lensing potential as

$$\phi(\hat{\mathbf{n}}) \;\equiv\; -2\int_0^{\chi^*} \mathrm{d}\chi\; \frac{f_K(\chi * -\chi)}{f_K(\chi*)\, f_K(\chi)} \Psi(\chi\hat{\mathbf{n}}, \eta_0 - \chi)\,, \tag{3.3}$$

so that $\boldsymbol{\alpha} = \nabla_{\hat{\mathbf{n}}}\phi$. Moreover, assuming a flat geometry, we get

$$\phi(\hat{\mathbf{n}}) \;\equiv\; -2\int_0^{\chi^*} \mathrm{d}\chi\; \frac{1}{\chi}\Big(1 - \frac{\chi}{\chi*}\Big)\Psi(\chi\hat{\mathbf{n}}, \eta_0 - \chi)\,. \tag{3.4}$$

In the above equation, the lensing potential appears to be formally divergent because of the $1/\chi$ term. However, this divergence only affects the monopole

potential, which does not contribute to the deflection angle. Therefore, setting the monopole term to zero, since the remaining multipoles will be finite, the lensing potential field is well defined.

It is useful to consider the 2-point correlation of the lensing potential, or equivalently, its harmonic transform, the lensing potential power spectrum. For a Gaussian lensing potential, indeed, its power spectrum and the cross-correlation with the CMB contain all the information we need to describe fully the statistics of the lensed CMB.
Assuming the gravitational potential, Ψ, is statistically homogeneous, its power spectrum is

$$\langle \Psi(\mathbf{k},\eta)\,\Psi^*(\mathbf{k}',\eta')\rangle \;=\; \frac{2\pi^2}{k^3}\mathcal{P}_\Psi(k,\eta,\eta')\delta(\mathbf{k}-\mathbf{k}')\,, \tag{3.5}$$

where we have expanded in harmonic space the gravitational potential as

$$\Psi(\mathbf{x},\eta) \;=\; \int \frac{\mathrm{d}^3\mathbf{k}}{(2\pi)^{3/2}}\,\Psi(\mathbf{k},\eta)e^{i\mathbf{k}\cdot\mathbf{x}}\,. \tag{3.6}$$

Using Eq. 3.5, we can now write the 2-point correlation function for the lensing potential

$$\begin{aligned}&\langle\phi(\hat{\mathbf{n}})\phi(\hat{\mathbf{n}}')\rangle \;= \\ &=\; 4\int_0^{\chi*}\mathrm{d}\chi\frac{1}{\chi}\Big(1-\frac{\chi}{\chi*}\Big)\int_0^{\chi*}\mathrm{d}\chi'\frac{1}{\chi'}\Big(1-\frac{\chi'}{\chi*}\Big)\int\frac{\mathrm{d}^3\mathbf{k}}{(2\pi)^3}\frac{2\pi^2}{k^3}\mathcal{P}_\Psi(k,\eta,\eta')e^{i\mathbf{k}\cdot\mathbf{x}}e^{-i\mathbf{k}\cdot\mathbf{x}'}\,,\end{aligned} \tag{3.7}$$

where $\mathbf{x}=\chi\hat{\mathbf{n}}$ and $\mathbf{x}'=\chi\hat{\mathbf{n}}'$. Using the plane wave expansion

$$e^{i\mathbf{k}\cdot\mathbf{x}} \;=\; 4\pi\sum_{\ell m} i^\ell j_\ell(k\chi)Y^*_{\ell m}(\hat{\mathbf{n}})Y^*_{\ell m}(\hat{\mathbf{k}})\,, \tag{3.8}$$

where $j_\ell(r)$ are the spherical Bessel functions, Eq. 3.7 becomes

$$\begin{aligned}\langle\phi(\hat{\mathbf{n}})\phi(\hat{\mathbf{n}}')\rangle \;=\; 16\pi\sum_{\ell\ell' mm'}&\int_0^{\chi*}\mathrm{d}\chi\frac{1}{\chi}\Big(1-\frac{\chi}{\chi*}\Big)\int_0^{\chi*}\mathrm{d}\chi'\frac{1}{\chi'}\Big(1-\frac{\chi'}{\chi*}\Big)\cdot \\ &\cdot\int\frac{\mathrm{d}k}{k}j_\ell(k\chi)j_\ell(k\chi')\mathcal{P}_\Psi(k,\eta,\eta')Y_{\ell m}(\hat{\mathbf{n}})Y_{\ell' m'}(\hat{\mathbf{n}}')\delta_{\ell\ell'}\delta_{mm'}\,,\end{aligned} \tag{3.9}$$

In the above calculation, we have also used the orthogonality of the spherical harmonics.
The lensing potential, $\phi(\hat{\mathbf{n}})$ is a scalar quantity and it can be expanded in spherical

harmonics as

$$\phi(\hat{\mathbf{n}}) \;=\; \sum_{\ell m} \phi_{\ell m} Y_{\ell m}(\hat{\mathbf{n}})\,, \tag{3.10}$$

where $Y_{\ell m}(\hat{\mathbf{n}})$ is a scalar spherical harmonics. If we assume a statistically isotropic field[1], we can assume that the coefficients $\phi_{\ell m}$s follow the normal distribution with zero mean value and non-zero variance, $C_\ell^{\phi\phi}$,

$$\langle \phi_{\ell m} \phi_{\ell' m'} \rangle \;=\; \delta_{\ell\ell'} \delta_{mm'} C_\ell^{\phi\phi}\,. \tag{3.11}$$

where $C_\ell^{\phi\phi}$ is the angular power spectrum of the lensing potential.
Computing the 2-point correlation function of Eq. 3.10, we get

$$\begin{aligned} \langle \phi(\hat{\mathbf{n}}) \phi(\hat{\mathbf{n}}') \rangle \;&=\; \sum_{\ell\ell' mm'} \langle \phi_{\ell m} \phi_{\ell' m'} \rangle\, Y_{\ell m}(\hat{\mathbf{n}}) Y^*_{\ell m}(\hat{\mathbf{n}}') \;= \\ &=\; \sum_{\ell\ell' mm'} \delta_{\ell\ell'} \delta_{mm'} C_\ell^{\phi\phi}\, Y_{\ell m}(\hat{\mathbf{n}}) Y^*_{\ell m}(\hat{\mathbf{n}}')\,. \end{aligned} \tag{3.12}$$

Definitely, comparing this result with Eq. 3.9, we find the theoretical power spectrum for the lensing potential

$$\begin{aligned} C_\ell^{\phi\phi} \;=\; 16\phi \int_0^{\chi*} \mathrm{d}\chi \int_0^{\chi*} \mathrm{d}\chi'\, \frac{1}{\chi}\Big(1 - \frac{\chi}{\chi*}\Big) \frac{1}{\chi'}\Big(1 - \frac{\chi'}{\chi*}\Big) \cdot \\ \cdot \int \frac{\mathrm{d}k}{k}\, j_\ell(k\chi) j_\ell(k\chi')\, \mathcal{P}_\Psi(k, \eta_0 - \chi, \eta_0 - \chi')\,. \end{aligned} \tag{3.13}$$

If we link the gravitational potential to the primordial comoving curvature perturbation, $\mathcal{R}$, via the transfer function, T_Ψ, as

$$\Psi(\mathbf{k}, \eta) \;=\; T_\Psi \mathcal{R}(\mathbf{k})\,, \tag{3.14}$$

the lensing potential power spectra can be rewritten as [112]

$$C_\ell^{\phi\phi} \;=\; 16\phi \int \frac{\mathrm{d}k}{k} \mathcal{P}_\mathcal{R}(k) \left[\int_0^{\chi*} \mathrm{d}\chi\; T_\Psi(k; \eta_0 - \chi) j_\ell(k\chi) \frac{1}{\chi}\Big(1 - \frac{\chi}{\chi*}\Big) \right]^2\,, \tag{3.15}$$

where $\mathcal{P}_\mathcal{R}(k)$ is the primordial power spectrum of curvature perturbations . This spectrum is related to the primordial power spectra of scalar perturbations

[1] This assumption is motivated by the fact that inflation predicts initial Gaussian perturbations.

through the following [113]:

$$\mathcal{P}_{\mathcal{R}}(k) = \left(\frac{aH}{\dot{\phi}^0}\right)^2 \mathcal{P}_{\phi}(k) \tag{3.16}$$

where $\dot{\phi}^0$ is the conformal derivative of the primordial field (inflaton).

This power spectrum can be computed easily along with other CMB power spectra using Boltzmann codes such as `camb` [52], as it is shown in Fig. 3.1.

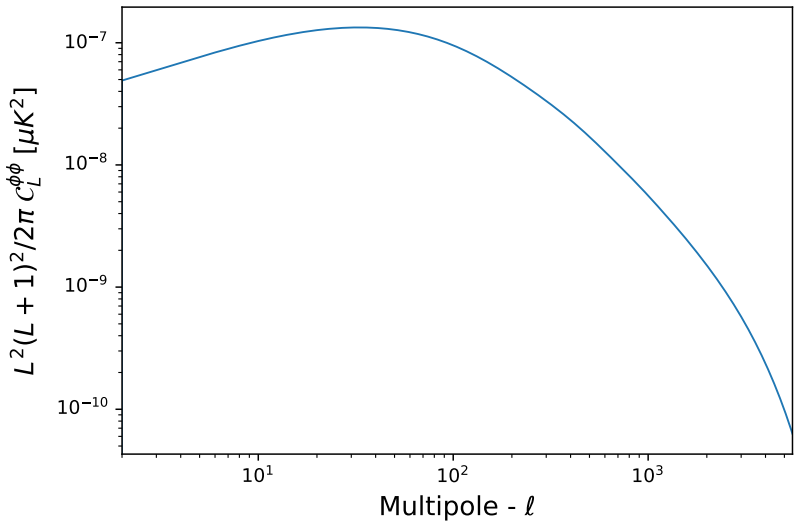

Figure 3.1: *Lensing potential power spectra. This plot has been produced using* `camb` *code with the Planck 2018 best-fit values for the* ΛCDM *parameters [55].*

Before moving on, let us define the magnification matrix in term of the derivative of the deflection angle as

$$A_{ij} \equiv \delta_{ij} + \frac{\partial}{\partial\theta_i}\alpha_j = \begin{pmatrix} 1-\kappa\gamma_1 & -\gamma_2+\omega \\ -\gamma_2-\omega & 1-\kappa+\gamma_1 \end{pmatrix}, \tag{3.17a}$$

where

$$\kappa = \frac{1}{2}\Big(\partial_1\partial_1 + \partial_2\partial_2\Big)\phi\,; \tag{3.17b}$$

$$\gamma_1 = \frac{1}{2}\Big(\partial_1\partial_1 - \partial_2\partial_2\Big)\phi\,; \tag{3.17c}$$

$$\gamma_2 = \partial_1\partial_2\phi\,. \tag{3.17d}$$

The κ and γ parameters, known as convergence and shear (precisely is $\gamma_1 + i\gamma_2$), respectively, quantify how lensed images are magnified, enlarged, and stretched. In the weak lensing approximation, these parameters are $\ll 1$. The ω parameter, instead, comes from second order effects. For more details see Ref. [114].

3.2 Lensed CMB power spectra

In this section, we calculate the effect of lensing on the CMB angular power spectra. We start calculating the lensed correlation function in the flat-sky limit. We will use the same approximation also in Sec. 3.5, since the effects of masking, as we will see, are largely on small scales.
In this approximation the lensing effect can be described as a remapping of the CMB, according to

$$\widetilde{T}(\mathbf{x}) = T(\mathbf{x}+\boldsymbol{\alpha}), \tag{3.18a}$$

$$\left[\widetilde{Q} \pm i\widetilde{U}\right](\mathbf{x}) = \left[Q \pm iU\right](\mathbf{x}+\boldsymbol{\alpha}), \tag{3.18b}$$

where $\boldsymbol{\alpha} \equiv \boldsymbol{\alpha}(\mathbf{x})$ is the deflection field defined in Eq. 3.1 and the tilded quantities are the lensed temperature and linear polarization fields.

Let us start from the temperature field. To compute the lensed temperature power spectra, we have to consider the lensed correlation function $\tilde{\xi}(r)$, that is

$$\tilde{\xi}(r) \equiv \langle \widetilde{T}(\mathbf{x})\, \widetilde{T}(\mathbf{x}') \rangle = \langle T(\mathbf{x}+\boldsymbol{\alpha})\, T(\mathbf{x}'+\boldsymbol{\alpha}') \rangle, \tag{3.19}$$

where $r = |\mathbf{x} - \mathbf{x}'|$. As we can see from Eq. 3.19, $\tilde{\xi}(r)$ only depends on the separation between the points, r[2].
From the above equation, it is clear that, in order to compute the lensed CMB power spectrum, we first have to calculate the correlation $\langle \boldsymbol{\alpha}\boldsymbol{\alpha}' \rangle$.
It is convenient to introduce the 2D Fourier transform of the lensing potential, $\phi(\boldsymbol{\ell})$, we have

$$\boldsymbol{\alpha} = i \int \frac{\mathrm{d}^2\boldsymbol{\ell}}{2\pi}\, \boldsymbol{\ell}\, \phi(\boldsymbol{\ell})\, e^{i\boldsymbol{\ell}\cdot\mathbf{x}}. \tag{3.20}$$

[2]As already done in Chpt. 1, we assume that the temperature fluctuations are statistically isotropic.

Therefore, the correlation tensor for the deflection angle can be written as

$$\langle \alpha_i(\mathbf{x})\alpha_j(\mathbf{x}')\rangle = \int \frac{\mathrm{d}^2\boldsymbol{\ell}}{(2\pi)^2}\,\ell_i\ell_j\,C_\ell^{\phi\phi}\,e^{i\ell\,\cdot\,(\mathbf{x}-\mathbf{x}')} = \\ = \frac{1}{4\pi}\int \mathrm{d}\ell\;\ell^3 C_\ell^{\phi} j_0(\ell r)\delta_{ij} - \frac{1}{2\pi}\int \mathrm{d}\ell\;\ell^3 C_\ell^{\phi} j_2(\ell r)\hat{r}_{\langle\, i}\hat{r}_{j\,\rangle}\,, \tag{3.21}$$

where $j_n(x)$ is a Bessel function of order n, $\mathbf{r} = \mathbf{x} - \mathbf{x}'$ and $\hat{\mathbf{r}}_{\langle\, i}\hat{\mathbf{r}}_{j\,\rangle} = \hat{\mathbf{r}}_i\hat{\mathbf{r}}_j - \delta_{ij}/2$ is the trace-free part of the tensor $\hat{\mathbf{r}}_i\hat{\mathbf{r}}_j$.
Following [115], let us introduce the quantities

$$C_{gl}(r) = \frac{1}{2\pi}\int \mathrm{d}\ell\;\ell^3 C_\ell^{\phi\phi}\,j_0(\ell r)\,, \tag{3.22a}$$

and

$$C_{gl,2}(r) = \frac{1}{2\pi}\int \mathrm{d}\ell\;\ell^3 C_\ell^{\phi\phi}\,j_2(\ell r)\,, \tag{3.22b}$$

so that, the correlation in Eq. 3.21 becomes

$$\langle \alpha_i(\mathbf{x})\alpha_j(\mathbf{x}')\rangle = \frac{1}{2}\,C_{gl}(r)\delta_{ij} - C_{gl,2}(r)\hat{\mathbf{r}}_{\langle\, i}\hat{\mathbf{r}}_{j\,\rangle}\,. \tag{3.23}$$

To move forward with the calculation of Eq. 3.19, we need to introduce the flat-sky 2D Fourier transform for the temperature field,

$$T(\mathbf{x}) = \int \frac{d\boldsymbol{\ell}^2}{2\pi}\,T(\boldsymbol{\ell})e^{i\boldsymbol{\ell}\,\cdot\,\mathbf{x}}\,, \qquad T(\boldsymbol{\ell}) = \int \frac{d\mathbf{x}^2}{2\pi}\,T(\mathbf{x})e^{-i\boldsymbol{\ell}\,\cdot\,\mathbf{x}}\,. \tag{3.24}$$

and the correlation function at two points of the temperature field, ξ, that, as $\tilde{\xi}$, only depends on the separation between the points, $r = |\mathbf{x} - \mathbf{x}'|$,

$$\xi(r) \equiv \langle T(\mathbf{x})T(\mathbf{x}')\rangle\,. \tag{3.25}$$

Using Eq. 3.24, we find

$$\langle T(\boldsymbol{\ell})T^*(\boldsymbol{\ell}')\rangle = \int \frac{\mathrm{d}^2\mathbf{x}}{2\pi}\int \frac{\mathrm{d}^2\mathbf{x}'}{2\pi}e^{-i\boldsymbol{\ell}\,\cdot\,\mathbf{x}}e^{i\boldsymbol{\ell}'\,\cdot\,\mathbf{x}'}\,\xi(|\mathbf{x}-\mathbf{x}'|) = \\ = \int \frac{\mathrm{d}^2\mathbf{x}}{2\pi}\int \frac{\mathrm{d}^2\mathbf{r}}{2\pi}\,e^{i(\boldsymbol{\ell}'-\boldsymbol{\ell})\,\cdot\,\mathbf{x}}\,e^{i\boldsymbol{\ell}'\,\cdot\,\mathbf{r}}\xi(r) = \\ = \delta(\boldsymbol{\ell}'-\boldsymbol{\ell})\int \mathrm{d}^2\mathbf{r}e^{i\boldsymbol{\ell}\,\cdot\,\mathbf{r}}\xi(r) = \delta(\boldsymbol{\ell}'-\boldsymbol{\ell})\,C_\ell^{TT}\,, \tag{3.26}$$

where we have defined the unlensed power spectrum C_ℓ^{TT}, as

$$C_\ell^{TT} = \int \mathrm{d}^2\mathbf{r}\, e^{\boldsymbol{\ell}\cdot\mathbf{r}}\xi(r) = \int r\mathrm{d}r \int \mathrm{d}\phi_{\mathbf{r}} e^{i\ell r\cos(\phi_{\boldsymbol{\ell}}-\phi_{\mathbf{r}})}\xi(r) = 2\pi\int r\mathrm{d}r\; j_0(\ell r)\xi(r)\,. \tag{3.27}$$

For more details about this calculation, see Ref. [112].
Hence, the lensed correlation function $\tilde{\xi}(r)$ is given by [115]

$$\begin{aligned}
\tilde{\xi}(r) &\equiv \langle\widetilde{T}(\mathbf{x})\,\widetilde{T}(\mathbf{x}')\rangle = \\
&= \int \frac{\mathrm{d}^2\boldsymbol{\ell}}{(2\pi)^2}\, C_\ell^{TT} e^{i\boldsymbol{\ell}\cdot\mathbf{r}}\langle e^{i\boldsymbol{\ell}\cdot[\alpha(\mathbf{x})-\alpha(\mathbf{x}')]}\rangle = \\
&= \frac{1}{2\pi}\int \mathrm{d}\ell\; \ell C_\ell^{TT} e^{-\ell^2\sigma^2(r)/2}\,\cdot \\
&\quad\cdot\left[\left(1+\frac{1}{16}\ell^4 C_{gl,2}^2(r)\right)j_0(\ell r) + \frac{1}{2}\ell^2 C_{gl,2}(r) j_2(\ell r) + \frac{1}{16}\ell^4 C_{gl,2}^2(r) j_4(\ell r)\right],
\end{aligned} \tag{3.28}$$

where $\sigma^2(r) \equiv C_{gl}(0) - C_{gl}(r)$. To reach the last step, we have expanded the exponential and integrated term by term, keeping only terms up to second order in $C_{gl,2}$. Higher order terms in $C_{gl,2}$ only contribute at the $O(10^{-4})$ level on the scales of interest (see Ref. [115] for a more detailed discussion).

The calculations are analogous but slightly more complicated for the polarization observables, since, as already discussed in Chpt. 1 and Chpt. 2, we have to deal with ± 2 spin quantities (see also App. B).
As it was done for temperature in Eq. 3.24, we expand the polarization field as [112]

$$P(\mathbf{x}) = \big[Q+iU\big](\mathbf{x}) = -\int \frac{\mathrm{d}^2\boldsymbol{\ell}}{2\pi}\Big[E(\boldsymbol{\ell})+iB(\boldsymbol{\ell})\Big]e^{2i\phi_{\boldsymbol{\ell}}}\, e^{i\boldsymbol{\ell}\cdot\mathbf{x}}\,; \tag{3.29a}$$

$$P^*(\mathbf{x}) = \big[Q-iU\big](\mathbf{x}) = -\int \frac{\mathrm{d}^2\boldsymbol{\ell}}{2\pi}\Big[E(\boldsymbol{\ell})-iB(\boldsymbol{\ell})\Big]e^{-2i\phi_{\boldsymbol{\ell}}}\, e^{i\boldsymbol{\ell}\cdot\mathbf{x}}\,, \tag{3.29b}$$

with their inverse relations

$$E(\boldsymbol{\ell})+iB(\boldsymbol{\ell}) = -\int \frac{\mathrm{d}^2\mathbf{x}}{2\pi}\, P\, e^{-2i\phi_{\boldsymbol{\ell}}}\, e^{-i\boldsymbol{\ell}\cdot\mathbf{x}}\,; \tag{3.29c}$$

$$E(\boldsymbol{\ell})-iB(\boldsymbol{\ell}) = -\int \frac{\mathrm{d}^2\mathbf{x}}{2\pi}\, P^*\, e^{2i\phi_{\boldsymbol{\ell}}}\, e^{i\boldsymbol{\ell}\cdot\mathbf{x}}\,. \tag{3.29d}$$

The $e^{\pm 2i\phi_{\boldsymbol{\ell}}}$ factors allow us to rotate between a natural basis defined in terms of

$\boldsymbol{\ell}$, and the fixed basis defined in terms of $\boldsymbol{e}_x$. Hence, the unlensed polarization correlation functions are defined as

$$\xi_+(r) \equiv \langle e^{-2i\phi_{\mathbf{r}}} P^*(\mathbf{x})\, e^{2i\phi_{\mathbf{r}}} P(\mathbf{x}')\rangle\,, \tag{3.30a}$$

$$\xi_-(r) \equiv \langle e^{2i\phi_{\mathbf{r}}} P(\mathbf{x})\, e^{2i\phi_{\mathbf{r}}} P^*(\mathbf{x}')\rangle\,, \tag{3.30b}$$

$$\xi_X(r) \equiv \langle T(\mathbf{x})\, e^{2i\phi_{\mathbf{r}}} P(\mathbf{x}')\rangle\,. \tag{3.30c}$$

Conventionally, X stands for TE. After some math, the lensed correlation functions up to the second-order in $C_{gl,2}$ are

$$\tilde{\xi}_+(r) = \frac{1}{2\pi}\int \mathrm{d}\ell\; \ell\Big(C_\ell^{EE} + C_\ell^{BB}\Big) e^{-\ell^2\sigma^2(r)/2}\left[\left(1+\frac{1}{16}\ell^4 C_{gl,2}^2(r)\right) j_0(\ell r) + \right.$$
$$\left. + \frac{1}{2}\ell^2 C_{gl,2}(r) j_2(\ell r) + \frac{1}{16}\ell^4 C_{gl,2}^2(r) j_4(\ell r)\right]; \tag{3.31a}$$

$$\tilde{\xi}_-(r) = \frac{1}{2\pi}\int \mathrm{d}\ell\; \ell\Big(C_\ell^{EE} - C_\ell^{BB}\Big) e^{-\ell^2\sigma^2(r)/2}\left[\left(1+\frac{1}{16}\ell^4 C_{gl,2}^2(r)\right) j_4(\ell r) + \right.$$
$$\left. + \frac{1}{2}\ell^2 C_{gl,2}(r) \frac{j_2(\ell r)+j_6(\ell r)}{2} + \frac{1}{16}\ell^4 C_{gl,2}^2(r) \frac{j_0(\ell r)+j_8(\ell r)}{2}\right]; \tag{3.31b}$$

$$\tilde{\xi}_X(r) = \frac{1}{2\pi}\int \mathrm{d}\ell\; \ell C_\ell^{TE} e^{-\ell^2\sigma^2(r)/2}\left[\left(1+\frac{1}{16}\ell^4 C_{gl,2}^2(r)\right) J_2(\ell r) + \right.$$
$$\left. + \frac{1}{2}\ell^2 C_{gl,2}(r) \frac{j_0(\ell r)+j_4(\ell r)}{2} + \frac{1}{16}\ell^4 C_{gl,2}^2(r) \frac{J_2(\ell r)+j_6(\ell r)}{2}\right]. \tag{3.31c}$$

See Ref. [115] for more details about this calculation.

The lensed correlation functions in Eq.3.28 and Eqs.3.31 are valid in the flat-sky approximation. This is actually a good approximation at small scales, but the spherical-sky case turns out to be crucial for getting high accuracy in the lensed power spectrum on arcminute scales. Without entering in detail, the above correlation functions can be generalized on a sphere. What will change is all the geometrical factors between the square brackets: the dependencies by the unlensed power spectra will remain the same.

The lensed angular power spectra in the spherical-sky case are therefore

$$\widetilde{C}_\ell^{TT} = 2\pi \int_{-1}^{1} \mathrm{d}\cos\beta\, \tilde{\xi}(\beta) d^\ell_{00}(\beta)\,; \tag{3.32a}$$

$$\widetilde{C}_\ell^{EE} - \widetilde{C}_\ell^{BB} = 2\pi \int_{-1}^{1} \mathrm{d}\cos\beta\, \tilde{\xi}_-(\beta) d^\ell_{2-2}(\beta)\,; \tag{3.32b}$$

$$\widetilde{C}_\ell^{EE} + \widetilde{C}_\ell^{BB} = 2\pi \int_{-1}^{1} \mathrm{d}\cos\beta\, \tilde{\xi}_+(\beta) d^\ell_{22}(\beta)\,; \tag{3.32c}$$

$$\widetilde{C}_\ell^{TE} = 2\pi \int_{-1}^{1} \mathrm{d}\cos\beta\, \tilde{\xi}_X(\beta) d^\ell_{20}(\beta)\,, \tag{3.32d}$$

where the correlation functions, $\tilde{\xi}$, are those defined in the spherical case, β is the angle between the two directions of observation $\hat{\mathbf{n}}_1$ and $\hat{\mathbf{n}}_2$, and

$$d^\ell_{ss'} = \sum_m {}_sY^*_{\ell m}(\hat{\mathbf{n}}_1)\, {}_s'Y_{\ell m}(\hat{\mathbf{n}}_2)\,. \tag{3.33}$$

The above expressions are discussed and fully computed in *e.g.* Refs. [115, 116]. A generalization, including EB and TB parity-violating power spectra can be found in [80]. For a complete review on CMB lensing, you may also look at [112].

Let us now briefly discuss these results, also shown in Fig. 3.2.
For what concerns TT and EE (but also TE), the lensing effect is to smooth out the acoustic peaks and troughs of the power spectrum. As anticipated, the effect becomes relevant at small scales. For the lensed B-mode polarization spectrum, the situation is clearly different. The lensing is dramatically modifying the primordial spectrum. The reason is obvious looking at Eqs.3.32: B-mode polarization is generated from E-mode polarization, even if the primordial BB power spectrum is zero. This is somehow similar to the imprint of GFE (see *e.g.* Eqs.2.49 and Fig. 2.5).

We have introduced the primordial B-modes in Chpt. 1, clarifying how their observation would be of great interest as a way of discriminating different classes of models of inflation and other models of the early Universe.
The problem is that we have no idea what the tensor amplitude is, in particular how small it could be. On top of this, we have just seen that the lensing of purely scalar E-mode polarization will produce a spurious lensed B modes in any case, even if $r = 0$ (see Fig. 1.12).
Recognizing the effect of lensing in the CMB maps and isolating it is therefore a fundamental task if we want to have at least the chance of measuring primordial

B-modes. In the next section, we outline how to reconstruct the lensing potential from the observed CMB maps.

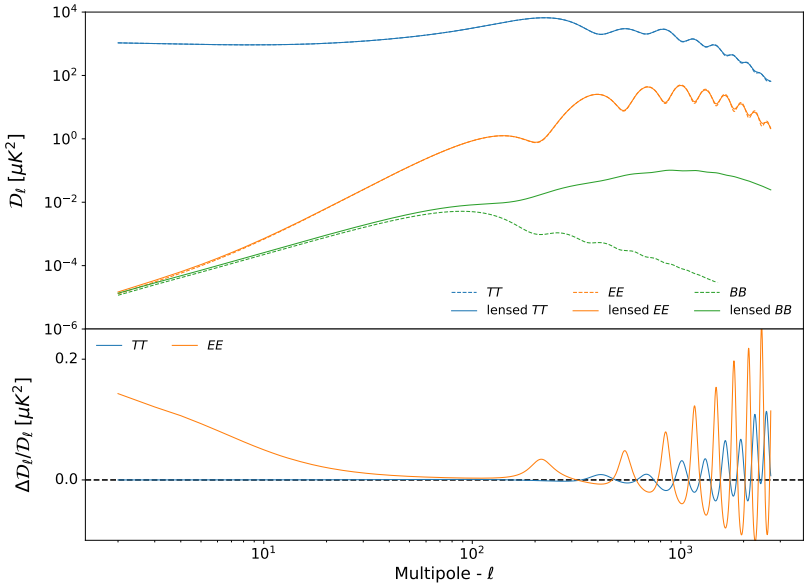

Figure 3.2: *Lensed CMB power spectra (solid) and the unlensed spectra (dashed). Both are computed assuming the best-fit Planck 2018 cosmology. On the bottom part, the fractional change in the power spectra due to lensing.*

3.3 Lensing reconstruction

We have seen that light is unavoidably bent by a gravitational potential. As a consequence, the CMB pattern that we see today is distorted, due to the *mass* bumped into by photons along their journey from the last scattering surface to us. The unlensed CMB field is therefore unobservable, but its statistics are very well understood, as discussed in Chpt. 1. This means that, from statistical measures of the lensed CMB fields, we should be able to constrain the lensing potential. Moreover, on small scales, where the power of unlensed CMB is small, the lensed CMB measures the small-scale lensing potential more or less directly.

Even though, the lensing potential can also be partly reconstructed using large-scale structure tracers, here we focus our attention on its reconstruction from the CMB temperature and polarization maps (assuming that the primordial fields are Gaussian).

We are going to work in the flat sky approximation, adopting the formalism for small sky patches [117], described in the previous section. You may also look at Ref. [118], where the approximation for the full sky case is discussed.

Let us start considering the temperature field, as defined in Eqs. 3.24. From Eq. 3.26, it is clear that harmonics with different $\boldsymbol{\ell}$ are uncorrelated. This is not true for the actual sky we observe: for a given fixed lensing potential, the distribution of the observed temperature will not be isotropic. This suggests that we might use the quadratic off-diagonal terms of the lensed correlation $\langle\widetilde{T}(\boldsymbol{\ell}_1)\widetilde{T}(\boldsymbol{\ell}_2)\rangle$ at fixed ϕ to constrain the lensing potential in our sky realization. In other words, we want to use correlations between the temperature anisotropies around each lensing clump to constrain the potential of the clump. This technique is called *quadratic estimator*.

Hence, averaging over realizations of the unlensed temperature field, the two-point correlation function becomes [117]

$$\langle\widetilde{T}(\boldsymbol{\ell}_1)\widetilde{T}(\boldsymbol{\ell}_2)\rangle_{CMB} \;=\; f_{TT}(\boldsymbol{\ell}_1\,,\boldsymbol{\ell}_2)\phi(\boldsymbol{L})\,, \tag{3.34a}$$

with

$$f_{TT}(\boldsymbol{\ell}_1\,,\boldsymbol{\ell}_2) \;=\; C^{TT}_{\ell_1}\boldsymbol{L}\cdot\boldsymbol{\ell}_1 + C^{TT}_{\ell_2}\boldsymbol{L}\cdot\boldsymbol{\ell}_2\,, \tag{3.34b}$$

where $\boldsymbol{L} = \boldsymbol{\ell}_1 + \boldsymbol{\ell}_2$, with $\boldsymbol{\ell}_1 \neq -\boldsymbol{\ell}_2$ and C^{TT}_ℓ is the unlensed temperature power spectrum. The correlation returns indeed the value of the lensing potential weighted with the unlensed power spectra.

This result can be used to build the quadratic estimator of the deflection field, $\alpha(\hat{\mathbf{n}})$, defined in Eq. 3.1. Let us therefore define the TT quadratic estimator of $\alpha(\hat{\mathbf{n}})$ as [117]

$$\hat{\alpha}_{TT}(\boldsymbol{L}) \;=\; \frac{A_{TT}(L)}{L}\int\frac{\mathrm{d}^2\boldsymbol{\ell}_1}{(2\pi)^2}\,\widetilde{T}(\boldsymbol{\ell}_1)\widetilde{T}(\boldsymbol{\ell}_2)F_{TT}(\boldsymbol{\ell}_1\,,\boldsymbol{\ell}_2)\,, \tag{3.35a}$$

where

$$A_{TT}(L) \;=\; L^2\left[\int\frac{\mathrm{d}^2\ell_1}{(2\pi)^2}\,f_{TT}(\boldsymbol{\ell}_1\,,\boldsymbol{\ell}_2)F_{TT}(\boldsymbol{\ell}_1\,,\boldsymbol{\ell}_2)\right]^{-1}, \tag{3.35b}$$

The normalization $A_{TT}(L)$ is chosen so that, averaging over an ensemble of realizations of the temperature field, we recover the true deflection field:

$$\langle\hat{\alpha}_{TT}(\boldsymbol{L})\rangle_{CMB} \;=\; \alpha(\boldsymbol{L}) \;\equiv\; L\phi(\boldsymbol{L})\,. \tag{3.36}$$

The function F_{TT} is usually called filter, and it can be optimally chosen in order

to minimize the variance of the estimator, $\langle \hat{\alpha}^*_{TT}(\boldsymbol{L})\hat{\alpha}_{TT}(\boldsymbol{L})\rangle$. Therefore, we get:

$$F_{TT}(\boldsymbol{\ell}_1,\boldsymbol{\ell}_2) \;=\; \frac{f_{TT}(\boldsymbol{\ell}_1,\boldsymbol{\ell}_2)}{2\,\widetilde{C}^{TT,tot}_{\ell_1}\widetilde{C}^{TT,tot}_{\ell_2}} \tag{3.37}$$

where $\widetilde{C}^{TT,tot}_{\ell} = \widetilde{C}^{TT}_{\ell} + N_\ell$, N_ℓ is the noise contribution. Basically, $\widetilde{C}^{TT,tot}_{\ell}$ is the observed lensed TT power spectra, so it might also account for the cosmic variance of the fields and the noise variance of the experiments.

Using the observed polarization maps instead of the temperature map, we find expressions similar to those above, Eq. 3.35.
In general, there are 6 estimators, corresponding to the 3! pairs of T,E,B. Actually, they are 5. Indeed, since the signal of the B-mode polarization is negligible compared with the others, $\hat{\alpha}_{BB}$ estimator has vanishing signal-to-noise. Hence, we can define the i-estimator as [117]

$$\hat{\alpha}_i(\boldsymbol{L}) \;=\; \frac{A_i(L)}{L}\int \frac{\mathrm{d}^2\boldsymbol{\ell}_1}{(2\pi)^2}\, X(\boldsymbol{\ell}_1)X'(\boldsymbol{\ell}_2)\,F_{XY}(\boldsymbol{\ell}_1,\boldsymbol{\ell}_2)\,, \tag{3.38a}$$

where

$$A_i(L) \;=\; L^2\left[\int \frac{\mathrm{d}^2\boldsymbol{\ell}_1}{(2\pi)^2}\, f_i(\boldsymbol{\ell}_1,\boldsymbol{\ell}_2)F_i(\boldsymbol{\ell}_1,\boldsymbol{\ell}_2)\right]^{-1}, \tag{3.38b}$$

$$F_i(\boldsymbol{\ell}_1,\boldsymbol{\ell}_2) \;=\; \frac{\widetilde{C}^{X'X',tot}_{\ell_1}\widetilde{C}^{XX,tot}_{\ell_2}\, f_i(\boldsymbol{\ell}_1,\boldsymbol{\ell}_2) \;-\; \widetilde{C}^{XX',tot}_{\ell_1}\widetilde{C}^{XX',tot}_{\ell_2}(\boldsymbol{\ell}_2,\boldsymbol{\ell}_1)}{\widetilde{C}^{XX,tot}_{\ell_1}\widetilde{C}^{X'X',tot}_{\ell_2}\widetilde{C}^{X'X',tot}_{\ell_1}\widetilde{C}^{XX,tot}_{\ell_2} \;-\; \left(\widetilde{C}^{XX',tot}_{\ell_1}\widetilde{C}^{XX',tot}_{\ell_2}\right)^2}\,, \tag{3.38c}$$

and

$$f_i(\boldsymbol{\ell}_1,\boldsymbol{\ell}_2) \;=\; \begin{cases} C^{TT}_{\ell_1}\,\boldsymbol{L}\cdot\boldsymbol{\ell}_1 \;+\; C^{TT}_{\ell_1}\,\boldsymbol{L}\cdot\boldsymbol{\ell}_2\,, & i = TT\,; \\ C^{TE}_{\ell_1}\cos(\varphi_{\boldsymbol{\ell}_1\boldsymbol{\ell}_2})\,\boldsymbol{L}\cdot\boldsymbol{\ell}_1 \;+\; C^{TE}_{\ell_1}\,\boldsymbol{L}\cdot\boldsymbol{\ell}_2\,, & i = TE\,; \\ C^{TE}_{\ell_1}\sin(\varphi_{\boldsymbol{\ell}_1\boldsymbol{\ell}_2})\,\boldsymbol{L}\cdot\boldsymbol{\ell}_1\,, & i = TB\,; \\ \left[C^{EE}_{\ell_1}\,\boldsymbol{L}\cdot\boldsymbol{\ell}_1 \;+\; C^{EE}_{\ell_2}\,\boldsymbol{L}\cdot\boldsymbol{\ell}_2\right]\cos(\varphi_{\boldsymbol{\ell}_1\boldsymbol{\ell}_2})\,, & i = EE\,; \\ \left[C^{EE}_{\ell_1}\,\boldsymbol{L}\cdot\boldsymbol{\ell}_1 \;-\; C^{BB}_{\ell_2}\,\boldsymbol{L}\cdot\boldsymbol{\ell}_2\right]\sin(\varphi_{\boldsymbol{\ell}_1\boldsymbol{\ell}_2})\,, & i = EB\,; \\ \left[C^{BB}_{\ell_1}\,\boldsymbol{L}\cdot\boldsymbol{\ell}_1 \;+\; C^{BB}_{\ell_2}\,\boldsymbol{L}\cdot\boldsymbol{\ell}_2\right]\cos(\varphi_{\boldsymbol{\ell}_1\boldsymbol{\ell}_2})\,, & i = BB\,, \end{cases} \tag{3.38d}$$

where $\varphi_{\boldsymbol{\ell}_1\boldsymbol{\ell}_2} \equiv \varphi_{\boldsymbol{\ell}_1} - \varphi_{\boldsymbol{\ell}_2} = \cos^{-1}(\hat{\mathbf{x}}\cdot\hat{\boldsymbol{\ell}}_1) - \cos^{-1}(\hat{\mathbf{x}}\cdot\hat{\boldsymbol{\ell}}_2)$ and C_ℓ are the unlensed power spectra.
The noise properties of these estimators follow from

$$\begin{aligned}\langle\hat{\alpha}_i^*(\boldsymbol{L})\hat{\alpha}_j(\boldsymbol{L}')\rangle \;&=\\ &= \delta(\boldsymbol{L}-\boldsymbol{L}')\big[C_L^{\alpha\alpha} + N_{ij}\big] \equiv \delta(\boldsymbol{L}-\boldsymbol{L}')\big[L^2\, C_L^{\phi\phi} + N_{ij}\big]\,,\end{aligned} \tag{3.39}$$

so that

$$\begin{aligned}N_{ij} \;=\; &\frac{A_i(L)A_j(L)}{L^2}\int\frac{\mathrm{d}^2\ell_1}{(2\pi)^2}F_i(\boldsymbol{\ell}_1,\boldsymbol{\ell}_2)\;\cdot\\ &\cdot\Big[F_j(\boldsymbol{\ell}_1,\boldsymbol{\ell}_2)\widetilde{C}_{\ell_1}^{X_iX_j,tot}\widetilde{C}_{\ell_2}^{X_i'X_j',tot} + F_j(\boldsymbol{\ell}_2,\boldsymbol{\ell}_1)\widetilde{C}_{\ell_1}^{X_iX_j',tot}\widetilde{C}_{\ell_2}^{X_i'X_j,tot}\Big]\,,\end{aligned} \tag{3.40}$$

where $i,j = TT, TE, TB, EE, EB$ and so *e.g.* if $i = TT$ and $j = TE$, $X_iX_j = TT$, $X_i'X_j' = TE$, $X_iX_j' = TE$ and so on. Notice that for the minimum variance filter, *i.e.* F_i as defined in Eq. 3.38c, $N_{ij} = A_i$.
At high-L, the individual estimators are noise limited (see *e.g.*, Ref. [118]). We can combine them to reduce the noise, obtaining the so-called minimum variance (MV) estimator

$$\hat{\alpha}_{MV}(\boldsymbol{L}) \;=\; \sum_i \omega_i\hat{\alpha}_i(\boldsymbol{L})\,, \tag{3.41a}$$

where

$$\omega_i \;=\; \frac{\sum_m (N_L^{-1})_{im}}{\sum_{mn}(N_L^{-1})_{mn}}\,, \tag{3.41b}$$

with $i,m,n = TT, TE, TB, EE, EB$. Therefore, from

$$\langle\hat{\alpha}_{MV}^*(\boldsymbol{L})\hat{\alpha}_{MV}(\boldsymbol{L}')\rangle \;=\; \delta(\boldsymbol{L}-\boldsymbol{L}')\big[C_L^{\alpha\alpha} + N_{MV}\big]\,, \tag{3.42}$$

we find the noise variance

$$N_{MV} \;=\; \frac{1}{\sum_{mn}(N_L^{-1})_{mn}}\,. \tag{3.43}$$

For current experiments $\hat{\alpha}_{MV}$ is dominated by the combinations involving temperature, TT in particular. However, as the sensitivity of the experiments improves, polarization will play a progressively more important role for the minimum variance estimator, being mostly dominated by EB.

Let us comment Eq. 3.40 and Eq. 3.43. The spectra appearing are the observed ones. So, one might wonder why it is the lensed fields that are determining the

noise level. This is indeed a property only of the quadratic estimator. More general methods have cosmic variance determined essentially by the unlensed fields.

The picture drawn so far seems quite simple. In practice, the reconstruction may not be so straightforward. The lensing signal can be complicated by contributions from the kinetic-SZ effect, and non-linear evolution that might became important on small scales. If not taken into account, these can significantly bias the result obtained from the simple quadratic estimator derived above [119, 120]. The kinetic-SZ signal comes predominantly from large clusters, so masking out these sources using thermal-SZ measurements can help to reduce this source of reconstruction error. Forthcoming high-resolution experiments, such as SO and CMB-S4, will require to mask more of these sources correlated with the underlying CMB lensing field. The question now is that this masking operation has an impact on the lensing reconstruction and on the estimated unlensed power spectra. We are going to discuss these two points in the next sections.
Using real data and masking region of the sky correlated with the lensing field complicate a little the situation. Hence, before moving on, it worth briefly reviewing the steps that we have followed in the lensing reconstruction implemented in the next section.

3.4 CMB lensing reconstruction biases from masking extragalactic sources[3]

So far we have seen that the observed CMB temperature and polarization maps are inevitably distorted by the gravitational lensing. However, the CMB maps are also inevitably contaminated by foregrounds, some of which are usually masked to perform the analysis. If this mask is correlated to the lensing signal, measurements over the unmasked sky may give biased estimates and hence biased cosmological inferences.

In the next section, we will see that the lensed (temperature) CMB power spectra can be substantially altered when only measured over the unmasked area. Here, instead, we quantify the size of the mask bias for lensing reconstruction, focussing primarily on the impact of masking resolved SZ clusters which are correlated with the CMB lensing potential. Moreover, we have considered

[3]Based on M. Lembo et al [13]

realistic numerical simulations which include non-Gaussian correlated maps of the CMB lensing convergence, tSZ and CIB emission at at 217 GHz to create a foreground mask by simply thresholding the aforementioned field. Furthermore, we considered masks to remove resolved radio point sources. We refer to Sec. *3.4.1* for more details.
Although estimated to be negligible for Planck [10], the impact may be substantially larger for forthcoming high-resolution experiments obtaining more of their information from the small-scale CMB where the foregrounds are more important.

In principle, the non-blackbody spectrum of the foregrounds can be used to clean the foregrounds by using combinations of observations at multiple frequencies. Foreground cleaning has been very successfully used, particularly on large scales, but inevitably comes with the cost of increased noise, especially on small scales where the observational noise becomes comparable to the observed signal. Alternatively, the foreground signal can simply be modelled, which is what is often done at the power spectrum level for CMB likelihood analysis. In both cases, it is often necessary to also apply some masking to the brightest sources, including the galactic plane (which is not correlated to large-scale structure and hence does not introduce a direct bias) but also extragalactic sources.
For CMB lensing reconstruction, the non-Gaussianity of the foregrounds is important and can produce a direct bias on lensing estimates that is difficult to model [121, 122]. For SZ foregrounds, the largest non-Gaussianity is associated with the brightest SZ clusters, and hence can be substantially reduced by cluster masking [121, 122]. Point source and CIB foreground non-Gaussianity can also be substantially reduced by masking the brightest sources. A variety of other methods have been suggested to reduce lensing biases from small-scale temperature reconstruction [120, 123–125], however, these are usually only applied after the brightest sources have already been masked out.
To extract reliable information from small-scale CMB temperature observations it is therefore likely to be necessary to understand the impact of the source masking, especially if the correlated masking introduces substantial biases. The foreground issue is less important for CMB lensing reconstruction using polarization, since the polarized foreground amplitudes are expected to have substantially lower amplitude, but should also be addressed. For near-future observations such as Simons Observatory (SO), the temperature signal still contains a substantial fraction of the available information, so fully exploiting the data will require robust modeling of the temperature signal, which is what we focus on here.

To quantify the various effects, we built different sets of masks, using the

WebSky simulations of Ref. [126] based on fast approximate numerical simulations of large-scale structure. These cover the entire sky over a broad range of redshifts and include correlated realizations of the various foregrounds and large-scale structure tracers, as well as halo catalogues. The CMB lensing convergence map is simulated in the Born approximation and includes the correlations to the halo catalogue and foreground maps.
After describing in more details the sets of masks that we have used for our analysis, Sec. *3.4.1*, in Sec. *3.4.2*, we first considered the case of directly masking the lensing convergence field. This does not correspond to what is usually done in practice, but it helps to roughly quantify the size of the expected direct effect on the lensing power. In Sec. *3.4.3* we consider the impact that of masking the lensed CMB fields on the reconstructed lensing potential.

3.4.1 Masks using WebSky simulation suite

We use the publicly available WebSky simulation suite[4] which includes maps of CMB lensing convergence κ, radio point sources, CIB, and tSZ produced from the same underlying mass distribution at $z \leq 4.5$, as well as the halo catalogues. In Fig. 3.3, we report histograms showing the mass, $M_{500,c}$ (left), angular size, $\theta_{500,c}$ (middle) and redshift, z (right), distributions of halos in the WebSky catalogue.

The aforementioned mass distribution was constructed with the accelerated N-body mass-Peak patch approach [127, 128] from a 15.4 Gpc^3, 12 2883 particle lightcone in a Planck 2018 cosmology. CIB and tSZ emission maps were constructed starting from the same matter distribution and using halo models matched to the latest CMB data from Planck, SPT (South Pole Telescope) and ACT (Atacama Cosmology Telescope) as well as Herschel[5] data at frequencies relevant for CMB experiments. We refer the reader to Ref. [126] for more details of the semi-analytical models adopted.

Using WebSky simulation, we build 5 sets of masks:

(i) *halo mass-thresholding ($W_{\rm halo}$)*
We constructed masks inspired by a mass-limited SZ survey. Given the noise properties of an experiment, the SZ flux limit corresponds to a mass-limit of detected objects. We created different masks ($W_{\rm halo}$), constructed by selecting all the halos present in the WebSky halo catalogue having a mass above a certain

[4] `https://mocks.cita.utoronto.ca/index.php/WebSky_Extragalactic_CMB_Mocks`
[5] The Herschel Space Observatory was a space observatory built and operated by the European Space Agency (ESA). It was active from 2009 to 2013, and was the largest infrared telescope ever launched.

mass cut, $M^{\rm cut}$. The mass cut has been done in term of $M_{500,c}$, a spherical overdensity enclosing 500 times the critical density of the Universe. We masked a disk centered on the halo position with a radius that is a multiple n of the $\theta_{500,c}$ halo angular size. In the following, we will adopt $n = 2$ as our default setup, and will show results for $M^{\rm cut} = (1.0, 1.8, 3.0) \cdot 10^{14}\, M_\odot$.

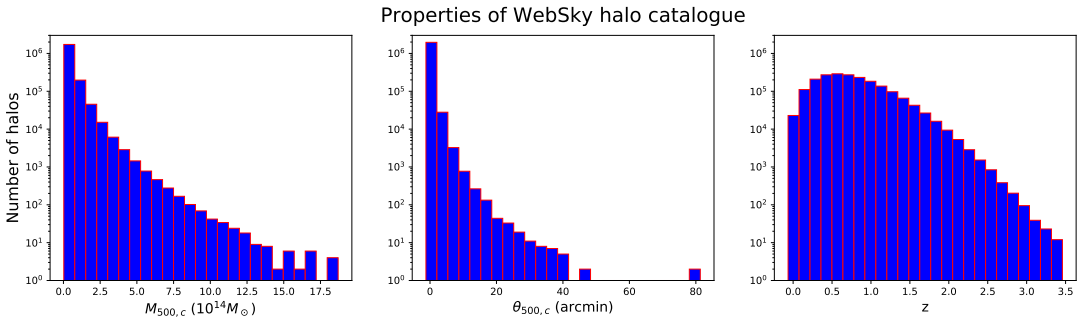

Figure 3.3: *Histograms showing the mass, $M_{500,c}$ (left), angular size, $\theta_{500,c}$ (middle) and redshift, z (right), distributions of halos in the WebSky catalogue. Here we have already considered a reduced catalogue, selecting only halos with $M_{200,m} > 10^{14} \cdot M_\odot$, that is the mass limit for detectable SZ clusters.*

(ii) *κ-thresholding (W_κ)*
We create a foreground masks by simply thresholding the CMB lensing κ field. These masks are therefore 100% correlated with CMB lensing.
Since the total bias is sensitive to the overall sky fraction removed by the mask, as well to the specific correlation between the mask and the convergence, we tested different configurations. To test the dependency on the sky fraction we thresholded the field masking all the pixels above a specific κ value so that a sky fraction f_{sky}^{mask} is removed. This generates masks with large numbers of small holes. To test the effect of the correlation scale of the deflection field and the shape of the mask, we also created masks by smoothing the κ field with Gaussian beams of different full width at half maximum (FWHM, $\theta_{1/2}$) prior to the thresholding step. This results in more regular and connected holes due to the longer correlation length, and also effectively reduces the shot noise of the foreground map (i.e. κ) due to the finite number of particles in the WebSky N-body simulation.
For reference, we have used $f_{sky}^{mask} = 0.6\%$, 2.3%, 6.7% and FWHM = 1.7, 5.1 arcmin.

(iii) *CIB-thresholding ($W_{\rm CIB}$)* The CIB is produced by star-forming galaxies through the absorption of stellar radiation by dust grains which is later re-

emitted in the infrared. The clustering of halos, and consequently of the galaxies within, then generates the observed CIB intensity fluctuations [129]. In addition to providing important constraints on the physics of star formation over a wide range of redshifts and halo and galaxy masses, especially for the objects with low luminosity that cannot be studied individually, the CIB acts as an important contaminating emission at microwave frequencies. Due to its spectral energy distribution (SED) similar to thermal dust emission it is difficult to disentangle CIB and galactic dust through component separation and perfectly remove both components, in particular at small angular scales and high observing frequencies. CIB residuals then propagate to data products derived from CMB maps. For CMB lensing and Compton y maps, CIB residuals are potentially particularly harmful as they are highly correlated with the underlying cosmological signals [130–132], and hence can then bias cosmological analyses. The CIB is therefore an example of a foreground highly correlated with CMB lensing (70% for $\ell = 1000$ where clustering of the emission is important).

We constructed a threshold mask (W_{CIB}) following the procedure outlined in the previous section starting from the WebSky CIB map at 217GHz. This frequency was chosen as it is the highest relevant frequency typically used for CMB power spectrum analysis based on multi-frequency cross-correlation as done for e.g. Planck.

(iv) *tSZ-thresholding (W_y)*

Observation of the tSZ effect, the inverse Compton scattering of CMB photons by free electrons, is a well established way to construct roughly mass-limited samples of galaxy clusters that are independent of redshift and thus very powerful cosmological probes [133–135]. tSZ clusters mark out large-scale density peaks, and as such have substantial correlation to CMB lensing, at the 30 - 50% level, and the emission also follows highly non-Gaussian statistics [136, 137]. If tSZ clusters are masked out, the CMB lensing-mask correlation can be substantial. Current CMB surveys from the ground and from space have blindly detected approximately 3200 tSZ clusters with redshift measurements to date [138–140]. Due to its characteristic spectral signature, tSZ emission can be subtracted from CMB maps using component separation. However this becomes difficult on small-scales where noise becomes important, and foreground-cleaning residuals are less simple to model. Thus tSZ is not usually cleaned for CMB power spectrum analysis, and its contribution to the observed power spectra is directly modeled and accounted for. Nevertheless, to minimize complex foreground residuals, for various higher-point statistics (including CMB lensing reconstruction) it is often useful and common practice to remove some of this source of highly non- Gaussian

signal by masking the SZ clusters (see e.g. [122]). Planck data were shown to be robust to these effects [10], however future ground-based surveys such as SO and S4 will detect one order of magnitude more clusters and thus cluster masking might potentially soon become a more significant issue.
We followed the same procedure outlined in previous sections and constructed a mask based on the thresholding of the WebSky tSZ Compton y parameter map W_y.
(v) *radio sources ($W_{\rm rs}$)*
Furthermore, we considered masks to remove resolved radio point sources, where the radio source catalogue is constructed from the Websky halos as described in Ref. [12]. Then, we selected all the sources with a measured flux above the detection limit of particular experiments, *Planck*, SO and S4. Each of these masks is built as product of three masks obtained selecting the sources in the three frequency bands most relevant for small-scales power spectra measurements, labelled LOW, MID and HIGH (for more details, see Table I of Ref. [12]). The size of the holes is $2\theta_{1/2}$.

Each of the above described masks W_X has been randomly rotated to give a new mask $W_X^{\rm rot}$, which is uncorrelated with the CMB lensing convergence field κ, but retains all the other non-trivial mode-coupling effects due to cut sky and hole shapes (we neglect the small area of residual correlation around the poles of the random rotation axis).

In Fig. 3.4, we show a zoom of both $\kappa^{\rm CMB}$ (top) and tSZ y-parameter maps (bottom) from the Websky simulation. The first two columns display the masked fields (the masked pixels are shown in black) for one of the $W_{\rm halo}$ masks employed in this work. The latter is the "random" version of the mask applied in the first column. In this case, there is no correlation between the mask and the field. In the other columns, we show the W_κ, $W_{\rm CIB}$, W_y and $W_{\rm rs}$ masks. Clearly, the W_κ is perfectly correlated, and the W_y directly removes the peaks of the y-parameter map. The $W_{\rm halo}$ mask is strongly correlated to the W_y mask, since the main peaks of the y-parameter map are associated with massive clusters.

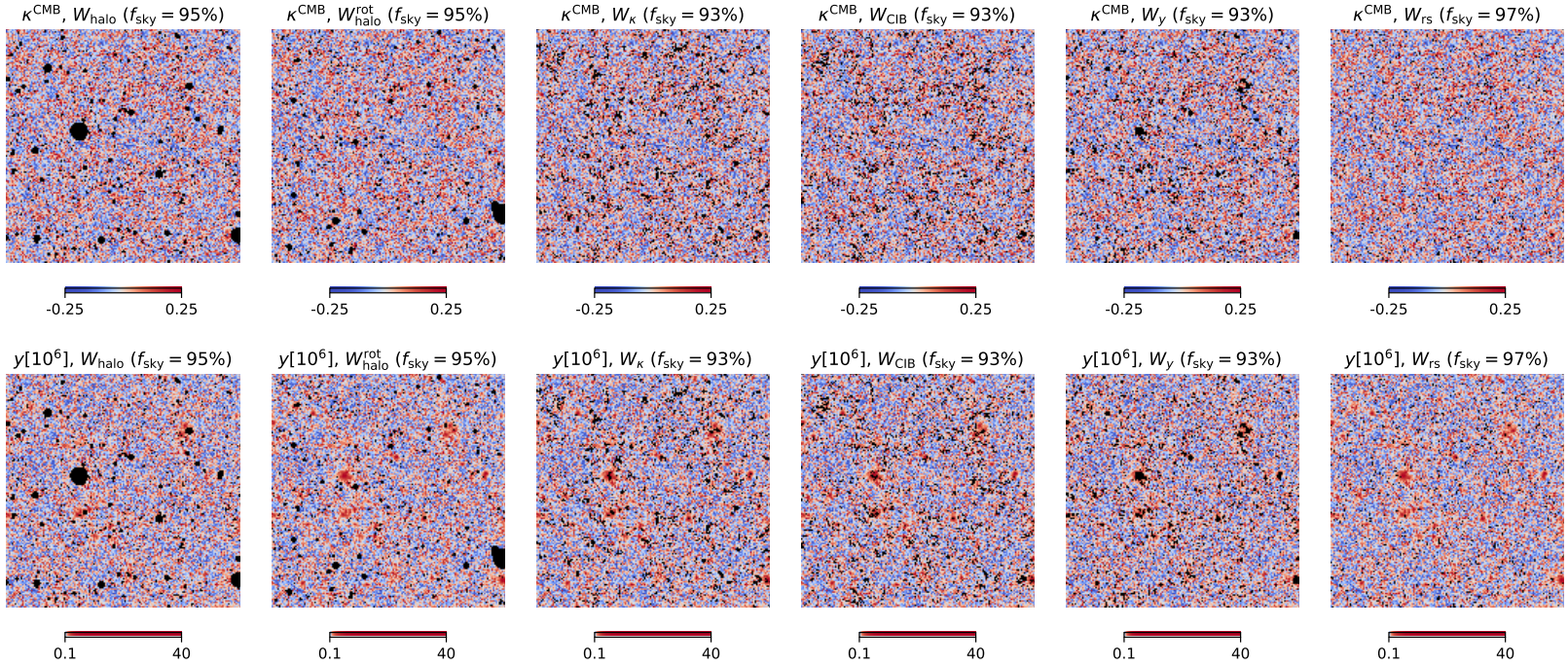

Figure 3.4: *20x20 deg^2 cutout of the $\kappa^{\rm CMB}$ (top) and tSZ y parameter maps (bottom) of the Websky simulation suite. We highlight the masked pixels (grey) for the different masks employed in this work. In the first two columns, the masks are constructed masking halos with $M > M^{\rm cut}$ in the simulation and cutting pixels within a radius $R < R^{\rm cut} = 2R_{500c}$. We denote with the superscript $^{\rm rot}$ the masks constructed randomizing the position of the masked halos prior to the masking. As it can be seen in the bottom row plots, the masked areas typically correspond to dense areas of strong tSZ emission (e.g. galaxy clusters). In the other columns, the masks are based on the peak thresholding on $\kappa^{\rm CMB}$, y-parameter, CIB 217 GHz ($f_{\rm sky} = 93\%$, $\theta_{1/2} = 5.10$ arcmin) and radio sources ($f_{\rm sky} = 97\%$, $\theta_{1/2} = 2.2, 1.4, 1.0$ arcmin, depending on the frequency, se Table I of [12]) maps for the same peak threshold.*

3.4.2 Masking the converge field

A conservative estimate of the effect of an LSS-correlated mask on the κ^{CMB} can be obtained computing the $\kappa\kappa-$power spectrum from the the masked κ^{CMB}. Even though, as the κ^{CMB} is not directly accessible but it has to be reconstructed from CMB maps this would only provide a good estimate of the expected amplitude of the effect if the lensing reconstruction delivered a fully local noiseless unbiased estimate of the true underlying field, but it nonetheless makes a useful benchmark for comparison that can also be modelled analytically. Hence, we applied the masks described in Sec. *3.4.1*, W_X, to the WebSky κ map. Then, we reconstruct the $\kappa\kappa-$power spectrum deconvolving the effect of the mask using the MASTER algorithm [141] as implemented in the publicly available code `NaMaster` [142][6]. Finally, we compare the reconstructed power spectrum with the true one, obtained from the WebSky κ map on the full sky. The results are shown in Fig. 3.5, for the considered W_X masks. The error bars correspond to the cosmic variance.

Our masks select areas of the sky where mass over-densities are present. Hence, as expected, the recovered power spectrum displays less power compared to its value computed on the full sky. Reducing $M^{\rm cut}$ or the cut-threshold, and hence increasing the fraction of sky area that is masked, the power deficit induced by masking becomes more important, with a clear suppression of power. This suppression is more relevant at very large scales and, at least for $W_{\rm halo}$ and W_y, at scales $L \sim 2000$. The shape of the biases induced by $W_{\rm halo}$ and W_y are similar. This is due to the fact that both these masks, even if they are build in different way, are masking almost the same area, see the discussion at the end of Sec. *3.4.1*. For the uncorrelated rotated masks, the biases are nearly zero as expected. See dashed lines in Fig. 3.5.

[6] https://github.com/LSSTDESC/NaMaster

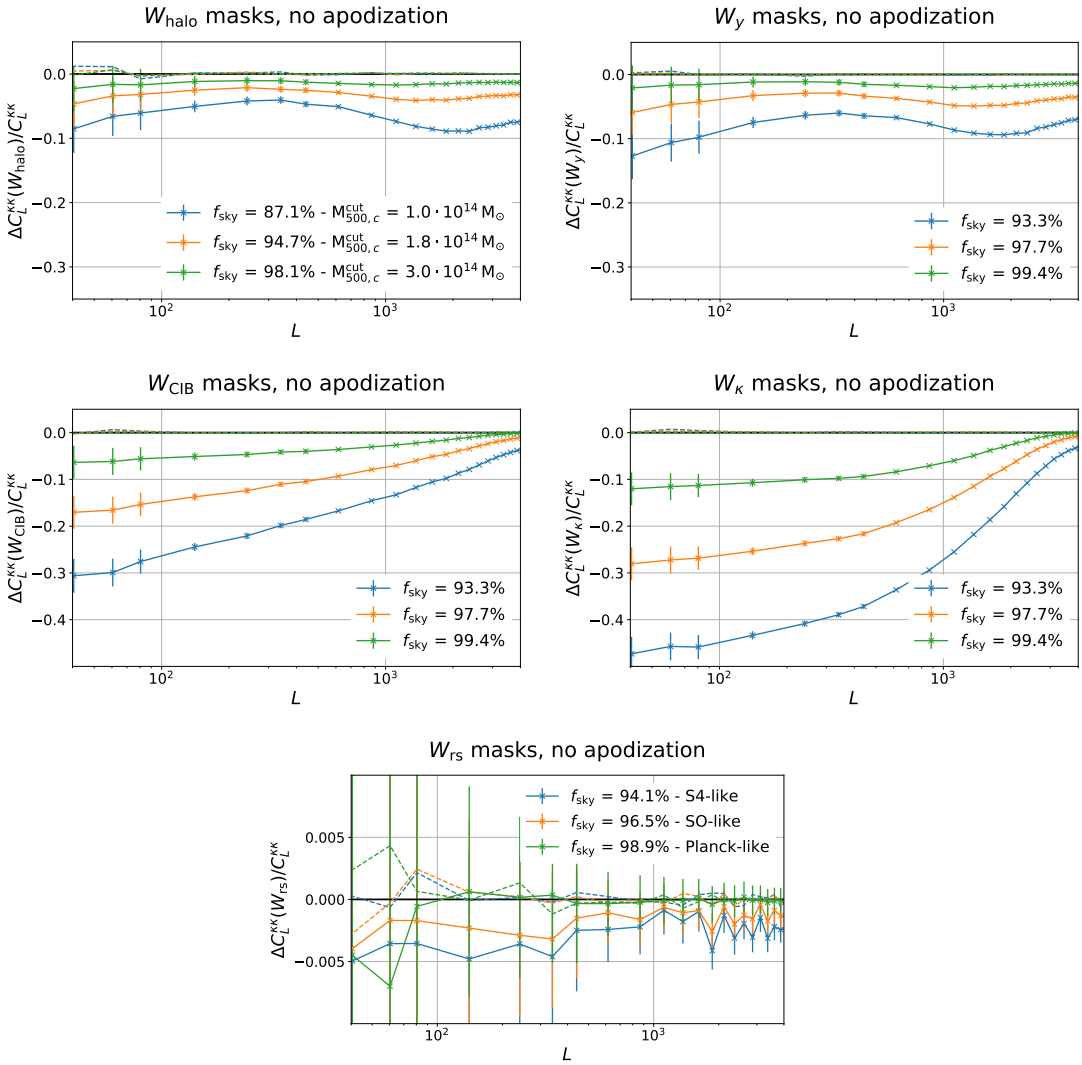

Figure 3.5: *Effect of masking on the CMB lensing convergence power spectrum $C_L^{\kappa\kappa}$ as fractional difference between the $C_L^{\kappa\kappa}$ computed on the masked sky and its value computed on the full sky. Different colors show the result for masks retaining different fractions of the sky after masking. No apodization is applied. Simulation measurements are shown as data points and the semi-analytic theory predictions in solid. Dashed lines correspond to rotated masks, where the should be no mask correlation. The top left plot shows the result for masking lines of sight containing halos with mass $M \geqslant M^{\rm cut}$, see Sec. 3.4.1, where the legend shows the corresponding $M^{\rm cut}$. Proceeding, we show the effect of W_y, $W_{\rm CIB}$, W_κ and $W_{\rm rs}$, respectively. The radio source masks $W_{\rm rs}$ are shown for the approximate source count detection limits of the experiments listed in the legend. The error bars correspond to the cosmic variance. Dashed lines correspond to rotated masks, $W_X^{\rm rot}$, cases.*

3.4.3 Lensing reconstruction on masked fields

In Sec. 3.4.2, we have directly masked the CMB lensing converge field κ to roughly quantify the bias induced by the foreground masks described in Sec. 3.4.1. In real-world analyses, we can not straightly access the κ field since it is reconstructed from the observed CMB maps. Hence, in this section, we mask CMB maps that are then used for quadratic-estimator reconstruction of the lensing potential.
For this first analysis, we only used the CMB temperature field, since the foreground contamination is less important for polarization and the properties of the polarized sources are currently much less well understood.

For the reconstruction of the lensing potential, we mainly followed the same steps as Planck lensing pipeline described in Ref. [10], which for reconstruction from the CMB temperature is an optimized and generalized version of the lensing quadratic estimator described in Sec. 3.3 (see also Ref. [118]). We also refer the reader to Ref. [143] for more details. For the implementation, we made use of the public `plancklens` code[7].

The procedure can be summarized in 4 steps: 1) Filtering of input "data" CMB maps 2) Construction of the lensing quadratic lensing estimator; 3) Mean-field subtraction and normalization; 4) Calculation of the lensing power spectrum and subtraction of additional biases (*i.e.* RD-$N^{(0)}$).

We created two sets of Monte Carlo simulations of lensed CMB realizations. In the first set (hereafter, NG set), the unlensed CMB realizations were all lensed using the same deflection field constructed from the WebSky κ simulation. In the second set (hereafter, G set), the same unlensed CMB simulations were each lensed with a different Gaussian random realizations of the deflection field having the same angular power spectrum as the WebSky κ map.
We used the NG set to isolate the bias as it would appear on real data, while the G set was used to compute the mean field and the RD-$N^{(0)}$ noise bias assuming no mask-lensing correlation. We discuss these two terms in the following. Moreover, we used the G set to estimate error bars on the auto- and cross-spectra estimators described in the following.

We start by convolving the input simulated lensed CMB sky with a beam of 1.5 arcmin FWHM, and adding homogeneous noise with a noise level of $\sim$6.7 μK-arcmin (for temperature). This corresponds to noise levels expected for the baseline SO configuration[8].

[7] `https://github.com/carronj/plancklens`

[8] Details of the noise model for SO can be found at `https://github.com/simonsobs/so_noise_models`

We have used a different noise only for the $W_{\rm rs}$ mask with $f_{\rm sky} = 94.1\%$ obtained selecting all the sources with a measured flux above the detection limit for CMB-S4, see Sec. 3.4.1. In this case, the input simulated lensed CMB sky are convolved with a beam of 1.0 arcmin FWHM, and isotropic uncorrelated noise is added with noise level $\sim$1 μK-arcmin (for temperature)[9].

The input maps are then masked using each of the unapodized W_X masks being considered in Sec. 3.4.1. Now, the first step, the filtering, is a linear operation that is applied to the CMB maps

$$\boldsymbol{X} = \tilde{\boldsymbol{X}} + \boldsymbol{n}\,, \tag{3.44}$$

where $\boldsymbol{n}$ is the instrumental noise and $\tilde{\boldsymbol{X}}$ is the beamed and lensed CMB given in terms of the unlensed field.
The results is a filtered CMB field

$$\bar{\boldsymbol{X}} \equiv \boldsymbol{\mathcal{F}}\,\boldsymbol{X}\,, \tag{3.45}$$

where $\boldsymbol{\mathcal{F}}$ is some linear filtering matrix that is designed to removed masked areas and (optionally but not in this case) down-weight noisier pixels or other noisy or contaminated modes. For optimal filtering, $\boldsymbol{\mathcal{F}}$ is non-diagonal and can be written as

$$\bar{\boldsymbol{X}} \equiv \left(\boldsymbol{b}C^{\rm fid}\boldsymbol{b}^T + \boldsymbol{N}\right)^{-1}\boldsymbol{X}\,, \tag{3.46}$$

where $\boldsymbol{b}$ is the transfer function (as discussed above, we consider a simple isotropic Gaussian beam of 1.5 or 1.0 arcmin FWHM), $\boldsymbol{N}$ is the covariance of the noise and $C^{\rm fid}$ is a set of fiducial lensed power spectra.
We used a fiducial lensed CMB temperature spectrum with multipoles between $100 \leq \ell \leq 4000$, cutting multipoles $\ell < 100$ (with little loss of information for lensing reconstruction). We use lensed CMB spectra in all terms of filter to make the estimator nearly unbiased to non-perturbative order [144, 145]. The cosmology used to build these spectra is consistent with the results of Planck 2018 and is the one used in WebSky simulation [126], discussed in the Sec. 3.4.1.

Optimal filtering is particularly valuable with the kind of masks we are using: Figure 3.6 shows how the filtering operation is able to fill some information inside small masked regions, effectively recovering information that was masked. This increases the information available, reduces any complications due to sharp mask cuts, and because the masked area is effectively reduced, can substantially

[9]Details can be found at `https://cmb-s4.org/wiki/index.php/Survey_Performance_Expectations`

reduce biases when the mask is correlated to the signal. We refer the reader to Refs. [143, 146–148] for more details.

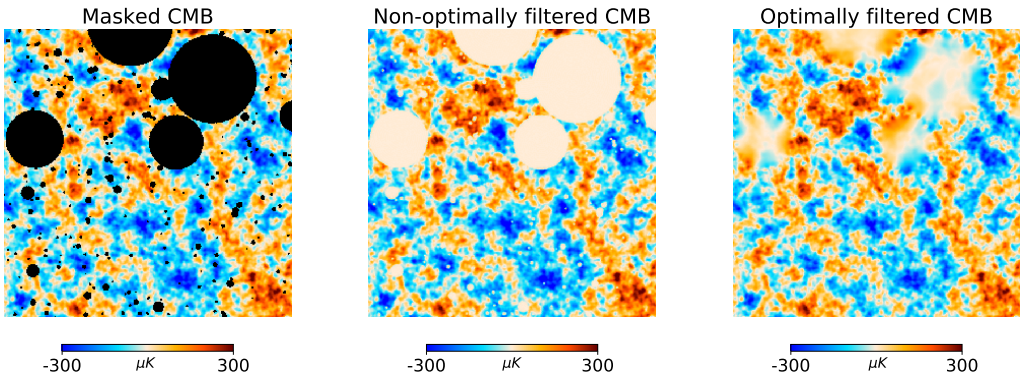

Figure 3.6: *We show the comparison between optimal and non-optimal filtering. From left to right, the masked CMB field ($f_{\rm sky} = 98\%$), the filtered CMB field using a non-optimal method and the filtered CMB field using optimal filtering, as described in* e.g. *Refs. [143, 146–148].*

Proceeding to the second step, the real-space lensing deflection estimator is then built from a pair of filtered maps discussed above. The gradient part[10] of the lensing deflection estimator, $\hat{g}_{LM}$, contains information on the lensing potential, which is then estimated by [10]

$$\hat{\phi}_{LM} \equiv \frac{1}{\mathcal{R}_L^{\phi}}\left(\hat{g}_{LM} - \langle \hat{g}_{LM}^{\rm MF} \rangle\right), \tag{3.47}$$

where $\mathcal{R}_L^{\phi}$ is the non-perturbative response function defined to make the lensing reconstruction unbiased on the full sky [120, 145]. This is defined by the condition

$$\langle \hat{g}_{LM} \rangle = \mathcal{R}_L^{\phi} \phi_{LM} \tag{3.48}$$

that is the same condition of Eq. 3.36.
The $\langle \hat{g}_{LM}^{\rm MF} \rangle$ term is instead the mean field that is the map-level signal expected from mask, noise and other anisotropic features of the map in the absence of lensing. We have to subtract it.
In our analysis, we construct two independent estimates of the mean field for each case considered (both correlated and uncorrelated masks), using two different independent sets of 25 G simulations.

[10] The curl component is expected to be zero to a good approximation, and is zero in the WebSky lensing field by construction.

Figure 3.7 shows a typical mean-field power spectrum (corrected for the response), estimated by cross-correlation of two independent pairs of estates of the mean field for a fixed halo mask to avoid reconstruction noise (computed over 50 G simulations in total). Note that we are constructing our lensing estimators in the null hypothesis of no lensing-mask correlation, as appropriate for quantifying the bias on standard methods (rather than, for example, defining the mean field by averaging over simulations with lensing fields correlated to the fixed mask). Since the mean field depends on the mask, for lensing-correlated masks the mean field is then correlated to the true lensing potential ϕ.

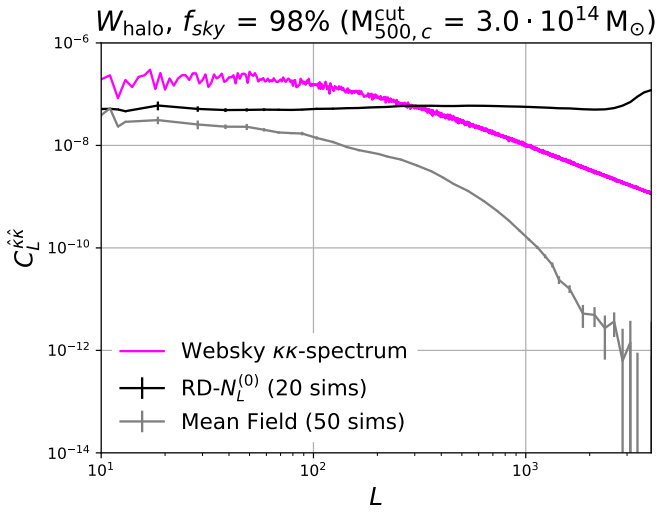

Figure 3.7: *The RD-$N_L^{(0)}$ bias (black, as described in Eq. 3.50) and mean-field power spectrum corrected for the response (grey) for the case of the fixed halo mask described in the plot title. We show (in purple) the WebSky κκ power spectrum on the full sky for comparison.*

From the two mean-field estimates we build two lensing map estimates $\hat{\phi}_1$ and $\hat{\phi}_2$ for each simulation. The estimate of the lensing power spectrum is then obtained from $\hat{\phi}_1$ and $\hat{\phi}_2$ using

$$\hat{C}_L^{\hat{\phi}_1\hat{\phi}_2} \equiv \frac{1}{(2L+1)f_{\rm sky}} \sum_{M=-L}^{L} \hat{\phi}^*_{1,LM}\hat{\phi}_{2,LM}\,, \tag{3.49}$$

where $f_{\rm sky} = \sum_p W_{Xp}/N_{\rm pix}$ is the unmasked sky fraction.

From the above estimator, we then subtract the realization-dependent estimate of the gaussian (disconnected) lensing bias, RD-$N_L^{(0)}$ [149]. Subtracting this term, together with the mean-field subtraction, has the effect of removing the disconnected signal expected from Gaussian fluctuations even in the absence of

lensing [144, 149]. The RD-$N_L^{(0)}$ bias is defined as

$$\text{RD-}N_L^{(0),d} \equiv \langle 4\hat{C}_L^{di} - 2\hat{C}_L^{ij} \rangle \,, \tag{3.50}$$

where angle brackets denote an average over pairs of distinct i, j G simulations. Here $\hat{C}_L^{di}$ is the estimator in Eq. 3.49 with $\hat{\phi}_1$ reconstructed from the d-th CMB realization of the NG set and $\hat{\phi}_2$ using the i-th simulation of the G set; $\hat{C}_L^{ij}$ is instead the estimator in Eq. 3.49 with $\hat{\phi}_1$ and $\hat{\phi}_2$ reconstructed from the i-th and the j-th simulations of the G set, respectively. For each mask (both correlated and uncorrelated), RD-$N^{(0),d}$ is calculated for each NG "data" simulation d using 20 different pairs of 20 independent G simulations. See Fig. 3.7 for a typical estimate.

The estimates of $\hat{\phi}$ are quadratic since they are built using 2-point functions of the CMB fields, thus the cross-spectrum $C_L^{\hat{\phi}\hat{\phi}}$ between estimates of $\hat{\phi}$ is related to the 4-point function (trispectrum) of the CMB. This term includes contributions from disconnected and connected pieces [11], some of which contain information about $C_L^{\phi\phi}$. The remaining part is usually called "noise bias" and has to be removed from $C_L^{\hat{\phi}\hat{\phi}}$.

The mean-field discussed above is one of this noise bias together with the realization-dependent Gaussian noise lensing bias, RD-$N^{(0)}$, that is called "$N^{(0)}$" because it is zeroth-order in $C_L^{\phi\phi}$. It is worth mentioning that, among the noise bias terms, there is also the so-called $N^{(1)}$, that instead depends linearly on $C_L^{\phi\phi}$. We are not considering this noise bias term in our analysis, that has been considered as part of the signal rather than trying to subtract it. For more details on this topic you may look Ref. [119].

Definitely, subtracting RD-$N^{(0)}$, together with the mean-field, has the effect of removing from $C_L^{\hat{\phi}\hat{\phi}}$ all the signals that are not related to $C_L^{\phi\phi}$.

Hence, reaching the fourth step, we define the lensing power spectrum estimator

$$C_L^{\hat{\phi}_1\hat{\phi}_2,\,\mathrm{RD}} = \left(\hat{C}_L^{\hat{\phi}_1\hat{\phi}_2} - \text{RD-}N_L^{(0)}\right), \tag{3.51}$$

This estimator is somewhat biased, so that even for Gaussian uncorrelated simulations $\langle C_L^{\hat{\phi}_1\hat{\phi}_2,\,\mathrm{RD}} \rangle \neq C_L^{\phi\phi}$ because there is a connected $N_L^{(1)}$ signal-dependent contraction [119]. Here, as anticipated, we regard $N_L^{(1)}$ as part of the signal contained in $C_L^{\hat{\phi}_1\hat{\phi}_2,\,\mathrm{RD}}$, and only consider differences between correlated and uncorrelated (rotated) masks. This remains a valid way to quantify the impact

[11] The n-point correlation functions are decomposed into parts, which are purely Gaussian in nature and those which signify departures from Gaussianity. These are also known as connected and disconnected terms because of their representation by respective diagrams (see Ref. [150])

of correlated masking on the total signal.

From the lensing reconstruction field, we also compute the cross-spectrum estimator with the true field

$$C_L^{\hat{\phi}\phi} \equiv \frac{1}{(2L+1)f_{\rm sky}} \sum_{M=-L}^{L} \hat{\phi}^*_{LM}\phi_{LM}\,, \tag{3.52}$$

where $\hat{\phi}$ is the lensing potential estimator (see Eq. 3.47) and ϕ is the true lensing potential field.

The entire pipeline has been repeated 20 times for each mask (both correlated and uncorrelated), choosing each time as data one of the NG simulations, and then averaging over simulations. This reduces Monte Carlo noise from variations of the unlensed CMB, but we cannot average over the cosmic variance of the lensing field since the entire set of NG simulations are based on the same single WebSky simulation that is currently available.

To make a comparison with the results obtained in Sec. *3.4.2*, we plot results for the reconstructed $\hat{\kappa}$ instead of $\hat{\phi}$[12].

The effect of the mean-field and RD-$N_L^{(0)}$ bias on the reconstructed $\hat{\kappa}\hat{\kappa}$-spectra is shown in the first row of Fig. 3.8 as relative differences between the reconstructed $\hat{\kappa}\hat{\kappa}$-spectrum and the true WebSky $\kappa\kappa$-spectrum for three different $W_{\rm halo}$ masks. From left to right, the reconstructed auto-spectra are plotted without mean-field and RD-$N_L^{(0)}$ corrections, then subtracting the mean field only, and finally subtracting both mean field and the RD-$N_L^{(0)}$. The main correction to the reconstructed $\hat{\kappa}\hat{\kappa}$-spectra comes from subtracting the RD-$N_L^{(0)}$ bias. The rise on small scales is related to $N_L^{(1)}$, and could be reduced by subtracting it (but here we regard it as part of the lensing reconstruction signal). The second row of Fig. 3.8 shows the effect of the mean-field subtraction on the relative differences between the cross spectrum $\hat{\kappa}\kappa$ and the true WebSky $\kappa\kappa$-spectrum. The bias induced by the mask on the $\hat{\kappa}\kappa$ spectra is strongly reduced, specially at intermediate scales, when we remove the mean-field term. In all the plots of Fig. 3.8, the full-sky cases are shown in black as reference. Similar results are obtained for all the other masks described in Sec. *3.4.1*.

By construction, the W_X masks are correlated with the CMB lensing potential field. To remove the effects due to this correlation, we subtract to the results obtained using W_X, those obtained using the rotated masks, $W_X^{\rm rot}$. This difference is uncorrelated with the lensing field, but retain all the other non-trivial mode-coupling effects due to cut sky and hole shapes.

[12]Note that $\hat{\kappa}_{LM} \equiv \frac{1}{2}L(L+1)\,\hat{\phi}_{LM}$

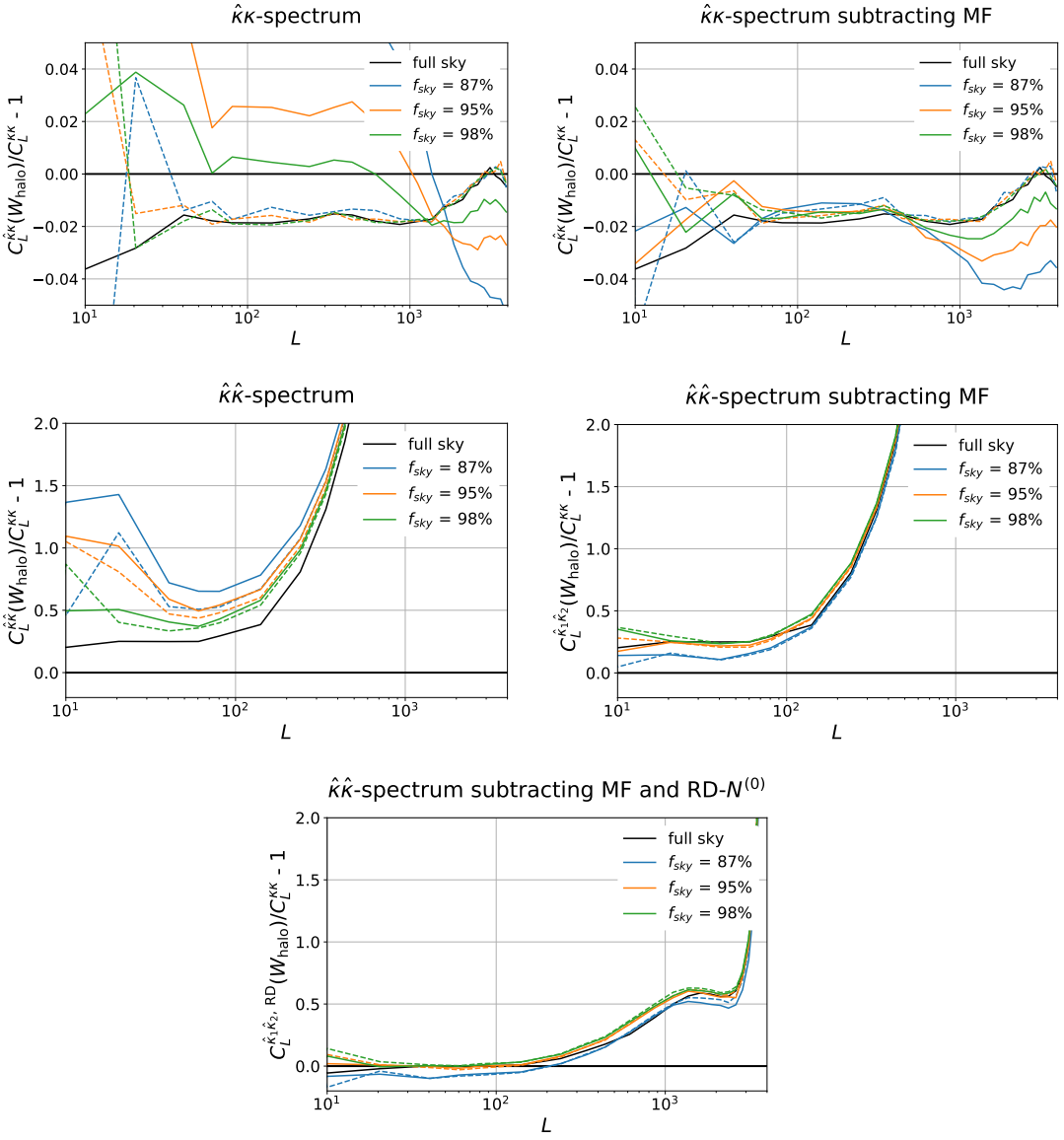

Figure 3.8: *From top left, proceeding in order, the reconstructed auto-spectra subtracting both mean field and the RD-$N_L^{(0)}$, the reconstructed cross-spectra without and with the mean-field subtraction, the reconstructed auto-spectra without mean-field and the RD-$N_L^{(0)}$ corrections, the reconstructed auto-spectra subtracting the mean field but without the RD-$N_L^{(0)}$ correction. The results shown are obtained using the $W_{\rm halo}$ masks,* i.e. *masking lines of sight containing halos with mass $M \geqslant M^{\rm cut}$, see Sec. 3.4.1. The legend shows the corresponding $f_{\rm sky}$. Black lines correspond to the full-sky analysis, where for the cross-correlation the result is dominated by the full-sky non-Gaussian $N^{(3/2)}$ reconstruction bias, and for the auto-spectrum is dominated by $N^{(1)}$. Dashed-lines are the results obtained using the randomly rotated (uncorrelated) masks, $W_{\rm halo}^{\rm rot}$. ($N^{(3/2)}$ is a typical negative bias, $\sim \left(C^{\phi\phi}\right)^{3/2}$, first identified in Ref. [151], where they investigated the effect of large-scale structure non-Gaussianity on CMB lensing reconstruction. See* e.g. *Refs. [120, 152] for more details on this topic.)*

The results of this subtraction are shown in Fig. 3.9 and Fig. 3.10 for the reconstructed auto and the cross spectra, respectively. We show the results for all the (unapodized) masks considered in this analysis, $W_{\rm halo}$, W_κ, $W_{\rm CIB}$, W_y and $W_{\rm rs}$. The error bars have been obtained using the CMB simulations of the G set. We compute the estimators in Eq. 3.49 and Eq. 3.52 for both W_X and $W_X^{\rm rot}$ using as "data" an independent set of 20 G simulations. The errors are then the standard deviations of the differences between correlated and uncorrelated (randomly rotated) masks results.

Figure 3.9 shows the bias as the difference between the reconstructed $C_L^{\hat{\phi}_1\hat{\phi}_2,\,\rm RD}$ (see Eq. 3.51) computed when using correlated and uncorrelated masks as a fraction of the true WebSky $\kappa\kappa$ spectrum. The biases induced by $W_{\rm halo}$ and W_y masks are relevant only at small scales, where we are dominated by errors. For the W_κ and $W_{\rm CIB}$ masks, instead, the bias is roughly constant across all the scales, and it is of $\sim 1-10\%$ level depending of the $f_{\rm sky}$. Clearly, the bias induced by W_κ is larger, since this is the limiting case where the mask is 100% correlated with the κ field (see Sec. *3.4.1* for more details). Finally, the bias induced by $W_{\rm rs}$ is completely negligible even for S4.

As expected, the biases become larger as we increase the masked fraction of the sky. However, the amplitude of the lensing reconstruction biases are significantly reduced with respect to those obtained from directly masking the lensing field in Sec. *3.4.2* (compare Fig. 3.9 with Fig. 3.5). The optimal filtering used by the lensing reconstruction pipeline substantially reduces the fraction of the lensing information that is removed by the mask, both because the filtering recovers some of the CMB modes inside the mask holes, and because the lensing reconstruction itself is able to recover much of the information about lensing modes on scales larger than the hole size.

In the next chapter, we will see if this bias is an effect that should be taken into account by the future ground-based experiments, that will deeply explore the small angular scales of the CMB.

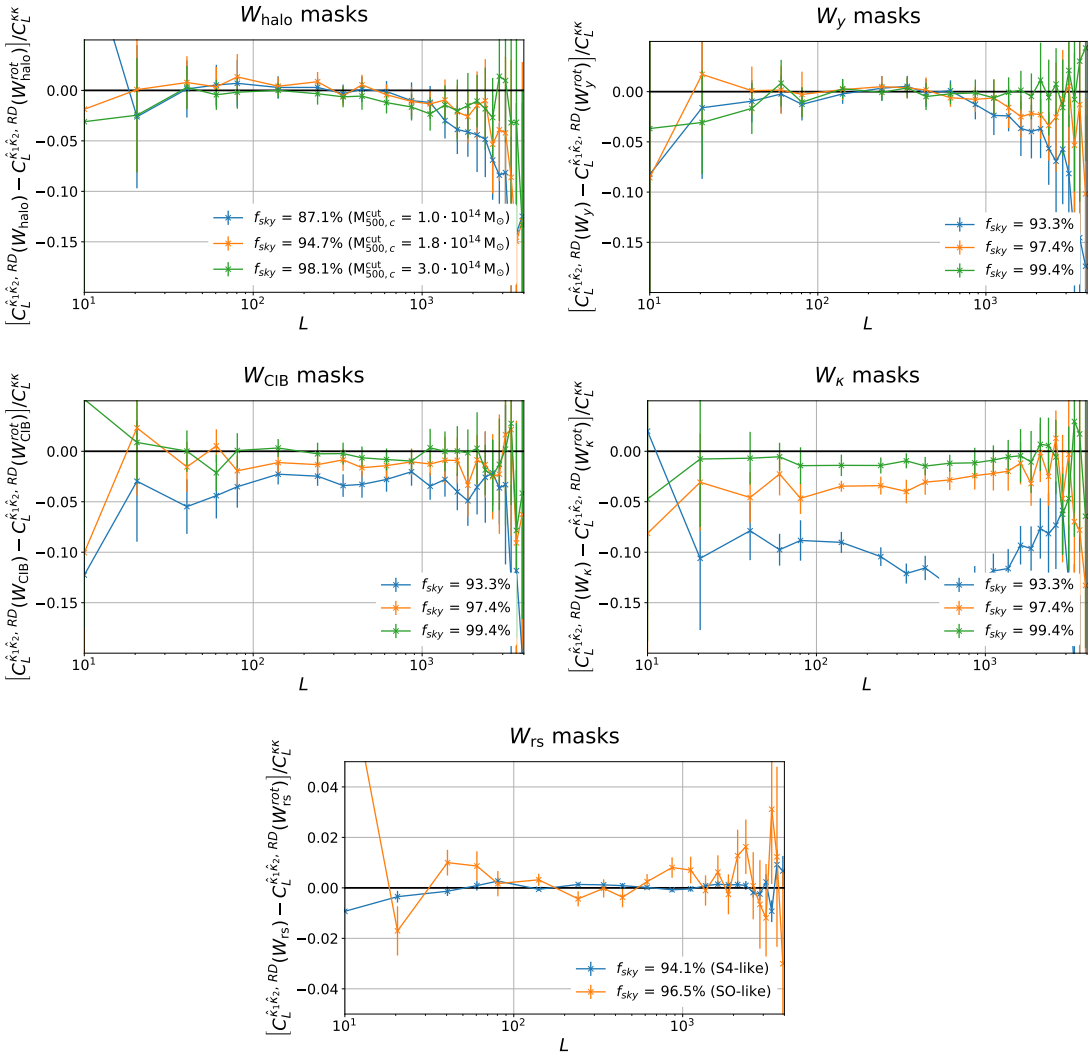

Figure 3.9: *Effect of masking on the CMB lensing convergence auto spectrum, after the lensing reconstruction, defined in Eq. 3.51. The mask biases are computed as differences between correlated and uncorrelated (randomly rotated) masks results. The top left plot shows the result for masking lines of sight containing halos with mass $M \geqslant M^{\rm cut}$, see Sec. 3.4.1, where the legend shows the corresponding $M^{\rm cut}$ in parenthesis. Proceeding, we show the effect of W_y, $W_{\rm CIB}$, W_κ and $W_{\rm rs}$, respectively. The radio source masks $W_{\rm rs}$ are shown for the approximate source count detection limits of the experiments listed in parentheses.*

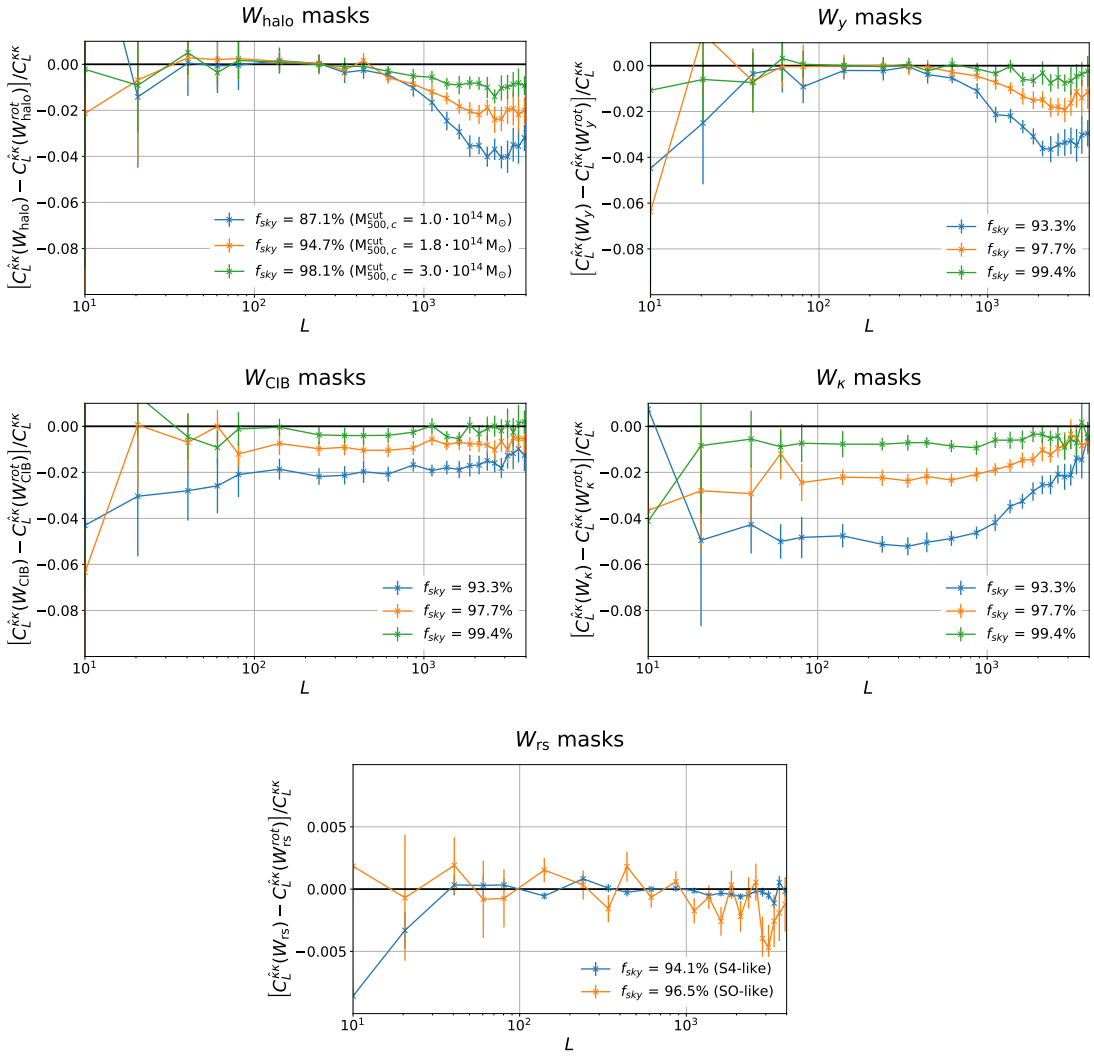

Figure 3.10: *Effect of lensing-correlated masking on the CMB lensing convergence cross spectrum, after the lensing reconstruction. The mask biases are computed as fractional differences between correlated and uncorrelated (randomly rotated) mask results. The top left plot shows the result for masking lines of sight containing halos with mass $M \geqslant M^{\rm cut}$, see Sec. 3.4.1, where the legend shows the corresponding $M^{\rm cut}$ in parenthesis. Proceeding, we show the effect of W_y, $W_{\rm CIB}$, W_κ and $W_{\rm rs}$, respectively. The radio source masks $W_{\rm rs}$ are shown for the approximate source count detection limits of the experiments listed in parentheses.*

3.5 Impact of masking bright extragalactic sources on CMB spectra[13]

In the previous section, we have discussed the impact of masking bright extragalactic sources on the reconstructed lensing potential. In this section, instead, the focus is on the lensed CMB power spectra.

The CMB is lensed by the large-scale structure along the line of sight, and hence some correlation between extra-galactic sources and the CMB lensing convergence is inevitable.

As already discussed in Sec. 3.2, the effect of CMB lensing on the full-sky CMB power spectra is a small smoothing of the peaks in the power spectrum and also an increase of the power in the CMB damping tail. These effects are both quadratic in the lensing.

However, if bright extra-galactic sources are masked, due to the correlation of the source density with the lensing, this will preferentially be removing peaks of the CMB lensing convergence. If the power spectrum is now estimated only using the unmasked area, there can be an additional net effect that is linear in the lensing. The correlation between the deflection angle around convergence peaks is relatively long range, peaking at around 20 arcmin, so every masked peak is associated with a surrounding area of correlated deflection angle that distorts (magnifies) the unlensed CMB. When these peaks are masked, the corresponding regions of demagnifying deflection angle are no longer fully balanced, and the net effect is a scale-dependent net average demagnification.

The effect of a constant demagnification on the CMB is easily understood: it simply shifts angular scales so that everything looks smaller and the CMB power spectrum is therefore shifted towards higher harmonic multipole ℓ. At any given observed ℓ, the CMB power is then the same as that at a lower, pre-demagnification ℓ, which on small scales is larger because the CMB power decreases rapidly with ℓ, leading to an increase in power on small scales (and a corresponding decrease on large scales). The angular acoustic scale is shifted to smaller values, corresponding to the acoustic peaks being shifted to smaller scales, and there is also a strongly oscillatory difference between the power spectra. Due to the steep fall of the CMB spectrum with ℓ in the damping tail, a small constant demagnification can lead to non-negligible signatures on the power spectrum. Plausible numbers may be given as follows: removing 2% of the sky on the convergence peaks would give a mean convergence $\langle\kappa\rangle \approx -0.003$ over

[13] Based on G. Fabbian, M. Lembo at al. [12]

the remaining unmasked area. This leads to a significant 1% change in the temperature spectrum at $\ell \sim 2000$, and larger on smaller scales.
This crude estimate is one motivation to the more careful analysis that we see in the following. In fact, for future data, with the CMB power spectrum measured to nearly cosmic variance out to small scales, any small percent-level corrections would have to be carefully accounted for. We will discuss this topic in the next chapter, see Sec. *4.3.2.5*.
In this constant demagnification picture, the effect would be almost degenerate with a change in the angular diameter distance to the CMB. However, this model is not accurate, since the effective net demagnification is both mode-orientation and scale dependent. The degree-scale acoustic features are only slightly affected because the deflection-convergence correlation peaks on smaller scales, about 20 arcmin. The corresponding effect on the power spectrum is therefore distinctive, and important corrections actually arise mostly from relatively smaller-scale lenses.

A simple leading-order analytic model for the effect is given in [12]. The model accounts for the case of masking the most relevant CMB extragalactic foreground emission correlated with CMB lensing: Poisson point sources (an approximate model for radio sources), and peaks above some threshold in a Gaussian isotropic convergence or foreground field (a model for tSZ sources and a component of the infrared sources).
In the following, we test this model, comparing analytical predictions with results based on realistic numerical simulations. The masks used are those described Sec. *3.4.1* except for $W_{\rm halo}$ and $W_{\rm rs}$ masks. See Sec. *3.4.1* for more details.
Before starting the analysis, we apodized all these masks, with different apodization lengths (reported in the figures) to control ringing effects in harmonic space. The apodization is realized using the C^2 function (effectively a cosine) [142]. This approach follows common practice in CMB analyses including small angular scales and is described by the analytical modeling presented in [12].

The bias induced by W_X is then estimated as the difference between the power spectra obtained using the original (unrotated) mask, and a randomly rotated mask, both using the same NG lensed CMB realizations.
As already discussed in Sec. *3.4.1*, the rotated mask $W_X^{\rm rot}$ is derived from a random rotation of the original W_X so that it is uncorrelated with the lensing field, but retains all the other non-trivial mode-coupling effects due to cut sky and hole shapes. The correlated mask bias evaluated in this way is therefore insensitive to numerical effects only due to an incomplete sky coverage. This procedure is completely analogous to what has been done in the previous section.

For each case, we have masked our simulated CMB map (NG, see Sec. *3.4*) and then we have computed the power spectrum of the masked CMB skies using a pseudo-C_ℓ method as implemented in the NaMaster package [142][14]. This is the same method that we have used in Sec. *3.4.2* to compute the lensing convergence power spectrum from the masked lensing convergence field. We have repeated this procedure on the G set of simulation (see Sec. *3.4*) to compute the error bars of our measurements. Hence, the error bars displayed in the figures do not include any non-Gaussian contribution to the covariance, and, therefore, they represent the error on the average measured on the G simulations.

The results are shown in Fig. 3.11, Fig. 3.12 and Fig. 3.13. We considered only the bias on the temperature power spectra, the effect on polarization is briefly discussed in the next chapter in view of the next-decade experiments.

Overall, the semi-analytical model describes the effect on large scales up to $\ell \approx 3000$ remarkably well for all the configurations considered here. On smaller scales, the agreement between simulations and predictions gets worse, but a better fit can be achieved using the non-perturbative calculations discussed in Appendix B of [12].

Precisely, in Fig. 3.11 we show the measurements of the correlated mask bias from simulations as data points, together with the semi-analytical perturbative prediction described in [12]. For this case, we have also considered the bias measured on CMB simulations lensed with a deflection field with an inverted sign (NG$^-$ set). As we can see the bias has the opposite sign compared to the case of the top panel on scales where the leading order predictions are accurate. This is due to the fact that the leading-order effect of the mask correlation is linear in the lensing.

Fig. 3.12 shows the correlated mask bias measured from simulations adopting the same C^2 function of the previous section and using two different apodization lengths ($3'$ and $12'$), again compared to the semi-analytic perturbative predictions. As for the case of the W_κ mask, the theoretical predictions match the simulation measurements very well up to scales $\ell \lesssim 2500$. The amplitude of the mask bias at small scales has a peak and then decreases on scales smaller than the characteristic scale imposed by the mask hole size. When masking the CIB peaks without applying any smoothing of the CIB maps prior to thresholding (orange lines and points in Fig. 3.12), there are many very small holes due to the relatively blue shape of the CIB angular power spectrum. A larger apodization scale increases

[14] As we discuss in Ref. [12], alternative estimators capable of effectively recovering the information inside the holes of the mask would give different results and potentially have a reduced effect.

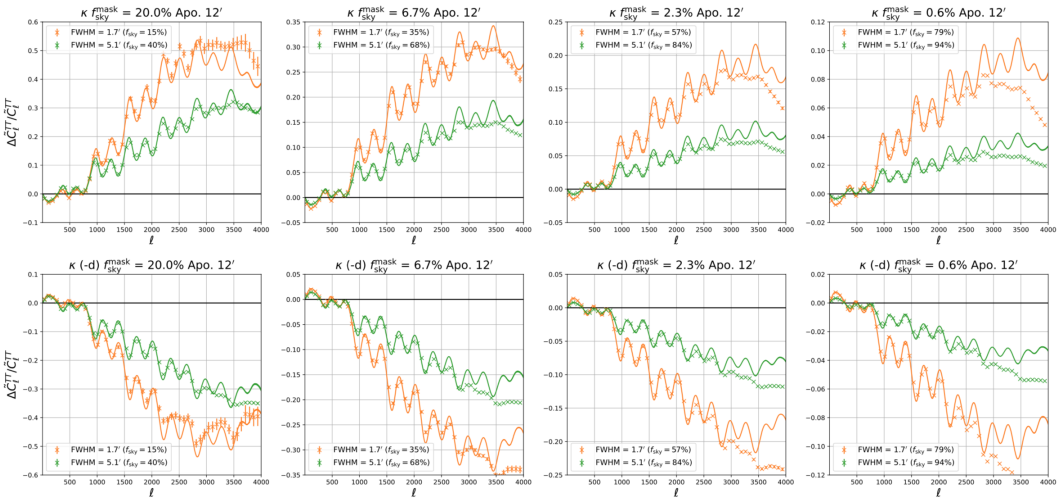

Figure 3.11: *Bias induced by masking the lensed CMB temperature with a foreground mask generated by thresholding the WebSky CMB lensing κ field after smoothing to a scale of $1.7'$ (orange) or $5.1'$ (green). In the top panel data points measured from simulations are compared to perturbative semi-analytic predictions in solid. The semi-analytic model is discussed in Ref. [12]. Results obtained by masking different sky areas are shown in different columns. We apodized each mask with an apodization length of 0.2 deg. The masked area prior to apodization is reported in the title and the effective sky area after apodization used to compute C_ℓ^{TT} is shown in the legend. The bottom panel shows the bias measured on CMB simulations lensed with a deflection field with an inverted sign (NG^- set).*

the fraction of sky that is masked for fixed underlying hole distribution, increasing the bias on larger scales (where noise and foreground power is lower, and therefore potentially more important in the analysis of real data).

Although masks on real data are usually not designed to remove peaks of CIB emission per se, the case where we masked the highest peaks so that only the 0.6% of the sky is removed is of particular interest. Infrared sources that are local dusty galaxies are expected to have a low correlation to CMB lensing due to the short path length. However, chance radial alignments of sources for the CIB, high-redshift protoclusters, and lensed high-redshift galaxies, may make up an important fraction of the point sources detected in CMB maps [153, 154], all of which may have a significant correlation to the line of sight CMB lensing [155–157]. The brightest of these objects are usually removed by point sources masks. Despite the reduced masked sky area, the bias in this case is potentially significant and could lead to important detectable effects as we will see in the following chapter.

In Fig. 3.13 we show the comparison of the theoretical predictions with the

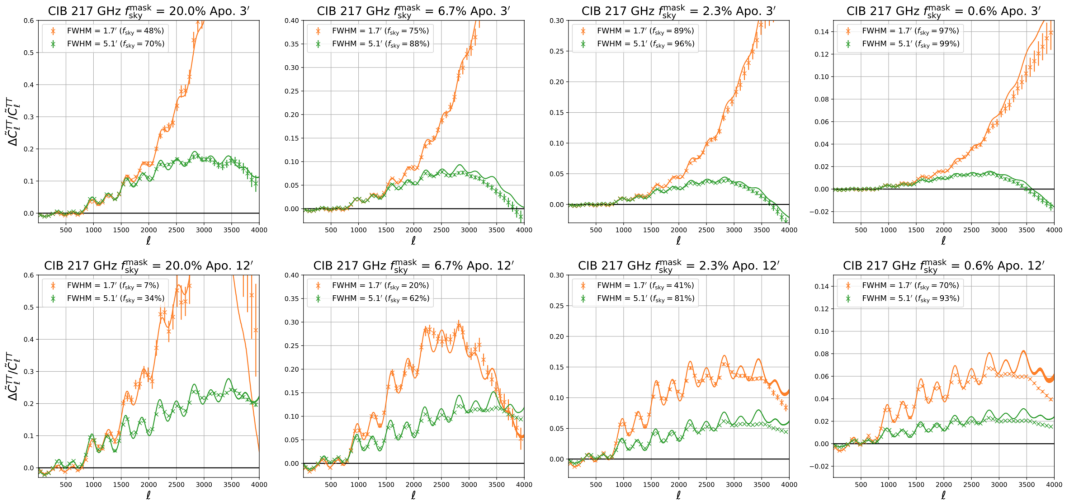

Figure 3.12: *Bias induced by masking the lensed CMB temperature with a foreground mask generated by thresholding the CIB map at 217 GHz of the WebSky suite after smoothing to a scale of* $1.7'$ *(orange) or* $5.1'$ *(green). Data points show the measurements of the bias on simulations while perturbative semi-analytic predictions are shown in solid lines. The semi-analytic model is discussed in Ref. [12]. Masks with different sky fractions are shown in different columns. The top row shows results with* $3'$ *mask apodization tapering function, the bottom row using a larger* $12'$ *apodization (giving substantially larger masked areas as shown in the legend).*

simulation measurements for the W_y case.

Compared to the case of κ and CIB thresholding, the agreement between the perturbative model and simulation results is worse, with significant discrepancies observed already at multipoles $\ell \approx 2500$ and reaching a factor between 2 to 4 at $\ell \approx 4000$ in particular when only the highest peaks are masked (right panel). For more aggressive masks where a significant fraction of the peak is masked however the agreement (left panel) between simulations and analytic predictions improve substantially. Since the bulk of the tSZ emission is localized in highly clustered and dense regions at relatively low redshift for a threshold that is sufficiently small, W_y contains holes with a larger angular size around the overdensity corresponding to the galaxy cluster. The masked region at each cluster may therefore remove a significant area of high lensing signal associated with the cluster (rather than just a small area at the very peak of the overdensity). We therefore checked whether higher-order effects beyond the linear term modelled in the previous section could be responsible for the observed discrepancy, for example from the reduction in lensed CMB signal over the cluster mask.

To test higher-order effects we constructed another set of lensed CMB simulations with the same masks as the NG set, but lensed with a deflection field with an inverted sign. We refer to this set of simulations as NG^- in the following. Since the leading-order effect of the mask correlation is linear in the lensing, in these maps it should have opposite sign (see Fig. 3.11). Higher-order effects that are quadratic or involve a higher even power of the lensing can be isolated on simulations using the half sum of the mask biases measured on the NG and NG^- sets using the same threshold mask for both NG and NG^-. In the bottom panel of Fig. 3.13 we show that higher-order effects induce a negative correction to the leading order predictions that explains the discrepancy. When only a reduced fraction of the sky is masked, the higher-order effects become important at $\ell \approx 2000$ and suppress the bias by a factor of 4 compared to the leading order predictions at $\ell \approx 4000$. In the limiting case where we mask a large fraction of the sky, the corrections become relevant at progressively smaller angular scales and their relative importance is reduced.

Corrections that are quadratic in the lensing largely account for a change in the underlying lensed CMB power spectrum due to the masking of areas where the lensing is larger. An approximate analytic estimate of this higher-order bias can be obtained by computing the lensed CMB power spectrum (approximately a convolution of the CMB lensing and the unlensed CMB power spectra) where the CMB lensing power spectrum is derived from the lensing convergence power spectrum computed over the masked sky using the W_y mask. Fig. 3.13 shows that this simple model describes the effect seen in the simulations quite accurately (a more accurate analytic calculation, including all orders for a Gaussian foreground, is described in the Appendix B of [12]).

To conclude, we have seen that these kind of masks correlated with the lensing signal, when applied on the observed CMB maps, can induce a bias in the lensed temperature power spectra recovered from the unmasked area. This bias is clearly relevant on small scales. We will discuss these results in view of the next-decade ground-based CMB experiments in the next chapter.

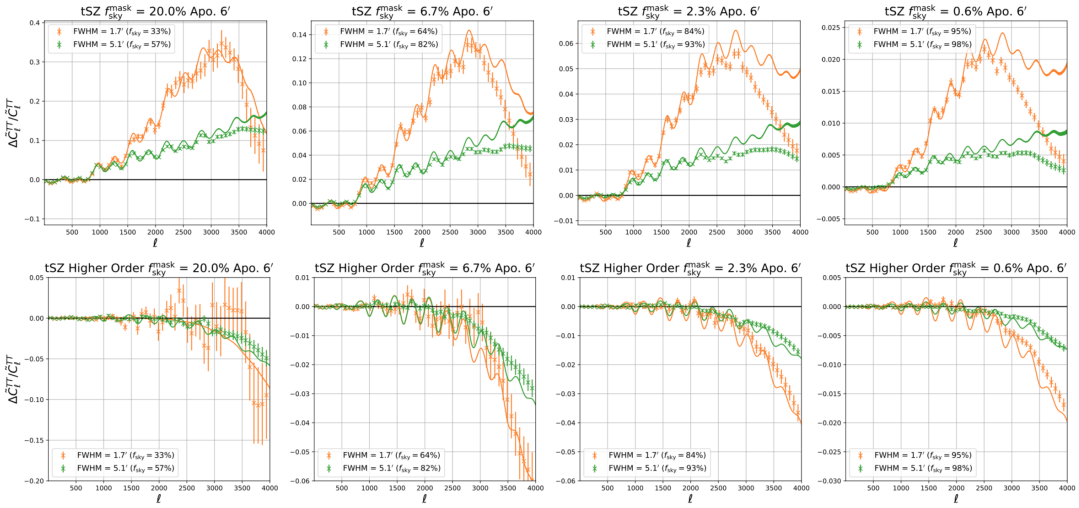

Figure 3.13: *Top: Bias induced by masking the peaks of the tSZ emission (after smoothing to a scale of* $1.7'$*, orange, or* $5.1'$*, green) on the lensed CMB temperature as measured on simulations compared to perturbative leading order analytical predictions (solid line). The semi-analytic model is discussed in Ref. [12]. Masks with different sky fractions are shown in different columns. We adopted a* $6'$ *apodization length for the mask tapering function. Bottom: Measurement on simulations of the even higher-order biases responsible for the discrepancies between the leading order predictions and the simulation results shown in the upper panel. Approximate analytical predictions of the second-order terms are shown as solid lines.*

4

Prospects for next-generation CMB experiments

Since its discovery 55 years ago, the cosmic microwave background radiation has played a primary role for cosmology. CMB radiation has been a powerful tool to confirm or rule out cosmological models and to strengthen our understanding of the fundamental physical laws of the Universe we live in. As we have seen in Chpt. 1, the physics behind a CMB map is straightforward and well understood. Starting with the COBE detection, the mapping of the primordial temperature and polarization anisotropies, produced by the WMAP and, with higher precision, Planck satellites, has allowed us to characterize the initial cosmological perturbations at about the percent level and to constrain with unprecedented accuracy the six parameters governing ΛCDM model.
Today, even after more than 50 years of intensive studies and observations, more accurate measurements can still provide new information improving our knowledge about the origin and the composition of our Universe.
Despite the incredible achievements of the last few years, ΛCDM model is not able to complete our understanding of the Universe, which is still based on unknown entities like dark energy, dark matter and the inflaton.

The aim of this last chapter is to provide, on one hand, an overview of the state-of-the-art CMB measurements and what we can (or not) extract from them, Sec. *4.1* and Sec. *4.2*, and, on the other hand, a hint of the near-future *plans*, Sec. *4.3*, placing our works in this context.

4.1 State of the art

Before addressing questions on *what comes next*, we have to make the point on *where we stand*. In Fig. 4.1, the most updated compilation of CMB data is shown. We can appreciate the amazing concordance between all the spectra from different datasets. The Planck measurements [6] are in blue, compared with those of other, contemporary, experiments: WMAP data from Ref. [158], ACT and ACTpol data from Refs. [159–161], SPT and SPTpol data from Refs. [162–164], PolarBear data from Ref. [165] and BICEP2/Keck data from Refs. [166, 167]. Planck dominates the temperature and the E-mode polarization power spectra up to $\ell \sim 1000$. For higher multipoles, up to $\ell \sim 3000$, as well as B-mode polarization, the ground-based experiments, with higher angular resolution and sensitivity, provide better measurements. Regarding the lensing power spectrum, the next generation of experiments is going to get better measurements.

Definitely, Planck mission has exhausted the information content of the CMB temperature anisotropies, reaching the cosmic variance limit down to ~ 5 arcmin angular scales, but we have only begun to tap the information encoded in CMB polarization, CMB lensing and other secondary effects.
Before moving forward, let us briefly review the outstanding Planck achievements, which include temperature and linear polarization maps. The state of the art of the CMB circular polarization has been already discussed in Sec. *2.2*.

4.1.1 Planck legacy

Planck was the third-generation space mission dedicated to measurements of CMB anisotropies. It was launched by ESA in May 2009 and operated until October 2013. Planck data, already shown in Fig. 4.1, are in remarkable agreement with the standard spatially-flat 6-parameter ΛCDM cosmology, having a power-law spectrum of adiabatic scalar perturbations. In Sec. *1.4*, even more in Fig. 1.11, we have indeed seen how the temperature power spectrum is sensible to the ΛCDM parameters.
In Fig. 4.2, the 68% confidence intervals for the base-ΛCDM parameters are shown. These constraints have been obtained combining Planck CMB power spectra with CMB lensing reconstruction and BAO (baryon acoustic oscillation). Alongside the six baseline-parameters, we see the constraints for the derived parameters, such as the Hubble constant, H_0, the matter density, Ω_m, and the matter fluctuation amplitude, σ_8. As already discussed in Sec. *1.4*, the ΛCDM model has indeed only six independent parameters, the others can be inferred from them.

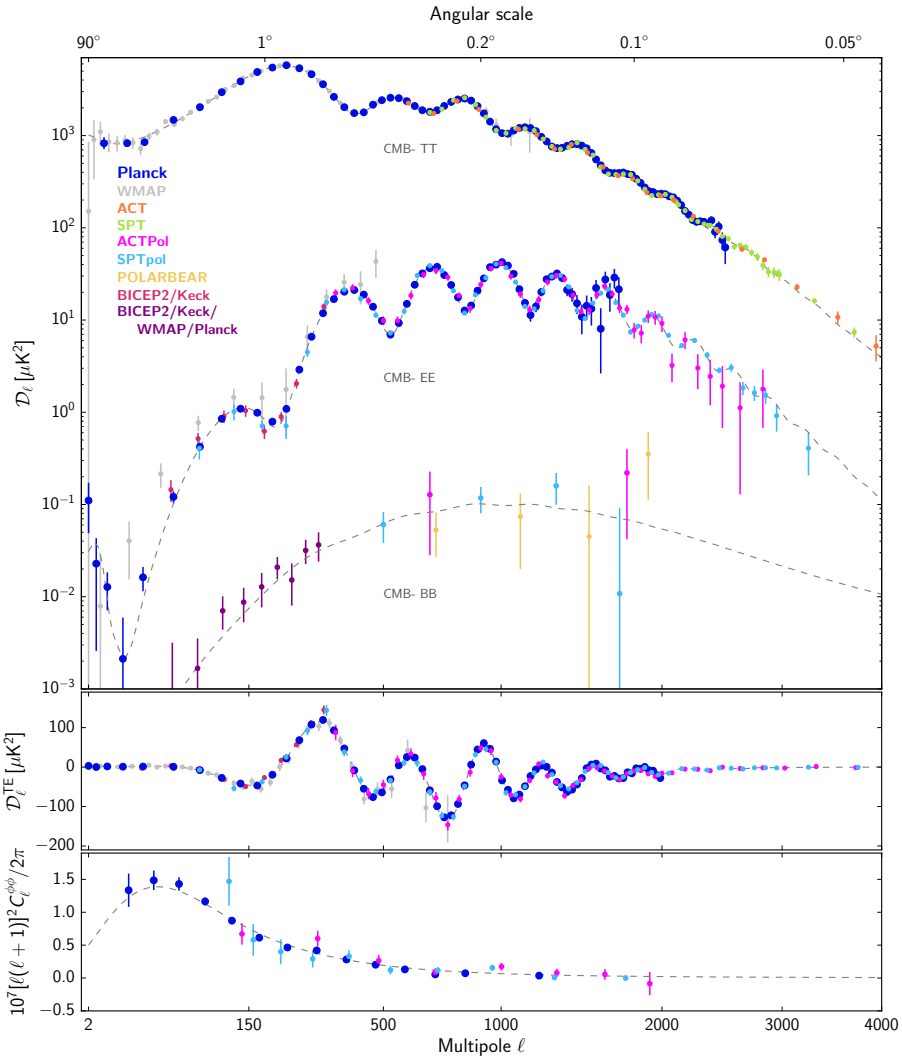

Figure 4.1: *Compilation of recent CMB angular power spectrum measurements. From top to bottom, power spectra of the temperature and E-mode and B-mode polarization signals, the cross-correlation spectrum between T and E and the lensing deflection power spectrum. Different colors correspond to different experiments, each retaining its original binning. For Planck, ACTPol, and SPTpol, the EE points with large error bars are not plotted (to avoid clutter). The dashed line shows the best-fit ΛCDM model to the Planck temperature, polarization, and lensing data. Credits: Planck Legacy Archive [6].*

Using only these 6 baseline-parameters, a very good fit of the temperature power spectrum is achieved. Hence, despite the many extensions that have been explored, there seems to be no statistically significant evidence for the need to add more parameters.

Parameter	TT+lowE 68% limits	TE+lowE 68% limits	EE+lowE 68% limits	TT,TE,EE+lowE 68% limits	TT,TE,EE+lowE+lensing 68% limits	TT,TE,EE+lowE+lensing+BAO 68% limits
$\Omega_b h^2$	0.02212 ± 0.00022	0.02249 ± 0.00025	0.0240 ± 0.0012	0.02236 ± 0.00015	0.02237 ± 0.00015	0.02242 ± 0.00014
$\Omega_c h^2$	0.1206 ± 0.0021	0.1177 ± 0.0020	0.1158 ± 0.0046	0.1202 ± 0.0014	0.1200 ± 0.0012	0.11933 ± 0.00091
$100\theta_{MC}$	1.04077 ± 0.00047	1.04139 ± 0.00049	1.03999 ± 0.00089	1.04090 ± 0.00031	1.04092 ± 0.00031	1.04101 ± 0.00029
τ	0.0522 ± 0.0080	0.0496 ± 0.0085	0.0527 ± 0.0090	$0.0544^{+0.0070}_{-0.0081}$	0.0544 ± 0.0073	0.0561 ± 0.0071
$\ln(10^{10} A_s)$	3.040 ± 0.016	$3.018^{+0.020}_{-0.018}$	3.052 ± 0.022	3.045 ± 0.016	3.044 ± 0.014	3.047 ± 0.014
n_s	0.9626 ± 0.0057	0.967 ± 0.011	0.980 ± 0.015	0.9649 ± 0.0044	0.9649 ± 0.0042	0.9665 ± 0.0038
H_0 [km s^{-1} Mpc^{-1}]	66.88 ± 0.92	68.44 ± 0.91	69.9 ± 2.7	67.27 ± 0.60	67.36 ± 0.54	67.66 ± 0.42
Ω_Λ	0.679 ± 0.013	0.699 ± 0.012	$0.711^{+0.033}_{-0.026}$	0.6834 ± 0.0084	0.6847 ± 0.0073	0.6889 ± 0.0056
Ω_m	0.321 ± 0.013	0.301 ± 0.012	$0.289^{+0.026}_{-0.033}$	0.3166 ± 0.0084	0.3153 ± 0.0073	0.3111 ± 0.0056
$\Omega_m h^2$	0.1434 ± 0.0020	0.1408 ± 0.0019	$0.1404^{+0.0034}_{-0.0039}$	0.1432 ± 0.0013	0.1430 ± 0.0011	0.14240 ± 0.00087
$\Omega_m h^3$	0.09589 ± 0.00046	0.09635 ± 0.00051	$0.0981^{+0.0016}_{-0.0018}$	0.09633 ± 0.00029	0.09633 ± 0.00030	0.09635 ± 0.00030
σ_8	0.8118 ± 0.0089	0.793 ± 0.011	0.796 ± 0.018	0.8120 ± 0.0073	0.8111 ± 0.0060	0.8102 ± 0.0060
$S_8 \equiv \sigma_8 (\Omega_m/0.3)^{0.5}$	0.840 ± 0.024	0.794 ± 0.024	$0.781^{+0.052}_{-0.060}$	0.834 ± 0.016	0.832 ± 0.013	0.825 ± 0.011
$\sigma_8 \Omega_m^{0.25}$	0.611 ± 0.012	0.587 ± 0.012	0.583 ± 0.027	0.6090 ± 0.0081	0.6078 ± 0.0064	0.6051 ± 0.0058
z_{re}	7.50 ± 0.82	$7.11^{+0.91}_{-0.75}$	$7.10^{+0.87}_{-0.73}$	7.68 ± 0.79	7.67 ± 0.73	7.82 ± 0.71
$10^9 A_s$	2.092 ± 0.034	2.045 ± 0.041	2.116 ± 0.047	$2.101^{+0.031}_{-0.034}$	2.100 ± 0.030	2.105 ± 0.030
$10^9 A_s e^{-2\tau}$	1.884 ± 0.014	1.851 ± 0.018	1.904 ± 0.024	1.884 ± 0.012	1.883 ± 0.011	1.881 ± 0.010
Age [Gyr]	13.830 ± 0.037	13.761 ± 0.038	$13.64^{+0.16}_{-0.14}$	13.800 ± 0.024	13.797 ± 0.023	13.787 ± 0.020
z_*	1090.30 ± 0.41	1089.57 ± 0.42	$1087.8^{+1.6}_{-1.7}$	1089.95 ± 0.27	1089.92 ± 0.25	1089.80 ± 0.21
r_* [Mpc]	144.46 ± 0.48	144.95 ± 0.48	144.29 ± 0.64	144.39 ± 0.30	144.43 ± 0.26	144.57 ± 0.22
$100\theta_*$	1.04097 ± 0.00046	1.04156 ± 0.00049	1.04001 ± 0.00086	1.04109 ± 0.00030	1.04110 ± 0.00031	1.04119 ± 0.00029
z_{drag}	1059.39 ± 0.46	1060.03 ± 0.54	1063.2 ± 2.4	1059.93 ± 0.30	1059.94 ± 0.30	1060.01 ± 0.29
r_{drag} [Mpc]	147.21 ± 0.48	147.59 ± 0.49	146.46 ± 0.70	147.05 ± 0.30	147.09 ± 0.26	147.21 ± 0.23
k_D [Mpc^{-1}]	0.14054 ± 0.00052	0.14043 ± 0.00057	0.1426 ± 0.0012	0.14090 ± 0.00032	0.14087 ± 0.00030	0.14078 ± 0.00028
z_{eq}	3411 ± 48	3349 ± 46	3340^{+81}_{-92}	3407 ± 31	3402 ± 26	3387 ± 21
k_{eq} [Mpc^{-1}]	0.01041 ± 0.00014	0.01022 ± 0.00014	$0.01019^{+0.00025}_{-0.00028}$	0.010398 ± 0.000094	0.010384 ± 0.000081	0.010339 ± 0.000063
$100\theta_{s,eq}$	0.4483 ± 0.0046	0.4547 ± 0.0045	0.4562 ± 0.0092	0.4490 ± 0.0030	0.4494 ± 0.0026	0.4509 ± 0.0020

Figure 4.2: *Parameter 68% intervals for the base-ΛCDM model from Planck CMB power spectra, in combination with CMB lensing reconstruction and BAO [55].*

One of the most significant findings, first made by WMAP satellite at modest statistical significance, is that the primordial power spectrum is not exactly scale-invariant: in other words, $n_s \neq 1$. This means that, at least at the sensitivity level of presently available data, the initial conditions of the Universe are described by just two numbers: the amplitude of primordial curvature perturbations, A_s, and its spectral index n_s. With this information, our capability to discern among different inflationary models is really low.

Only upper limits are available on other quantities that can provide more detailed information about inflation such as the "running" of the spectral index of scalar perturbations, *i.e.* its dependence on the scale of perturbations, $\mathrm{d}n_s/\mathrm{dln}k$, the amplitude, A_t, and spectral index, n_t, of tensor perturbations or better the tensor to scalar ratio $r = A_t/A_s$, just to mention a few. For example, combining Planck data with data from BAO, BICEP2, and Keck Array data, Planck collaboration places a limit on the tensor-to-scalar ratio $r_{0.002} < 0.06$. Crucial information is expected to be obtained from primordial B-mode polarization. In this sense, near future CMB experiments can provide more detailed information about the physics of the inflationary era.

Despite this almost perfect picture, the improvement in estimating the uncertainties has also led to tensions between the preferred values of some cosmological parameters. Precisely, the tension is between the value obtained from fits to cosmological data sets assuming ΛCDM model and direct measurements of these

cosmological parameters.
There is a 4.4σ tension in the preferred value of the Hubble constant (as shown in Fig. 4.2, Planck provides a value of $67.37 \pm 0.54\,\mathrm{kms}^{-1}\mathrm{Mpc}^{-1}$ while the cosmological distance ladder measurement by SH0ES a value of $74.02 \pm 1.42\,\mathrm{kms}^{-1}\mathrm{Mpc}^{-1}$ [168]), followed by the $2-3\sigma$ tension on $S_8 = \sigma_8\sqrt{\Omega_m/0.3}$, which measures matter clustering, between Planck and weak lensing experiments and clustering abundance surveys [169–171].
The disagreement might be explained by an underestimated or unmodeled systematic (see e.g. Refs. [172–177]). Nevertheless, since these tensions exist between multiple data sets breaking down the cosmological epoch, they might suggest the need for physics beyond the standard model of cosmology. There are many attempts to solve these tensions, please see Refs. [178–190] (this is definitely not a comprehensive list).

Additionally, it is worth mentioning the $\sim 2.5\sigma$ tension between the preferred values of parameters like the physical cold dark matter density, ω_c, between Planck TT $\ell \leq 1000$ and Planck TT $\ell > 1000$, which can be resolved by allowing the amplitude of the lensing contribution to the CMB power spectra to vary. This consists in extending ΛCDM to include a phenomenological amplitude, A_L, which rescales the amplitude of the lensing power spectrum. $A_L = 1$ corresponds to the expected weak lensing scenario [191].

Regarding extensions to the ΛCDM model, it is worth mentioning the already anticipated (see Sec. *2.1*) latest constraints on the cosmic birefringence. Regarding anisotropic birefringence, in Ref [87], using Planck 2018 CMB polarized data, no evidence of birefringence was found within the error budget, obtaining as constraints $A_{\Delta\delta\chi\Delta\delta\chi} < 0.104\,\left[\mathrm{deg}^2\right]$ and $A_{\Delta\delta\chi T} = 1.50^{+2.41}_{-4.10}\,[\mu K \cdot \mathrm{deg}]$ both at 95% C.L.. However, these limits, especially the latter, are competitive in constraining a few early dark energy models. This kind of models have been recently proposed to alleviate the H_0 tension, see *e.g.* [183].
The latest constraints on isotropic birefringence using Planck 2018 CMB polarized data are instead reported in Ref. [83]. As already discussed in Sec. *2.1*, the novelty lies in the independent treatment of the systematic error using Galactic foreground emission. The quoted value for $\Delta\bar{\chi}$ is $0.35 \pm 0.14\,\mathrm{deg}$, which excludes $\Delta\bar{\chi} = 0$ by 99.2 % C.L.. This measurement is still consistent with the result found by Planck collaboration with the 2015 data release [81, 82], but the uncertainty has been remarkably reduced, since it no longer contains the ground calibration uncertainty.

This section is a very short summary of the achievements reached by Planck. Please see Refs. [6, 10, 55] for more details.

4.2 Open questions

The ΛCDM model provides an extremely good fit of the data, so even though, as discussed in the previous section, there exists some tensions, deviations from the model are not expected to be too drastic from the phenomenological point of view, even if they can be conceptually really different. We can therefore consider the ΛCDM model as an approximation to a more realistic scenario that still needs to be fully understood.

To emerge from the fog, in the next decades, the target of both theorists and experimentalists will be to answer the following questions:

- What is the nature of dark energy and dark matter?
- Did the Universe have an inflationary period? How did it happen? What is the level of non-gaussianities?
- Is the Universe flat or closed?
- How much does a neutrino weigh? Is there any sterile neutrino?
- Do we actually need physics beyond the standard model Model (SM) of particle physics?
- What is the origin of baryogenesis?
- What is the origin of the sharpened tension in the observed and inferred values of H_0 and S_8? And what about A_L? Is there an underlying new physics that can accommodate this tension?

This (definitely not complete) list of questions can be largely reduced (or at least modified with new questions) in the next decade, thanks to a coordinated effort from the side of theory, data analysis, and observation.

The next decade will provide a compelling and complementary view of the cosmos through a combination of upgraded experiments, next-generation space-missions and facilities on Earth. A wealth of data, not only CMB observations, mainly polarization, but also LSS measurements, will be available soon. An optimal combination of cosmological and astrophysical datasets will bring us any closer to *understand the detailed nature of the Universe.*

4.3 Next-decade CMB experiments

Next-generation projects have the makings of solving some questions listed above, providing a dramatic leap forward in our understanding of the *cosmos*. The focus will be on CMB polarization, measuring E-mode polarization down to the cosmic variance limit over a wide range of angular scales and pushing the search for primordial B-modes down to a tensor-to-scalar ratio $r \sim 0.001$.

Several projects have already been planned to start over the next decade. Among them, let us mention LiteBIRD, the Simons Observatory and CMB-Stage4.

LiteBIRD is satellite-mission proposed by JAXA (the japanese equivalent of ESA) in early 2015 and is expected to be launched in the middle of the 2020s. It is designed to measure CMB temperature and polarization anisotropies over the full sky in the multipole range $2 \leq \ell \leq 200$.

LiteBIRD, in a 3-year mission, will map the entire sky in 15 microwave frequency bands from 34 to 448 GHz, using two telescopes, a Low Frequency Telescope (LFT) and a High Frequency Telescope (HFT). Each telescope is equipped with a half-wave plate system for polarization signal modulation and a focal plane filled with polarization-sensitive TES bolometers [192].

Unlike Planck, LiteBIRD is designed and optimized for measuring polarization. Moreover, as already mentioned in Chpt. 2, studying the non-idealities of the HWP we can constrain the amount of circular polarization in the CMB radiation.

The Simons Observatory (SO) is a new CMB ground-based experiment, and it is expected to start observations in the early 2020s. SO is located in the Atacama Desert (in Chile), sharing the site with other ground-based experiments, such as ACT, CLASS and the planned CMB-Stage 4.

The SO collaboration, that is made of more than 200 scientists from around 40 institutions, is building a Large ApertureTelescope (LAT) with a 6-meter primary and three 0.5-meter refracting Small Aperture Telescopes (SATs). The initial plan is to deploy a total of around 60 000 detectors, approximately evenly split between the LAT and the set of SATs. The plan for sky coverage is to observe $\sim 40\%$ of the sky with the LAT, and $\sim 10\%$ with the SATs. This amount of detectors represents a record: it is about more than an order of magnitude over the size of current microwave detector arrays, and moreover, it is more than the number of total detectors deployed by all previous microwave background experiments combined together. With this equipment, SO will observe the sky in six frequency bands: 27, 39, 93, 145, 225 and 280 GHz [8].

As for LiteBIRD, primordial B-mode polarization at large angular scales is the

main target. Additionally, instead of LiteBIRD, SO has the capability to explore the small angular scales, ranging from an arcmin to tens of degrees. This will allow us to shed light on the phenomena affecting the damping tail (high-ℓ region) of the CMB power spectra both in temperature and in polarization, as well as the growth of structure revealed by CMB lensing.

CMB-Stage 4 (CMB-S4) is another CMB ground-based experiment, covering more than 50% of the sky, over the frequency range $\sim 20 - 280$ GHz [9]. The construction phase is planned to start in 2021 [193]. CMB-S4 collaboration targets to deploy $\sim 500\,000$ detectors, so more than an order of magnitude over the SO number. Again, these detectors will be almost equally split among LAT and SATs, and they will be located in both the Atacama Desert and the South Pole.
Small telescopes have the role of setting the most sensitive constraints on the degree scale, *i.e.* on the recombination peak of polarization power spectra. Large telescope, instead, will have primary apertures in the $2 - 10\,m$ diameter range, in order to achieve angular scales between $1 - 4$ arcminutes: CMB-S4 will provide us measurements of CMB power spectra up $l_{max} \sim 5000$ [194].

4.3.1 Satellite vs ground-based

From the above descriptions, the first thing that stands out, comparing satellite missions with ground-based experiments, is that measurements from Earth have the advantage of employing large aperture telescopes, with diameters of several meters. SO and CMB-S4 can achieve much higher multipoles, *i.e.* small angular scales. In principle, a large telescope could be launched in space too. Nevertheless, this would require exorbitant cost. Large ground-based programs, instead, can target amazing sensitivities and angular resolutions with a far lower amount of money. They can operate for much longer times and are able to easily take advantage of the latest technological advances.

On the other hand, a crucial point is that ground-based experiments can cover a limited number of frequency bands due to atmospheric emission. This limits their capability of removing foreground emissions (see Ref. [195] for more details), and limits the observations only to the cleanest sky regions, *i.e.* reduced sky coverage than satellite mission.

It is therefore necessary a synergy between satellite-based and ground-based measurements. In the next-decade SO and, even more, CMB-S4 will provide us the definitive CMB measurements at angular scales from tens of degrees to arc minutes, while LiteBIRD will cover the largest angular scales, corresponding at multipoles $\ell < 20$.

4.3.2 Science goals

4.3.2.1 Tensor-to-scalar ratio

The first and probably major science goal, that the aforementioned experiments will target, is the measurements of the imprint of primordial gravitational waves on the CMB polarization pattern. In other words, the aim is to measure or, possibly, to set an upper bound on the tensor-to-scalar ratio, r. Both LiteBIRD and CMB-S4 will set an upper limit of $r < 0.002$ at 95% C.L., if they do not detect any signal. In any case, this is a huge improvement over current limits, and would significantly advance our understanding of inflation, ruling out broad classes of inflationary models. For a detailed discussion, see Refs. [8, 9, 192, 193]. Of course, if they will instead effectively measure r, the impact of such a discovery will be enormous. It would constitute direct evidence for cosmic inflation , and, as already discussed in Sec. *1.4*, we can infer from r also information on the energy scale of inflation.

4.3.2.2 Cosmic Birefringence and GFE

As a byproduct of this primary scientific target, the future CMB experiments will significantly improve constraints on cosmic birefringence. In Fig. 4.3, we show the corresponding expected 68% C.L. bounds on the amplitude of the scale-invariant rotation-angle spectrum A^{χ} (in Fig. 4.3, $\chi \equiv \alpha$). The current bound derived using Planck 2018 data [87] is close to the green line. The improvement will be remarkable. As already discussed in Chpt. 2, the prospect of accurate measurements of this effect presents an opportunity for probing physics beyond the standard model, such as parity-violating axion-photon interactions. In Ref. [196], the bound on A^{χ} is indeed translated into in a bound on the axion-photon coupling,$f^{-}1_{a}$, finding for CMB-S4 $f_a \geq$ few $\times 10^3 V$, where V is the energy scale of inflation. This limit will place stringent constraints on the string theory axions.

The formalism proposed in Chpt. 2 perfectly fits in this context. Comic birefringence is indeed a limiting case, as shown in Sec. *2.3.2.1*.
Given the wealth of CMB polarization data that will become available by the end of 2020s, the formalism described in Chpt. 2 (see from Sec. *2.3*) can be used to easily obtain constraints on the GFE parameters, as it has been done for the toy model considered in Sec. *2.4.1*.
Regarding this model of a wavenumber-independent susceptibility tensor, future linear polarization measurements will further improve the constraints on β_V^2 and

β_E^2 (for the observational constraints found using current linear polarization data, see Sec. 2.4.2).

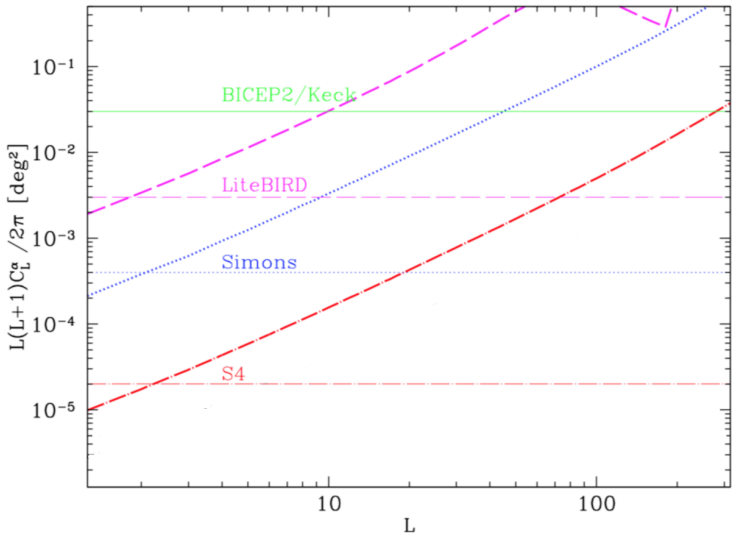

Figure 4.3: *The thick lines show the statistical uncertainty in C^χ ($\equiv C^{\alpha\alpha}$) forecasted for the four experiments considered in Ref. [196]. The thinner horizontal lines indicate the corresponding expected 68% CL bounds on the amplitude of the scale-invariant angle-rotation spectrum A^χ. The thin green solid line shows the current bound on A^χ from BICEP2/Keck. Figure from Ref. [196].*

Let us remember that while the β_V^2 parameter is basically related to cosmic birefringence, the β_E^2 parameter is instead responsible for the generation of a degree of circular polarization in the CMB radiation from the coupling with linear polarization. We have shown that much better constraints on β_E^2 can be found using current linear polarization data. This allow us to set more stringent constraints on the amount of CMB circular polarization allowed than the amount predicted by current circular polarization data.
Moreover, future linear polarization measurements from the LiteBIRD satellite will improve the bound on β_E^2 by roughly a factor 3, down to $\beta_E^2 < 0.05$. These bounds could be further improved using SO and CMB-S4 data.
We thus argue that linear polarization measurements from forthcoming experiments will likely yield stronger constraints on GFE than direct observations of circular polarization, at least in the case of a wavenumber-independent effective susceptibility tensor.

As already discussed in Chpt. 2, cosmic birefringence and CMB circular polarization could be the *symptom* of parity-violating physics. Hence, the

formalism proposed in Sec. 2.3 will give us the chance of using CMB polarization as a tool to constrain the optical properties of the Universe. This can be particularly useful to achieve one of the goals of the future CMB experiments: constraining physics beyond the standard model.

4.3.2.3 Constraining Cosmology from the high angular scales: optical depth

Moving to a different topic, but still related to the improvement on polarization measurements, LiteBIRD, covering very high angular scales, will be the only experiment able to access the predicted "reionization bump" in the B-mode power spectrum at $\ell < 10$. The height of the reionization bump is related to the optical depth, τ (as we have seen in Sec. 1.4). LiteBIRD will provide a cosmic variance limited determination of τ. This value of τ, on one hand, will provide us an integrated constraint on the reionization history of the Universe, on the other hand, will reduce the uncertainty in the neutrino mass by more than a factor of two [192].

4.3.2.4 Constraining Cosmology from the small angular scales

A complementary constrain of the neutrino mass will be provided by the small angular scales of both SO and CMB-S4. CMB-S4 is also particularly sensitive to the possible existence of additional neutrinos that interact even more weakly than the neutrinos in the standard model, the so-called sterile neutrinos [9, 197].

Regarding the small angular scales reached by SO, and, even more, by CMB-S4, these measurements will allow us to also improve the constrains on the number of relativistic species in the early Universe, N_{eff}, the expansion rate of the Universe, H_0, the abundances of primordial elements and the particle nature of dark matter and its interactions. These are, indeed, all phenomena affecting the damping tail (high-ℓ region) of the CMB power spectra in both temperature and polarization. See Refs. [8, 9, 193].

4.3.2.5 CMB gravitational lensing: impact of masking extragalactic sources

To conclude, SO and even more CMB-S4 are expected to produce high-fidelity maps over large fractions of the sky, improving on the signal-to-noise of the Planck lensing maps by more than an order of magnitude. Therefore, to extract reliable information from small-scales observations it is of the utmost importance

to understand the impact of the source masking, especially because applying correlated masks introduces substantial biases, as we have seen in Sec. 3.4 and Sec. 3.5.

Despite not being detectable on current data sets (*e.g.* Planck), in Sec. 3.5, we have seen that correlated masks can introduce substantial biases on the power spectrum if not accounted for, and they may be important for forthcoming more sensitive experiments that measure small angular scales. We therefore calculated the detectability of the biases induced by masking of tSZ and CIB for SO and S4 assuming a sky coverage of $f_{sky} = 40\%$. We have used the realistic publicly available noise power spectra in temperature and polarization after a component separation procedure based on a standard[1] internal linear combination algorithm. Details of the noise model for SO can be found at `https://github.com/simonsobs/so_noise_models`, while the noise specifications for S4 have been taken from `https://cmb-s4.org/wiki/index.php/Survey_Performance_Expectations`. For SO we used the so-called baseline noise.

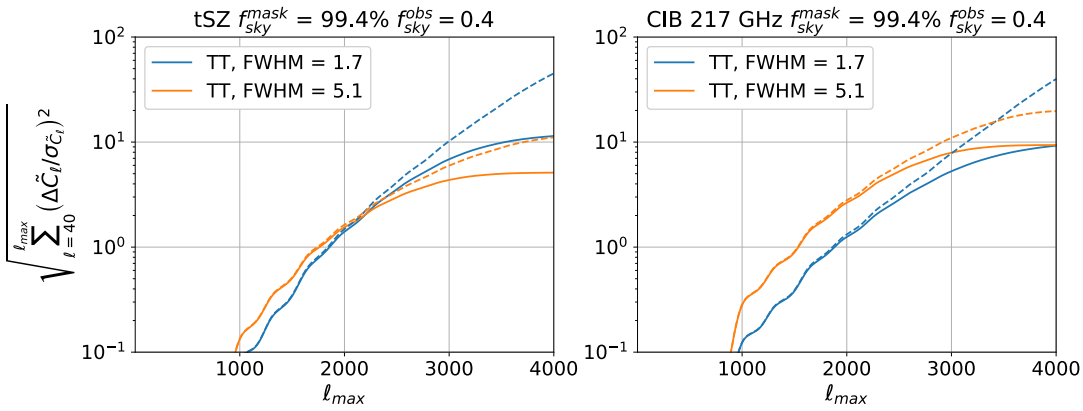

Figure 4.4: *Detection significance of the mask bias as a function of maximum multipole $\ell_{\rm max}$ included in the analysis for different sources for future high-resolution ground-based experiments. SO is shown in solid line while S4 is shown in dashed line. We made the conservative choice of no apodization applied to the mask prior to the computation of the power spectrum to retain the largest sky area $f_{\rm obs} = 40\%$. The retained fraction of the sky area after masking based on foreground thresholding is shown in the title as $f_{\rm sky}^{\rm mask}$. The significance reported is assuming the full sky CMB spectra are known perfectly (and an error model only accounting for foreground-cleaned noise).*

In Fig. 4.4, we can see the detectability of the bias in terms of achievable

[1]We consider the standard version of the algorithm the one that does not explicitly deproject any extragalactic foreground component.

detection significance as a function of the highest multipole included in the analysis. More details about this discussion can be found in [12]. If tSZ and the brightest regions of CIB emission are masked, biases on the lensed temperature power spectrum, $\tilde{C}^{TT}$, will be detected with a statistical significance well above 5σ for both SO and CMB-S4.

Regarding polarization, we have seen that measurements of the lensed E-mode polarization power spectrum, $\tilde{C}^{EE}$, are generally less affected by the bias. The effect can be neglected for SO, while for S4 it will be needed to account for it, as the statistical significance is $\sim 3\sigma$.
Regarding the lensed B-mode polarization spectrum, the size of the bias is, instead, highly dependent on the choice of the estimator. Standard pseudo-C_ℓ estimators not accounting for E-to-B leakage due to partial sky coverage in the E-B separation will lead to a very significant detection of the bias also on sub-degree scales. However, estimators that remove the E-to-B leakage, such as the pure-pseudo-C_ℓ, can remove the majority of the bias and leave the residual effect below the detection threshold.

So overall, the bias from masking bright extragalactic sources can be relevant for fourth-generation CMB observations. Hence, for future data, with much larger populations of resolved sources, care will be required to either include the correlated mask bias in the model, or ensure that mask hole sizes and number densities are sufficiently low that the bias remains negligible.

We have performed a similar analysis on the lensing reconstruction bias described in Sec. *3.4*. The results for all the W_X masks considered in this analysis are shown in Fig. 4.5, where the detection significance of the mask bias as a function of maximum multipole $L_{\rm max}$ is reported. The even columns show the bias obtained directly masking the κ convergence field (see Sec. *3.4.2*) while the odd columns show the bias obtained masking the observed CMB field and then reconstructing the κ convergence field, as discussed above. Comparing the even columns with the odds, we can see that the bias is mitigated to some extent by optimal filtering of the CMB maps, which effectively fills some of the information in the small mask holes (see also Fig. 3.6). Moreover, we show the ideal case of total coverage (first and second columns) together with the more realist case where $f_{\rm sky}^{\rm obs} = 40\%$. Hence, looking at the third column for each mask, we see that the bias is indeed detectable with a statistical significance $\lesssim 1\sigma$. It is worth underline that, except for $W_{\rm rs}$ with $f_{\rm sky} = 94.1\%$ (obtained selecting all the sources with a measured flux above the detection limit for CMB-S4), all the analysis has been done considering only the SO baseline noise. It is not excluded therefore that the bias can be relevant for CMB-S4.

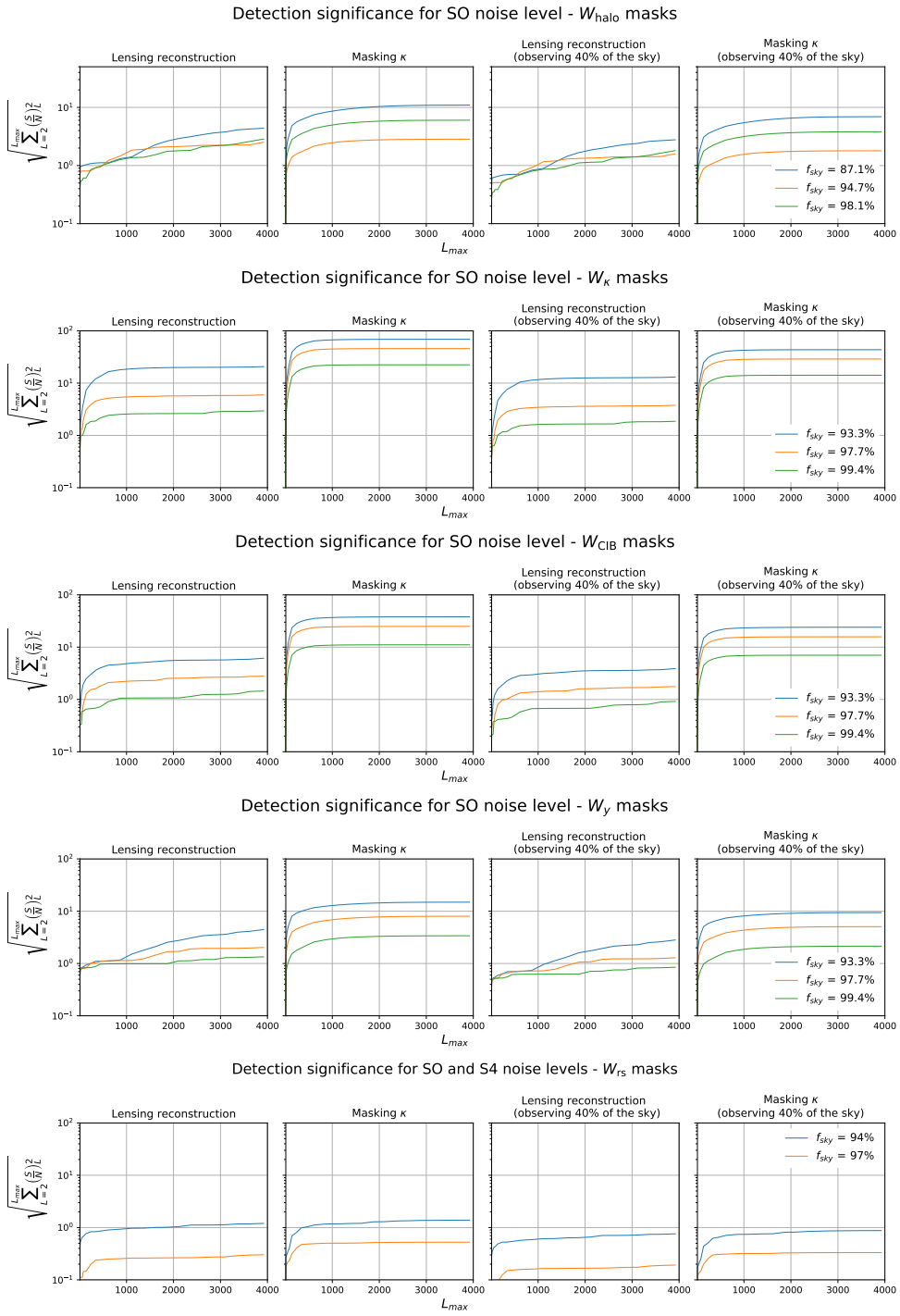

Figure 4.5: *Detection significance of the mask bias as a function of maximum multipole $L_{\rm max}$ included in the analysis for different sources for future high-resolution ground-based experiments. We show the ideal case of total coverage (first and second columns) together with the more realist case where fobs = 40%. The even columns show the bias obtained directly masking the κ convergence field (see Sec. 3.4.2) while the odd columns show the bias obtained masking the observed CMB field and then reconstructing the κ convergence field from the these maps, using the pipeline described above in this section.*

Conclusions

In this thesis, we have dug into the Cosmic Microwave Background (CMB) radiation looking for what remains to be uncovered.
On one hand, we have presented a new tool to extract, from CMB polarization, information regarding the optical properties of our Universe. On the other hand, we have assessed the impact of masking bright extragalactic sources on both the reconstructed CMB lensing potential and the lensed CMB power spectra.
These lines of research are particularly timing given the wealth of CMB data that will become available in the next decade or so.

We have opened this thesis, in Chpt. 1, laying the foundations for the full comprehension of the following chapters. We gave a detailed description of the processes that lead to the CMB anisotropies formation and we explained the physics encoded inside the CMB power spectra, showing how the parameters of the standard cosmological model (ΛCDM) affect their shape.

In Chpt. 2, we have focused our attention on the polarization of the CMB. Since the physics that governs the CMB is purely electromagnetic, the properties of the CMB pattern can be used to constrain deviations from the standard model of particle physics. We have therefore introduced the cosmic birefringence, that, due to a rotation of the plane of linear polarization, generates parity-violating power spectra, and the CMB circular polarization, also known as V-modes. Both these phenomena can be used as potential tracers of new, isotropy- and/or parity-violating physics. Hence, in the second part of this chapter, reserved for the original work, we have studied the in-vacuo conversion between polarization states of propagating radiation in a cosmological setting. We have presented a unified framework able to describe such conversion. The framework expounds the generalized Faraday effect (GFE), *i.e.* the mixing among all polarization components occurring when the natural modes of the radiation are elliptically

polarized. This reproduces, in the appropriate limits, both Faraday rotation (natural modes of the radiation are circularly polarized) and Faraday conversion (natural modes of the radiation are linearly polarized). We have applied the framework to derive general formulas that allow for an easy computation of the CMB spectra in the presence of GFE, see Eqs. 2.49. To derive these equations, we have neglected the linear polarization generated at the time of cosmic reionization and the effect of gravitational lensing due to matter distribution along the line of sight.

Eqs. 2.49 are one of the main results of this thesis, they encode, in a very general way, the modifications due to GFE, linking the modified power spectra to the power spectra that we would have in absence of this effect. They follow quite generally from the transfer equation for polarized radiation in a weakly anisotropic medium, see Eq. 2.21.

Then, we did a step forward. We connected the observed spectra to the components of an effective "cosmic susceptibility tensor" describing, in a completely model-independent way, the optical properties of the Universe between us and the CMB last scattering surface. We tested our formalism, considering a toy model, where the susceptibility tensor is wavenumber-independent, see Eqs. 2.84. We have derived bounds on the parameters of the GFE and on the components of the cosmic susceptibility tensor from the most up-to-date observations of CMB polarization, including circular polarization. This allowed us to set an observational bound on a GFE-induced CMB circularly polarized power spectrum, at $C_\ell^{VV} < 2 \cdot 10^{-5} \mu K^2$ at its peak at $\ell \simeq 370$, at the 95 % CL, which is some three order of magnitude better than presently available direct VV measurements. To our knowledge, it is the first times that such limits appear in the literature.

The GFE parameters themselves are proxies for parity- or isotropy- violation effects occurred in the Universe at $z < 1000$. Hence, these results might change the way in which in-vacuo conversion of polarization states in a cosmological setting is understood, and significantly help advancement in this field.

Even though the mixing of CMB polarization states had been studied in the literature, most of the previous studies concentrated on specific models giving rise to mixing between linear polarization, or to the conversion of linear to circular polarization. There was no attempt to provide a general, model-independent framework to study these effects. We have filled that gap, also providing a neat physical description of the GFE as the precession of the Stokes vector.

Moreover, the results are of interest for a broad audience, going from theorists to observers. It deepens understanding of a physical effect that is potentially observable and can be used to probe the properties of the cosmic medium between

us and the last scattering surface. Theorists will benefit from the framework that allows to quickly derive observational predictions. Observers will have a new target for future measurements.

In Chpt. 3, we have moved our attention to CMB lensing. The CMB pattern we observe today are indeed unavoidably distorted by the presence of mass between us and the last scattering surface. CMB lensing, together with CMB polarization, are, without any doubt, the key-observables for next-decade CMB experiments. Hence, a not completely exhaustive comprehension of this effect could preclude us the possibility of constraining cosmology, or even the chance of faithfully reconstruct the spectrum of primordial B-modes.
We opened the chapter, reviewing the bases of lensing theory. We computed the relations that link the unlensed power spectra (that are undetectable) with the lensed CMB power spectra and we discussed how to reconstruct the CMB lensing potential from these spectra. As before, we reserved the second part of this chapter to the presentation of original results. We have studied the masking complications of the real data and the impact that these masks could have on both the lensed CMB power spectra and the reconstructed CMB lensing power spectrum. The CMB that we actually observe is indeed contaminated by both galactic dust and other extragalactic signals, such as the cosmic infrared background (CIB), the Sunyaev-Zel'dovich (SZ) effect and radio sources. Some of these foregrounds, particularly the bright sources, can be problematic and are often masked out to perform the analysis. This means that the CMB power spectra, including the CMB lensing spectrum, are extracted from the unmasked area only. We built our masks, using the WebSky simulations [126], based on fast approximate numerical simulations of large-scale structure. These simulations cover the entire sky over a broad range of redshifts and include correlated realizations of the various foregrounds and large-scale structure tracer, as well as halo catalogues. We quantified the size of the mask bias for lensing reconstruction, focussing primarily on the impact of masking resolved SZ clusters which are correlated with the CMB lensing potential. Our results are shown in Fig. 3.8 and Figs. 3.9 - 3.10 . The bias is mitigated to some extent by optimal filtering of the CMB maps, which effectively fills some of the information in small mask holes (see Fig. 3.6), but a power spectrum bias remains at the $\sim 1-10\%$ level depending of the masked fraction of the sky, $f_{\rm sky}$.
Then, we have shown that the lensed CMB power spectra can be substantially altered when only measured over the unmasked area. The results are shown in Fig. 3.11 - Fig. 3.13.

We finally opened Chpt. 4 presenting the state-of-the-art of CMB measure-

ments and briefly reviewing the amazing achievements reached by Planck. We have then put the spotlight on the questions that, in spite of all the accurate measurements and intensive studies carried on in the last 50 years, have still to be assessed. Our understanding of the Universe is still based on unknown entities like dark energy, dark matter and the inflaton. We devoted the last part of the chapter to introduce the next-decade CMB experiments, and to frame in them the researches proposed in this thesis.
We discussed the goals of LiteBIRD satellite, that will provide us measurements on the large angular scales. This data will definitely improve our constrain on cosmic birefringence and more in general on GFE parameters. This will help us to constrain extensions to the standard model of both cosmology and particles. For examples, for the aforementioned toy model (with the wavenumber-independent susceptibility tensor), we have shown that LiteBIRD satellite will improve the bound on the GFE parameter sourcing CMB circular polarization by roughly a factor 3. Future linear polarization surveys, expected within this decade, will therefore provide, as a byproduct, superior bounds on GFE-induced circular polarization of the CMB. This is a great step forward for constraining models predicting a non-zero value of circular polarization, since, from the observational point of view, current data allow a large amount of CMB circular polarization.

Alongside LiteBIRD satellite, still in Chpt. 4, we discussed the next-decade ground-based CMB experiments, Simons Observatory (SO) and CMB-Stage4 (CMB-S4), which are devoted to the exploration of the small angular scales. They are therefore complementary to the LiteBIRD mission. We reviewed the results found in Chpt. 3 in light of these experiments.
Using available noise data of SO and CMB-S4 experiments, we showed the detectability of the biases on both the reconstructed lensing potential and the lensed CMB spectra induced by masking extragalactic sources. The results are shown in Fig. 4.4 and Fig. 4.5. For the reconstructed CMB lensing potential, we saw that the effect is still under control, at least for SO. The situation may be different for the lensed (temperature) power spectra, where we found a statistical significance well above 5σ to detect the biases if tSZ and the brightest regions of CIB emission are masked. Hence, for future data, with much larger populations of resolved sources, care will be required to either include the correlated mask bias in the model, or ensure that mask hole sizes and number densities are sufficiently low that the bias remains negligible.

To conclude, the advancement of CMB experiments over the last decades, from the pioneer satellite COBE to the outstanding Planck mission, have transformed Cosmology from a qualitative *venture* to a precision science. The CMB

radiation, our window to the history of the Universe, provided the most stringent constraints on cosmological parameters and it has been crucial to unveil aspects of fundamental physics. Nevertheless, many questions remain still open. The next-decade CMB experiments will play a crucial role in our attempt to comprehensively understand the Universe where we live.

Acknowledgment

First, I would like to express my deepest gratitude to my supervisor Massimiliano Lattanzi for his support and guidance. His constant encouragement, patience and his wealth of knowledge have largely contributed to the completion of this work (and of my PhD in general). Thank you also for smoothing my anxieties!
I would like to thank Prof Paolo Natoli for all the stimulating science-related (but not only) discussions and to having been my mentor during these years.
Thanks to Luca Pagano, a wonderful person inside but also outside the workplace. I do not have enough words to thank you. Thanks also to Martina Gerbino and Laura Salvati for being such an inspiration.
A special thanks to all my office mates (Luca C., Serena, Shaz, Cate, Dani e Silvia) for putting up with me and for making easy and amusing even tough moments. I am already missing you guys!

I wish to thank Prof Antony Lewis and Giulio Fabbian, not only because without them part of this thesis would have no way to exist, but also for the hospitality and great availability during my stay at Sussex University, providing me with all the tools I needed to complete this work.
A Giulio un grazie speciale per la *pazienza* avuta nel seguirmi, per la compagnia nel freddo inverno inglese e, soprattutto, per avermi fatto conoscere l'hummus e i pizzoccheri.

Grazie ad Umberto, nonostante i nostri bisticci sei stato una parte fondamentale di questo percorso. Grazie per aver condiviso le mie infinite lamentele e per avermi sempre supportato nei periodi di scoforto. *Competere* con te mi sprona a fare sempre meglio!

Un grazie di cuore a Cate, per essermi stata accanto, durante le sconfitte e le amarezze, per aver condiviso i momenti di gioia e soddisfazione, il tutto sempre

davanti a uno spritz, forse due. Grazie per la tua *paxxerellositá*!
Un ringraziamento particolare a te Dani, che forse piú di tutti hai condiviso con me questo percorso. Senza di te non ce l'avrei mai fatta.
Grazie Fora per essere stato il primo ad avermi insegnato come "fare ricerca" (oltre ad avermi iniziato all'arte del debugging) e grazie Linda per aver fatto in modo che io non mi sentissi mai spaesata, specialmente all'inizio di questo percorso!
Un ringraziamento speciale va a tutti gli amici "ferraresi", per avermi accolto e mostrato affetto sin da subito. Avete reso questi 3 anni indimenticabili. Grazie anche agli "adini" per le battaglie, le conversazioni intrise di ideali e soprattutto per i fiumi di alcool che hanno caratterizzato i nostri incontri!

Grazie agli "amici di Chiara", senza i quali probabilmente non avrei nemmeno iniziato questo percorso.

Grazie alla mia famiglia, la mia roccia. Grazie per avermi sempre ascoltato e supportato (probabilmente anche sopportato). Un sincero grazie anche ai miei zietti adorati, per essermi stati sempre vicini anche a *distanza*.

Last but not least, grazie alle mie amiche di sempre, senza di loro non sarei nulla.

A

Wigner-3j symbols

In this appendix, we summarize the basic properties of the Wigner-3j symbols. For more details, see Ref. [198].
The Wigner-3j symbol, somehow also called 3j symbol or Wigner coefficient,

$$\begin{pmatrix} \ell_1 & \ell_2 & \ell_3 \\ m_1 & m_2 & m_3 \end{pmatrix}, \tag{A.1}$$

is related to the Clebsh-Gordan coefficients, which, in turn, describe coupling of two angular momenta in the quantum mechanics.
The parameters of the Wigner-3j symbol have to satisfy the following selection rules:

(i) $-\ell_i \leq m_i \leq \ell_i$ for $i = 1, 2, 3$;

(ii) $m_1 + m_2 + m_3 = 0$;

(iii) $|\ell_1 - \ell_2| \leq \ell_3 \leq \ell_1 + \ell_2$ (tso-called triangular inequalities);

(iv) $\ell_1 + \ell_2 + \ell_3$ is an integer, and, moreover, if $m_1 = m_2 = m_3 = 0$ an even integer (so-called integer rule).

In other words, the Wigner 3-j symbol is zero unless all these conditions are satisfied.

Symmetry properties The Wigner 3-j symbol is invariant under even permutations of the columns

$$\begin{pmatrix} \ell_1 & \ell_2 & \ell_3 \\ m_1 & m_2 & m_3 \end{pmatrix} = \begin{pmatrix} \ell_3 & \ell_1 & \ell_2 \\ m_3 & m_1 & m_2 \end{pmatrix} = \begin{pmatrix} \ell_2 & \ell_3 & \ell_1 \\ m_2 & m_3 & m_1 \end{pmatrix} . \tag{A.2}$$

An odd permutation of the columns gives, instead, a phase factor

$$\begin{pmatrix} \ell_1 & \ell_2 & \ell_3 \\ m_1 & m_2 & m_3 \end{pmatrix} (-1)^{\ell_1+\ell_2+\ell_3} =$$

$$= \begin{pmatrix} \ell_2 & \ell_1 & \ell_3 \\ m_2 & m_1 & m_3 \end{pmatrix} = \begin{pmatrix} \ell_1 & \ell_3 & \ell_2 \\ m_1 & m_3 & m_2 \end{pmatrix} = \begin{pmatrix} \ell_3 & \ell_2 & \ell_1 \\ m_3 & m_2 & m_1 \end{pmatrix} . \tag{A.3}$$

Hence, if $\ell_1 + \ell_2 + \ell_3$ is even, it is invariant under odd permutations.
The phase also changes under the transformation of $m_1 + m_2 + m_3 \to -(m_1 + m_2 + m_3)$

$$\begin{pmatrix} \ell_1 & \ell_2 & \ell_3 \\ m_1 & m_2 & m_3 \end{pmatrix} = \begin{pmatrix} \ell_1 & \ell_2 & \ell_3 \\ -m_1 & -m_2 & -m_3 \end{pmatrix} (-1)^{\ell_1+\ell_2+\ell_3} . \tag{A.4}$$

Again, if $\ell_1 + \ell_2 + \ell_3$ is even, it is invariant.

Orthogonality relations The Wigner 3-j symbol has the following orthogonality properties:

$$(2\ell_3 + 1) \sum_{m_1 m_2} \begin{pmatrix} \ell_1 & \ell_2 & \ell_3 \\ m_1 & m_2 & m_3 \end{pmatrix} \begin{pmatrix} \ell_1 & \ell_2 & \ell'_3 \\ m_1 & m_2 & m'_3 \end{pmatrix} = \delta_{\ell_3 \ell'_3} \delta_{m_3 m'_3} , \tag{A.5}$$

and

$$\sum_{\ell_3 m_3} (2\ell_3 + 1) \begin{pmatrix} \ell_1 & \ell_2 & \ell_3 \\ m_1 & m_2 & m_3 \end{pmatrix} \begin{pmatrix} \ell_1 & \ell_2 & \ell_3 \\ m'_1 & m'_2 & m_3 \end{pmatrix} = \delta_{m_1 m'_1} \delta_{m_2 m'_2} . \tag{A.6}$$

Other useful relations The first one is:

$$\frac{1}{\sqrt{2\ell+1}}\sum_{m=-\ell}^{+\ell}(-1)^{\ell-m}\begin{pmatrix}\ell & \ell & \ell'\\ m & -m & 0\end{pmatrix}=\delta_{\ell'0}\,. \tag{A.7}$$

Using the above relation, we also found

$$\begin{pmatrix}\ell & 0 & \ell\\ -2 & 0 & 2\end{pmatrix}=\frac{(-1)^{\ell}}{\sqrt{2\ell+1}}\,. \tag{A.8}$$

Another property, involving two Wigner-3j symbols is

$$\sum_{m_1,m_2}(-1)^{m_1+m_2}\begin{pmatrix}\ell_1 & \ell & \ell_2\\ m_1 & m_2-m_1 & -m_2\end{pmatrix}\begin{pmatrix}\ell_2 & \ell' & \ell_1\\ m_2 & m_1-m_2 & -m_1\end{pmatrix}=\frac{(-1)^{\ell}\delta_{\ell\ell'}}{2\ell+1}\,. \tag{A.9}$$

Proof of Eq. A.9:

First of all, using the selection rules, the orthogonality relation, Eq. A.5 can be rewritten as:

$$(2\ell+1)\sum_{m_1=-\ell_1}^{+\ell_1}\begin{pmatrix}\ell_1 & \ell_2 & \ell\\ m_1 & -m_1-m & m\end{pmatrix}\begin{pmatrix}\ell_1 & \ell_2 & \ell'\\ m_1 & -m_1-m' & m'\end{pmatrix}=\delta_{\ell\ell'}\delta_{mm'}\,. \tag{A.10}$$

Now, let us consider the LHS of (A.9):

$$S\equiv\sum_{m_1=-\ell_1}^{+\ell_1}\sum_{m_2=-\ell_2}^{+\ell_2}(-1)^{m_1+m_2}\begin{pmatrix}\ell_1 & \ell & \ell_2\\ m_1 & m_2-m_1 & -m_2\end{pmatrix}\begin{pmatrix}\ell_2 & \ell' & \ell_1\\ m_2 & m_1-m_2 & -m_1\end{pmatrix}=$$

$$=(-1)^{\ell+\ell'}\sum_{m_1=-\ell_1}^{+\ell_1}\sum_{m_2=-\ell_2}^{+\ell_2}(-1)^{m_1+m_2}\begin{pmatrix}\ell_1 & \ell_2 & \ell\\ m_1 & -m_2 & m_2-m_1\end{pmatrix}\begin{pmatrix}\ell_1 & \ell_2 & \ell'\\ m_1 & -m_2 & m_2-m_1\end{pmatrix} \tag{A.11}$$

where in the last equality we have used the symmetry properties of the $3j$'s to change the order of the columns and the signs of the m's. The terms in the sum on the RHS can be put in a similar form as the terms on the LHS of Eq. A.10 by

changing variable from m_2 to $m = m_2 - m_1$:

$$S = (-1)^{\ell+\ell'} \sum_{m_1=-\ell_1}^{+\ell_1} \sum_{m=-\ell_2-m_1}^{+\ell_2-m_1} (-1)^m \begin{pmatrix} \ell_1 & \ell_2 & \ell \\ m_1 & -m_1 - m & m \end{pmatrix} \begin{pmatrix} \ell_1 & \ell_2 & \ell' \\ m_1 & -m_1 - m & m \end{pmatrix} \tag{A.12}$$

Now we would like to exchange the two sums but it seems like this is not possible because apparently the extrema of the m-sum depend on m_1. However, the sum can be performed by letting m run from $-\ell$ to $+\ell$ without changing the result. Here is how to see it: if $\ell_2 - m_1 > \ell$, all terms with $m > \ell$ will be zero because of the selection rule $|m| \leq \ell$, so we can cut the sum there. On the other hand, if $\ell_2 - m_1 < \ell$, the terms with $m > \ell_2 - m_1$ will vanish since they violate the selection rule $|m + m_1| < \ell_2$, and we can extend the sum up to $m = +\ell$. A similar argument holds for the lower bound of the sum. Then,

$$S = (-1)^{\ell+\ell'} \sum_{m=-\ell}^{+\ell} (-1)^m \sum_{m_1=-\ell_1}^{+\ell_1} \begin{pmatrix} \ell_1 & \ell_2 & \ell \\ m_1 & -m_1 - m & m \end{pmatrix} \begin{pmatrix} \ell_1 & \ell_2 & \ell' \\ m_1 & -m_1 - m & m \end{pmatrix} . \tag{A.13}$$

Eq. A.10 implies that the internal sum is equal to $\delta_{\ell\ell'}/(2\ell+1)$, and

$$S = \frac{\delta_{\ell\ell'}}{2\ell+1} \sum_{m=-\ell}^{+\ell} (-1)^m = \frac{(-1)^\ell \delta_{\ell\ell'}}{2\ell+1} , \tag{A.14}$$

which is Eq. A.9.

Another useful relation. Taking $m = m'$ in Eq. A.10 and summing over m on both sides, gives:

$$\sum_{m=-\ell}^{+\ell} \sum_{m_1=-\ell_1}^{+\ell_1} \begin{pmatrix} \ell_1 & \ell_2 & \ell \\ m_1 & -m_1 - m & m \end{pmatrix} \begin{pmatrix} \ell_1 & \ell_2 & \ell' \\ m_1 & -m_1 - m & m \end{pmatrix} = \delta_{\ell\ell'} \tag{A.15}$$

B

Spin-weighted functions

In this Appendix, we review the theory of spin-weighted functions and their expansion in spin-s spherical harmonics following the discussion of Goldberg (1967) [199], which is based on the work by Penrose (1967) [200].

If we consider a given direction on the sphere specified by the angles (θ, ϕ), we can define three orthogonal vectors, one radial, $\mathbf{n}$, and two tangential to the sphere, $\hat{\mathbf{e}}_1$ and $\hat{\mathbf{e}}_2$.
The function ${}_sf(\theta, \phi)$, defined on the sphere, is said to have spin-s if, under a right-handed rotation of $(\hat{\mathbf{e}}_1, \hat{\mathbf{e}}_2)$ by an angle α, it transform as

$$ {}_sf'(\theta, \phi) \;=\; e^{-is\alpha}\, {}_sf(\theta, \phi)\,. \tag{B.1} $$

It is possible to raise, or to lower, the spin of a spin-weighted function through the spin raising, or lowering, operators, $\eth$ and $\bar{\eth}$, respectively. Their explicit expression is given by

$$ \eth\ {}_sf(\theta, \phi) \;=\; -\sin^s(\theta)\left[\frac{\partial}{\partial\theta} + i\csc(\phi)\frac{\partial}{\partial\theta}\right]\sin^{-s}(\theta)\ {}_sf(\theta, \phi)\,; \tag{B.2a} $$

$$ \bar{\eth}\ {}_sf(\theta, \phi) \;=\; -\sin^{-s}(\theta)\left[\frac{\partial}{\partial\theta} - i\csc(\phi)\frac{\partial}{\partial\theta}\right]\sin^{s}(\theta)\ {}_sf(\theta, \phi)\,. \tag{B.2b} $$

In this thesis we are interested in CMB polarization, so, as you can read in Appendix C, we have to deal with spin-2 quantities. If we want to work with spin-0 quantities, we need to act twice on a function ${}_{\pm2}f(\theta, \phi)$ with the $\bar{\eth}$ and

$\eth$ operators, respectively. Hence, Eqs.B.2 become

$$\eth^{\,2}\ {}_{-2}f(\mu,\phi) \;=\; \left(-\partial_\mu - \frac{m}{1-\mu^2}\right)^2 \Big[\big(1-\mu^2\big)\ {}_{-2}f(\mu,\phi)\Big]\,; \tag{B.3a}$$

$$\bar{\eth}^{\,2}\ {}_{2}f(\mu,\phi) \;=\; \left(-\partial_\mu + \frac{m}{1-\mu^2}\right)^2 \Big[\big(1-\mu^2\big)\ {}_{2}f(\mu,\phi)\Big]\,, \tag{B.3b}$$

where $\mu = \cos(\theta)$ and m is given by $\partial_\phi\ {}_s f = im\ {}_s f$.

Once we have defined the spin-weighted functions, we can introduced the spin-weighted spherical harmonics. As a scalar field on the sphere can be expanded in spherical harmonics, $Y_{\ell m}(\theta,\phi)$, spin-weighted functions with $s \neq 0$, can be expanded on the sphere in terms of the spin-s spherical harmonics, ${}_sY_{\ell m}(\theta,\phi)$. These sets of functions (one set for each particular spin, s) satisfy the analogue completeness and orthogonality relations of the spin-0 spherical harmonics

$$\int_0^{2\pi} \mathrm{d}\phi \int_{-1}^{1} \mathrm{d}\cos\theta\ \ {}_sY^*_{\ell' m'}(\theta,\phi)\ \ {}_sY_{\ell m}(\theta,\phi) \;=\; \delta_{\ell\ell'}\,\delta_{mm'}\,; \tag{B.4a}$$

$$\sum_{\ell m}\ {}_sY^*_{\ell m}(\theta,\phi)\ \ {}_sY_{\ell m}(\theta',\phi') \;=\; \delta\big(\phi-\phi'\big)\,\delta\big(\,\cos\theta - \cos\theta'\big)\,. \tag{B.4b}$$

Using the spin raising and lowering operators, Eqs.B.2, we can express the spin-s spherical harmonics ${}_sY_{\ell m}$ in terms of the spin-0 spherical harmonics $Y_{\ell m}$ as

$${}_sY_{\ell m} \;=\; \left[\frac{(\ell+2)!}{(\ell-2)!}\right]^{-1/2} \eth^{\,s} Y_{\ell m}\,, \qquad \text{with } 0 \le s \le \ell\,; \tag{B.5a}$$

$${}_sY_{\ell m} \;=\; \left[\frac{(\ell+2)!}{(\ell-2)!}\right]^{1/2} (-1)^s\,\bar{\eth}^{\,-s} Y_{\ell m}\,, \qquad \text{with } -\ell \le s \le \ell\,. \tag{B.5b}$$

The following properties of spin-weighted harmonics are also useful:

$$ {}_sY^*_{\ell m} \;=\; (-1)^s \; {}_{-s}Y_{\ell -m}\,; \tag{B.6a} $$

$$ \eth \; {}_sY_{\ell m} \;=\; \Big[\big(\ell - s\big)\big(\ell + s + 1\big)\Big]^{1/2} \; {}_{s+1}Y_{\ell m}\,; \tag{B.6b} $$

$$ \bar{\eth} \; {}_sY_{\ell m} \;=\; -\Big[\big(\ell + s\big)\big(\ell - s + 1\big)\Big]^{1/2} \; {}_{s-1}Y_{\ell m}\,; \tag{B.6c} $$

$$ \bar{\eth}\,\eth \; {}_sY_{\ell m} \;=\; -\big(\ell - s\big)\big(\ell + s + 1\big) \; {}_sY_{\ell m}\,. \tag{B.6d} $$

For the calculations computed in this thesis, it is also convenient to remember the relation for the integral of three spin-weighted harmonics in terms of the 3-j symbols, that reads

$$ \int \mathrm{d}\Omega \;\; {}_{s_1}Y_{\ell_1 m_1} \;\; {}_{s_2}Y_{\ell_2 m_2} \;\; {}_{s_3}Y_{\ell_3 m_3} \;= $$

$$ = \sqrt{\frac{\big(2\ell_1 + 1\big)\big(2\ell_2 + 1\big)\big(2\ell_3 + 1\big)}{4\pi}} \begin{pmatrix} \ell_1 & \ell_2 & \ell_3 \\ m_1 & m_2 & m_3 \end{pmatrix} \begin{pmatrix} \ell_1 & \ell_2 & \ell_3 \\ -s_1 & -s_2 & -s_3 \end{pmatrix}, \tag{B.7} $$

with the condition $s_1 + s_2 + s_3 = 0$.

C

Stokes parameters

The Stokes parameters are a powerful mathematical tools introduced by George Gabriel Stokes in 1852 in order to describe polarized light.

Let me consider a monochromatic, or nearly monochromatic[1], plane electromagnetic wave, with frequency ω_0, propagating in the z-direction. The components of the electric field at given point in the space can be written as

$$E_x = a_x(t)\cos(\omega_0 t - \theta_x(t))\,, \qquad \text{and} \qquad E_y = a_y(t)\cos(\omega_0 t - \theta_y(t))\,, \quad \text{(C.1)}$$

where a_x, a_y are the amplitudes and θ_x, θ_y are the phase angles. The requirement that the wave is at least nearly monochromatic ensures that the amplitudes and the phase angles are slowly varying functions of time.
The Stokes parameters are then defined as [30]

$$I \equiv < a_x^2 > + < a_y^2 > ; \quad \text{(C.2a)}$$

$$Q \equiv < a_x^2 > - < a_y^2 > ; \quad \text{(C.2b)}$$

$$U \equiv < 2a_x a_y \cos(\theta_x - \theta_y) > ; \quad \text{(C.2c)}$$

$$V \equiv < 2a_x a_y \sin(\theta_x - \theta_y) > , \quad \text{(C.2d)}$$

where $< ... >$ are time averages. The I parameters gives the intensity of the radiation, which, by definition, is alway positive. The other three parameters are, instead, related to the polarization state of the wave, and can have either positive and negative sign. More precisely, the U and Q parameters carry information about the linear polarization, whereas V is a measure of the elliptical polarization,

[1] We can relax this condition, and consider a nearly monochromatic wave. Nearly in the sense that its frequency components are closely distributed around the mean frequency, ω_0.

with the special case of circular polarization when $a_x = a_y$ and $\delta = \theta_x - \theta_y = \pm\pi/2$. Unpolarized radiation is defined by the condition $Q = U = V = 0$.

An important thing to be mentioned is that I and V are physical observables, independent from the choice of a particular coordinate system, whereas Q and U depend on the orientation of the x and y axes. If we rotate the x and y axes by an angle ϕ, the Stokes Q and U parameters transform as

$$Q' = Q\cos(2\phi) + U\sin(2\phi)\,; \tag{C.3a}$$

$$U' = -Q\sin(2\phi) + U\cos(2\phi)\,. \tag{C.3b}$$

From the equations above, we can easily verify that the quantity $Q^2 + U^2$ is invariant under the considered rotation. Moreover, it can be defined the angle

$$\Phi = \frac{1}{2}\arctan\left(\frac{U}{Q}\right), \tag{C.4}$$

which identify a constant direction.
Hence, the physically observable for a linearly polarized wave is the vector $\mathbf{P}$, defined as orthogonal to the direction of propagation, having magnitude $\left(Q^2 + U^2\right)^{1/2}$ and polar angle Φ.

From Eqs.C.3, we can formally say that the Q and U parameters, under a coordinate transformation defined as

$$x_i' = A_i^k\, x_k\,, \tag{C.5a}$$

transform as

$$P_{ij}' = A_i^k A_j^l\, P_{kl}\,. \tag{C.5b}$$

More explicitly, Q and U are the components of a symmetric trace-free 2 x 2 tensor

$$\begin{pmatrix} Q' & U' \\ U' & -Q' \end{pmatrix} = \begin{pmatrix} \cos\phi & \sin\phi \\ -\sin\phi & \cos\phi \end{pmatrix} \begin{pmatrix} Q & U \\ U & -Q \end{pmatrix} \begin{pmatrix} \cos\phi & -\sin\phi \\ \sin\phi & \cos\phi \end{pmatrix}, \tag{C.6}$$

or, equivalently, a spin-2 field.

It is interesting to verify the behavior under parity transformation of the Stokes parameters. Basically, we are considering a transformation that, in spherical coordinates, reverses the sign of the azimut angle but leaves the other unchanged.

Hence, the Stokes parameters transform as

$$T(\hat{\mathbf{n}}') = T(\hat{\mathbf{n}})\,; \tag{C.7a}$$

$$Q(\hat{\mathbf{n}}') = Q(\hat{\mathbf{n}})\,; \tag{C.7b}$$

$$U(\hat{\mathbf{n}}') = -U(\hat{\mathbf{n}})\,; \tag{C.7c}$$

$$V(\hat{\mathbf{n}}') = -V(\hat{\mathbf{n}})\,, \tag{C.7d}$$

where $T \propto I^4$.

D

E and B modes

The common way to deal with the CMB polarization field is to introduce the two combination $Q+iU$ and $Q-iU$, that are still spin-2 quantities. As we have seen in Appendix C, these quantities are not rotationally invariant

$$\big(Q' \pm iU'\big) \;=\; e^{\mp i\phi}\big(Q \pm iU\big)\,. \tag{D.1}$$

Hence, unlike a scalar (spin-0) function, as $T \propto I^4$ and V , linear polarization can not be expanded by the usual spherical harmonics on the surface of a sphere. The mathematical machinery necessary to represent angular distribution of the linear polarization of the CMB on the celestial sphere is actually the spin-weighted harmonics ${}_sY_{\ell m}(\hat{\mathbf{n}})$. More details about these functions are given in Appendix B.

Expanding $Q \pm iU$ in the appropriate spin-weighted basis, we get

$$\big(Q+iU\big)(\hat{\mathbf{n}}) \;=\; \sum_{\ell m}\; {}_2a_{\ell m}\; {}_2Y_{\ell m}(\hat{\mathbf{n}})\,; \tag{D.2a}$$

$$\big(Q-iU\big)(\hat{\mathbf{n}}) \;=\; \sum_{\ell m}\; {}_{-2}a_{\ell m}\; {}_{-2}Y_{\ell m}(\hat{\mathbf{n}}) \tag{D.2b}$$

By using Eqs.B.6, it can be shown that the expansion coefficients for the polarization variables satisfy ${}_{-2}a^*_{\ell m} = {}_2a_{\ell -m}$.

It is more convenient to deal with spin-0 quantities as they are rotationally invariant, and, moreover, it is meaningless to deal with power spectra computed from observer-dependent quantities as the Stokes Q and U parameters. We can get spin-0 quantities by using the spin raising, $\eth$, and lowering, $\bar{\eth}$, operators, respectively. These operators are properly defined in Appendix B. Thus, acting

twice with and on $Q \pm iU$, we get

$$\bar{\eth}^{\,2}\big(Q+iU\big)(\hat{\mathbf{n}}) \;=\; \sum_{\ell m}\left[\frac{(\ell+2)!}{(\ell-2)!}\right]^{1/2} {}_2a_{\ell m}Y_{\ell m}(\hat{\mathbf{n}})\,; \tag{D.3a}$$

$$\eth^{\,2}\big(Q-iU\big)(\hat{\mathbf{n}}) \;=\; \sum_{\ell m}\left[\frac{(\ell+2)!}{(\ell-2)!}\right]^{1/2} {}_{-2}a_{\ell m}Y_{\ell m}(\hat{\mathbf{n}})\,. \tag{D.3b}$$

The expressions for the expansion coefficients are

$$\begin{aligned} {}_2a_{\ell m} \;&=\; \int \mathrm{d}\Omega\; {}_2Y^*_{\ell m}(\hat{\mathbf{n}})\big(Q+iU\big)(\hat{\mathbf{n}}) \;= \\ &=\; \left[\frac{(\ell+2)!}{(\ell-2)!}\right]^{-1/2} \int \mathrm{d}\Omega\; Y^*_{\ell m}(\hat{\mathbf{n}})\bar{\eth}^{\,2}\big(Q+iU\big)(\hat{\mathbf{n}})\,; \end{aligned} \tag{D.4a}$$

$$\begin{aligned} {}_{-2}a_{\ell m} \;&=\; \int \mathrm{d}\Omega\; {}_{-2}Y^*_{\ell m}(\hat{\mathbf{n}})\big(Q+iU\big)(\hat{\mathbf{n}}) \;= \\ &=\; \left[\frac{(\ell+2)!}{(\ell-2)!}\right]^{-1/2} \int \mathrm{d}\Omega\; Y^*_{\ell m}(\hat{\mathbf{n}})\eth^{\,2}\big(Q-iU\big)(\hat{\mathbf{n}})\,. \end{aligned} \tag{D.4b}$$

Finally, we can introduce, in real space, the two quantities that are commonly used by the CMB community, namely the gradient-E and curl-B fields

$$E(\hat{\mathbf{n}}) \;=\; \sum_{\ell m} a^E_{\ell m}\, Y_{\ell m}(\hat{\mathbf{n}})\,; \tag{D.5a}$$

$$B(\hat{\mathbf{n}}) \;=\; \sum_{\ell m} a^B_{\ell m}\, Y_{\ell m}(\hat{\mathbf{n}})\,, \tag{D.5b}$$

where we have defined the two linear combinations of ${}_{\pm2}a_{\ell m}$ as

$$a^E_{\ell m} \;=\; -\frac{{}_2a_{\ell m} \;+\; {}_{-2}a_{\ell m}}{2}\,; \tag{D.6a}$$

$$a^B_{\ell m} \;=\; -\frac{{}_2a_{\ell m} \;-\; {}_{-2}a_{\ell m}}{2i}\,. \tag{D.6b}$$

The quantities in Eqs.D.5, $E(\hat{\mathbf{n}})$ and $B(\hat{\mathbf{n}})$, are the rotationally invariant parameters we were looking for.

Last thing to be noticed is again the behavior under parity transformation of

these parameters. Using Eqs.D.8 and Eqs. B.2, we find

$$\bar{\eth}^{\,2}\big(Q+iU\big)'(\hat{\mathbf{n}}') \;=\; \eth^{\,2}\big(Q+iU\big)(\hat{\mathbf{n}})\,; \tag{D.7a}$$

$$\eth^{\,2}\big(Q-iU\big)'(\hat{\mathbf{n}}') \;=\; \bar{\eth}^{\,2}\big(Q+iU\big)(\hat{\mathbf{n}})\,. \tag{D.7b}$$

Hence,

$$E(\hat{\mathbf{n}}') \;=\; E(\hat{\mathbf{n}})\,; \tag{D.8a}$$

$$B(\hat{\mathbf{n}}') \;=\; -B(\hat{\mathbf{n}})\,. \tag{D.8b}$$

The two new variables behave differently: E is invariant under parity transformations, while B is not. This explain the choice of the two letter, reminding the analogy with electric and magnetic fields.

E

$\mathcal{G}$'s, $\mathcal{H}$'s, $\mathcal{K}$'s kernels

G's kernels The explicit form of the G's kernels appearing in the $\mathcal{G}$'s and $\mathcal{H}$'s kernels is

$$G_{L_1L_2L} \equiv F_{\ell_1\ell_2\ell} \begin{pmatrix} \ell_1 & \ell_2 & \ell \\ m_1 & m_2 & -m \end{pmatrix} \begin{pmatrix} \ell_1 & \ell_2 & \ell \\ -2 & 0 & 2 \end{pmatrix}; \tag{E.1a}$$

$$G'_{L_1L_2L} \equiv F_{\ell_1\ell_2\ell} \begin{pmatrix} \ell_1 & \ell_2 & \ell \\ m_1 & m_2 & -m \end{pmatrix} \begin{pmatrix} \ell_1 & \ell_2 & \ell \\ -2 & 2 & 0 \end{pmatrix}; \tag{E.1b}$$

$$G''_{L_1L_2L} \equiv F_{\ell_1\ell_2\ell} \begin{pmatrix} \ell_1 & \ell_2 & \ell \\ m_1 & m_2 & -m \end{pmatrix} \begin{pmatrix} \ell_1 & \ell_2 & \ell \\ 2 & -4 & 2 \end{pmatrix} \tag{E.1c}$$

and $F_{\ell\ell_1\ell_2} = \Big[(2\ell{+}1)\big(2\ell_1{+}1\big)\big(2\ell_2{+}1\big)/\big(4\pi\big)\Big]^{(1/2)}$. We have also used the compact notation $L = (\ell, m)$, that will be widely used in the rest of this appendix.

Eq. A.7 and Eq. A.8 imply the following properties of the G's kernels:

$$\frac{1}{2\ell+1}\sum_{m=-\ell}^{+\ell}(-1)^m G_{LL_2L} = \frac{\delta_{\ell_2 0}}{\sqrt{4\pi}}\,, \tag{E.2a}$$

$$\frac{1}{2\ell+1}\sum_{m=-\ell}^{+\ell}(-1)^m G'_{LL_2L} = 0\,, \tag{E.2b}$$

$$\frac{1}{2\ell+1}\sum_{m=-\ell}^{+\ell}(-1)^m G''_{LL_2L} = 0\,. \tag{E.2c}$$

Note that the first and third indices in the G's are the same.

For what concerns the (double) sums of the product of two G's kernels, we are interested in computing *e.g.*:

$$\begin{aligned}
&\sum_{m_1 m_2}(-1)^{m_1+m_2} G_{L_1 L L_2}\, G_{L_2 L' L_1}\delta_{m,m_2-m_1}\delta_{m',m_1-m_2} \;= \\
&= F_{\ell_1\ell\ell_2}F_{\ell_2\ell'\ell_1}\begin{pmatrix}\ell_1 & \ell & \ell_2\\ -2 & 0 & 2\end{pmatrix}\begin{pmatrix}\ell_2 & \ell' & \ell_1\\ -2 & 0 & 2\end{pmatrix}\cdot \\
&\quad\cdot \underbrace{\sum_{m_1 m_2}(-1)^{m_1+m_2}\begin{pmatrix}\ell_1 & \ell & \ell_2\\ m_1 & m & -m_2\end{pmatrix}\begin{pmatrix}\ell_2 & \ell' & \ell_1\\ m_2 & m' & -m_1\end{pmatrix}\delta_{m,m_2-m_1}\delta_{m',m_1-m_2}}_{S_{m_1 m_2}}\,.
\end{aligned} \tag{E.3}$$

Focusing on the m_1, m_2 sum, we have

$$\begin{aligned}
S_{m_1 m_2} &= (-1)^m\delta_{m',-m}\sum_{m_1}\begin{pmatrix}\ell_1 & \ell & \ell_2\\ m_1 & m & -m-m_1\end{pmatrix}\begin{pmatrix}\ell_2 & \ell' & \ell_1\\ m+m_1 & m' & -m_1\end{pmatrix} = \\
&= (-1)^m\delta_{m',-m}(-1)^{\ell+\ell'}\sum_{m_1}\begin{pmatrix}\ell_1 & \ell_2 & \ell\\ m_1 & -m-m_1 & m\end{pmatrix}\begin{pmatrix}\ell_1 & \ell_2 & \ell'\\ m_1 & -m-m_1 & m\end{pmatrix} = \\
&= \frac{(-1)^m\delta_{m',-m}\delta_{\ell\ell'}}{2\ell+1}
\end{aligned} \tag{E.4}$$

where we have used Eq. A.10 in the last equality. Then

$$\sum_{m_1 m_2} (-1)^{m_1+m_2} G_{L_1 L L_2}\, G_{L_2 L' L_1} \delta_{m,m_2-m_1} \delta_{m',m_1-m_2} \;=$$

$$= (-1)^m F^2_{\ell_1 \ell \ell_2} \left[\begin{pmatrix} \ell_1 & \ell & \ell_2 \\ -2 & 0 & 2 \end{pmatrix} \right]^2 \frac{\delta_{\ell\ell'} \delta_{m,-m'}}{2\ell+1} \,. \tag{E.5}$$

This equation can be written in a more convenient way, as

$$\sum_{m_1 m_2} G_{L_1 L L_2}\, G_{L_1 L' L_2} \delta_{m,m_2-m_1} \delta_{m',m_2-m_1} = F^2_{\ell_1 \ell \ell_2} \left[\begin{pmatrix} \ell_1 & \ell & \ell_2 \\ -2 & 0 & 2 \end{pmatrix} \right]^2 \frac{\delta_{\ell\ell'} \delta_{m,m'}}{2\ell+1} \,. \tag{E.6}$$

Similarly,

$$\sum_{m_1 m_2} G'_{L_1 L L_2}\, G'_{L_1 L' L_2} \delta_{m,m_2-m_1} \delta_{m',m_2-m_1} = F^2_{\ell_1 \ell \ell_2} \left[\begin{pmatrix} \ell_1 & \ell & \ell_2 \\ -2 & 2 & 0 \end{pmatrix} \right]^2 \frac{\delta_{\ell\ell'} \delta_{m,m'}}{2\ell+1} \,, \tag{E.7}$$

$$\sum_{m_1 m_2} G_{L_1 L L_2}\, G'_{L_1 L' L_2} \delta_{m,m_2-m_1} \delta_{m',m_2-m_1} = F^2_{\ell_1 \ell \ell_2} \begin{pmatrix} \ell_1 & \ell & \ell_2 \\ -2 & 0 & 2 \end{pmatrix} \begin{pmatrix} \ell_1 & \ell & \ell_2 \\ -2 & 2 & 0 \end{pmatrix} \frac{\delta_{\ell\ell'} \delta_{m,m'}}{2\ell+1} \,, \tag{E.8}$$

$$\vdots$$

$\mathcal{G}$'s and $\mathcal{H}$'s kernels The explicit form of the $\mathcal{G}$'s and $\mathcal{H}$'s kernels that appears for the first time in Eqs. 2.45 is

$$\mathcal{G}^{(1)}_{L_1 L} \;=\; (-1)^m\, i \sum_{\substack{\ell_2 \\ \ell+\ell_1+\ell_2 \text{ odd} \\ m_2 = m-m_1}} G_{L_1 L_2 L}\, b_{V,L_2} \,; \tag{E.9a}$$

$$\mathcal{G}^{(2)}_{L_1 L} \;=\; (-1)^m \sum_{\substack{\ell_2 \\ \ell+\ell_1+\ell_2 \text{ even} \\ m_2 = m-m_1}} G_{L_1 L_2 L}\, b_{V,L_2} \,; \tag{E.9b}$$

$$\mathcal{G}^{(3)}_{L_1L} = (-1)^m\, i \sum_{\substack{\ell_2 \\ m_2=m-m_1}} G'_{L_1L_2L}\Big[\big(b_{-2,L_2} - (-1)^{\ell+\ell_1+\ell_2}\, b_{2,L_2}\big)\Big]\,; \tag{E.9c}$$

$$\mathcal{G}^{(4)}_{L_1L} = (-1)^m \sum_{\substack{\ell_2 \\ m_2=m-m_1}} G'_{L_1L_2L}\Big[\big(b_{-2,L_2} + (-1)^{\ell+\ell_1+\ell_2}\, b_{2,L_2}\big)\Big]\,; \tag{E.9d}$$

$$\mathcal{H}^{(1)}_{L_1L} = \frac{(-1)^m}{2} \sum_{\substack{\ell_2 \\ \ell+\ell_1+\ell_2\,\text{even} \\ m_2=m-m_1}} G_{L_1L_2L}\,\left(\mathcal{B}_{VV,L_2} + \mathcal{B}_{+-,L_2}\right)\,; \tag{E.9e}$$

$$\mathcal{H}^{(2)}_{L_1L} = \frac{(-1)^m}{2}\, i \sum_{\substack{\ell_2 \\ \ell+\ell_1+\ell_2\,\text{odd} \\ m_2=m-m_1}} G_{L_1L_2L}\,\left(\mathcal{B}_{VV,L_2} + \mathcal{B}_{+-,L_2}\right)\,; \tag{E.9f}$$

$$\mathcal{H}^{(3)}_{L_1L} = \frac{(-1)^m}{4} \sum_{\substack{\ell_2 \\ m_2=m-m_1}} G''_{L1L_2L}\Big[\big(\mathcal{B}_{--,L_2} + (-1)^{\ell+\ell_1+\ell_2}\, \mathcal{B}_{++,L_2}\big)\Big]\,; \tag{E.9g}$$

$$\mathcal{H}^{(4)}_{L_1L} = \frac{(-1)^m}{4}\, i \sum_{\substack{\ell_2 \\ m_2=m-m_1}} G''_{L_1L_2L}\Big[\big(\mathcal{B}_{--,L_2} - (-1)^{\ell+\ell_1+\ell_2}\, \mathcal{B}_{++,L_2}\big)\Big]\,; \tag{E.9h}$$

$$\mathcal{H}^{(5)}_{L_1L} = \frac{(-1)^m}{2} \sum_{\substack{\ell_2 \\ m_2=m-m_1}} G'_{L1L_2L}\Big[\big(\mathcal{B}_{-V,L_2} + (-1)^{\ell+\ell_1+\ell_2}\, \mathcal{B}_{+V,L_2}\big)\Big]\,; \tag{E.9i}$$

$$\mathcal{H}^{(6)}_{L_1L} = \frac{(-1)^m}{2}\, i \sum_{\substack{\ell_2 \\ m_2=m-m_1}} G'_{L_1L_2L}\Big[\big(\mathcal{B}_{-V,L_2} - (-1)^{\ell+\ell_1+\ell_2}\, \mathcal{B}_{+V,L_2}\big)\Big]\,, \tag{E.9j}$$

where the G's kernels are defined in Eqs. E.1

Note that the $\mathcal{G}$'s are complex quantities satisfying:

$$\mathcal{G}^{(\cdot)*}_{LL'} = (-1)^{m'-m}\, \mathcal{G}^{(\cdot)}_{-L-L'}\,, \tag{E.10}$$

where we use the notation $-L \equiv (\ell,\, -m)$. This relation is still valid considering the $\mathcal{H}$'s kernels. Moreover, we found

$$\mathcal{G}^{(1)}_{LL'} = (-1)^{m'-m+1}\mathcal{G}^{(1)}_{-L'-L}\,; \tag{E.11a}$$

$$\mathcal{G}^{(2)}_{LL'} = (-1)^{m'-m}\mathcal{G}^{(2)}_{-L'-L}\,, \tag{E.11b}$$

and

$$\mathcal{H}^{(1)}_{LL'} = (-1)^{m'-m}\mathcal{H}^{(1)}_{-L'-L}\,; \tag{E.11c}$$

$$\mathcal{H}^{(2)}_{LL'} = (-1)^{m'-m-1}\mathcal{H}^{(2)}_{-L'-L}\,. \tag{E.11d}$$

No similar property for the other $\mathcal{G}$'s and $\mathcal{H}$'s kernels.

Computing m-averages of the $\mathcal{G}$'s and $\mathcal{H}$'s kernels Using Eqs. (E.2) it is pretty straightforward to show that

$$\frac{1}{2\ell+1}\sum_{m=-\ell}^{+\ell}\mathcal{G}^{(n)}_{LL} = 0 \qquad n = 1,\,3,\,4\,; \tag{E.12}$$

$$\frac{1}{2\ell+1}\sum_{m=-\ell}^{+\ell}\mathcal{G}^{(2)}_{LL} = \frac{1}{2}\frac{b_{V,00}}{\sqrt{4\pi}}\,, \tag{E.13}$$

and, analogously, for the $\mathcal{H}$'s kernels,

$$\frac{1}{2\ell+1}\sum_{m=-\ell}^{+\ell}\mathcal{H}^{(n)}_{LL} = 0 \qquad n = 2,\,3,\,4\,5\,6\,; \tag{E.14}$$

$$\frac{1}{2\ell+1}\sum_{m=-\ell}^{+\ell}\mathcal{H}^{(1)}_{LL} = \frac{\mathcal{B}_{VV,L_2}+\mathcal{B}_{+-,L_2}}{\sqrt{4\pi}}\,, \tag{E.15}$$

Now let us turn to the m-averages of the product of two kernels, starting from:

$$\begin{aligned}
&\sum_{m_1,m_2}\mathcal{G}^{(1)}_{L_1L_2}\mathcal{G}^{(1)}_{L_2L_1} = \\
&\quad= \sum_{\substack{\ell\ell'\\ \ell_1+\ell_2+\ell\,\text{odd}\\ \ell_1+\ell_2+\ell'\,\text{odd}\\ m=m_2-m_1\\ m'=m_1-m_2}}\left[\sum_{m_1m_2}(-1)^{m_1+m_2+1}G_{L_1LL_2}\,G_{L_2L'L_1}\right]b_{V,L}b_{V,L'} = \\
&\quad= \sum_{\substack{LL'\\ \ell_1+\ell_2+\ell\,\text{odd}\\ \ell_1+\ell_2+\ell'\,\text{odd}}}\left[\sum_{m_1m_2}(-1)^{m_1+m_2+1}G_{L_1LL_2}\,G_{L_2L'L_1}\,\delta_{m,m_2-m_1}\delta_{m',m_1-m_2}\right]b_{V,L}b_{V,L'} =
\end{aligned}$$

$$= \sum_{\substack{LL' \\ \ell_1+\ell_2+\ell \text{ odd} \\ \ell_1+\ell_2+\ell' \text{ odd}}} \left\{ (-1)^{m+1} F^2_{\ell_1 \ell \ell_2} \left[\begin{pmatrix} \ell_1 & \ell & \ell_2 \\ -2 & 0 & 2 \end{pmatrix} \right]^2 \frac{\delta_{\ell\ell'}\delta_{m,-m'}}{2\ell+1} \right\} b_{V,L} b_{V,L'} =$$

$$= \frac{(2\ell_1+1)(2\ell_2+1)}{4\pi} \sum_{\substack{\ell m \\ \ell_1+\ell_2+\ell \text{ odd}}} \left\{ (-1)^{m+1} \left[\begin{pmatrix} \ell_1 & \ell & \ell_2 \\ -2 & 0 & 2 \end{pmatrix} \right]^2 \right\} b_{V,\ell m} b_{V,\ell -m} =$$

$$= \quad -\frac{(2\ell_1+1)(2\ell_2+1)}{4\pi} \sum_{\substack{\ell m \\ \ell_1+\ell_2+\ell \text{ odd}}} \left[\begin{pmatrix} \ell_1 & \ell & \ell_2 \\ -2 & 0 & 2 \end{pmatrix} \right]^2 |b_{V,\ell m}|^2 \,. \qquad \text{(E.16)}$$

Similarly,

$$\sum_{m_1,m_2} \mathcal{G}^{(2)}_{L_1 L_2} \mathcal{G}^{(2)}_{L_2 L_1} = \sum_{\substack{\ell\ell' \\ \ell_1+\ell_2+\ell \text{ even} \\ \ell_1+\ell_2+\ell' \text{ even} \\ m=m_2-m_1 \\ m'=m_1-m_2}} \left[\sum_{m_1 m_2} (-1)^{m_1+m_2} G_{L_1 L L_2} \, G_{L_2 L' L_1} \right] b_{V,L} b_{V,L'} =$$

$$\ldots\ldots \quad =$$

$$= \frac{(2\ell_1+1)(2\ell_2+1)}{4\pi} \sum_{\substack{\ell m \\ \ell_1+\ell_2+\ell \text{ even}}} \left[\begin{pmatrix} \ell_1 & \ell & \ell_2 \\ -2 & 0 & 2 \end{pmatrix} \right]^2 |b_{V,\ell m}|^2 \,; \qquad \text{(E.17)}$$

$$\sum_{m_1,m_2} \mathcal{G}^{(1)}_{L_1 L_2} \mathcal{G}^{(2)}_{L_2 L_1} = i \sum_{\substack{\ell\ell' \\ \ell_1+\ell_2+\ell \text{ odd} \\ \ell_1+\ell_2+\ell' \text{ even} \\ m=m_2-m_1 \\ m'=m_1-m_2}} \left[\sum_{m_1 m_2} (-1)^{m_1+m_2} G_{L_1 L L_2} \, G_{L_2 L' L_1} \right] b_{V,L} b_{V,L'} =$$

$$\ldots\ldots \quad =$$

$$= i \sum_{\substack{LL' \\ \ell_1+\ell_2+\ell \text{ odd} \\ \ell_1+\ell_2+\ell' \text{ even}}} \left\{ (-1)^{m} F^2_{\ell_1 \ell \ell_2} \left[\begin{pmatrix} \ell_1 & \ell & \ell_2 \\ -2 & 0 & 2 \end{pmatrix} \right]^2 \frac{\delta_{\ell\ell'}\delta_{m,-m'}}{2\ell+1} \right\} b_{V,L} b_{V,L'} = 0 \,; \quad \text{(E.18)}$$

$$\sum_{m_1,m_2} \mathcal{G}^{(3)}_{L_1L_2}\mathcal{G}^{(3)*}_{L_1L_2} =$$

$$= \sum_{\substack{\ell\ell' \\ m=m_2-m_1 \\ m'=m_2-m_1}} \left[\sum_{m_1m_2} G'_{L_1LL_2}\, G'_{L_1L'L_2}\right] \cdot$$

$$\cdot \left[b_{-2,L} - (-1)^{\ell+\ell_1+\ell_2}\, b_{2,L}\right]\left[b_{-2,L'} - (-1)^{\ell'+\ell_1+\ell_2}\, b_{2,L'}\right]^* =$$

$$= \sum_{LL'} F^2_{\ell_1\ell\ell_2} \left[\begin{pmatrix} \ell_1 & \ell & \ell_2 \\ -2 & 2 & 0 \end{pmatrix}\right]^2 \frac{\delta_{\ell\ell'}\delta_{m,m'}}{2\ell+1} \cdot$$

$$\cdot \left[b_{-2,L} - (-1)^{\ell+\ell_1+\ell_2}\, b_{2,L}\right]\left[b_{-2,L'} - (-1)^{\ell'+\ell_1+\ell_2}\, b_{2,L'}\right]^* =$$

$$= \frac{(2\ell_1+1)(2\ell_2+1)}{4\pi} \sum_{\ell m} \left[\begin{pmatrix} \ell_1 & \ell & \ell_2 \\ -2 & 2 & 0 \end{pmatrix}\right]^2 \left|b_{-2,L} - (-1)^{\ell+\ell_1+\ell_2}\, b_{2,L}\right|^2 ; \qquad \text{(E.19)}$$

and so on.
At the end, this is what we get for the various products:

$$\sum_{m_1,m_2} \mathcal{G}^{(1)}_{L_1L_2}\mathcal{G}^{(1)*}_{L_1L_2} = \frac{(2\ell_1+1)(2\ell_2+1)}{4\pi} \sum_{\substack{\ell m \\ \ell_1+\ell_2+\ell\,\text{odd}}} \left[\begin{pmatrix} \ell_1 & \ell & \ell_2 \\ -2 & 0 & 2 \end{pmatrix}\right]^2 |b_{V,\ell m}|^2 ; \qquad \text{(E.20a)}$$

$$\sum_{m_1,m_2} \mathcal{G}^{(2)}_{L_1L_2}\mathcal{G}^{(2)*}_{L_1L_2} = \frac{(2\ell_1+1)(2\ell_2+1)}{4\pi} \sum_{\substack{\ell m \\ \ell_1+\ell_2+\ell\,\text{even}}} \left[\begin{pmatrix} \ell_1 & \ell & \ell_2 \\ -2 & 0 & 2 \end{pmatrix}\right]^2 |b_{V,\ell m}|^2 ; \qquad \text{(E.20b)}$$

$$\sum_{m_1,m_2} \mathcal{G}^{(1)}_{L_1L_2}\mathcal{G}^{(2)*}_{L_1L_2} = 0 ; \qquad \text{(E.20c)}$$

$$\sum_{m_1,m_2} \mathcal{G}^{(3)}_{L_1L_2}\mathcal{G}^{(3)*}_{L_1L_2} = \frac{(2\ell_1+1)(2\ell_2+1)}{4\pi}\sum_{\ell m}\left[\begin{pmatrix}\ell_1 & \ell & \ell_2\\ -2 & 2 & 0\end{pmatrix}\right]^2 \left|b_{-2,L} - (-1)^{\ell+\ell_1+\ell_2}\, b_{2,L}\right|^2 \tag{E.20d}$$

$$\sum_{m_1,m_2} \mathcal{G}^{(4)}_{L_1L_2}\mathcal{G}^{(4)*}_{L_1L_2} =$$

$$= \frac{(2\ell_1+1)(2\ell_2+1)}{4\pi}\sum_{\ell m}\left[\begin{pmatrix}\ell_1 & \ell & \ell_2\\ -2 & 2 & 0\end{pmatrix}\right]^2 \left|b_{-2,L} + (-1)^{\ell+\ell_1+\ell_2}\, b_{2,L}\right|^2 ; \tag{E.20e}$$

$$\sum_{m_1,m_2} \mathcal{G}^{(1)}_{L_1L_2}\mathcal{G}^{(3)*}_{L_1L_2} =$$

$$= \frac{(2\ell_1+1)(2\ell_2+1)}{4\pi}\sum_{\substack{\ell m\\ \ell_1+\ell_2+\ell\,\text{odd}}}\begin{pmatrix}\ell_1 & \ell & \ell_2\\ -2 & 0 & 2\end{pmatrix}\begin{pmatrix}\ell_1 & \ell & \ell_2\\ -2 & 2 & 0\end{pmatrix} b_{V,L}\left(b^*_{-2,L} + b^*_{2,L}\right); \tag{E.20f}$$

$$\sum_{m_1,m_2} \mathcal{G}^{(1)}_{L_1L_2}\mathcal{G}^{(4)*}_{L_1L_2} =$$

$$= i\,\frac{(2\ell_1+1)(2\ell_2+1)}{4\pi}\sum_{\substack{\ell m\\ \ell_1+\ell_2+\ell\,\text{odd}}}\begin{pmatrix}\ell_1 & \ell & \ell_2\\ -2 & 0 & 2\end{pmatrix}\begin{pmatrix}\ell_1 & \ell & \ell_2\\ -2 & 2 & 0\end{pmatrix} b_{V,L}\left(b^*_{-2,L} - b^*_{2,L}\right); \tag{E.20g}$$

$$\sum_{m_1,m_2} \mathcal{G}^{(2)}_{L_1L_2}\mathcal{G}^{(3)*}_{L_1L_2} =$$

$$= -i\,\frac{(2\ell_1+1)(2\ell_2+1)}{4\pi}\sum_{\substack{\ell m\\ \ell_1+\ell_2+\ell\,\text{even}}}\begin{pmatrix}\ell_1 & \ell & \ell_2\\ -2 & 0 & 2\end{pmatrix}\begin{pmatrix}\ell_1 & \ell & \ell_2\\ -2 & 2 & 0\end{pmatrix} b_{V,L}\left(b^*_{-2,L} - b^*_{2,L}\right); \tag{E.20h}$$

$$\sum_{m_1,m_2} \mathcal{G}^{(2)}_{L_1L_2}\mathcal{G}^{(4)*}_{L_1L_2} =$$

$$= \frac{(2\ell_1+1)(2\ell_2+1)}{4\pi} \sum_{\substack{\ell m \\ \ell_1+\ell_2+\ell \,\text{even}}} \begin{pmatrix} \ell_1 & \ell & \ell_2 \\ -2 & 0 & 2 \end{pmatrix} \begin{pmatrix} \ell_1 & \ell & \ell_2 \\ -2 & 2 & 0 \end{pmatrix} b_{V,L} \left(b^*_{-2,L} + b^*_{2,L} \right) ; \tag{E.20i}$$

$$\vdots$$

$\mathcal{K}$'s kernels We have defined the $\mathcal{K}$ kernels as

$$\mathcal{K}^{a\,b}_{\ell_1\ell} = (2\ell+1)^{-1} \sum_{m_1,m} \mathcal{G}^{(a)}_{L_1L}\mathcal{G}^{(b)*}_{L_1L} , \tag{E.21}$$

so that,

$$\mathcal{K}^{11}_{\ell_1\ell} = \frac{1}{2\ell+1}\sum_{m_1,m}\mathcal{G}^{(1)}_{L_1L}\mathcal{G}^{(1)*}_{L_1L} =$$

$$= \frac{2\ell_1+1}{4\pi}\sum_{\substack{L_2\\ \ell_1+\ell_2+\ell\,\text{odd}}}\left[\begin{pmatrix}\ell_1 & \ell_2 & \ell\\ -2 & 0 & 2\end{pmatrix}\right]^2 |b_{V,L_2}|^2\ ; \tag{E.22a}$$

$$\mathcal{K}^{22}_{\ell_1\ell} = \frac{1}{2\ell+1}\sum_{m_1,m}\mathcal{G}^{(2)}_{L_1L}\mathcal{G}^{(2)*}_{L_1L} =$$

$$= \frac{2\ell_1+1}{4\pi}\sum_{\substack{L_2\\ \ell_1+\ell_2+\ell\,\text{even}}}\left[\begin{pmatrix}\ell_1 & \ell_2 & \ell\\ -2 & 0 & 2\end{pmatrix}\right]^2 |b_{V,L_2}|^2; \tag{E.22b}$$

$$\mathcal{K}^{13}_{\ell_1\ell} = \frac{1}{2\ell+1}\sum_{m_1,m}\mathcal{G}^{(1)}_{L_1L}\mathcal{G}^{(3)*}_{L_1L} =$$

$$= \frac{2\ell_1+1}{4\pi}\sum_{\substack{L_2\\ \ell_1+\ell_2+\ell\,\text{odd}}}\begin{pmatrix}\ell_1 & \ell_2 & \ell\\ -2 & 0 & 2\end{pmatrix}\begin{pmatrix}\ell_1 & \ell_2 & \ell\\ -2 & 2 & 0\end{pmatrix} b_{V,L_2}\left(b^*_{-2,L_2}+b^*_{2,L_2}\right)\ ; \tag{E.22c}$$

$$\mathcal{K}^{23}_{\ell_1\ell} = \frac{1}{2\ell+1}\sum_{m_1,m}\mathcal{G}^{(2)}_{L_1L}\mathcal{G}^{(3)*}_{L_1L} =$$

$$= -i\,\frac{2\ell_1+1}{4\pi}\sum_{\substack{L_2\\ \ell_1+\ell_2+\ell\,\text{even}}}\begin{pmatrix}\ell_1 & \ell_2 & \ell\\ -2 & 0 & 2\end{pmatrix}\begin{pmatrix}\ell_1 & \ell_2 & \ell\\ -2 & 2 & 0\end{pmatrix} b_{V,L_2}\left(b^*_{-2,L_2}-\ b^*_{2,L_2}\right); \tag{E.22d}$$

$$\mathcal{K}^{24}_{\ell_1\ell} = \frac{1}{2\ell+1}\sum_{m_1,m}\mathcal{G}^{(2)}_{L_1L}\mathcal{G}^{(4)*}_{L_1L} =$$

$$= \frac{2\ell_1+1}{4\pi}\sum_{\substack{L_2\\ \ell_1+\ell_2+\ell\,\text{even}}}\begin{pmatrix}\ell_1 & \ell_2 & \ell\\ -2 & 0 & 2\end{pmatrix}\begin{pmatrix}\ell_1 & \ell_2 & \ell\\ -2 & 2 & 0\end{pmatrix} b_{V,L_2}\left(b^*_{-2,L_2}+\ b^*_{2,L_2}\right); \tag{E.22e}$$

$$\mathcal{K}^{14}_{\ell_1\ell} = \frac{1}{2\ell+1}\sum_{m_1,m}\mathcal{G}^{(1)}_{L_1L}\mathcal{G}^{(4)*}_{L_1L} =$$

$$= i\,\frac{2\ell_1+1}{4\pi}\sum_{\substack{L_2\\ \ell_1+\ell_2+\ell\,\mathrm{odd}}}\begin{pmatrix}\ell_1 & \ell_2 & \ell\\ -2 & 0 & 2\end{pmatrix}\begin{pmatrix}\ell_1 & \ell_2 & \ell\\ -2 & 2 & 0\end{pmatrix} b_{V,L_2}\left(b^*_{-2,L_2} - b^*_{2,L_2}\right); \quad \text{(E.22f)}$$

$$\mathcal{K}^{33}_{\ell_1\ell} = \frac{1}{2\ell+1}\sum_{m_1,m}\mathcal{G}^{(3)}_{L_1L}\mathcal{G}^{(3)*}_{L_1L} =$$

$$= \frac{2\ell_1+1}{4\pi}\sum_{L_2}\left[\begin{pmatrix}\ell_1 & \ell_2 & \ell\\ -2 & 2 & 0\end{pmatrix}\right]^2\left|b_{-2,L_2} - (-1)^{\ell+\ell_1+\ell_2}\,b_{2,L_2}\right|^2; \quad \text{(E.22g)}$$

$$\mathcal{K}^{44}_{\ell_1\ell} = \frac{1}{2\ell+1}\sum_{m_1,m}\mathcal{G}^{(4)}_{L_1L}\mathcal{G}^{(4)*}_{L_1L} =$$

$$= \frac{2\ell_1+1}{4\pi}\sum_{L_2}\left[\begin{pmatrix}\ell_1 & \ell_2 & \ell\\ -2 & 2 & 0\end{pmatrix}\right]^2\left|b_{-2,L_2} + (-1)^{\ell+\ell_1+\ell_2}\,b_{2,L_2}\right|^2, \quad \text{(E.22h)}$$

Bibliography

[1] Arno A. Penzias and Robert Woodrow Wilson. A Measurement of excess antenna temperature at 4080-Mc/s. *Astrophys. J.*, 142:419–421, 1965.

[2] Francois R. Bouchet. Looking at the universe with Planck. *PoS*, ICHEP2010:532, 2010.

[3] C.L. Bennett et al. The Microwave Anisotropy Probe (MAP) mission. *Astrophys. J.*, 583:1–23, 2003.

[4] J.M. Nagy et al. A New Limit on CMB Circular Polarization from SPIDER. *Astrophys. J.*, 844(2):151, 2017.

[5] R. Mainini, D. Minelli, M. Gervasi, G. Boella, G. Sironi, A. Baú, S. Banfi, A. Passerini, A. De Lucia, and F. Cavaliere. An improved upper limit to the CMB circular polarization at large angular scales. *JCAP*, 08:033, 2013.

[6] N. Aghanim et al. Planck 2018 results. I. Overview and the cosmological legacy of Planck. *Astron. Astrophys.*, 641:A1, 2020.

[7] H. Ishino et al. LiteBIRD: lite satellite for the study of B-mode polarization and inflation from cosmic microwave background radiation detection. *Proc. SPIE Int. Soc. Opt. Eng.*, 9904:99040X, 2016.

[8] Peter Ade et al. The Simons Observatory: Science goals and forecasts. *JCAP*, 02:056, 2019.

[9] Kevork N. Abazajian et al. CMB-S4 Science Book, First Edition. 10 2016.

[10] N. Aghanim et al. Planck 2018 results. VIII. Gravitational lensing. *Astron. Astrophys.*, 641:A8, 2020.

[11] Margherita Lembo, Massimiliano Lattanzi, Luca Pagano, Alessandro Gruppuso, Paolo Natoli, and Francesco Forastieri. Through a dark crystal: CMB polarization as a tool to constrain the optical properties of the Universe. 7 2020.

[12] G. Fabbian, J. Carron, A. Lewis, and M. Lembo. Lensed CMB power spectrum biases from masking extragalactic sources. 11 2020.

[13] Margherita Lembo, Giulio Fabbian, Julien Carron, and Antony Lewis. CMB lensing reconstruction biases from masking extragalactic sources. in prep.

[14] Ralph A. Alpher and Robert Herman. Evolution of the Universe. *Nature*, 162(4124):774–775, 1948.

[15] G. Gamow. The Evolution of the Universe. *Nature*, 162(4122):680–682, 1948.

[16] F.R. Bouchet et al. COrE: Cosmic Origins Explorer - A White Paper. 2015.

[17] Erik M. Leitch, J.M. Kovac, C. Pryke, B. Reddall, E.S. Sandberg, M. Dragovan, J.E. Carlstrom, N.W. Halverson, and W.L. Holzapfel. Measuring polarization with DASI. *Nature*, 420:763–771, 2002.

[18] Uros Seljak and Matias Zaldarriaga. A Line of sight integration approach to cosmic microwave background anisotropies. *Astrophys. J.*, 469:437–444, 1996.

[19] L. Knox, N. Christensen, and C. Skordis. The age of the universe and the cosmological constant determined from cosmic microwave background anisotropy measurements. *Astrophys. J. Lett.*, 563:L95–L98, 2001.

[20] Alexei A. Starobinsky. Multicomponent de Sitter (Inflationary) Stages and the Generation of Perturbations. *JETP Lett.*, 42:152–155, 1985.

[21] Andrei D. Linde. A New Inflationary Universe Scenario: A Possible Solution of the Horizon, Flatness, Homogeneity, Isotropy and Primordial Monopole Problems. *Adv. Ser. Astrophys. Cosmol.*, 3:149–153, 1987.

[22] Alan H. Guth. The Inflationary Universe: A Possible Solution to the Horizon and Flatness Problems. *Adv. Ser. Astrophys. Cosmol.*, 3:139–148, 1987.

[23] William H. Kinney. TASI Lectures on Inflation. 2 2009.

[24] Andrei D. Linde. *Particle physics and inflationary cosmology*, volume 5. 1990.

[25] Peter W. Higgs. Broken Symmetries and the Masses of Gauge Bosons. *Phys. Rev. Lett.*, 13:508–509, 1964.

[26] D. Boyanovsky. Phase transitions in the early and the present universe: From the big bang to heavy ion collisions. In *International School of Astrophysics 'Daniel Chalonge' 8th Course: Opening the 3rd Millennium, Phase Transitions in the Early Unverse: Theory and Observations*, pages 3–44, 2 2001.

[27] Gary Steigman. Big bang nucleosynthesis: Current status. In *2nd Oak Ridge Symposium on Atomic and Nuclear Astrophysics*, 3 1998.

[28] Maxim Pospelov and Josef Pradler. Big Bang Nucleosynthesis as a Probe of New Physics. *Ann. Rev. Nucl. Part. Sci.*, 60:539–568, 2010.

[29] Scott Dodelson. *Modern Cosmology.* Academic Press, Amsterdam, 2003.

[30] Arthur Kosowsky. Cosmic microwave background polarization. *Annals Phys.*, 246:49–85, 1996.

[31] Steven Weinberg. *Cosmology.* 9 2008.

[32] Paolo Cabella and Marc Kamionkowski. Theory of cosmic microwave background polarization. In *International School of Gravitation and Cosmology: The Polarization of the Cosmic Microwave Background*, 3 2004.

[33] Matias Zaldarriaga and Uros Seljak. An all sky analysis of polarization in the microwave background. *Phys. Rev. D*, 55:1830–1840, 1997.

[34] Arthur Kosowsky and Abraham Loeb. Faraday rotation of microwave background polarization by a primordial magnetic field. *The Astrophysical Journal*, 469:1, Sep 1996.

[35] Asantha Cooray, Alessandro Melchiorri, and Joseph Silk. Is the cosmic microwave background circularly polarized? *Physics Letters B*, 554(1):1 – 6, 2003.

[36] Massimo Giovannini. v-mode polarization of the cosmic microwave background. *Phys. Rev. D*, 80:123013, Dec 2009.

[37] Paulo Montero-Camacho and Christopher M. Hirata. Exploring circular polarization in the CMB due to conventional sources of cosmic birefringence. *JCAP*, 08:040, 2018.

[38] N. Lemarchand, J. Grain, G. Hurier, F. Lacasa, and A. Ferté. Secondary CMB anisotropies from magnetized haloes - I. Power spectra of the Faraday rotation angle and conversion rate. *Astron. Astrophys.*, 630:A149, 2019.

[39] M. Zarei, E. Bavarsad, M. Haghighat, R. Mohammadi, I. Motie, and Z. Rezaei. Generation of circular polarization of the cmb. *Phys. Rev. D*, 81:084035, Apr 2010.

[40] Stephon Alexander, Joseph Ochoa, and Arthur Kosowsky. Generation of Circular Polarization of the Cosmic Microwave Background. *Phys. Rev. D*, 79:063524, 2009.

[41] Stephon Alexander, Evan McDonough, Anthony Pullen, and Bradley Shapiro. Physics beyond the standard model with circular polarization in the CMB and CMB-21cm cross-correlation. *Journal of Cosmology and Astroparticle Physics*, 2020(01):032–032, jan 2020.

[42] Stephon Alexander and Evan McDonough. Primordial circular polarization in the cosmic microwave background. *Physics Letters B*, 789:197 – 202, 2019.

[43] Mahdi Sadegh, Rohoollah Mohammadi, and Iman Motie. Generation of circular polarization in cmb radiation via nonlinear photon-photon interaction. *Phys. Rev. D*, 97:023023, Jan 2018.

[44] Keisuke Inomata and Marc Kamionkowski. Circular polarization of the cosmic microwave background from vector and tensor perturbations. *Phys. Rev. D*, 99:043501, Feb 2019.

[45] Ali Vahedi, Jafar Khodagholizadeh, Rohoollah Mohammadi, and Mahdi Sadegh. Generation of circular polarization of CMB via polarized compton scattering. *Journal of Cosmology and Astroparticle Physics*, 2019(01):052–052, jan 2019.

[46] Nicola Bartolo, Ahmad Hoseinpour, Sabino Matarrese, Giorgio Orlando, and Moslem Zarei. Cmb circular and b-mode polarization from new interactions. *Phys. Rev. D*, 100:043516, Aug 2019.

[47] Nicola Bartolo, Ahmad Hoseinpour, Sabino Matarrese, Giorgio Orlando, and Moslem Zarei. CMB V modes from photon-photon forward scattering revisited. 6 2020.

[48] Jun John Sakurai and Jim Napolitano. *Modern Quantum Mechanics*. Quantum physics, quantum information and quantum computation. Cambridge University Press, Cambridge, 2017.

[49] J. D. Barrow. On the origin of cosmic turbulence. *"Mon. Not. Roy. Astron. Soc."*, 179:47P–49P, May 1977.

[50] Chung-Pei Ma and Edmund Bertschinger. Cosmological perturbation theory in the synchronous and conformal Newtonian gauges. *Astrophys. J.*, 455:7–25, 1995.

[51] R.A. Frewin, A.G. Polnarev, and P. Coles. Gravitational waves and the polarization of the cosmic microwave background. *Mon. Not. Roy. Astron. Soc.*, 266:L21, 1994.

[52] Antony Lewis, Anthony Challinor, and Anthony Lasenby. Efficient computation of cosmic microwave background anisotropies in closed friedmann-robertson-walker models. *The Astrophysical Journal*, 538(2):473–476, aug 2000.

[53] Patrick Peter and Jean-Philippe Uzan. *Primordial Cosmology*. Oxford Graduate Texts. Oxford University Press, 2 2013.

[54] John David Jackson. *Classical Electrodynamics*. Wiley, 1998.

[55] N. Aghanim et al. Planck 2018 results. VI. Cosmological parameters. 7 2018.

[56] R. K. Sachs and A. M. Wolfe. Perturbations of a cosmological model and angular variations of the microwave background. *Astrophys. J.*, 147:73–90, 1967.

[57] Joseph Silk. Cosmic black body radiation and galaxy formation. *Astrophys. J.*, 151:459–471, 1968.

[58] Wayne Hu and Naoshi Sugiyama. The Small scale integrated Sachs-Wolfe effect. *Phys. Rev. D*, 50:627–631, 1994.

[59] M. J. Rees and D. W. Sciama. Large scale Density Inhomogeneities in the Universe. *Nature*, 217:511–516, 1968.

[60] Scott Dodelson and Jay M. Jubas. Reionization and its imprint on the cosmic microwave background. *Astrophys. J.*, 439:503–516, 1995.

[61] Wayne Hu, Douglas Scott, and Joseph Silk. Reionization and cosmic microwave background distortions: A Complete treatment of second order Compton scattering. *Phys. Rev. D*, 49:648–670, 1994.

[62] Naoshi Sugiyama, Joseph Silk, and Nicola Vittorio. Reionization and cosmic microwave anisotropies. *Astrophys. J. Lett.*, 419:L1, 1993.

[63] N. Aghanim et al. Planck 2013 results. XXVII. Doppler boosting of the CMB: Eppur si muove. *Astron. Astrophys.*, 571:A27, 2014.

[64] R. A. Sunyaev and Ya. B. Zeldovich. The Velocity of clusters of galaxies relative to the microwave background. The Possibility of its measurement. *Mon. Not. Roy. Astron. Soc.*, 190:413–420, 1980.

[65] Nick Hand et al. Evidence of Galaxy Cluster Motions with the Kinematic Sunyaev-Zel'dovich Effect. *Phys. Rev. Lett.*, 109:041101, 2012.

[66] Max Tegmark, Daniel J. Eisenstein, Wayne Hu, and Angelica de Oliveira-Costa. Foregrounds and forecasts for the cosmic microwave background. *Astrophys. J.*, 530:133–165, 2000.

[67] Clive Dickinson. CMB foregrounds - A brief review. In *51st Rencontres de Moriond on Cosmology*, pages 53–62, 6 2016.

[68] Arthur Kosowsky, Milos Milosavljevic, and Raul Jimenez. Efficient cosmological parameter estimation from microwave background anisotropies. *Phys. Rev. D*, 66:063007, 2002.

[69] O.W. Greenberg. CPT violation implies violation of Lorentz invariance. *Phys. Rev. Lett.*, 89:231602, 2002.

[70] Luca Pagano, Paolo de Bernardis, Grazia De Troia, Giulia Gubitosi, Silvia Masi, Alessandro Melchiorri, Paolo Natoli, Francesco Piacentini, and Gianluca Polenta. CMB Polarization Systematics, Cosmological Birefringence and the Gravitational Waves Background. *Phys. Rev. D*, 80:043522, 2009.

[71] Damian Ejlli. On the CMB circular polarization: I. The Cotton–Mouton effect. *Eur. Phys. J. C*, 79(3):231, 2019.

[72] Chiara Caprini, Ruth Durrer, and Tina Kahniashvili. The Cosmic microwave background and helical magnetic fields: The Tensor mode. *Phys. Rev. D*, 69:063006, 2004.

[73] Sean M. Carroll, George B. Field, and Roman Jackiw. Limits on a Lorentz and Parity Violating Modification of Electrodynamics. *Phys. Rev. D*, 41:1231, 1990.

[74] Sean M. Carroll. Quintessence and the rest of the world. *Phys. Rev. Lett.*, 81:3067–3070, 1998.

[75] Mingzhe Li and Xinmin Zhang. Cosmological CPT violating effect on CMB polarization. *Phys. Rev. D*, 78:103516, 2008.

[76] Maxim Pospelov, Adam Ritz, Constantinos Skordis, Adam Ritz, and Constantinos Skordis. Pseudoscalar perturbations and polarization of the cosmic microwave background. *Phys. Rev. Lett.*, 103:051302, 2009.

[77] Arthur Kosowsky and Abraham Loeb. Faraday rotation of microwave background polarization by a primordial magnetic field. *Astrophys. J.*, 469:1–6, 1996.

[78] Claudia Scoccola, Diego Harari, and Silvia Mollerach. B polarization of the CMB from Faraday rotation. *Phys. Rev. D*, 70:063003, 2004.

[79] L. Campanelli, A.D. Dolgov, M. Giannotti, and F.L. Villante. Faraday rotation of the CMB polarization and primordial magnetic field properties. *Astrophys. J.*, 616:1–7, 2004.

[80] Giulia Gubitosi, Matteo Martinelli, and Luca Pagano. Including birefringence into time evolution of CMB: current and future constraints. *JCAP*, 12:020, 2014.

[81] A. Gruppuso, M. Gerbino, P. Natoli, L. Pagano, N. Mandolesi, A. Melchiorri, and D. Molinari. Constraints on cosmological birefringence from Planck and Bicep2/Keck data. *JCAP*, 06:001, 2016.

[82] N. Aghanim et al. Planck intermediate results. XLIX. Parity-violation constraints from polarization data. *Astron. Astrophys.*, 596:A110, 2016.

[83] Yuto Minami and Eiichiro Komatsu. New Extraction of the Cosmic Birefringence from the Planck 2018 Polarization Data. *Phys. Rev. Lett.*, 125(22):221301, 2020.

[84] Yuto Minami, Hiroki Ochi, Kiyotomo Ichiki, Nobuhiko Katayama, Eiichiro Komatsu, and Tomotake Matsumura. Simultaneous determination of the cosmic birefringence and miscalibrated polarization angles from CMB experiments. *PTEP*, 2019(8):083E02, 2019.

[85] Yuto Minami. Determination of miscalibrated polarization angles from observed cosmic microwave background and foreground EB power spectra: Application to partial-sky observation. *PTEP*, 2020(6):063E01, 2020.

[86] Arthur Kosowsky, Tina Kahniashvili, George Lavrelashvili, and Bharat Ratra. Faraday rotation of the Cosmic Microwave Background polarization by a stochastic magnetic field. *Phys. Rev. D*, 71:043006, 2005.

[87] Alessandro Gruppuso, Diego Molinari, Paolo Natoli, and Luca Pagano. Planck 2018 constraints on anisotropic birefringence and its cross-correlation with CMB anisotropy. 8 2020.

[88] Soma De and Hiroyuki Tashiro. Circular Polarization of the CMB: A probe of the First stars. *Phys. Rev. D*, 92(12):123506, 2015.

[89] Iman Motie and She-Sheng Xue. Euler-Heisenberg Lagrangian and Photon Circular Polarization. *EPL*, 100(1):17006, 2012.

[90] R.F. Sawyer. Photon-photon interactions can be a source of CMB circular polarization. 8 2014.

[91] Rohoollah Mohammadi. Evidence for cosmic neutrino background form CMB circular polarization. *Eur. Phys. J. C*, 74(10):3102, 2014.

[92] E. Bavarsad, M. Haghighat, Z. Rezaei, R. Mohammadi, I. Motie, and M. Zarei. Generation of circular polarization of the CMB. *Phys. Rev. D*, 81:084035, 2010.

[93] Don Colladay and V.Alan Kostelecky. Lorentz violating extension of the standard model. *Phys. Rev. D*, 58:116002, 1998.

[94] Fabio Finelli and Matteo Galaverni. Rotation of Linear Polarization Plane and Circular Polarization from Cosmological Pseudo-Scalar Fields. *Phys. Rev. D*, 79:063002, 2009.

[95] Stephon Alexander, Evan McDonough, and Robert Sims. V-mode Polarization in Axion Inflation and Preheating. *Phys. Rev. D*, 96(6):063506, 2017.

[96] Damian Ejlli. Millicharged fermion vacuum polarization in a cosmic magnetic field and generation of CMB elliptic polarization. *Phys. Rev. D*, 96(2):023540, 2017.

[97] Damian Ejlli. Magneto-optic effects of the cosmic microwave background. *Nucl. Phys. B*, 935:83–128, 2018.

[98] Nicola Bartolo, Ahmad Hoseinpour, Sabino Matarrese, Giorgio Orlando, and Moslem Zarei. CMB Circular and B-mode Polarization from New Interactions. *Phys. Rev. D*, 100(4):043516, 2019.

[99] Sean Alan Bryan. Half-wave Plates for the Spider Cosmic Microwave Background Polarimeter. Other thesis, 2 2014.

[100] Sean A. Bryan, Thomas E. Montroy, and John E. Ruhl. Modeling dielectric half-wave plates for cosmic microwave background polarimetry using a Mueller matrix formalism. *Appl. Opt.*, 49:6313–6323, 2010.

[101] Ivan L. Padilla et al. Two-year Cosmology Large Angular Scale Surveyor (CLASS) Observations: A Measurement of Circular Polarization at 40 GHz. 11 2019.

[102] V. N. Sazonov and V. N. Tsytovich. Polarization effects during generation and radiation transfer of relativistic electrons in a magnetoactive plasma. *Radiophysics and Quantum Electronics*, 11(9):731–737, September 1968.

[103] V. N. Sazonov. Generation and Transfer of Polarized Synchrotron Radiation. *Sov. Astr.*, 13:396, Dec 1969.

[104] Donald Melrose. *Quantum Plasmadynamics*, volume 854. 2013.

[105] D. B. Melrose and R. C. McPhedran. *Electromagnetic Processes in Dispersive Media*. 2005.

[106] N. Aghanim et al. Planck 2018 results. V. CMB power spectra and likelihoods. 7 2019.

[107] P. A. R. Ade et al. Constraints on primordial gravitational waves using *planck*, wmap, and new bicep2/*keck* observations through the 2015 season. *Phys. Rev. Lett.*, 121:221301, Nov 2018.

[108] P. A. R. Ade et al. Joint Analysis of BICEP2/*KeckArray* and *Planck* Data. *Phys. Rev. Lett.*, 114:101301, 2015.

[109] Antony Lewis and Sarah Bridle. Cosmological parameters from cmb and other data: A monte carlo approach. *Phys. Rev. D*, 66:103511, Nov 2002.

[110] Andrew Gelman and Donald B. Rubin. Inference from Iterative Simulation Using Multiple Sequences. *Statist. Sci.*, 7:457–472, 1992.

[111] Thomas Essinger-Hileman et al. CLASS: the cosmology large angular scale surveyor. 9153:491 – 513, 2014.

[112] Antony Lewis and Anthony Challinor. Weak gravitational lensing of the CMB. *Phys. Rept.*, 429:1–65, 2006.

[113] Daniel Baumann. Inflation. In *Theoretical Advanced Study Institute in Elementary Particle Physics: Physics of the Large and the Small*, pages 523–686, 2011.

[114] Matthias Bartelmann and Peter Schneider. Weak gravitational lensing. *Phys. Rept.*, 340:291–472, 2001.

[115] Anthony Challinor and Antony Lewis. Lensed CMB power spectra from all-sky correlation functions. *Phys. Rev. D*, 71:103010, 2005.

[116] Gayoung Chon, Anthony Challinor, Simon Prunet, Eric Hivon, and Istvan Szapudi. Fast estimation of polarization power spectra using correlation functions. *Mon. Not. Roy. Astron. Soc.*, 350:914, 2004.

[117] Wayne Hu and Takemi Okamoto. Mass reconstruction with cmb polarization. *Astrophys. J.*, 574:566–574, 2002.

[118] Takemi Okamoto and Wayne Hu. CMB lensing reconstruction on the full sky. *Phys. Rev. D*, 67:083002, 2003.

[119] Michael H. Kesden, Asantha Cooray, and Marc Kamionkowski. Lensing reconstruction with CMB temperature and polarization. *Phys. Rev. D*, 67:123507, 2003.

[120] Giulio Fabbian, Antony Lewis, and Dominic Beck. CMB lensing reconstruction biases in cross-correlation with large-scale structure probes. *JCAP*, 10:057, 2019.

[121] A. van Engelen, S. Bhattacharya, N. Sehgal, G.P. Holder, O. Zahn, and D. Nagai. CMB Lensing Power Spectrum Biases from Galaxies and Clusters using High-angular Resolution Temperature Maps. *Astrophys. J.*, 786:13, 2014.

[122] Stephen J. Osborne, Duncan Hanson, and Olivier Doré. Extragalactic Foreground Contamination in Temperature-based CMB Lens Reconstruction. *JCAP*, 03:024, 2014.

[123] Mathew S. Madhavacheril and J. Colin Hill. Mitigating Foreground Biases in CMB Lensing Reconstruction Using Cleaned Gradients. *Phys. Rev. D*, 98(2):023534, 2018.

[124] Omar Darwish et al. The Atacama Cosmology Telescope: A CMB lensing mass map over 2100 square degrees of sky and its cross-correlation with BOSS-CMASS galaxies. 4 2020.

[125] Emmanuel Schaan and Simone Ferraro. Foreground-Immune Cosmic Microwave Background Lensing with Shear-Only Reconstruction. *Phys. Rev. Lett.*, 122(18):181301, 2019.

[126] George Stein, Marcelo A. Alvarez, J. Richard Bond, Alexander van Engelen, and Nicholas Battaglia. The Websky Extragalactic CMB Simulations. *JCAP*, 10:012, 2020.

[127] George Stein, Marcelo A. Alvarez, and J. Richard Bond. The mass-Peak Patch algorithm for fast generation of deep all-sky dark matter halo catalogues and its N-Body validation. *Mon. Not. Roy. Astron. Soc.*, 483(2):2236–2250, 2019.

[128] J.R. Bond and S.T. Myers. The Hierarchical peak patch picture of cosmic catalogs. 1. Algorithms. *Astrophys. J. Suppl.*, 103:1, 1996.

[129] M.P. Viero et al. HerMES: Cosmic Infrared Background Anisotropies and the Clustering of Dusty Star-Forming Galaxies. *Astrophys. J.*, 772:77, 2013.

[130] Yong-Seon Song, Asantha Cooray, Lloyd Knox, and Matias Zaldarriaga. The Far-infrared background correlation with CMB lensing. *Astrophys. J.*, 590:664–672, 2003.

[131] P.A.R. Ade et al. Planck 2015 results. XXIII. The thermal Sunyaev-Zeldovich effect–cosmic infrared background correlation. *Astron. Astrophys.*, 594:A23, 2016.

[132] N. Aghanim et al. Planck 2015 results. XXII. A map of the thermal Sunyaev-Zeldovich effect. *Astron. Astrophys.*, 594:A22, 2016.

[133] Mark Birkinshaw. The Sunyaev-Zel'dovich effect. *Phys. Rept.*, 310:97–195, 1999.

[134] John E. Carlstrom, Gilbert P. Holder, and Erik D. Reese. Cosmology with the Sunyaev-Zel'dovich effect. *Ann. Rev. Astron. Astrophys.*, 40:643–680, 2002.

[135] Tony Mroczkowski et al. Astrophysics with the Spatially and Spectrally Resolved Sunyaev-Zeldovich Effects: A Millimetre/Submillimetre Probe of the Warm and Hot Universe. *Space Sci. Rev.*, 215(1):17, 2019.

[136] William R. Coulton et al. Non-Gaussianity of secondary anisotropies from ACTPol and Planck. *JCAP*, 09:022, 2018.

[137] Leander Thiele, J. Colin Hill, and Kendrick M. Smith. Accurate analytic model for the thermal Sunyaev-Zel'dovich one-point probability distribution function. *Phys. Rev. D*, 99(10):103511, 2019.

[138] M. Hilton et al. The Atacama Cosmology Telescope: A Catalog of > 4000 Sunyaev-Zel'dovich Galaxy Clusters. 9 2020.

[139] L.E. Bleem et al. The SPTpol Extended Cluster Survey. *Astrophys. J. Suppl.*, 247(1):25, 2020.

[140] P.A.R. Ade et al. Planck 2015 results. XXVII. The Second Planck Catalogue of Sunyaev-Zeldovich Sources. *Astron. Astrophys.*, 594:A27, 2016.

[141] E. Hivon, K.M. Gorski, C.B. Netterfield, B.P. Crill, S. Prunet, and F. Hansen. Master of the cosmic microwave background anisotropy power spectrum: a fast method for statistical analysis of large and complex cosmic microwave background data sets. *Astrophys. J.*, 567:2, 2002.

[142] David Alonso, Javier Sanchez, and Anže Slosar. A unified pseudo-C_ℓ framework. *Mon. Not. Roy. Astron. Soc.*, 484(3):4127–4151, 2019.

[143] Julien Carron and Antony Lewis. Maximum a posteriori CMB lensing reconstruction. *Phys. Rev. D*, 96(6):063510, 2017.

[144] Duncan Hanson, Anthony Challinor, George Efstathiou, and Pawel Bielewicz. CMB temperature lensing power reconstruction. *Phys. Rev. D*, 83:043005, 2011.

[145] Antony Lewis, Anthony Challinor, and Duncan Hanson. The shape of the CMB lensing bispectrum. *JCAP*, 03:018, 2011.

[146] Kendrick M. Smith, Oliver Zahn, and Olivier Dore. Detection of Gravitational Lensing in the Cosmic Microwave Background. *Phys. Rev. D*, 76:043510, 2007.

[147] Moritz Münchmeyer and Kendrick M. Smith. Fast Wiener filtering of CMB maps with Neural Networks. 5 2019.

[148] Mark Mirmelstein, Julien Carron, and Antony Lewis. Optimal filtering for CMB lensing reconstruction. *Phys. Rev. D*, 100(12):123509, 2019.

[149] Toshiya Namikawa, Duncan Hanson, and Ryuichi Takahashi. Bias-Hardened CMB Lensing. *Mon. Not. Roy. Astron. Soc.*, 431:609–620, 2013.

[150] F. Bernardeau, S. Colombi, E. Gaztanaga, and R. Scoccimarro. Large scale structure of the universe and cosmological perturbation theory. *Phys. Rept.*, 367:1–248, 2002.

[151] Vanessa Böhm, Marcel Schmittfull, and Blake D. Sherwin. Bias to CMB lensing measurements from the bispectrum of large-scale structure. *Phys. Rev. D*, 94(4):043519, 2016.

[152] Vanessa Böhm, Blake D. Sherwin, Jia Liu, J. Colin Hill, Marcel Schmittfull, and Toshiya Namikawa. Effect of non-Gaussian lensing deflections on CMB lensing measurements. *Phys. Rev. D*, 98(12):123510, 2018.

[153] J.D. Vieira et al. Extragalactic millimeter-wave sources in South Pole Telescope survey data: source counts, catalog, and statistics for an 87 square-degree field. *Astrophys. J.*, 719:763–783, 2010.

[154] J.D. Vieira et al. Dusty starburst galaxies in the early Universe as revealed by gravitational lensing. *Nature*, 495:344, 2013.

[155] F. Bianchini et al. Cross-correlation between the CMB lensing potential measured by Planck and high-z sub-mm galaxies detected by the Herschel-ATLAS survey. *Astrophys. J.*, 802(1):64, 2015.

[156] Federico Bianchini et al. Toward a tomographic analysis of the cross-correlation between Planck CMB lensing and H-ATLAS galaxies. *Astrophys. J.*, 825(1):24, 2016.

[157] M. Aguilar Faúndez et al. Cross-correlation of POLARBEAR CMB Polarization Lensing with High-z Sub-mm Herschel-ATLAS galaxies. *Astrophys. J.*, 886(1):38, November 2019.

[158] C.L. Bennett et al. Nine-Year Wilkinson Microwave Anisotropy Probe (WMAP) Observations: Final Maps and Results. *Astrophys. J. Suppl.*, 208:20, 2013.

[159] Sudeep Das et al. The Atacama Cosmology Telescope: temperature and gravitational lensing power spectrum measurements from three seasons of data. *JCAP*, 04:014, 2014.

[160] Thibaut Louis et al. The Atacama Cosmology Telescope: Two-Season ACTPol Spectra and Parameters. *JCAP*, 06:031, 2017.

[161] Blake D. Sherwin et al. Two-season Atacama Cosmology Telescope polarimeter lensing power spectrum. *Phys. Rev. D*, 95(12):123529, 2017.

[162] E.M. George et al. A measurement of secondary cosmic microwave background anisotropies from the 2500-square-degree SPT-SZ survey. *Astrophys. J.*, 799(2):177, 2015.

[163] R. Keisler et al. Measurements of Sub-degree B-mode Polarization in the Cosmic Microwave Background from 100 Square Degrees of SPTpol Data. *Astrophys. J.*, 807(2):151, 2015.

[164] K.T. Story et al. A Measurement of the Cosmic Microwave Background Gravitational Lensing Potential from 100 Square Degrees of SPTpol Data. *Astrophys. J.*, 810(1):50, 2015.

[165] P.A.R. Ade et al. A Measurement of the Cosmic Microwave Background B-Mode Polarization Power Spectrum at Sub-Degree Scales from 2 years of POLARBEAR Data. *Astrophys. J.*, 848(2):121, 2017.

[166] P.A.R. Ade et al. BICEP2 / Keck Array V: Measurements of B-mode Polarization at Degree Angular Scales and 150 GHz by the Keck Array. *Astrophys. J.*, 811:126, 2015.

[167] P.A.R. Ade et al. Improved Constraints on Cosmology and Foregrounds from BICEP2 and Keck Array Cosmic Microwave Background Data with Inclusion of 95 GHz Band. *Phys. Rev. Lett.*, 116:031302, 2016.

[168] Adam G. Riess, Stefano Casertano, Wenlong Yuan, Lucas M. Macri, and Dan Scolnic. Large Magellanic Cloud Cepheid Standards Provide a 1% Foundation for the Determination of the Hubble Constant and Stronger Evidence for Physics beyond ΛCDM. *Astrophys. J.*, 876(1):85, 2019.

[169] Shahab Joudaki et al. KiDS-450 + 2dFLenS: Cosmological parameter constraints from weak gravitational lensing tomography and overlapping redshift-space galaxy clustering. *Mon. Not. Roy. Astron. Soc.*, 474(4):4894–4924, 2018.

[170] T.M.C. Abbott et al. Dark Energy Survey Year 1 Results: Cosmological constraints from cluster abundances and weak lensing. *Phys. Rev. D*, 102(2):023509, 2020.

[171] H. Hildebrandt et al. KiDS+VIKING-450: Cosmic shear tomography with optical and infrared data. *Astron. Astrophys.*, 633:A69, 2020.

[172] M. Rigault et al. Evidence of Environmental Dependencies of Type Ia Supernovae from the Nearby Supernova Factory indicated by Local Hα. *Astron. Astrophys.*, 560:A66, 2013.

[173] M. Rigault et al. Strong Dependence of Type Ia Supernova Standardization on the Local Specific Star Formation Rate. *Astron. Astrophys.*, 644:A176, 2020.

[174] D. O. Jones et al. Should Type Ia Supernova Distances be Corrected for their Local Environments? *Astrophys. J.*, 867(2):108, 2018.

[175] Tom Shanks, Lucy Hogarth, and Nigel Metcalfe. Gaia Cepheid parallaxes and 'Local Hole' relieve H_0 tension. *Mon. Not. Roy. Astron. Soc.*, 484(1):L64–L68, 2019.

[176] Adam G. Riess, Stefano Casertano, D'Arcy Kenworthy, Dan Scolnic, and Lucas Macri. Seven Problems with the Claims Related to the Hubble Tension in arXiv:1810.02595. 10 2018.

[177] W. D'Arcy Kenworthy, Dan Scolnic, and Adam Riess. The Local Perspective on the Hubble Tension: Local Structure Does Not Impact Measurement of the Hubble Constant. *Astrophys. J.*, 875(2):145, 2019.

[178] Hong-Jian He, Yin-Zhe Ma, and Jiaming Zheng. Resolving Hubble Tension by Self-Interacting Neutrinos with Dirac Seesaw. *JCAP*, 11:003, 2020.

[179] Maximilian Berbig, Sudip Jana, and Andreas Trautner. The Hubble tension and a renormalizable model of gauged neutrino self-interactions. *Phys. Rev. D*, 102(11):115008, 2020.

[180] Osamu Seto and Yo Toda. Comparing early dark energy and extra radiation solutions to the Hubble tension with BBN. 1 2021.

[181] Kevin Aylor, MacKenzie Joy, Lloyd Knox, Marius Millea, Srinivasan Raghunathan, and W. L. Kimmy Wu. Sounds Discordant: Classical Distance Ladder \& ΛCDM -based Determinations of the Cosmological Sound Horizon. *Astrophys. J.*, 874(1):4, 2019.

[182] Alireza Hojjati, Eric V. Linder, and Johan Samsing. New Constraints on the Early Expansion History of the Universe. *Phys. Rev. Lett.*, 111(4):041301, 2013.

[183] Vivian Poulin, Tristan L. Smith, Tanvi Karwal, and Marc Kamionkowski. Early Dark Energy Can Resolve The Hubble Tension. *Phys. Rev. Lett.*, 122(22):221301, 2019.

[184] Eleonora Di Valentino, Eric V. Linder, and Alessandro Melchiorri. Vacuum phase transition solves the H_0 tension. *Phys. Rev. D*, 97(4):043528, 2018.

[185] Francesco D'Eramo, Ricardo Z. Ferreira, Alessio Notari, and José Luis Bernal. Hot Axions and the H_0 tension. *JCAP*, 11:014, 2018.

[186] Kanhaiya L. Pandey, Tanvi Karwal, and Subinoy Das. Alleviating the H_0 and σ_8 anomalies with a decaying dark matter model. *JCAP*, 07:026, 2020.

[187] Kyriakos Vattis, Savvas M. Koushiappas, and Abraham Loeb. Dark matter decaying in the late Universe can relieve the H0 tension. *Phys. Rev. D*, 99(12):121302, 2019.

[188] Janina Renk, Miguel Zumalacárregui, Francesco Montanari, and Alexandre Barreira. Galileon gravity in light of ISW, CMB, BAO and H_0 data. *JCAP*, 10:020, 2017.

[189] Nima Khosravi, Shant Baghram, Niayesh Afshordi, and Natacha Altamirano. H_0 tension as a hint for a transition in gravitational theory. *Phys. Rev. D*, 99(10):103526, 2019.

[190] Christina D. Kreisch, Francis-Yan Cyr-Racine, and Olivier Doré. Neutrino puzzle: Anomalies, interactions, and cosmological tensions. *Phys. Rev. D*, 101(12):123505, 2020.

[191] Erminia Calabrese, Anze Slosar, Alessandro Melchiorri, George F. Smoot, and Oliver Zahn. Cosmic Microwave Weak lensing data as a test for the dark universe. *Phys. Rev. D*, 77:123531, 2008.

[192] M. Hazumi et al. LiteBIRD: A Satellite for the Studies of B-Mode Polarization and Inflation from Cosmic Background Radiation Detection. *J. Low Temp. Phys.*, 194(5-6):443–452, 2019.

[193] Kevork Abazajian et al. CMB-S4 Science Case, Reference Design, and Project Plan. 7 2019.

[194] Maximilian H. Abitbol et al. CMB-S4 Technology Book, First Edition. 6 2017.

[195] J. Delabrouille et al. Exploring cosmic origins with CORE: Survey requirements and mission design. *JCAP*, 04:014, 2018.

[196] Levon Pogosian, Meir Shimon, Matthew Mewes, and Brian Keating. Future CMB constraints on cosmic birefringence and implications for fundamental physics. *Phys. Rev. D*, 100(2):023507, 2019.

[197] K.N. Abazajian et al. Neutrino Physics from the Cosmic Microwave Background and Large Scale Structure. *Astropart. Phys.*, 63:66–80, 2015.

[198] M. Rotenberg. *The 3-j and 6-j Symbols: Manuel Rotenberg ... [et Al.].* Crosby Lockwood & Son, 1959.

[199] Joshua N. Goldberg. Invariant transformations and newman-penrose constants. *Journal of Mathematical Physics*, 8(11):2161–2166, 1967.

[200] Roger Penrose. *Conserved Quantities and Conformal Structure in General Relativity*, volume 8. 1967.

[201] Michael J. Wilson and Martin White. Cosmology with dropout selection: straw-man surveys \& CMB lensing. *JCAP*, 10:015, 2019.

[202] J. Gonzalez-Nuevo et al. Herschel-ATLAS: towards a sample of ~1000 strongly-lensed galaxies. *Astrophys. J.*, 749:65, 2012.

[203] Mattia Negrello et al. The Detection of a Population of Submillimeter-Bright, Strongly-Lensed Galaxies. *Science*, 330:800, 2010.

[204] F. Bianchini et al. Cross-correlation between the CMB lensing potential measured by Planck and high-z sub-mm galaxies detected by the Herschel-ATLAS survey. *Astrophys. J.*, 802(1):64, 2015.

[205] Federico Bianchini et al. Toward a tomographic analysis of the cross-correlation between Planck CMB lensing and H-ATLAS galaxies. *Astrophys. J.*, 825(1):24, 2016.

[206] M. Aguilar Faúndez et al. Cross-correlation of POLARBEAR CMB Polarization Lensing with High-z Sub-mm Herschel-ATLAS galaxies. 3 2019.

[207] J.D. Vieira et al. Dusty starburst galaxies in the early Universe as revealed by gravitational lensing. *Nature*, 495:344, 2013.

[208] N. Aghanim et al. Planck 2015 results. XI. CMB power spectra, likelihoods, and robustness of parameters. *Astron. Astrophys.*, 594:A11, 2016.

[209] J.T. Sayre et al. Measurements of B-mode Polarization of the Cosmic Microwave Background from 500 Square Degrees of SPTpol Data. *Phys. Rev. D*, 101(12):122003, 2020.

[210] J.W. Henning et al. Measurements of the Temperature and E-Mode Polarization of the CMB from 500 Square Degrees of SPTpol Data. *Astrophys. J.*, 852(2):97, 2018.

[211] P. Padovani et al. Active galactic nuclei: what's in a name? *Astron. Astrophys. Rev.*, 25(1):2, 2017.

[212] Gianfranco De Zotti, Marcella Massardi, Mattia Negrello, and Jasper Wall. Radio and Millimeter Continuum Surveys and their Astrophysical Implications. *Astron. Astrophys. Rev.*, 18:1–65, 2010.

[213] Kendrick M. Smith, Mathew S. Madhavacheril, Moritz Münchmeyer, Simone Ferraro, Utkarsh Giri, and Matthew C. Johnson. KSZ tomography and the bispectrum. 10 2018.

[214] Alan R. Duffy, Joop Schaye, Scott T. Kay, and Claudio Dalla Vecchia. Dark matter halo concentrations in the Wilkinson Microwave Anisotropy Probe year 5 cosmology. *Mon. Not. Roy. Astron. Soc.*, 390:L64, 2008. [Erratum: Mon.Not.Roy.Astron.Soc. 415, L85 (2011)].

[215] Asantha Cooray and Ravi K. Sheth. Halo Models of Large Scale Structure. *Phys. Rept.*, 372:1–129, 2002.

[216] P.A.R. Ade et al. Planck 2015 results. XV. Gravitational lensing. *Astron. Astrophys.*, 594:A15, 2016.

[217] Matias Zaldarriaga and Uros Seljak. Gravitational lensing effect on cosmic microwave background polarization. *Phys. Rev. D*, 58:023003, 1998.

[218] Daniel Baumann. Advanced Cosmology.

[219] Antony Lewis. Camb notes, 2011.

[220] James M. Cline. Baryogenesis. In *Les Houches Summer School - Session 86: Particle Physics and Cosmology: The Fabric of Spacetime*, 9 2006.